Technische Universität München

Max-Planck-Institut für Physik
(Werner-Heisenberg-Institut)

A Study of Cosmic Electrons between 100 GeV and 2 TeV with the MAGIC Telescopes

Daniela Borla Tridon

Vollständiger Abdruch der von der Fakultät für Physik der Technischen Universität München zur Erlangung des akademischen Grades eines

Doktors der Naturwissenschaften

genehmigten Dissertation.

Vorsitzender: Univ. - Prof. Dr. A. J. Buras
Pfüfer der Dissertation:

1. Hon. - Prof. Dr. S. Bethke
2. Univ. - Prof. Dr. L. Oberauer

Die Dissertation wurde am 21.06.2011 bei der Technischen Universität München eingereicht und durch die Fakultät für Physik am 13.09.2011 angenommen.

to my family

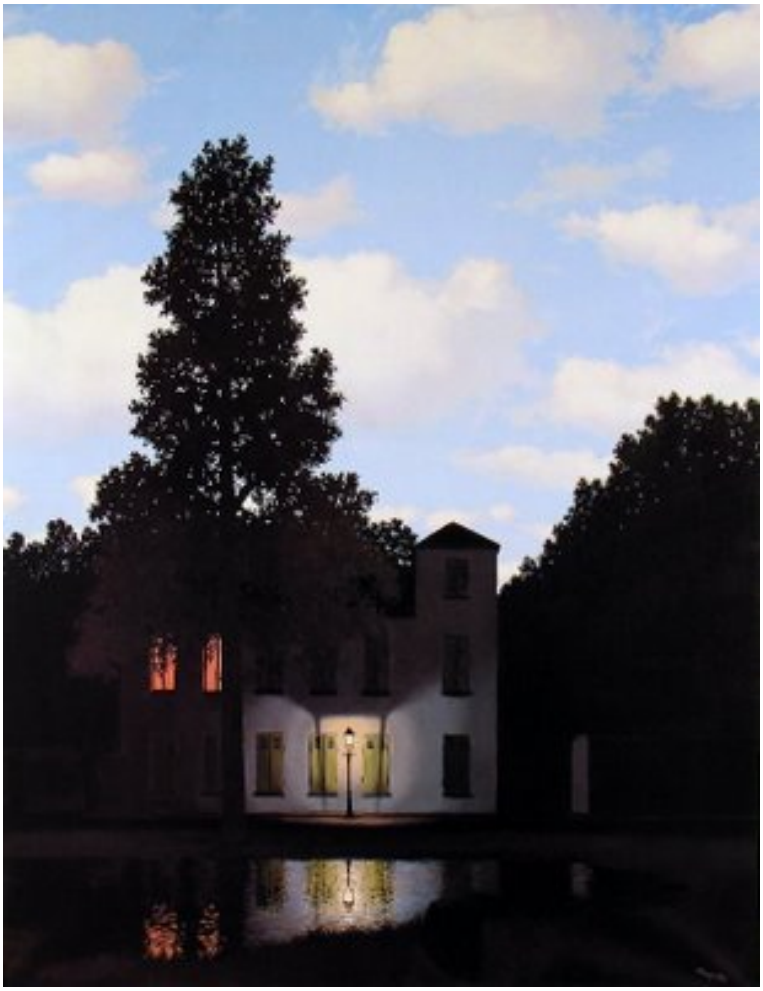

L'empire des lumieres
- Rene Magritte -

"Sometimes what we think
is impossible
is closer than we think."

-Abstract-

This thesis is motivated by open questions about the origin of the cosmic electrons. Unexpected features in the cosmic electron spectrum above 100 GeV measured by some experiments could point out to the presence of a possible, still unknown source of cosmic electrons. Many interpretations in terms of classical astrophysical objects or dark matter have been proposed.
Measurements of the electron spectrum by the Fermi, ATIC and H.E.S.S. experiments show a higher flux and harder spectrum than expected from secondary electrons produced in cosmic ray interactions within the galaxy. Nevertheless, discrepancies between the spectrum measured by Fermi, H.E.S.S. and ATIC have been found between 300 and 800 GeV. In this energy range the MAGIC stereo system is sensitive to the electron flux and can provide a new measurement. MAGIC is a ground-based system of two 17m Cherenkov telescopes that can measure cosmic electrons via the observation of the air showers generated by impinging particles in the atmosphere. Therefore, with a different method, MAGIC can provide an independent measurement of the cosmic electron spectrum.
My PhD studies, as a member of the MAGIC collaboration, involved new developments both of technical and scientific character. The technical activities involved the characterization and quality tests of photosensors for the camera of the second MAGIC telescope, brought into operation recently. A significant part of the thesis is, instead, devoted to the development of the analysis tools for the study of diffuse cosmic electrons, including extensive simulations of the hadronic cosmic ray background. In fact, since MAGIC normally observe γ-ray point sources, a new analysis tool had to be developed to be able to investigate diffuse cosmic electrons. This study, which was performed for the first time within the MAGIC experiment, is presented in this thesis. The new developed analysis technique is based on the identification of the electrons via the shape of the air shower (without any arrival direction, as in case of γ-ray point sources). A Random Forest classification method is used to discriminate electron from hadron showers and thus to reject the hadronic background in order to extract the electron signal. This new method can also be used in the analysis of γ-rays. It has been tested on a sample of Crab Nebula data. The obtained spectrum is compatible with the one resulting from the standard method used for γ-ray point source analysis. The first cosmic electron spectrum derived with MAGIC is well described by a simple power-law: $dF/dE = k(E/1\mathrm{TeV})^{-\Gamma}$, with $k = (1.47 \pm 0.21_{(stat)} \pm 0.44_{(syst)}) \times 10^{-7}\,\mathrm{GeV}^{-1}\mathrm{m}^{-2}\mathrm{s}^{-1}\mathrm{sr}^{-1}$ and $\Gamma = 3.00 \pm 0.12_{(stat)}$, in the energy range from ~ 100 GeV to ~ 2 TeV. Within the uncertainties, this result agrees with Fermi, H.E.S.S. and ATIC, confirming the presence of possible additional sources on top of the secondary cosmic electron produced in galactic cosmic ray interactions. Nevertheless, the feature of the electron spectrum measured by ATIC between 300 GeV and 800 GeV can neither be confirmed nor excluded by MAGIC, due to large uncertainties. The latter are mainly due to the Monte Carlo simulations which reproduce the background. Therefore, a larger simulation data set will reduce the statistical uncertainties significantly and would lead to a conclusive interpretation of the MAGIC cosmic electron spectrum.

-Zusammenfassung-

Zielsetzung dieser Doktorarbeit ist dazu beizutragen die noch offenen Fragen über die Quelle der kosmischen Elektronen zu klären, da einige Messungen ein unerwartetes Verhalten im Spektrum der kosmischen Elektronen oberhalb von 100GeV zeigten. Das beobachtete Verhalten deutet darauf hin, dass es für die kosmischen Elektronen eine noch unbekannte Quelle geben könnte. Als Ursprung der Elektronen werden sowohl klassische Astrophysikalische Objekte als auch die Dunkle Materie diskutiert. Messungen der Experimente Fermi, ATIC und H.E.S.S. weisen im Spektrum der kosmischen Elektronen einen höheren Fluss und ein härteres Spektrum hin, als es von Sekundärelektronen die durch Wechselwirkungsprozesse in unser Galaxie entstehen, zu erwarten wäre. Zudem weisen die gemessenen Spektren Abweichungen im Bereich von 300 bis 800 GeV auf. In diesem Energiebereich ist das MAGIC Teleskop mit seiner hohen Sensitivität in der Lage weitere Messungen liefern und zur Klärung der offenen Fragen beitragen. Das Magic Projekt besteht aus zwei erdgebundenen 17 m Cherenkov-Teleskopen die kosmische Elektronen indirekt nachweisen können. Dabei zeichnet es das Cherenkovlicht auf das entsteht wenn die kosmischen Elektronen in der Erdatmosphäre eine Teilchenkaskade auslösen in der sich geladene Partikel mit Übermediumlichtgeschwindikeit bewegen. Diese Methode unterscheidet sich von denen des Fermi und des ATIC Experimentes und stellt daher eine unabhängige Messung dar.

Meine Doktorarbeit die in der MAGIC Kollaboration erarbeitet wurde befasst sich mit Neuentwicklungen sowohl im technischen als auch im wissenschaftlichen Bereich. So beinhaltet sie unteranderem die Charakterisierung und Qualitätstests der Photosensoren für das MAGIC II Teleskop das kürzlich in Betrieb genommen wurde. Der Hauptteil dieser Dissertation befasst sich mit der Entwicklung einer Analysemethode für die Untersuchung der diffusen kosmischen Elektronen, wofür ausführliche Simulationen des kosmischen Hintergrundes, nötig waren. Da MAGIC darauf ausgelegt ist Punktquellen von Gammastrahlung zu beobachtet musste für die Analyse zusätzliche Methoden entwickelt werden um es grundsätzlich zu ermöglichen die diffuse kosmischen Elektronen zu detektieren. Die Ergebnisse dieser Arbeit werden in der Vorliegenden Dissertation vorgestellt wohin erstmals gezeigt wird, dass es mit MAGIC möglich ist das Spektrum der komischen Elektronen zu messen. Das von mir neu entwickelte Verfahren beruht hauptsächlich auf der Identifikation und Selektion der unterschiedlichen Schauerbilder in der Kamera, die je nach schauerauslösendem Teilchen variieren (ohne Richtung, wie im Falle der Gammastrahlungs-Punktquellen). Um das Signal der komischen Elektronen vom hadronischen Hintergrund zu separieren wurde eine sogenannte Random forest Klassifikation angewendet. Dadurch ist es möglich vom eigentlichen Signal (diffuse Elektronen) den hadronischen Hintergrund abzuziehen. Die neu entwickelte Technik kann sowohl für die Erforschung dws Elektronen als auch für Gammastrahlung angewendet werden. Das Verfahren wurde an den Daten des Krebsnebels getestet und zeigt gute Übereinstimmung mit dem Spektrum das das Standartverfahren für Gamma-Punktquellen liefert. Das mit dieser Methode erstmals mit MAGIC gemessene Elektronenspektrum folgt einem einfachen Potenzgesetz $dF/dE = k(E/1\mathrm{TeV})^{-\Gamma}$ mit $k = (1.47 \pm 0.21_{(stat)} \pm 0.44_{(syst)}) \times 10^{-7}\,\mathrm{GeV}^{-1}\mathrm{m}^{-2}\mathrm{s}^{-1}\mathrm{sr}^{-1}$ und $\Gamma = 3.00 \pm 0.12_{(stat)}$ und konnte im Energiebereich von $\sim 100\,\mathrm{GeV}$ bis $\sim 2\,\mathrm{TeV}$

bestimmt werden. Innerhalb der angegebenen Unsicherheiten stimmen die gemessenen Daten gut mit den Ergebnissen von Fermi, H.E.S.S. und ATIC überein. Somit zeigen auch meine Resultate ein anderes Verhalten als es von Kosmischen Elektronen die durch Wechselwirkungsprozesse innerhalb unserer Galaxie entstehen zu erwarten wären. Die Ergebnisse lassen den Schluss zu, dass es möglicherweise eine zusätzliche Quelle für kosmische Elektronen gibt. Wegen der grossen Unsicherheiten kann das von ATIC gemessene Verhalten des Elektronenspektrums im Bereich vom 300 bis 800 GeV weder bestätigt noch ausgeschlossen werden. Die grossen Unsicherheiten resultieren Grossteiles aus den Monte Carlo Simulationen die für die Hintergrundreproduktion benötigt werden. Daher würde ein grösserer Simulationsdatensatz die statistischen Unsicherheiten signifikant reduzieren und es ermöglichen aussagekräftigere Interpretationen des von MAGIC gemessenen Spektrums der kosmischen Elektronen erstellen.

Contents

Introduction and Goals of the Thesis

At the beginning of the XXth century, through a series of balloon flights, Victor Hess discovered high energy cosmic radiation impinging on the Earth's atmosphere. The main part of this radiation is made up of protons and atomic nuclei, while only a small fraction consists of electrons and positrons. Cosmic electrons and positrons have a steeper[1] spectrum compared to that of protons because of the energy loss due to synchrotron radiation caused by the galactic magnetic field. These losses limit the distance from where they come and their lifetime. Therefore, their energy spectra give information about their acceleration and propagation in the nearby Universe.
Recently, several measurements of cosmic electrons and positrons have shown some features in their spectra, which have excited astrophysicists in the field. Many interpretations in terms of dark matter scenarios or astrophysical sources such as pulsars or supernova remnants are invoked.
Until recently, energy spectrum measurements of electrons and positrons were obtained by balloon and satellite experiments. At TeV energies, however, the sensitivity of these instruments is insufficient due to their small sizes and short exposure time of flight. Nowadays, ground-based Cherenkov telescopes, with their large collection areas and better sensitivity, represent an excellent tool for measuring high energy cosmic electrons and positrons, via the indirect observation of the air showers that very high energy cosmic ray particles generate in the atmosphere. MAGIC, with the two largest single dish Cherenkov telescopes world-wide, is now one of the most suited experiments that can contribute to this study. It has the potential to overlap with the energy range of the other experiments (Fermi, ATIC and H.E.S.S. among the others), extending the measurement of the electron spectrum to TeV energies.
Determination of the cosmic electron and positron spectrum is very challenging and is a non-standard task for MAGIC, which is built for observing γ-rays. The diffuse cosmic electron and positron signal has to be isolated in data dominated by hadronic cosmic rays and containing also the γ-ray showers. While γ-rays are not deflected by the magnetic fields and thus their arrival direction points directly to their source, electrons, positrons (and also protons) are isotropically diffused. Therefore, the identification of charged particles cannot be done through the arrival direction information. The identification of electrons and positrons must be done only via the shape of the image, which is produced by the air showers in the atmosphere and recorded by the telescopes. The data are modelled with simulations of electron showers and the background is rejected by applying selection criteria. The method has been proved to work. Still it suffers from large systematic uncertainties because the background can

[1] i.e. dominated by low-energy particles

be estimated only by simulations of hadronic showers, whose interactions are still not completely known. In addition, since this method does not separate electrons from gammas, a small contamination from diffuse gammas can not be excluded.
The electron flux is very small compared to the hadronic background rate. This makes the analysis even more challenging. Therefore a meticulous and selective analysis has been developed. In addition there is the necessity to produce a considerable amount of Monte Carlo events for the hadronic background estimation. These challenges make this topic exciting and interesting, beyond the scientific importance of understanding the electron spectrum at TeV energies. Moreover, it is the first time the MAGIC collaboration, during its 7-8 years old history, explores this new field.

This thesis is structured as follows:

An introduction to the physics of the cosmic electrons and positrons is presented in Chapter 1, together with current measurements of the cosmic electron and positron spectra and possible interpretations.

The development of air showers, the MAGIC telescopes and the imaging atmospheric Cherenkov technique are described in Chapter 2.

Detailed tests performed on the photosensors for the recently built imaging camera of the second MAGIC telescope are presented in the Chapter 3.

The diffuse-source analysis method developed for the cosmic electron study is described in Chapter 4. An overview of Monte Carlo simulations is also presented there.

Performance of the stereo system for both point-source and diffuse-souce analysis method is presented in Chapter 5.

Results of the electron and positron signal and relative spectrum are presented in Chapter 6.

Interpretation of the measurement and conclusions are discussed in Chapter 7.
At the end, an outlook and the prospects for future electron and positron measurements are presented.

1

Cosmic Electron and Positron Physics

The scientific motivations of the cosmic electrons study are given in this chapter. Past and current measurements of the electron and positron spectra from different experiments are presented in section 1.1, together with a more general view on cosmic rays (CR). In section 1.2 origins of spectra are explained as well as the energy loss mechanism and possible sources of cosmic rays.
Cherenkov telescope measurements, which are used for this thesis, cannot distinguish between electrons and positrons. Therefore from now on I will talk about 'electrons' by meaning particles regardless of charge; the terms 'negative electrons' or 'positrons' will be instead used when distinction will be needed.

1.1 The Cosmic Ray Energy Spectrum and Composition

Cosmic radiation arrives on Earth with a spectrum spreading over a wide range of energies, covering almost 12 decades. This radiation includes elementary particles and atomic nuclei. Many experiments measured the fluxes of the CR particles. At low energies (up to $10^{14}\,\mathrm{eV}$), most of the particles are stopped by the atmosphere. Therefore only direct measurements, with ionization calorimeters, nuclear emulsion or magnetic spectrometers on balloons or satellites outside the atmosphere, are used. For higher energies ($> 10^{14}\,\mathrm{eV}$), the particle flux is too low to achieve sufficient statistic with instruments of small ($\sim 1\,\mathrm{m}^2$) collection area. Thus, indirect measurement are more suitable for measuring the high energy particles, which hit the Earth atmosphere. Basically, ground-based experiments use the atmosphere as calorimeter. They have the advantage of larger collection area and longer exposure time.
The CR spectra, shown in figure 1.1, follow roughly a power law, with some features that might point to different origins. At energies below 10 GeV, particles are influenced by the solar wind and are decelerated by the expanding magnetized plasma generated

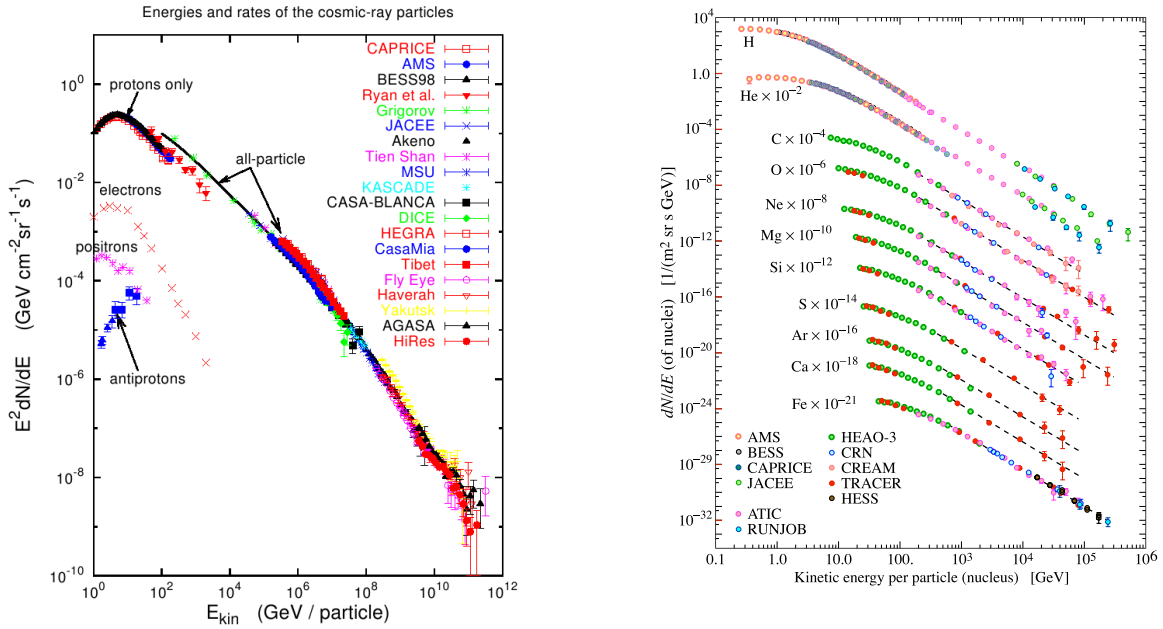

Fig. 1.1: Measurements of cosmic ray fluxes over a wide energy range, collected by Gaisser [82] on the left plot. Together with the hadrons, also leptons are shown. Spectra of the major components of the primary cosmic rays from [29] are shown on the right plot.

by the Sun. Accordingly, an anti-correlation between solar activity and intensity of the cosmic rays is seen. The all-particle spectrum (fig. 1.1 left) falls off steeply at the energy of $\sim 3{\times}10^{15}$ eV (the so-called *knee*), with a change in the spectral index from -2.7 to -3.1. At $3{\times}10^{18}$ eV (the so-called *ankle*), the spectrum hardens again with a spectral index of -2.7. At even higher energies the statistic of current measurement is too small. Nevertheless at energies higher than few 10^{15} eV the so-called GZK-cutoff is predicted. The CR would interact with cosmic microwave background photons producing pions and thus, a cutoff in the CR spectrum.
On the right plot of figure 1.1, the spectra of the individual components of the cosmic rays are shown. At GeV energies about 2% of the CRs are electrons and 98% are nuclei. The composition of the latter component consists of ≈87% of protons, ≈12% of helium and a small contribution from heavier nuclei [137]. This large contribution of protons is important for this work since protons dominate completely the background for the electron signal analysis.

Electrons

Concerning cosmic electrons, their spectrum is shown in figure 1.2 on the left panel from different measurements. In the same figure, on the right panel, also the positron fraction is shown as measured from different experiments. So far the cosmic electron flux was measured by several balloon-borne experiments, several space missions and by ground-based Cherenkov telescopes. In the balloon-borne experiments the technology

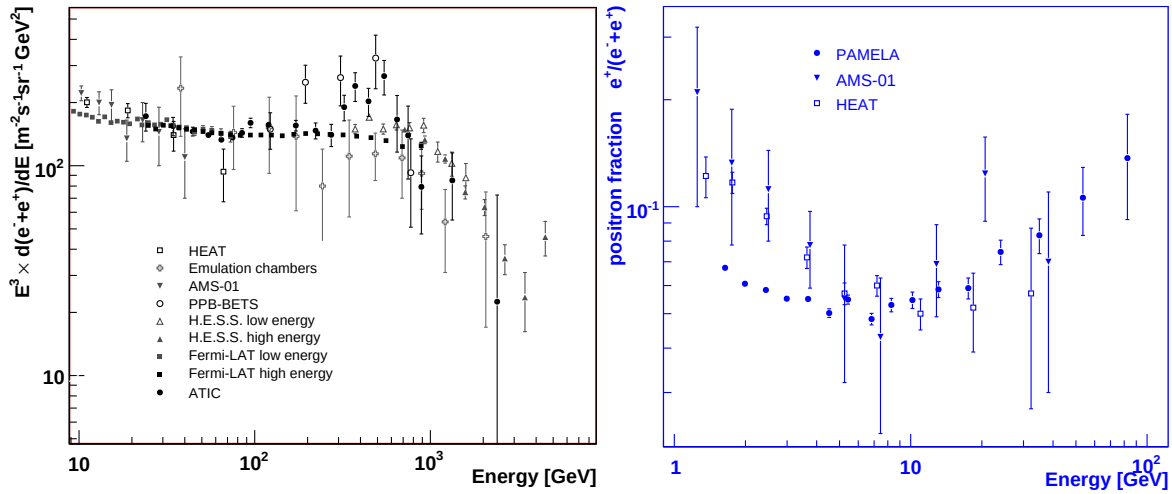

Fig. 1.2: On the left: spectrum of cosmic ray electrons. On the right: positron to total electron ratio. Data are from: HEAT([61], Emulsion chambers([94])AMS([28]), PPB-BETS([150], [141]), H.E.S.S.([14], [13]), ATIC([49]), Fermi-LAT([7]) and PAMELA([10]).

used in the past was the emulsion chambers [94], which allow to detect the electron showers by naked eye scanning. With the introduction of a magnetic spectrometer it was possible to distinguish the sign of the charged particles. The High-Energy Antimatter Telescope (HEAT) [61] combined a magnetic spectrometer with a transition radiation detector, an electromagnetic calorimeter and time-of-flight scintillators. The combination of these detectors allows one to determine the lateral shower development and could be used to reject the hadronic background. HEAT was designed to observe high energy CR antiprotons, but is also suited for the observation of electrons and positrons below few tens of GeV. The Polar Patrol Balloon (PPB-BETS) [150], with a system of scintillating optical fibers placed in the electromagnetic calorimeter structure, is able to observe the development of the showers and images them with a CCD camera. The high dynamic range of the CCD camera allows to detect up to 1 TeV electron showers. The discrimination of electrons from hadrons is based on the analysis of the image shape. The Advanced Thin Ionization Calorimeter (ATIC) [49] uses an ionization calorimeter and a silicon matrix to determine the particle charge and energy. Recently, ATIC and PPB-BETS measured a controversial excess of electrons with a peak between 300 and 800 GeV and a steepening of the spectrum above 1 TeV. Regarding space missions, the Alpha Magnetic Spectrometer AMS [28] on board of the space shuttle Discovery, was designed to measure different components of CRs. For this purpose, the detector comprises a magnet, tracker planes, an anti-coincidence scintillator system, a time-of-flight system and a threshold aerogel Cherenkov detector. With these instruments both electrons and positrons were measured. The Large Area Telescope (LAT) on board of the Fermi gamma-ray space telescope (Fermi) [5] [7], designed for detecting gamma rays in the energy range from a few keV to few hundreds GeV, is also able to detect electrons due to the similarity of the electromagnetic cascades. LAT is a pair-conversion telescope with a precision tracker, a segmented calorimeter and an anti-coincidence detector. It measured an electron spectrum with

an index $\sim$-3.0, from 20 GeV to 1 TeV, which does not exhibit any prominent spectral features.
The ground-based H.E.S.S. Cherenkov telescopes [14] [13], measured a spectrum with a broken power law, with a change in the spectral index from -3.0 to -4.1 at 900 GeV. Very recently, anomalous positron abundance in the CR spectrum was instead found between 1.5 GeV and 100 GeV by the PAMELA satellite [10]. With a magnet spectrometer and a tracking system, the Payload for Antimatter Matter Exploration and Light-nuclei Astrophysics mission can identify different particles. The positron-to-electron ratio was found to increase at high energies instead to decrease, as expected (fig.1.2). While at energies of a few GeV the observed amount of positrons is explained by the interaction of cosmic rays with the interstellar medium (secondary positrons), at energies above 10 GeV the observed positron flux is an order of magnitude larger than the expected flux of secondary positrons. Thus, the increase in the positron fraction, together with the structure of the electron spectrum could rather be related to contributions from individual astrophysical sources or some dark matter process.
In this context, a new measurement of the cosmic electron spectrum by MAGIC is of particular interest. MAGIC should be able to verify or discard the ATIC excess, which has neither been confirmed by Fermi nor by H.E.S.S.. The large systematic errors of the two experiments and an energy resolution of about 15% contribute to smoothing-out any possible excess. In the case of ATIC, on the other side, although the systematic errors are large, the good energy resolution (few percent) gives credit to the structure observed in the spectrum.

1.2 Features of the Electron Energy Spectrum in our Galaxy

In the following sections the propagation in the galaxy and possible sources of cosmic electrons are discussed. According to our current understanding, the CRs below around 10^{15} eV are largely produced as a result of shock acceleration in Supernovae explosions, accelerating both nuclei and negative electrons. Since no evidence of the contrary, negative electrons are accelerated along with nuclei and likely with the same spectrum. Nevertheless, the observed electron spectrum shows a steeper spectrum compared to that of nuclei.
Electrons and all the other charged particles propagate diffusely due to deflection by the local magnetic fields. Therefore, when observed at ground, their direction cannot be extrapolated to their sources (unlike the neutral gamma-rays) and thus do not carry direct information about their origin. Moreover, while propagating, electrons undergo stronger energy losses than nuclei do, due to their smaller mass. Since the energy loss is in inverse proportion to the square of the mass of the particle, for electrons this loss is $\approx (2000)^2$ bigger than that for protons. Electrons lose energy mainly due to inverse Compton scattering off ambient photons, and because of synchrotron radiation in the magnetic field of the galaxy. These are the processes responsible for the steeper spectrum of electrons compared to nuclei. They are explained below, together with a description of possible cosmic electron sources.

The calculations below are taken from [100] and the discussions are based on the output of the workshop held in Paris [4].

1.2.1 Propagation and Energy Loss Processes

Before trying to understand the steepening of the electron spectrum, the cosmic electron propagation is discussed. The latter can be expressed in the form:

$$\frac{dN(E)}{dt} = \frac{d}{dE}[b(E) \cdot N(E)] + Q(E,t) + D\nabla^2 N(E) - \frac{N(E)}{\tau_{esc}} \tag{1.1}$$

where $N(E)$ is the number of electrons, E the energy of the electrons and t is the time. $Q(E,t)$ is the rate of production of electrons, with an injection spectrum of $Q(E) = kE^{-p}$. The coefficient D is due to the diffusion gradient, $b(E) = -dE/dt$ takes into account the energy losses and τ_{esc} is the time during which particles remain in the acceleration region.
As a first approximation, if we consider only the acceleration of the particles at the sources, the terms $Q(E,t)$ and $D\nabla^2 N(E)$ are zero. The steady solution $\frac{dN(E)}{dt} = 0$ of the eq. 1.1 then leads to

$$\frac{d}{dE}\left[-\frac{dE}{dt} \cdot N(E)\right] - \frac{N(E)}{\tau_{esc}} = 0 \tag{1.2}$$

In 1949 Fermi proposed a mechanism of acceleration [66], in which charged particles are accelerated by being reflected on irregularities of the magnetic field in the interstellar clouds. Slowly they gain energy statistically in these reflections. The energy increase is

$$\frac{dE}{dt} = \frac{4}{3}\left(\frac{V^2}{cL}\right)E = \alpha E \tag{1.3}$$

where V is the velocity of the clouds and L the mean free path between them. Equation 1.3 represents the Second order Fermi mechanism, in which the energy gain is of second order in V. Taking into account this second order term in equation 1.2, the solution is

$$N(E) \propto E^{-\Gamma} \tag{1.4}$$

with $\Gamma = 1 + (\alpha\tau_{esc})^{-1}$. This leads to a power law with a non-constant index and a very slow energy gain.
A more efficient mechanism is instead the 'First order Fermi acceleration', [41] [37] [33] [96] . In this case particles gain energy passing through a supersonic shock wave. Due to scattering, when particles cross the shock, their velocity distribution becomes isotropic. Moreover, particles gain energy every time they cross the shock, independently on the direction. In this case $\frac{dE}{dt} \propto \frac{V}{c}$, i.e. proportional in first order to the velocity of the shock. It can then be shown that the power law solution for the equation 1.2 has an injection index $p = 2$.
This energy spectrum, which is valid for the charged particles accelerated in such an environment, follows then a power law. Then, the index of the electron spectrum

changes during propagation because of the energy loss processes. The term for the electron energy losses in eq. 1.1 is:

$$b(E) = -\frac{dE}{dt} = C_1 \left(\ln \frac{E}{m_e c^2} + 19.8 \right) + C_2 E + C_3 E^2 \tag{1.5}$$

where the term with constant C_1 describes ionisation losses, the term with C_2 bremsstrahlung and adiabatic losses and the term with C_3 the inverse Compton scattering and synchrotron radiation. At low energies, the main processes for energy losses are ionization and the solution $N(E) \propto E^{-(p-1)}$ (with p the injection index) of the eq. 1.1 produces a relatively flatter spectrum by one power of E. Above few tens of MeV bremsstrahlung becomes dominant, and together with the adiabatic losses gives the unchanged spectrum $N(E) \propto E^{-p}$. Adiabatic losses are typical for expanding volumes such as in supernova remnants. Above GeV energies, the spectrum is getting steeper due to Compton scattering losses and synchrotron radiation losses and the solution is $N(E) \propto E^{-(p+1)}$. Thus, if we assume that the injection index is p=2, above GeV energies, the spectrum at the Earth can not be harder than $N(E) \propto E^{-3}$. In the energy domain in which MAGIC operates, the involved loss mechanisms are Compton and synchrotron radiation losses. Therefore I will only discuss these processes from here on.
The energy loss rate of electrons for both inverse Compton and synchrotron processes is expressed as:

$$-\frac{dE}{dt} = \frac{4}{3} \frac{\sigma_t c}{(mc^2)^2} E^2 (U_{mag} + U_{rad}) \tag{1.6}$$

where σ_t=6.65·10^{-25} cm^2 is the Thomson cross section, U_{mag} is the energy density of the magnetic field and U_{rad} the energy density of photons, which includes optical from starlight, infrared from thermal dust and cosmic microwave background (CMB) at T=2.7 K. Both the processes are inversely proportional to the square of the mass of the electron. Inverse Compton and synchrotron are important whenever a high energy electron propagates through a radiation or magnetic field. If we consider the case of our galaxy, for a typical magnetic field of B=3-5 μG and an energy density of optical photons due to stars U_{rad}= 0.6 eVcm^{-3}, the ratio $U_{rad}/U_{mag} \approx 3$. Thus, in our galaxy both processes are nearly equally important. If we consider instead the case of the intergalactic space, the energy density of the magnetic field can be considered negligible, while the omnipresent cosmic microwave background has a U_{rad}=0.265 eVcm^{-3}. Thus, electrons lose their energy by inverse Compton scattering off the CMB photons. From the energy loss rate (eq. 1.6,) we can calculate the mean lifetime (defined as the time in which electrons lose 1/e of their initial energy) of high energy electrons in the Universe as

$$\tau(E) = \frac{E}{dE/dt} = \frac{3}{4} \frac{(mc^2)^2}{\sigma_t c E U_{rad}} \tag{1.7}$$

Thus, for 100 GeV electrons $\tau \approx 10^6$ y, while TeV electrons cannot exceed a lifetime of $\approx 10^5$ y. These lifetimes limit the distance for observing sources that accelerate electrons [32].

1.3 Sources of Cosmic High Energy Electrons

From the calculations performed in [32] and [15], taking into account the diffusion coefficient D in eq. 1.1 and the lifetime of electrons τ, the characteristic diffusion radius is $r \sim 2\sqrt{D\tau}$, where the diffusion coefficient depends on the energy. Thus for TeV electrons, the maximum distance to observable sources is $\sim$300 pc, while at few GeV the distance can be larger than 1 kpc. This implies the existence of a nearby source of TeV electrons within our galaxy. With this argument, at high energies, the standard interpretation of the high energy electron spectrum in the framework of the standard leaky-box or diffusion model [55] must be incomplete. In fact these models assume a uniform and continuous distribution of sources in the galactic volume. For electrons, instead, their energy losses imply the presence of nearby and point sources, rather then a uniform spatial distribution of sources.
In this regard, it is important to point out that two different origins can be considered: a primary and a secondary. Primary electrons are produced and accelerated in astrophysical sources, such as supernova remnants and pulsars or in some more exotic sources, such as the dark matter, as discussed below. Secondary electrons are instead produced by interaction of hadronic CRs within the interstellar medium (ISM).

1.3.1 Secondary electrons

One of the processes which lead to the production of the secondary electrons is the spallation. Since it involves interaction of positively charged particles with nuclei, charge conservation implies that in this process more positrons are created than electrons [92], [57].
Secondaries are then generated by means of proton-proton collision (or p+He, α+H, α+He):

$$p + p \rightarrow \pi^{\pm} X, \pi^{\pm} \rightarrow \mu^{\pm}\nu_e(\bar{\nu_e}), \mu^{\pm} \rightarrow e^{\pm}\nu_e(\bar{\nu_e})\bar{\nu_\nu}(\nu_\nu) \tag{1.8}$$

$$p + p \rightarrow \pi^{0} X, \pi^{0} \rightarrow 2\gamma, \gamma \rightarrow e^{+} + e^{-} \tag{1.9}$$

For details on the secondary electrons I refer to [57], [114] and [138].

To clarify the origin of primary and secondary cosmic electrons and their propagation, complementary constrains come from the **diffuse γ-rays**. From equation 1.9 in fact, via Inverse Compton (IC) scattering and bremsstrahlung, electrons make a large contribution to the diffuse γ-ray flux in the MeV range [138]. Measurements curried out by Fermi in the energy range from a few hundred MeV to $\sim$0.1 TeV, for galactic latitudes $|b| \geq 10^o$, show a spectrum of the diffuse γ-ray emission with a power law index of $\approx$-2.4 (see fig. 1.3). The flux measured in the GeV region lies orders of magnitude below the flux of the cosmic electrons. At TeV energies only extrapolations give a flux comparable to that of the cosmic electrons. However, extragalactic absorption, due to pair production should cause a significant drop in the extragalactic γ-ray flux [93].
In the present work the used method is not sensitive enough to discriminate between electrons and diffuse γ-rays. From the Fermi measurement at around 100 GeV the contamination from the diffuse γ-rays is expected to be much less than 1% of the

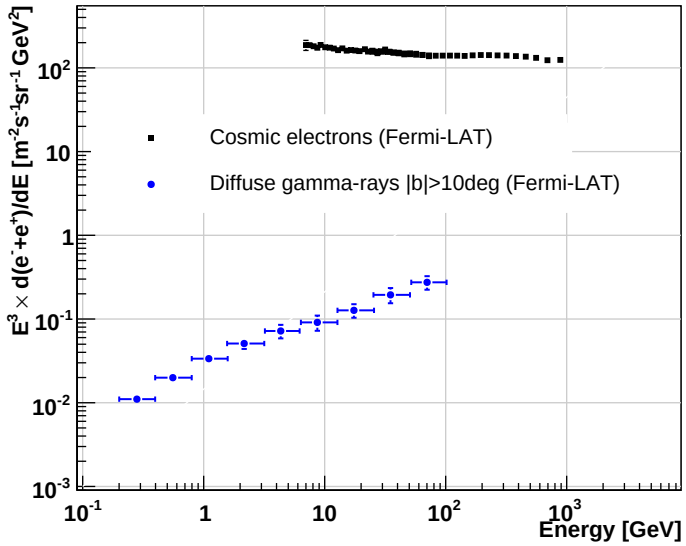

Fig. 1.3: Spectrum of diffuse gammas as measured by Fermi [6] (in blue dots) for galactic latitude $|b| \geq 10^o$ and compared with the cosmic electrons measured by Fermi [7] (in black rectangles).

electron flux, as one can see in figure 1.3, so one can neglect this.

Coming back to the discussion on electrons, following the model proposed by [114] for a continuous distribution of sources in the galaxy, electrons propagate in a cylindrical space (with radius R = 30 kpc and thickness z = 3 kpc). This large-scale diffuse galactic component (which includes the secondary electrons) produces a spectrum shown in figures 1.7 as a black-dotted line. Since this galactic component alone is not enough to explain the observed fluxes, additional sources are needed. The possible kind of sources are described in the following.

1.3.2 Supernova Remnants

Supernova (SN) remnants are the results of extremely violent and luminous stellar explosions. From this explosion, most of the energy released goes into neutrinos in the first instants. The remaining energy is converted into kinetic energy. This energy accelerates the stellar material to a speed greater than the speed of sound causing a shock wave, which moves outwards from the central star into the ISM. Over time, the latter is compressed and heated up. Together with the expanding material, the swept up ISM forms a supernova remnant (SNR).
In the context of this work I focus on the development of a supernova remnant and on the phases responsible for the acceleration of the electrons. Details on different kind of SNRs and on the origins of such objects can be found elsewhere [100], [145], [60], [146], [144].
A SNR evolves, according to the basic theories, in three phases:

- *free expansion.* The shock wave expanding from the central region heats the ISM up to 10^8 K, ionizing the medium and generating X-rays. The ISM accelerated by the shock wave forms a thin shell which expands with approximately the same velocity as the initial shock front of about 10^4 km/s. This phase lasts for several hundred years in which the mass swept up by the shock is much less than the mass of the stellar ejecta. During this time the SNR radiates thermal X-rays and synchrotron radiation (from radio to X-rays). However, because of high initial energy involved, the radiation energy losses in this phase are negligible.

- *adiabatic phase.* Once the amount of swept up mass becomes comparable to the ejected one, the outer shell of the expanding wave starts to slow down. Consequently the matter density inside the expanding volume increases at the inner edge of the shell. This generates an internal supersonic shock, which in turn heats up the outer shell. As a result, the ejected gas inside the volume, which started to cool down, is reheated through the kinetic energy of the new shock, whose direction is back to the center of the object. This reheated gas emits X-rays.
  This phase, also known as Sedov phase (named after Leonid I. Sedov, who described the dynamics by the adiabatic solution), is responsible, together with the *free expansion* phase, for the acceleration of negative electrons. Through the first order Fermi mechanism, electrons are accelerated whenever crossing the shock front. These electrons in turn produce X-rays via synchrotron radiation and also VHE γ-rays by the inverse Compton process.

- *radiative phase.* After about 10^4 years, as the shock wave cools, the radiation energy losses start to dominate. Once the temperature drops below 10^4 K, electrons start to recombine with ions emitting UV lines. The SNR cools down until it gets dispersed in the surrounding medium.

These phases of a SNR evolution limit the time in which electrons can be accelerated. In addition, the diffusion of electrons (eq. 1.1) puts a constraint on the maximum distance for SNRs being a source of cosmic electrons. Referring to [95] the electron flux is strongly correlated to the source age and distance. As shown in figure 1.4 **possible SNR sources have to be younger than 10^5 years and closer than 1 kpc**. In these cases, the electron fluxes are calculated assuming an output energy of electrons over 1 GeV to be 10^{48} erg per SNR and a SNR rate of 1/30 year in a Galaxy with disk radius of 15 kpc. In the same figure above, the fluxes are shown for a power-law distribution with different cutoff energies and a specific diffusion coefficient. Examples for candidate SNRs are Vela, Cygnus Loop, Monogem.
In figure 1.5 a model proposed by [42] is shown to reproduce the Fermi electron spectrum (on the left panel) and the positron excess measured by Pamela (on the right panel). This model suggest that the positrons are created as secondary products of hadronic interactions inside SNRs in the same region where cosmic rays are being accelerated. Therefore, secondary electrons and positrons are also accelerated and exhibit a spectrum, which is responsible, after propagation in the Galaxy, for the observed excess. In this model a SNR with $\tau_{SN} \approx 10^4$ years is considered.

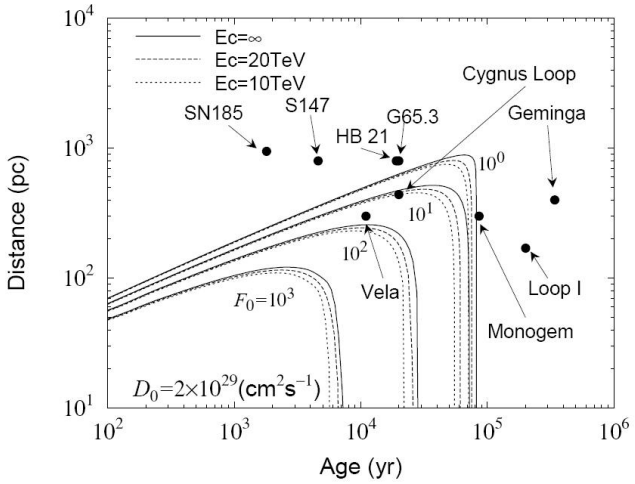

Fig. 1.4: Profiles of the electron flux at 3 TeV in distance vs age of each SNR plot. Here the injection spectra follow a power law where E_c are the cutoff for a specific diffusion coefficient D_0. Lines show equal flux contour for $F_0 = J(E/GeV)^3 GeV^2 m^{-2} s^{-1} sr^{-1}$, where J is the flux of electrons at 3 TeV, [95].

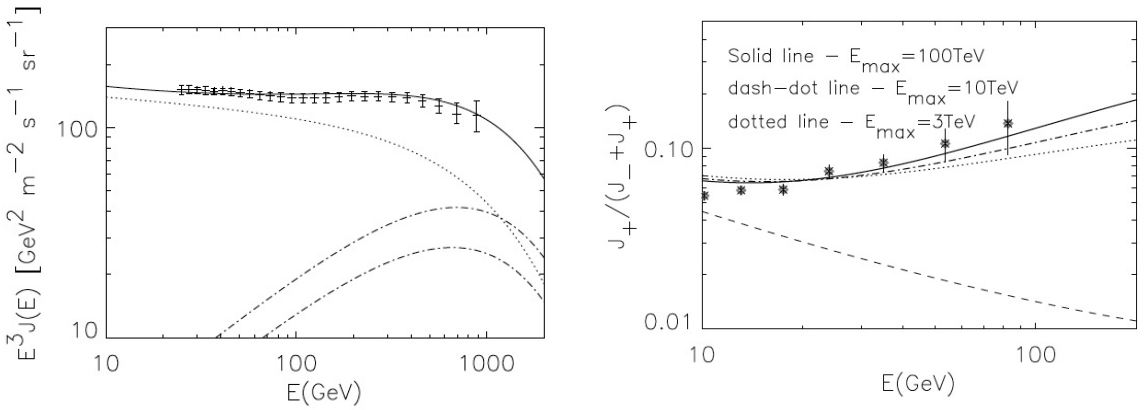

Fig. 1.5: On the left panel: the electron spectrum measured by Fermi. The model is from [42]: the dotted line refers to primary electrons, the dot-dashed lines are the fluxes of positrons (upper curve) and electrons (lower curve) from production in the SNR. The thick solid line is the total flux. On the right panel: Positron fraction measured by Pamela. The solid line refers to the case of maximum energy of the accelerated particles (and therefore also of the secondary particles after reacceleration) $E_{max} = 100$ TeV, while the dash-dotted and dotted lines refer respectively to $E_{max} = 10$ TeV and $E_{max} = 3$ TeV. The dashed curve represents the standard contribution to the positron fraction from secondary diffuse pairs. In this model a SNR with $\tau_{SN} \approx 10^4$ years is considered [42]

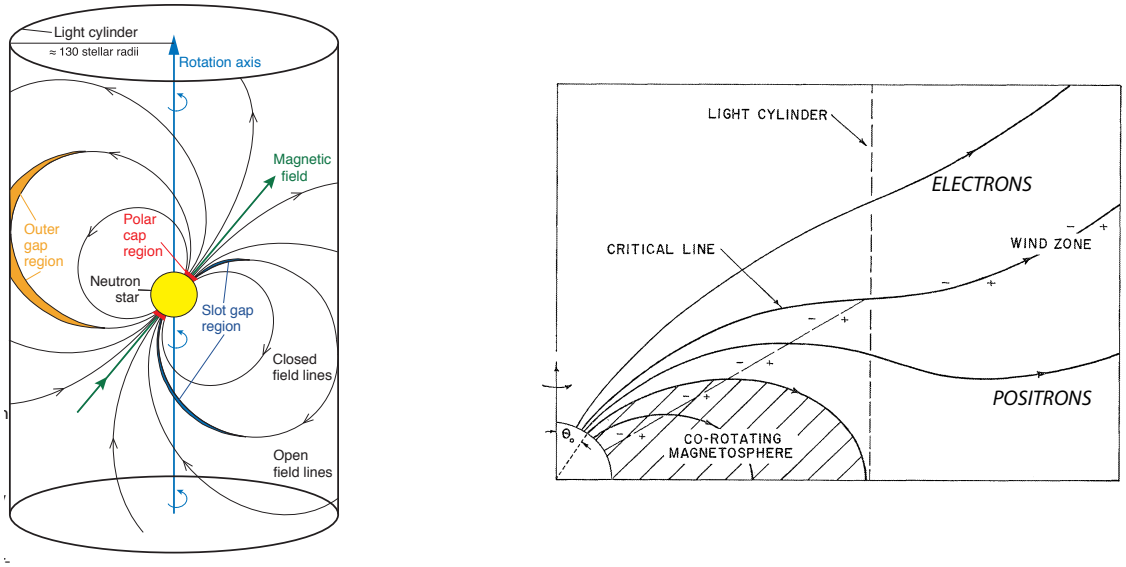

Fig. 1.6: On the left panel: geometry of a pulsar magnetosphere. The polar cap (in red), outer gap (in orange) and slot cap (in blue) models regions in which particles are accelerated are also shown [25]. On the right panel: both the near and the wind zone are shown [74].

1.3.3 The Pulsar Magnetosphere as a possible source of electrons

From a SN explosion, the remnant can sometimes include in its center a compact object ($\sim$1.5-3 solar masses, [44]), which is also thought to accelerate electrons. If it is a rotating neutron star, this object is called a pulsar. The characteristics of this object are a very fast rotation speed (with a rotation period between seconds and milliseconds) and extremely high magnetic field of the order of $B \sim 10^{12}$ G generated in the gravitational collapse by the high conductive plasma. Such a high magnetic field induces, in the rotation, an electric field $\bar{E} \propto (\bar{v} \times \bar{B})$ which can accelerate particles to ultra-relativistic energies. In addition, the rotation axis of the pulsar and the magnetic dipole moment are not aligned. This generates a cone of electromagnetic radiation, in which the radiated pulsed-emission has the same frequency as the rotation frequency of the pulsar.
The structure of a pulsar can be divided roughly in three zones [74]:

- *near and wind zones.* In the near zone, also known as light-cylinder, with dimension $r = c/\Omega$, where Ω is the angular velocity, the plasma velocity is lower than c. Magnetic field lines are closed and the attached charged particle co-rotate with them. From this region particles can not escape. Outside this region, in the wind zone, because of the rotation of the neutron star, the magnetic field lines are open and the particles stream out along them. These lines start from the proximity of the magnetic poles. Negative electrons stream out along higher-latitude lines, in which the electric potential difference between the plasma and the ISM is negative and thus, they are accelerated. The opposite happens for positrons, which stream out along lower-latitude lines, where the electric potential is positive. In figure 1.6, the scheme on the left pictures the near zone defined by the

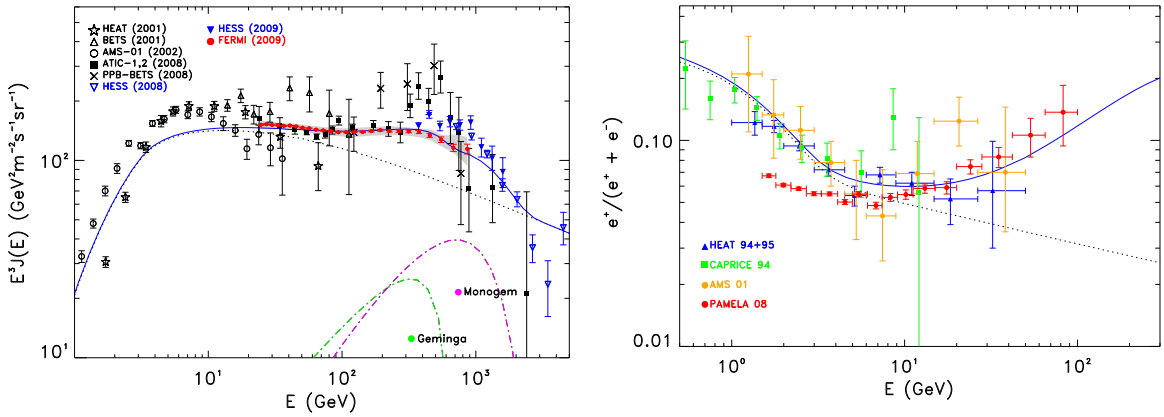

Fig. 1.7: On the left: the electron spectrum (blue continuous line) is computed in a case in which only observed pulsars with distance d <1 kpc plus the large scale Galactic electrons background component are taken into account. The dominant contribution of Monogem and Geminga pulsars is shown as colored dot-dashed lines, while the Galactic electron background component, computed with GALPROP, is shown as a black-dotted line. On the right: Positron fraction computed for the same conditions of the left plot. Figure taken from [75]

light cylinder. On the right scheme, instead, both the near zone with the co-rotating magnetosphere and the wind zone are shown. At the critical magnetic field line the electric potential is null. Above this line, in the direction of the poles, it is shown that negative electrons are accelerated, while below positrons are accelerated.

- *boundary zone.* The boundary zone is somehow arbitrarily considered to extend up to the end of the supernova cavity, where the electric field vanishes (since the ISM is a good conductor). In this zone the magnetic field lines are not equipotentials. The charged particles, which always move along the magnetic field lines (due to the strong magnetic field) cross the equipotential lines and are accelerated. Therefore this region is the most effective for the electrons acceleration. This is also favoured by the fact that the plasma density is low enough.

In general particles are accelerated if the electric field component parallel to the magnetic field is not zero: $\bar{E} \cdot \bar{B} \neq 0$. As source of high energy electrons, pulsars can be described by two different classes of models. In polar cap [132] models, the particle acceleration takes place in a gap near the stellar surface, where the field lines are open. In this gap electron-positron pairs are created due to high potential difference of about 10^{12} V.
In outer gap [52] and slot cap [79], [30] models, the acceleration of charged particles takes place farther out in the magnetosphere close to the light cylinder border. In this case electron-positron pairs are created from photon-photon collision. For a visualization of the acceleration regions involved in the two types of models see figure 1.6.
To explain the recent electron fluxes measurements and in particular the Pamela positron excess, a pulsar is required to be not too young, otherwise the ejected elec-

trons are still confined in the PWN or in the SN envelope. On the other side the pulsar has also to be not too old; in that case the produced electrons are too diffuse.
Considering this and referring to [75], a set of sources is selected to be closer than d <1 kpc and with an age T >10^4 years. In figure 1.7 one can see the contribution of two selected sources: Monogem ($d = 290$ pc, $T = 1.1 \cdot 10^5$ years, [105]) and Geminga ($d = 160$ pc, $T = 3.7 \cdot 10^5$ years, [48]). Here both Fermi electron data and Pamela positron fraction can be fitted by a calculated spectrum with a contribution of the diffuse galactic component plus the two considered pulsars (blue lines in figures 1.7).

1.3.4 Dark Matter as a source of cosmic electrons?

Although it is possible to explain the recent data with conventional sources, many authors are trying to involve also possible Dark Matter (DM) particles. We have a limited knowledge about DM. What is probable is that DM particles have to be massive, because of their gravitational effect on the cosmological scale, and they have to be weakly interacting, and thus, difficult to detect. The nature of these particles is one of the most prominent open question in science today. Weakly interacting massive particles (WIMP) from supersymmetric theories (such as neutralinos), additional Higgs doublets, or particles resulting from theories with extra dimensions, like Kaluza-Klein (KK) particle, are one of the most prominent candidates for dark matter. They are considered in many models as responsible for the electron excess at high energy [65]. Supersymmetric theories may suppress the direct production of e^+ e^- pairs, resulting in an electron spectrum that has a broad peak, further broadened by propagation. In contrast, e.g. KK particles would directly generate e^+ e^- pairs and the resulting electron spectrum would be represented by a delta function at the particle mass, eventually broadened at lower energies by propagation. Indeed the ATIC spectrum could be fitted by KK models with a mass of 620 GeV [49].
Among the buzz of theories which try to model the observations ([62] [91] [152] [109] [151] [86] [125] [51] [117] [127] [90] [68] [76] [126] [89] [88] [50] [53] [115] [153] [98] [128] [110] [124] [31] [27] [77] [123] [106] [73] [34] ...), for illustrative purposes, in figure 1.8 one example of annihilation in different channels (from [39]) is shown, compared with data.
In addition for the DM scenarios to be self consistent and explain the high cosmic electron flux measured by PAMELA, ATIC, Fermi and H.E.S.S., other requirements are:

- Since most of the DM annihilation or decay models predict both leptons and hadrons, an excess in the antiproton flux is also expected. However, PAMELA recently published a measurement of the antiproton flux which did not show any specific features [9].

- Constraints for photons at all wavelengths (CMB, X-ray, γ-ray) have also to be taken into account. DM annihilation should give rise to a γ-ray excess from the galactic center, where DM is expected to be more concentrated. A smoother γ-ray distribution is instead expected from DM decay [108]. On the other hand,

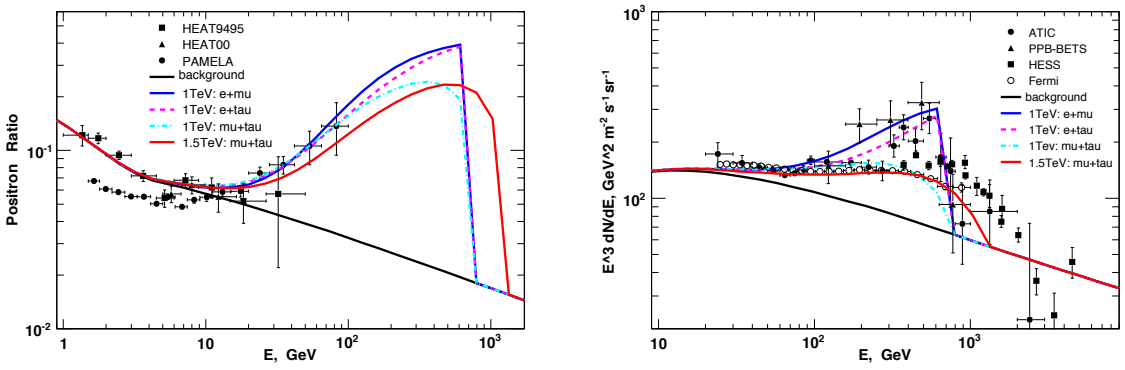

Fig. 1.8: Calculation of dark matter annihilation contribution through different channel for the positron fraction (left figure) and electron spectrum (right figure). Figure from [39].

measurements of the CMB from the galactic center done by the WMAP experiment [85] show a hard component (WMAP haze) that could be explained by synchrotron radiation from electrons produced from DM annihilation in the galactic center.

1.4 Anisotropy of the expected electron direction

A big step in discriminating different origins may come from the measurement of an anisotropy in the arrival direction of cosmic electrons. In general the CR angular distribution is made isotropic by the interstellar magnetic fields that tangle the trajectory of the charged particles. Therefore, the particles cannot be tracked back to the origin and the measured intensity of CRs is almost constant in all the directions. Nevertheless if the distribution of CR sources is not homoeneous in space, a small anisotropy is expected. The degree of anisotropy due to single sources can be characterized by $\delta \sim \frac{\bigtriangledown\phi(E)}{\phi(E)}$, where $\bigtriangledown\phi$ consider the electron flux from a single source or defined direction in the sky and ϕ is the total galactic electron flux.
Fermi experiment calculated upper limits on the anisotropy in the electron flux [8], which can be seen in figure 1.9 for 95% confidence level. Constraints have been set on pulsar and DM models. For illustrative purposes, in figure 1.9 (on the left panel) the integral anisotropy, as a function of minimum energy, computed for a pulsars model plus a SNRs model is shown [58]. One can notice that the main contribution to the electron flux come from pulsars (especially from Monogem in the referred model), but a contribution from local SNRs is also considered. On the right panel of figure 1.9, the Fermi upper limits are compared with the integral anisotropy for different annihilation channels and masses of the DM [47]. At around 500 GeV the expected anisotropy in case of astrophysical contribution is at the level of $\delta_{AP} \sim 10^{-1}$, while the expected one in case of DM is at the level of $\delta_{DM} \sim 2{\cdot}10^{-2}$. If a positive detection of anisotropy will occur, and the anisotropy will be found larger than δ_{DM}, one can then exclude the

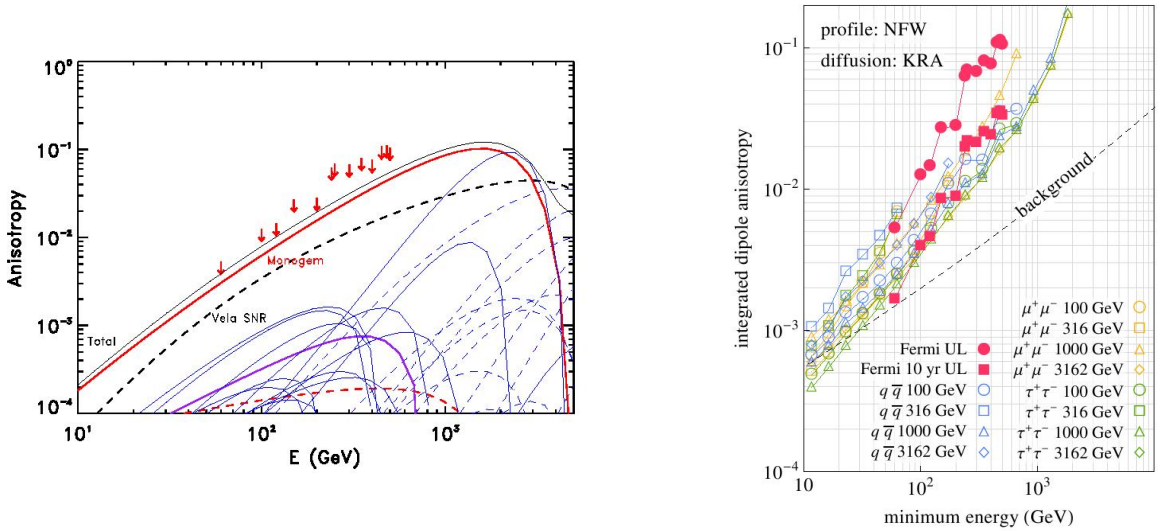

Fig. 1.9: On the left panel: The black line represents the integral anisotropy, as a function of minimum energy, computed for a pulsars model + SNRs model. The contribution from Monogem is shown in the red line, while the contribution from Vela SNR in black dashed line. The Fermi upper limits at the 95% C.L. are also shown [58]. On the right panel: Integral anisotropy of DM. The points correspond to different annihilation channels and masses of the DM particle. A comparison is made with the standard astrophysical background (black dashed line), current Fermi upper limits (red circles) and the sensitivity (red rectangles) expected after 10 years of data taking (actual limits rescaled by a factor $\sqrt{10}$) [47].

predominant contribution of DM. This would point then to an astrophysical source (such as pulsars) dominated scenario.

2
The MAGIC Telescopes

Currently the *Major Atmospheric Gamma Imaging Cherenkov* (MAGIC) telescopes are the world-wide largest *Imaging Air Cherenkov Telescopes* (IACTs) in operation. They are two telescopes designed to detect very high energy (VHE) γ-rays in the energy range from 50 GeV to tens of TeV. IACTs are the standard detectors of VHE γ-ray astrophysics. They detect γ-rays from the observed source, because γ-rays, unlike charged particles, are not deflected by the galactic and extragalactic magnetic fields. The objects of interest for MAGIC are both galactic and extragalactic. In the first category are SNRs [18], pulsars and PWNs [26], and binary systems [20]. Extragalactic sources are blazars [1], radio galaxies [19], starburst galaxies, and gamma-ray bursts (GRBs) [17]. Beyond that, MAGIC also tries to answer some fundamental questions regarding basic properties of the universe. Studies in that direction concentrate on questions of fundamental physics of dark-matter [24], [21], extragalactic background light [102], quantum gravity [103] and cosmic rays.
IACTs detect γ-rays indirectly by using the Cherenkov imaging technique. High energy γ-rays, interacting in the atmosphere, produce charged particles in a well collimated shower. The Cherenkov light emitted by these cascading particles is then detected by the telescopes. With the measurement of the intensity and the light distribution of the showers, one can estimate the primary particle direction and energy and distinguish between particle types.
The history of gamma-ray studies with IACTs started in 1989 with the first strong detection of γ-rays from the Crab Nebula by the Whipple Observatory [143]. Today several other experiments along with MAGIC follow the same principle: H.E.S.S. [83] in Namibia, VERITAS [84] in Arizona and CANGAROO in Australia [97].
In this chapter the Cherenkov imaging technique (section 2.1) and the instrumentation which allow us to detect cosmic electrons (section 2.2) are described.

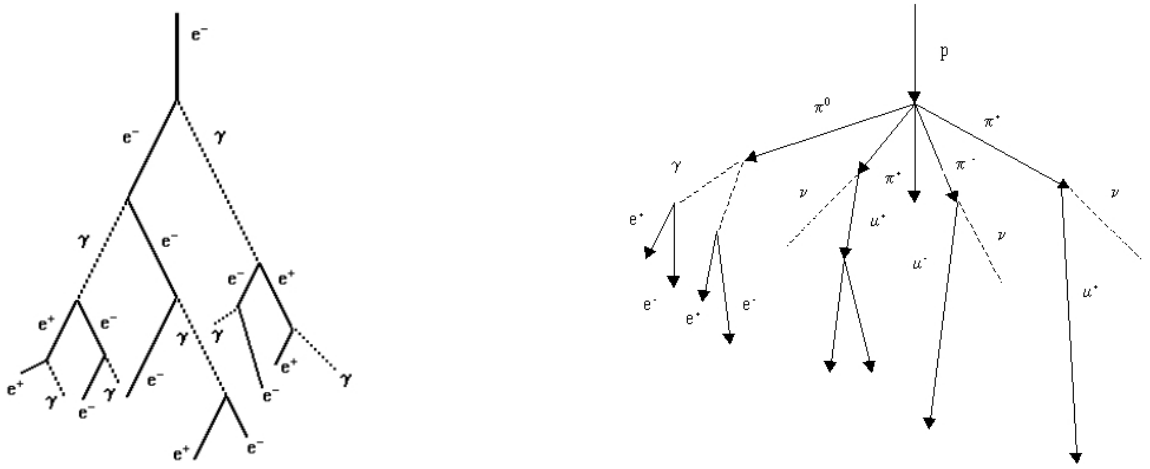

Fig. 2.1: Schematic development of EAS. Left: an electromagnetic shower initiated by an electron. Right: a hadronic shower, which develops a hadronic, an electromagnetic and a muonic components.

2.1 Extensive Air Showers (EAS) and IACT Technique

Cosmic Rays (CRs) interact with molecules in the upper part of the atmosphere and generate secondary particles, which in turn again interact with the nuclei and create a cascade of secondary particles. For vertically incident particles, the entire atmosphere corresponds to 28 radiation lengths (rl) and 11 hadronic absorption lengths. The cascade of secondary particles is commonly called "extensive air shower" (EAS). The secondary particles generated by a high energy particle (E>5 GeV) are strongly collimated along the direction of the primary because of relativistic beaming.
When traversing the increasingly denser atmosphere a large fraction of the secondary particles, in particular secondary electrons, exceed the velocity of light in the air (at that density), and emit Cherenkov light. This light is weak and of very short duration, but can be observed by IACTs.
The characteristics and the shape of the air showers strongly depend on the type of the primary particles. Showers can be classified into electromagnetic and hadronic showers (see fig.2.1).

2.1.1 Electromagnetic Showers

An electromagnetic shower is initiated by a cosmic electron or a γ-ray in the presence of a nucleus in the atmosphere. γ-rays above a critical energy of few tens of MeV ($\approx 80\,\mathrm{MeV}$ in the air) generate electron-positron pairs in the Coulomb field of an air nucleus. Electrons instead, radiate in atmosphere due to bremsstrahlung when their energy is above the critical energy. Below this energy the energy loss is dominated by ionisation. The average rate of energy loss due to bremsstrahlung is directly

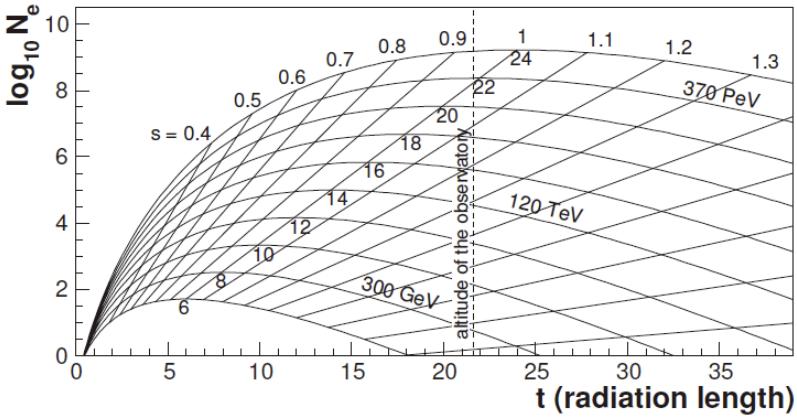

Fig. 2.2: Longitudinal development of an EM shower. The x axis corresponds to the atmospheric depth, the y axis shows the number of secondary electrons in the shower. Different curves correspond to different energies of the primary and below each curve the value $\ln E_0/E_c$ is written. The higher the energy, the deeper the shower penetrates in atmosphere. The shower age s is also shown. At s=1 the shower has its maximum, [131].

proportional to their energy [100]:

$$-\frac{dE_e}{dx} = \frac{E_e}{X_0^e} \tag{2.1}$$

with X_0^e= 37.2 g/cm^2 the column density after which, on average, the electrons energy will fall to 1/e of its initial value in air (i.e. the radiation length). For pair creation, the mean free path for γ is $X_0^\gamma = \frac{9}{7}X_0^e$ [69].
In the initial phase of a shower the number of secondary particles increases exponentially until the mean energy of the secondary particles drops to values where energy losses by means of hadronic interaction (hadronic secondary particles) or by pair production, or bremsstrahlung drops to that of ionisation losses. The shower reaches a maximum and dies out thereafter. The number of particles, which are generated at the maximum multiplicity of the shower, is directly proportional to the energy of the primary particle. The higher the energy of the primary, the further the shower penetrates into the atmosphere. Therefore, it is important to study the longitudinal and the lateral development of a shower.

The **longitudinal development** represents the variation of the total number of electrons in the shower above the critical energy with the atmospheric depth. The parameter that defines the development of the shower is the shower age. It is defined as $s = \frac{3t}{t+2\beta_0}$, where t is the atmospheric depth, expressed as x/X_0 and β_0 =log(E_0/E_c) the number of radiation lengths, with E_0 the energy of the primary particle and E_c the critical energy. The shower age is equal to 1 at the maximum of the extension,<1 before reaching the maximum and >1 thereafter. For $s = 1$, $t = \beta_0$ and the depth of the atmosphere in which the shower maximum occurs is referred to as X_{max}. For electrons the shower maximum occurs about half a radiation length ($\approx$20 g/cm^2) higher in atmosphere than for γ [69].

The total number of electrons as a function of the atmospheric depth for different energies is shown in figure 2.2.

The **lateral development** describes the density of electrons and positron as a function of the distance from the shower axis. Electromagnetic showers are strongly collimated because the transverse spread is dominated only by multiple scattering and the weak deflection of the electrons by the earth magnetic field.

2.1.2 Hadronic Showers

Hadronic showers are generated when cosmic nucleons (protons, α particles,..) interact with atmospheric nucleons. Most of the secondaries are mesons (90% pions, some kaons and very few heavier mesons), while also some additional baryons can be produced. Besides π^0 and some decaying mesons most of the secondary particles interact hadronically and eventually a shower is formed. The secondary particles undergo in turn hadronic interactions up to their critical energy. In hadronic interactions secondary particles get some sizable transverse momentum kick (typically around the pion mass, extending rarely to beyond 1 GeV at highest energies), thus hadron showers are more extended laterally. The differences in the shower transverse extensions can be used to discriminate between electromagnetic and hadronic showers.

Most of the mesons created in hadronic interactions are π^+, π^-, π^0 and the energy of the primary is divided equally among them. Some of the charge pions and kaons decay into muons and neutrinos before undergoing a hadronic interaction. Muons have a very small cross section and a long mean life time (for a 10 GeV μ with lorentz factor $g \sim 100$ $\tau_\mu = 2.2 \times 10^{-4}$ s, so they can traverse ~ 70 km), thus they rarely decay before reaching the ground. Muons rather lose energy by ionization when traversing the atmosphere. Neutral pions decay in just 10^{-16} s (in the rest system) into two photons, which give the major contribution to the **electromagnetic component** of hadronic shower:

$$\pi^0 \longrightarrow \gamma\gamma$$

Gammas in turn create electron-positron pairs, which initiate electromagnetic subshowers. As in hadronic interactions always a sizable energy is transferred to π^0 and in turn in electromagnetic showers, very rarely the complementary process of producing hadrons takes place in electromagnetic showers. Therefore a hadronic shower contains at its end mostly electrons, gammas and only a few mesons, baryons and a few muons and neutrinos.

Hadronic showers also have larger fluctuations due to complex processes that create many different particles of a wide spread in momentum. Their images have more irregular shapes. Moreover, since the hadronic mean free path of inelastic scattering is $X_0 \sim 80$ g/cm^2, the shower maximum penetrate deeper in atmosphere than electromagnetic showers. Differences between gamma and proton initiated showers are shown in figure 2.3, where EAS-s created by a primary 100 GeV γ-ray (on the left panels) and a 300 GeV proton (on the right panels) are compared. Three times higher energy for proton is chosen in order to have about the same amount of Cherenkov light produced from the EAS. On the first two upper panels vertical and horizontal projections of the showers are shown for kinetic energies above 0.1 MeV for electromagnetic components

and 0.1 GeV for muons and hadrons. On the last two panels the thresholds energies are of 26 MeV for electromagnetic components, 5.3 GeV for muons and 47 GeV for hadron. These different component tracks are shown with different colors: red for electromagnetic components, blue for hadrons and green for muons; white regions indicates high track density.

All ultra-fast charged particles emit Cherenkov light which is detected by MAGIC telescopes, as it is shown in the following.

2.1.3 Cherenkov light emission from EAS

A charged particle entering a medium (atmosphere), with refraction index n, induces polarization of that medium. Therefore the medium emits spherical electromagnetic waves along the particle trajectory and if the particle velocity is higher than the local speed of light ($v = \beta c > c/n$) a photonic shock wave is produced, as shown in figure 2.4. This radiation is called Cherenkov light. The energy threshold of the Cherenkov emission for a particle with rest mass m_0 is:

$$E_{th} = \frac{m_0 c^2}{\sqrt{1 - n^{-2}}} \tag{2.2}$$

It depends on the refraction index n and thus on the altitude. At see level, given $n = 1.0003$, the threshold energy is $E^e_{th} = 21\,\text{MeV}$ for electrons and $E^p_{th} = 38\,\text{GeV}$ for protons, while at the MAGIC site (2200 m a.s.l.), given $n = 1.0002$, the threshold energy for electrons is $E^e_{th} = 26\,\text{MeV}$ while for protons it is $E^p_{th} = 47\,\text{GeV}$. In figure 2.3, on the two lower panels, only the tracks of the EAS components which generate Cherenkov light are shown, for the MAGIC site. Comparing with the two upper panels one can notice that only a small fraction of the EAS generates Cherenkov light.

Cherenkov light is emitted in a narrow cone with an emission angle given by:

$$\cos\theta_c = \frac{1}{\beta n} \tag{2.3}$$

θ_c increases as a function of the reflective index n, as the particle move deeper in atmosphere (figure 2.5 right). The value of θ_c is about 1.2^o at 2200 m a.s.l. for a light emitted by $e^{\pm}$ of $\beta \cong 1$. Cherenkov photons form a thin disk traversing the atmosphere along the shower axis. The Cherenkov radiation of an EAS consists of cumulative Cherenkov photons by the ultra-relativistic particles of the shower. The light of each single particle illuminates a disk on the ground and the superposition of all the disks from all the particles is called "Cherenkov light pool". The resulting lateral light density distribution is shown in figure 2.5 on the left. The density is proportional to the energy of the primary particle and it is almost constant up to ~ 120 m from the center of the pool at 2200 m a.s.l., with the main contribution originating from the high density of fast particles in the shower core. The light beyond 120 m is produced by shower halo particles. The number of Cherenkov photons emitted along the track

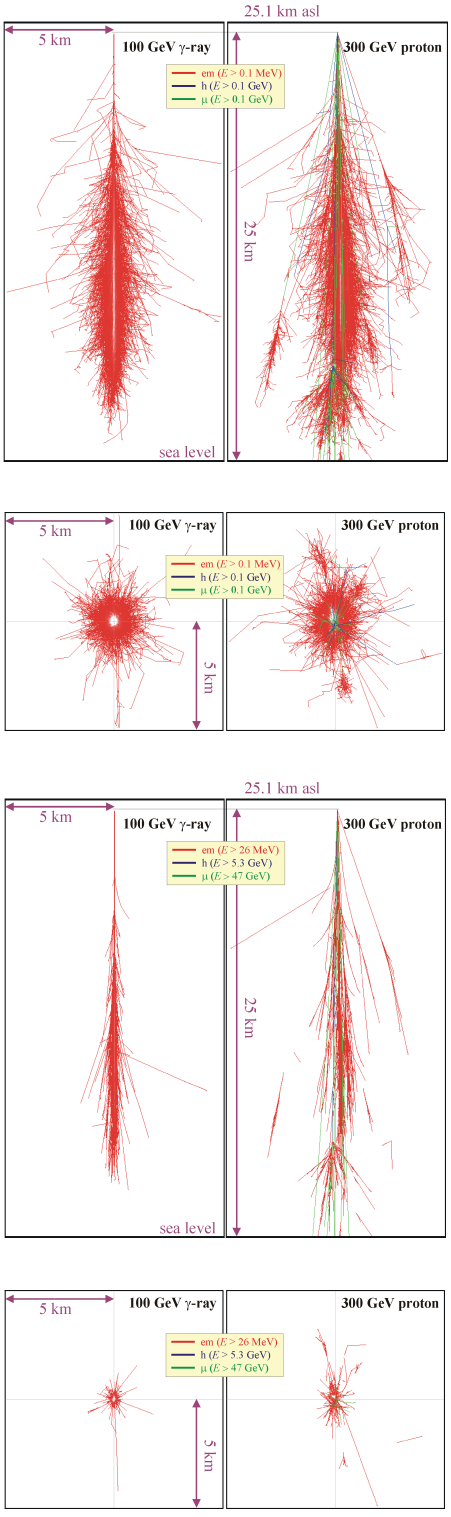

Fig. 2.3: Vertical (first and third panels) and horizontal (second and last panels) projection of an EAS initiated by 100 GeV gamma on the left and 300 GeV proton on the right. On the first two upper panels the kinetic energy threshold is 0.1 MeV for electromagnetic components and 0.1 GeV for muons and hadrons. On the last two bottom panels the kinetic energy threshold is 26 MeV for electromagnetic components, 5.3 GeV for muons and 47 GeV for hadrons. In all the plots, the incident angle of the primary particle is 0^o and the height of the first interaction is 25 km a.s.l. [87], [135].

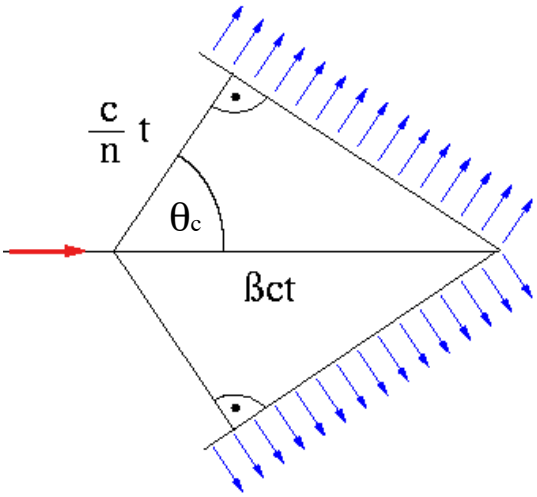

Fig. 2.4: Construction of Cherenkov waves. A particle with velocity higher than the local speed of light generates a photonic shock wave.

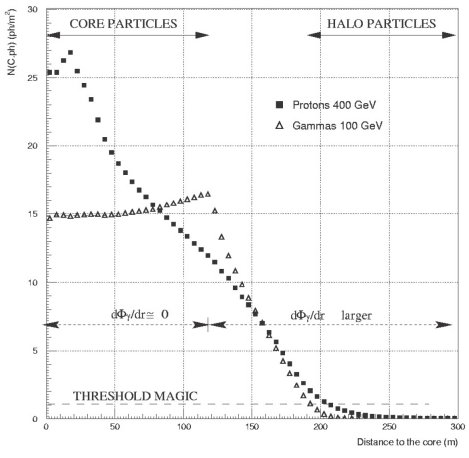

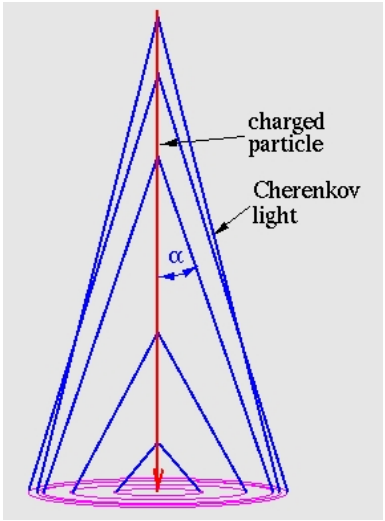

Fig. 2.5: On the left: Lateral distribution of Cherenkov photon densities for a 100 GeV γ (triangles) and a 400 GeV proton (squares) showers at an altitude of 2200 m for a zenith angle of 0^o [35]. In case of low to medium energy gamma showers the lateral light distribution shows a 'hump' at around 120 m. This hump is due to the increasing of the emission angle as increasing of the refraction index with the decrease of altitude, leading to a focusing effect. This effect is less pronounced in case of hadrons induced showers because of the larger transverse momenta. On the right: The Cherenkov light emitted in a narrow cone around the direction of a straightly flying $\beta \cong 1$ particle (muon). The opening angle increases as a function of the refractive index, as the particle moves deeper into atmosphere.

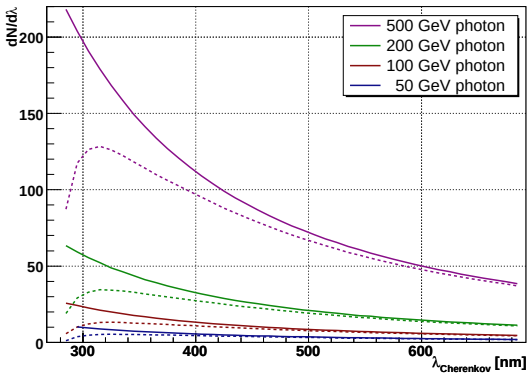

Fig. 2.6: Spectra of Cherenkov light for different primary energies at 10 km height (solid curves) and the corresponding spectra as detected at 2200 m a.s.l. (dashed curves). The spectra at 2200 m are affected by Ozone absorption, Rayleigh and Mie scattering in the air (plot taken from [142]).

of a particle is given by [149]:

$$\frac{d^2N}{dxd\lambda} = \frac{2\pi\alpha}{\lambda^2}\left(1 - \frac{c^2}{v^2n^2(\lambda)}\right) \tag{2.4}$$

$$\frac{d^2N}{dxdE} \approx 370\sin^2\theta_c(E)\,\mathrm{eV}^{-1}\mathrm{cm}^{-1} \tag{2.5}$$

with the fine-structure constant $\alpha \approx 1/137$ and the wavelength λ. The intensity of Cherenkov light is increasing with atmospheric depth due to the increasing density. It has a strong dependency on the photon wavelength λ. Most of the photons are emitted in the UV region as one can see from figure 2.6, after absorption with a peak at roughly 320 nm: Rayleigh and Mie scattering and absorption by ozone are the relevant processes. Rayleigh scattering occurs on air molecules which are much smaller that the wavelength of light, and it affects mostly the UV part of the Cherenkov spectrum. The scattering cross section is proportional to λ^{-4}. Mie scattering is caused by aerosols and dust in the air with particle sizes larger than the wavelength of the Cherenkov light. Mie scattering is a rather complex effect and cannot be completely described by a function. Moreover, light with λ <280 nm is strongly attenuated by the absorption of the ozone molecules. Light with λ >700 nm suffers from infrared absorption caused by H_2O and CO_2 molecules.

2.1.4 The Imaging Technique

Very high energy gamma-ray astronomy has been very successful and developed very fast in the last two decades due to the use of the so-called imaging technique. A reflector surface collects the Cherenkov light produced by an EAS in the field of view and focuses it onto the focal plane camera, which consists of highly sensitive and fast photosensors. There the light is converted into electrical signals and is read out. The image on the camera is a geometrical projection of the EAS (fig.2.7). The great advantage of this

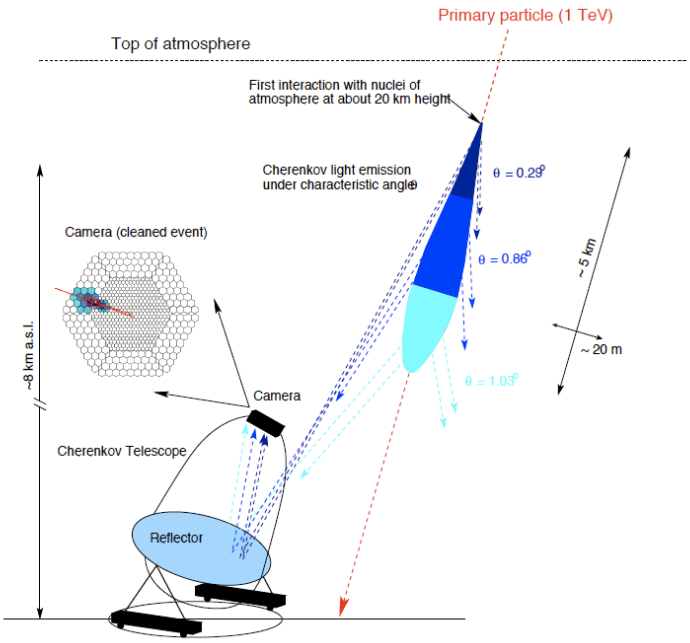

Fig. 2.7: Schematics of the imaging technique.

kind of observation technique compared to direct observations from space (see chapter 1) is that the former has much larger collection area and thus can cover a higher energy range. In addition, a large collection area, high quantum efficiency photosensors and a big reflector allows one to achieve high sensitivity.
The recorded images can be classified in three types: hadronic showers, Cherenkov light from muons (which can be confused with compact images of low energy gamma showers) and electromagnetic showers. The details of the image reconstruction and discrimination are given in the analysis of the shower image in chapter 4.
In the next section the telescopes that were used to detect showers are described.

2.2 The MAGIC Florian Goebel Telescopes

MAGIC is a stereoscopic system of two imaging atmospheric Cherenkov telescopes (IACT). Among the operational IACTs, they have the world-largest dishes with 17m diameter each. They are located at the Observatory of the Roque de los Muchachos on the Canary Island of La Palma (28.75^o N, 17.86^o W, 2200 m a.s.l.).
The first telescope, MAGIC-I, is in operation since 2004. The construction of the second telescope, MAGIC-II, has been finished in 2008 and since fall 2009 MAGIC is fully operational in stereoscopic mode. The telescopes have been renamed MAGIC *Florian Goebel Telescopes* in memory of our colleague and friend, the project manager of MAGIC-II, who accidentally died in 2008.
Compared to a single one, the two telescope system is designed to provide an improved sensitivity in the stereoscopic operation mode and to lower the analysis energy threshold. For a single 17 m reflector the achieved sensitivity is 1.6% of the Crab nebula flux

in 50 hours of observation, while with the stereo system it falls below 1% (see chapter 5).

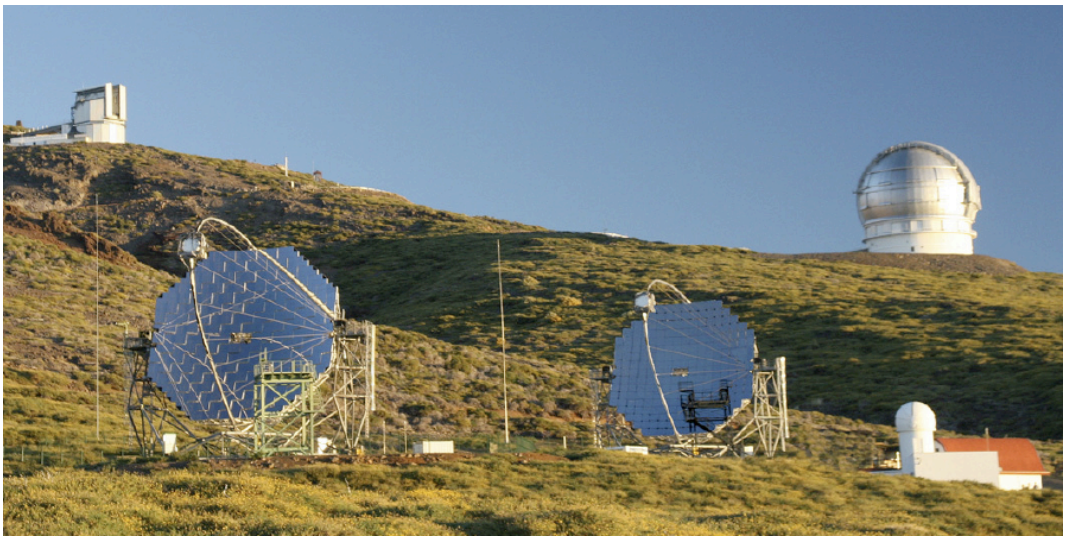

Fig. 2.8: The MAGIC telescopes.

The telescopes are located at a distance of 85 m to each other. MAGIC-II is a clone of MAGIC-I. The 17 m diameter tessellated reflector with a focal length of 17 m ($f/1$) has a parabolic shape. The parabolic shape has the advantage of isochronous properties in preserving fast timing. A so-called active mirror control system (AMC) focuses the mirrors to compensate dish deformations with varying elevation angle, as described in details in[40]. In zenith position the reflector is normally focused to a distance of 10 km, where the shower maximum is (from gammas of ~ 50 GeV).
The whole reflector is mounted on a lightweight carbon fiber tubular frame, which allows fast rotation, due to a low weight of only 5 tons. The average positioning time is less than 20 s for a 180^o turn, making MAGIC the fastest moving Cherenkov telescope system in the world and therefore suitable for detecting transient phenomena such as GRBs.
A starguider CCD camera is installed in the center of the mirror dish, in order to monitor the tracking system and correct for possible offsets. The best pointing accuracy of MAGIC is about 30 arcsec. For more details I refer to the MAGIC design report [35].
In the following the details of each single telescope are presented.

2.2.1 MAGIC-I

The reflector

The reflector dish of MAGIC I comprises of 956 mirror elements with a total area of 234 m^2. Each mirror element has a square shape of 0.495 m length and has a spherical profile, each with a curvature radius optimized to best obtain the total paraboloid.

Fig. 2.9: The PMTs camera of MAGIC I.

Always four mirrors are grouped together and mounted on one support panel. The mirror elements are light-weight all aluminum sandwich construction and their diamond-turned reflective surface is coated with a thin quartz layer against corrosion and acid rain [59]. The overall adjusted reflector has a point spread function (PSF) of $\sim 10\,\mathrm{mm}$ diameter in the focal plane.

The camera

MAGIC I has a hexagonally shaped camera comprising 576 pixels of two different sizes, covering a total FoV of 3.5^o. The inner part of the camera is equipped with 396 PMTs (ET9116 type) of 0.1^o each. They are surrounded by 180 PMTs (ET9117 type) of 0.2^o each, which form the outer part of the camera (see fig. 2.9). The PMTs are coated with a light scattering lacquer doped with P-terphenyl, a wavelength shifter to increase the sensitivity of the UV light and enhance the QE over the wavelength range between 300 nm and 650 nm [56]. On the front side, the PMTs are equipped with Winston cone type light guides to minimize the dead area between the PMTs [118]. Due to the special shape of the light catcher and hemispherical PMTs most photon trajectories pass the hemispherical photocathode twice thus increasing the chance of the photon to photoelectron conversion. The combined enhancement of the QE due to the diffuse wavelength shifter doped coating and the special Winston cone is about 15-25 % (varying a bit due to the transmission of the semitransparent cathode). In front of the Winston cone plate a UV transmitting Plexiglas cover seals the camera, making it water tight.
The signal from the PMTs is converted into light and transmitted via optical fiber to the read-out. For more information see also [121] and [70].

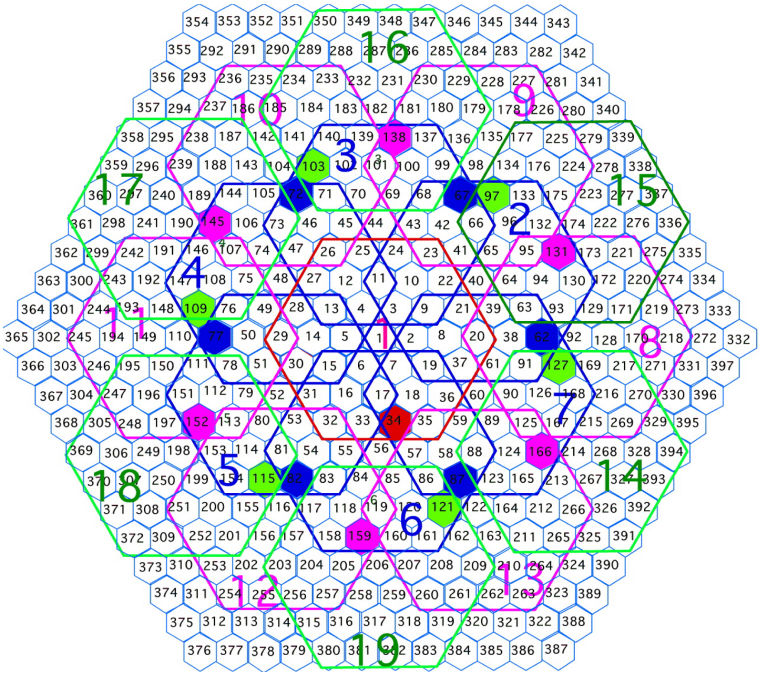

Fig. 2.10: Trigger topology of MAGIC I. 19 macro-cells are forming the trigger area. They overlap to give a high trigger efficiency.

The data acquisition system

Until February 2007 a dual gain 300 MSamples/s 8-bit FADC system [71] has been used. The current read-out system is based on a multiplexing FADC system (MUX). It uses a single 2 GSample/s FADC to digitize consecutively 16 read-out channels. The 16 analog signals are delayed using optical fibers. Each channel is delayed by 40 ns with respect to the previous one. The signals are then routed to the FADC. A trigger is generated using a fraction of the light, which is branched off by fiber-optic light splitters before the delay fibers. The data from the FADCs is sent to the central data acquisition system (MUXDAQ), [72].

The trigger system

The trigger area of MAGIC-I covers the inner camera section with a radius of 0.9^o.
The trigger system is composed of a level 0 (L0) and a level 1 (L1) trigger. L0 trigger consists of discriminators for each pixel. The discriminator thresholds (DT) are automatically adjusted, for each PMT, by an individual pixel rate control (IPRC). This avoids exceeding rates due to stars in the field of view. L1 is based on a logical combination of 19 macro-cells, the schematics of which is shown in figure 2.10. The L1 looks for next-neighbour coincidences within a 6 ns window. Most common used trigger configurations are 3NN and 4NN [122]. This allows to reach a trigger threshold of ~ 50 GeV.
Since October 2007, an additional trigger system, called *Analog Sum Trigger*, can used in parallel to the standard one. This trigger operates on the analog sum of signals

from groups of 18 neighboring pixels before the discriminator. It has allowed to lower the trigger threshold of the MAGIC-I telescope to 25 GeV, particularly important for the detection of the Crab pulsars [26]. This trigger system has not been used for the study of this thesis, therefore for details see [130].

The calibration system

Calibration constants for converting the FADC charge counts into a number of photoelectrons have to be obtained as well as the conversion for the signal timing.
A light pulser using three different colour LEDs is used to illuminate uniformly the PMT camera with different intensities, covering the whole dynamic range of the PMTs. Since the number of photoelectrons (phe) converted from a light pulser is Poisson distributed, the number of phe can be estimated for absolute calibration (through the F-factor method, which is described in chapter 3). Calibration events are recorded in dedicated calibration runs as well as during regular data taking (interleaved calibration). Details on the calibration can be found in [136] and [70].

2.2.2 MAGIC-II

The structure is built as a clone of MAGIC-I, although MAGIC-II has some improved components.

The reflector

The reflector is tessellated with 247 1-m^2 mirror elements of spherical curvature, which are adjusted by an active mirror control system. Two different mirror technologies are used. The central part of the reflector is composed of 143 mirrors made in aluminum sandwich panels using the diamond milling method (the same as MAGIC-I). The adjusted mirrors of the reflector show an excellent focal spot of ~ 9 mm size (one sigma value), while the reflectivity is $\sim 80\%$. The two outer rings of the reflector there comprise 104 mirror elements. They have been manufactured using a new technology: two 2 mm thick glass plates are reinforced by using an Al honeycomb in between. The front plates are coated with a reflecting Al layer. These mirrors show a similar performance as the all-Al mirror with $\sim$ 85% reflectivity.

The camera

The camera of the telescope is placed in the focus of the reflector at a distance of 17.5 m above the mirror. MAGIC-II has an improved camera equipped uniformly with 1039 pixels of 0.1^o diameter each covering the same FoV as MAGIC-I. Always seven pixels are grouped in a hexagonal configuration to form a cluster. The clusters are inserted into holes between two carrying cooling plates. In these two plates the cooling liquid is running through pipes in order to stabilize the temperature of the camera. The modular design allows easier control and maintenance of the camera. On the front side the pixels are equipped with Winston cones. Higher QE of MAGIC-II PMTs compared to the MAGIC-I ones in the UV region increases the detection efficiency of the Cherenkov light. We operate the 6 dynode PMTs at a rather low gain of 3×10^4 in

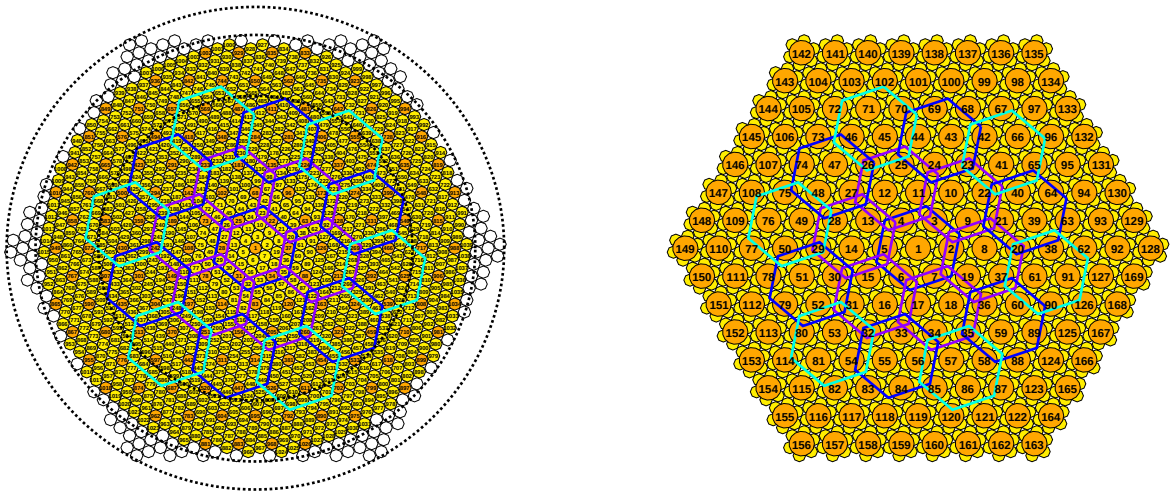

Fig. 2.11: Left: single pixels distribution in a total round configuration of the MAGIC II camera. Right: clusters arrangement. Each cluster contain 7 pixels (less on the border). In the center the configuration of the trigger is shown.

order to perform observations also under moderate moonlight conditions. The electrical signal output of the PMT is converted using the vertical-cavity surface-emitting laser (VCSEL) diodes into light, which is then transmitted by optical fibers of 160 m length to the readout system in the counting house. The camera electronics is powered by two 5 V power supplies mounted in two boxes placed in the bottom, outside the camera housing. [45].
During my PhD I contributed to the calibration and commissioning of the camera. In chapter 3 this work is presented.

The slow control of the camera

Each cluster is controlled by a slow control cluster processor (SCCP). A SCCP board installed in each cluster controls the operations of the camera and reads several parameters. The high voltage (HV) of each pixel is set individually and the PMT current, the HV and the temperature at the VCSEL are continuously monitored. A test-pulse generator board installed near each PMT to test the electrical chain is also controlled by the SCCP [46].

The data acquisition system

The optical signals from each pixel are transmitted via optical fibers to the counting house, where they are converted back to electrical signals. The latter are split in two branches. One branch is further amplified and transmitted to the digitizers, while the other branch goes to a discriminator with an adjustable threshold. This generated digital signal is sent to the trigger system. The 2 GSample/s digitization and acquisition system is based upon a low power analog sampler called Domino Ring Sampler II [139]. The analog signals are stored in a multi-capacitor bank that is organized as a ring buffer. Each single capacitor in the bank is sequentially enabled by a shift register driven by an internally generated 2 GHz clock locked by a phase locked loop

to a common synchronization signal of 100 MHz. Once the trigger occurs, the signals in the ring buffer are read-out at a frequency of maximal 40 MHz and digitized with a 12 bits resolution ADC. The maximal acquisition rate is ~ 150 MByte/s, corresponding to a event rate of 1 kHz. The bandwidth of the Domino II is about 250 MHz.

The MAGIC-II trigger system

Although the same principle of MAGIC I is still used, the MAGIC II trigger has a 1.7 times increased area thanks to a different distribution of the macro-cells (see fig.2.11). The larger trigger area increased the trigger efficiency for gammas. This increases the statistic and enlarges the effective area leading to a somewhat higher sensitivity.

The stereo trigger system

It is used when the two telescopes are operated in stereo mode. It is a coincidence trigger between the two telescopes, and rejects events triggered by only one telescope. The triggers produced by the individual telescopes are delayed by a time which depends on the pointing direction, in order to minimize the time gate of the coincidence trigger, which is about 100 ns.

The calibration system

The calibration of the MAGIC II electronic chain uses the F-factor method (chapter 3). A calibration box is mounted in the middle of the mirror dish. It includes a Nd-YAG laser operated at 3rd harmonic ($\lambda = 355$ nm) and two filter wheels, for a total combination of 28 different attenuations in order to cover the whole dynamic range of the PMTs. The laser produces pulses with 700 ps width and an Ulbricht sphere integrated in the system diffuses the light to illuminate the camera uniformly.

2.2.3 Future upgrades

During this and the next year an upgrade of the MAGIC-I camera is foreseen. The new camera will be a clone of the MAGIC-II camera. In addition a better Domino Ring Sampler read-out will substitute the present Domino, both for MAGIC-I and MAGIC-II.
An upgrade of the camera of the MAGIC-II telescope is also foreseen for the near future. A new photodetector type, the so-called Hybrid Photo Detectors (HPD), will substitute part of the PMTs in the second camera. The HPDs consist of a vacuum tube operated at 6 - 8 kV and an avalanche diode as electron-bombarded anode with internal gain. Thanks to the new camera design the HPD clusters can easily replace the PMT ones, since HPDs are grouped in the same modules as PMTs. The HPDs have higher QE than the PMTs and thus they will provide more photoelectrons for the same input light [133]. The good single photoelectron (SPE) resolution of HPDs and the low afterpulse rate are other advantages of HPDs compared to PMTs, in particular better detection efficiency will lead to lower the threshold.

3

The Characterization of the Photosensors of the MAGIC-II Camera

IACTs rely on the usage of photodetectors for observing high energy cosmic particles impinging on the earth atmosphere. Photodetectors convert the Cherenkov light produced in air showers, generated by the cosmic radiations, into an electric signal. Since the Cherenkov light intensity is weak and the light pulses few nanoseconds short, photomultipliers (PMTs) are currently the only suited photodetectors.
During my PhD studies I was strongly involved in the characterization and test of the PMT selected for the MAGIC-II telescope. I was also involved in the commissioning of the whole camera, which is shown in pictures 3.1 just after the installation.
In this chapter the characteristics and the performance of the PMT of the MAGIC-II camera are investigated and presented in detail.

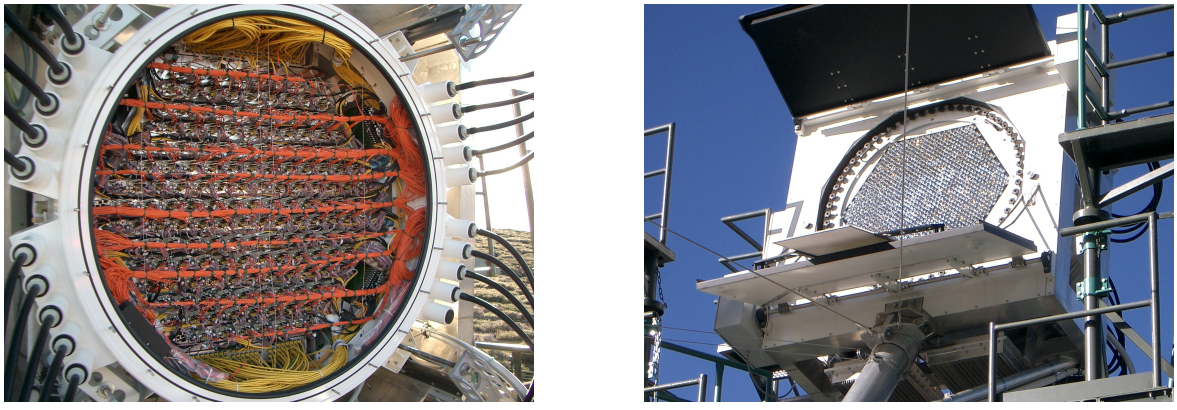

Fig. 3.1: On the left picture the MAGIC-II camera is seen from the back. The cover is removed and it is possible to see the cabling of all the clusters. On the right picture the camera is seen from the front. In the central part it is possible to see the PMTs equipped with Winston cones.

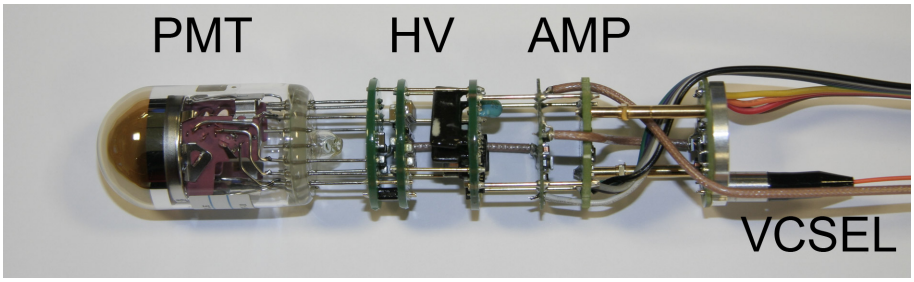

Fig. 3.2: Pixel of the MAGIC-II camera consisting of PMT, HV generator, amplifier and VCSEL. (Picture from T. Jogler)

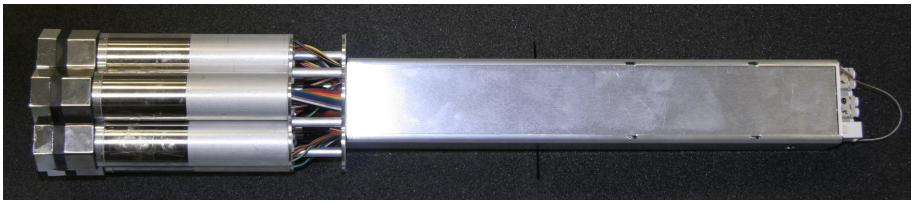

Fig. 3.3: Cluster of the MAGIC-II camera consisting of 7 pixels and the control board. (Picture from T. Jogler)

3.1 The photosensors of the MAGIC-II camera

As already described in section 2.2.2, the MAGIC-II camera comprises 1039 PMT pixels. The PMTs are Hamamatsu R10408 6-stage ones with a hemispherical photocathode [78]. The photocathode converts a fraction of the incident photons into photoelectrons (phe). It is made of a thin, semitransparent semiconductor layer consisting of an alloy of potassium, sodium and cesium with antimonite. Recently, Hamamatsu improved the purity of the semiconductor and decreased the reflectivity, therefore the lacquer coating applied to the PMTs (as in the MAGIC-I camera) is not efficient for these PMTs. The PMTs are coupled with a Crockroft-Walton high voltage (HV) generator manufactured by Hamamatsu. The pixel and cluster assembly is carried out at the MPI in Munich. Picture 3.2 shows an assembled pixel but without a Winston cone. The pixel unit includes a PMT (with an hexagonal Winston cone on top of it), a socket with an HV generator, a preamplifier, a coaxial cable for test pulse and a VCSEL[1] diode. The Winston cone, which is also designed at the MPI, is used for maximizing the collection of incoming light. It concentrates the light on the sensitive region of the PMT and rejects large angle NSB photons. In fact the cone has an acceptance of $\sim 30^o$, thus only photons which are reflected from the mirrors are focused to the PMTs. The HV generator is a Cockroft-Walton type DC-DC converter, that converts DC electrical power from a low voltage level to a higher DC voltage level. The PMT has 6 dynodes and the dynodes voltage distribution is such that the voltage between the photocathode and the first dynode is three times the voltage between the following dynodes. The preamplifier has 700 MHz bandwidth. An AC coupling between the

[1]Vertical cavity surface emitting laser

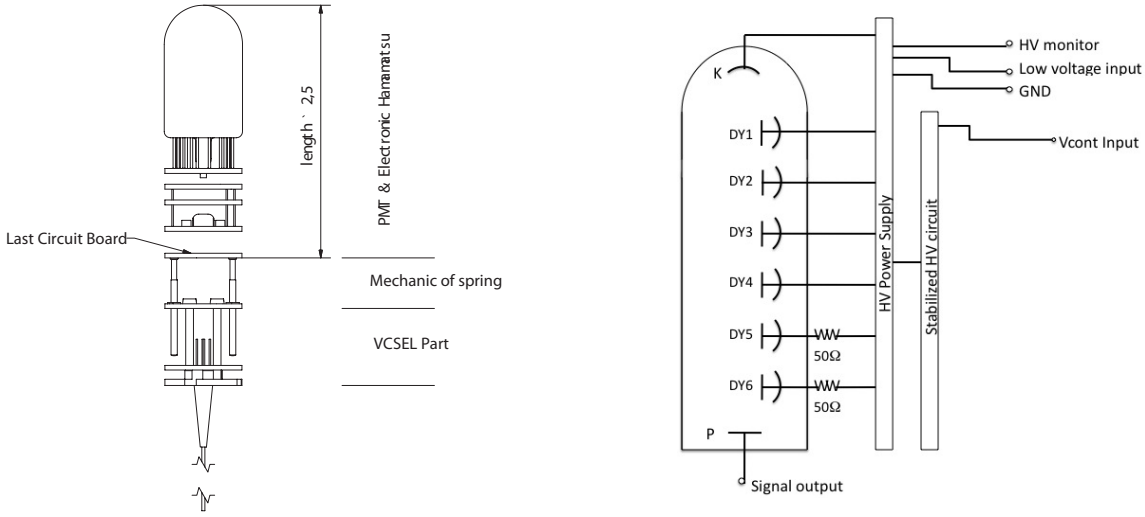

Fig. 3.4: On the left: scheme of the Pixel module: the PMT and the HV generator are connected to the preamplifier boards and VCSEL. On the right: scheme of the PMT with the dynodes distribution (from DY1 to DY6). The Cockroft-Walton HV generator is such that the voltage between the photocathode (K) and the first dynode (DY1) is three times the voltage between the following dynodes. The signal output is from the anode (P).

PMT output and the amplifier transmits only the fast AC component from the PMT output via a capacitor. The coaxial cable is used for injecting a pulse signal before the preamplifier and test the entire electronics chain after the PMT without setting the HV. The VCSEL is supplied by a small current ($\sim 3\,\mathrm{mA}$) to operate it in the stable lasing mode. In figure 3.4 on the left, a scheme of the pixel module is provided, which includes the PMT module and the HV generator provided by the company plus the components produced and assembled at the MPI. On the right panel of figure 3.4 a sketch of the PMT shows the dynodes distributions and the electrical connectors.
Each pixel is electrically shielded by an aluminum foil. In addition, each pixel is shield against the earth magnetic field by a thin sheet of mu-metal. Seven pixels are grouped together in a cluster as shown in picture 3.3. Each cluster provides the slow control (SCCP) of all seven pixels. The SCCP controls the setting and the read-out of several parameters of each individual pixel: HV setting and reading, VCSEL bias current setting, VCSEL temperature and photo-diode current reading, PMT current reading and test pulse injection setting.
The main characteristics of the PMTs chosen for the MAGIC-II camera are described in the following.

3.1.1 The parameters chosen for the MAGIC-II camera

High quantum efficiency (QE)

The QE is defined as the number of phe emitted from the photocathode divided by the number of incident photons. In figure 3.5 (on the left) the QE as a function of the wavelength λ is shown both for the PMTs of MAGIC-I and MAGIC-II. The band of

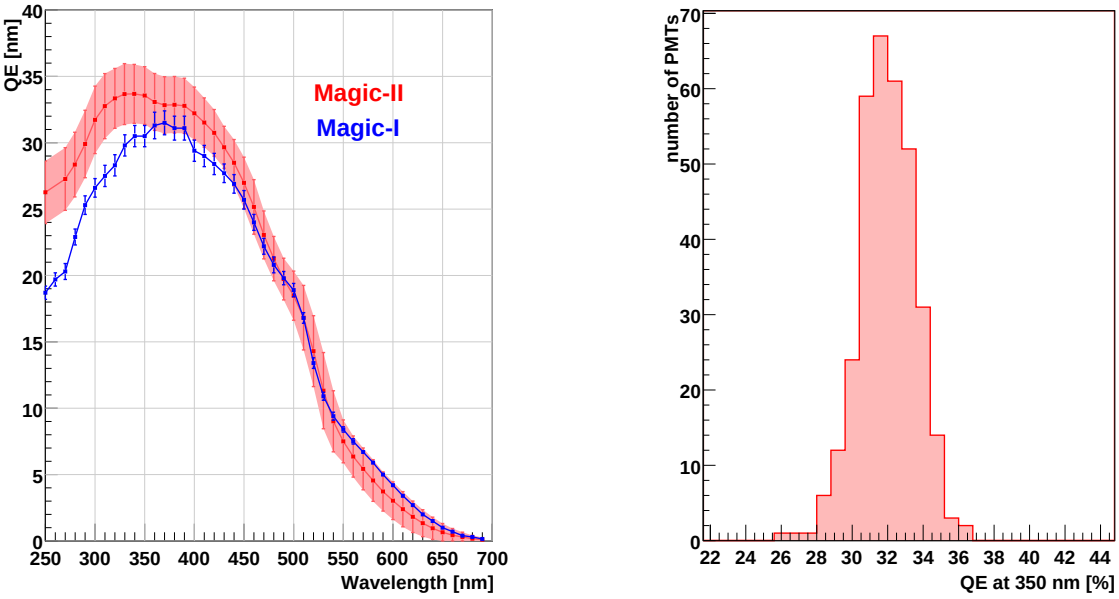

Fig. 3.5: Left panel: Quantum efficiency as a function of the wavelength for MAGIC-I (in blue) and MAGIC-II (in red) PMTs. The band of MAGIC-II curve represents the spread over different PMTs, for MAGIC-I instead, the error bars are the errors in the measurement of a single PMT. Right panel: distribution of the QE values for MAGIC-II PMTs at $\lambda = 350\,\mathrm{nm}$

MAGIC-II curve represents the spread over different PMTs. In the case of MAGIC-I instead, the error bars are the errors in the measurement of a single PMT. One can notice that the MAGIC-II PMTs have a higher QE compared to those of MAGIC-I, particularly at smaller wavelengths. In fact, the Cherenkov light intensity decreases with $1/\lambda^2$, while the intensity of the NSB increases with increasing λ. Figure 3.5 (on the right) shows the distribution of the QE values at $\lambda = 350\,\mathrm{nm}$ (where the Cherenkov light has its highest intensity) with a mean value of 32%.

The phe collection efficiency in the PMT front-end

A high QE is a necessary prerequisite but not sufficient to get a high sensitivity because not all photoelectrons are collected in the PMT front-end region.
The collection efficiency is the ratio between the number of electrons reaching the first dynode and the number of phe emitted at the photocathode. It varies with the initial velocity of the phe and therefore is dependent on the wavelength of the incident photon, the geometry of the front-end system and the electrical field strength between the photocathode and the first dynode. It is not uniform over the entire surface of the photocathode and therefore depends on the geometry of the latter. It also depends on the focusing of the phe by the electric field, which depends on the voltage applied between the photocathode and the first dynode. The collection efficiency is very difficult to measure. A coarse estimate for the used PMTs and 300 V between cathode and the first dynode yields a collection efficiency of $\approx 85\%$.

Low gain

The gain of a PMT is defined as the ratio between the anode current and the photocathode current. For a N-stage PMT the gain can be expressed as:

$$G = \eta \prod_{i=1}^{N} \delta_i \eta_i \tag{3.1}$$

where η is the collection efficiency of the first dynode, δ_i the secondary emission coefficient of the ith dynode and η_i the collection efficiency of the ith multiplier stage. The gain increases with the applied voltage and follows approximately a power law $G \approx V^N$, where V is the applied voltage and N the number of dynodes. Since MAGIC observes also in moon and twilight conditions, the gain of the PMTs is chosen to be relatively low ($1{\cdot}10^4$ - $6{\cdot}10^4$), in order not to damage the PMTs with too high current. This is achieved by using PMTs with only 6 dynodes.

Hemispherical photocathode and 0.1^o diameter size

The hemispherical shape of the photocathode has the advantage of increasing the light collection efficiency because often the trajectory of the photons pass the semitransparent photocathode twice thus increasing considerably ($\approx 15\%$) the chance of conversion. In addition the curved shape decreases the time jitter. The photoelectrons, in fact, travel the same distance from the entire photocathode surface to the first dynode. In addition, the 0.1^o diameter size of the PMT ($\sim 25\,\mathrm{mm}$) is chosen in order to have a good angular resolution and to be of the same size of the point spread function of the reflector, which is approximately 10 mm radius.

Time spread

Cherenkov pulses from air showers last only a few nanoseconds. In order to preserve the time structure of the pulses, PMTs are chosen to have time response shorter than the Cherenkov pulse. Fast time response is also achieved with the usage of few dynodes. The transition time spread is in fact due to the multiplication of the phe at each dynode and to different path lengths of the electrons between the dynodes.

Afterpulsing

Afterpulses are caused by ions liberated by photoelectrons from the first dynode and accelerated towards the photocathde. Due to imperfection in the evacuation of the PMTs there are residual gases and residual molecules adsorbed by the dynodes. During acceleration, a photoelectron can ionize the residual gas and molecules. Due to high potential, these ions fly back to the photocathode and can produce additional phe. These afterpulses are then time correlated with the main pulses. The NSB can induce large afterpulses that trigger the telescopes. The afterpulse rate can be reduced by decreasing the voltage applied from the photocathode to the first dynode, albeit with a reduction in collection efficiency.

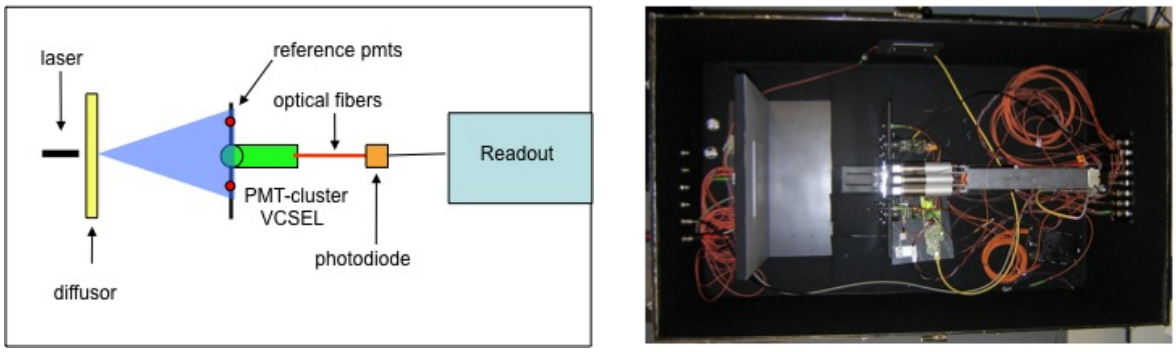

Fig. 3.6: Schematics of the measurement setup (left) and physical realisation (right).

Dynamic range

In order to detect γ-ray showers from few tens of GeV to few tens of TeV, PMTs have to resolve signals of just a few phes as well as very large signals. A wide dynamic range is then necessary. Moreover the PMTs have to have a linear response in the range 1-1000 phes.

Single Photoelectron resolution

The resolution of the single photoelectron ($Sphe$) pulses is important for the calibration of the telescopes and for determining the conversion factor from number of incident photons in each pixel to number of recorded FADC counts. The phe to FADC count conversion factor can be calculated by measuring the excess-noise factor F (F-factor) of the PMTs [111]. One can define the PMT excess noise factor as:

$$F = \sqrt{1 + \frac{Var(G)}{\overline{G}^2}} \tag{3.2}$$

where $Var(G)$ is the variance of the measured $Sphe$ distribution and $\overline{G}$ its mean. The number of phe can then be calculated as:

$$N_{phe} = \frac{\overline{Q}^2}{Var(Q)} \cdot F^2 \tag{3.3}$$

where $Var(Q)$ is the variance of the measured charge distribution and $\overline{Q}$ its mean.

3.2 Measurements Setup

The measurements we performed for all the clusters installed in the MAGIC-II camera comprise dynamic range, gain, time spread and single photoelectron. The used measurement setup is described in the following.
A 100 cm × 60 cm × 40cm black box with a copper layer is used to shield the cluster from external radiation. Inside the box the cluster under test is illuminated by a laser light. Two different configurations of the input light are used: direct and indirect.

In the direct light configuration, the laser light ($\lambda = 440\,\mathrm{nm}$) connected to an optical fiber, illuminates directly the cluster through a rotating, selectable filter wheel and a spectralon diffuser. In this configuration the light is found to be homogeneous at the 90% level over the cluster area. In the indirect configuration instead, the laser light ($\lambda = 375\,\mathrm{nm}$) is divided by an optical splitter into three spots and reflected by the spectralon panel before illuminate the cluster. The latter configuration is used to simulate better the conditions of the reflector; the incident angle of the light corresponds roughly to the incident angle of the photons reaching the MAGIC camera from the mirror dish ($\pm$ 30º). With this second configuration the light is measured to be homogeneous at the 95% level over the cluster area. By adding manual attenuators at the entrance of the optical fiber connected to the laser it is possible to reduce the light intensity down to *Sphe* level.
On the same panel where the three laser spots are placed, four reference PMTs are placed in a squared configuration (see fig. 3.6). These PMTs are the same type as the ones in the cluster. They are controlled by separate SCCP and are read out directly (i.e. without the use of VCSEL). Two of them are operated at low gain for monitoring high intensity pulse during linearity measurements, while the other two are operated at high gain for good *Sphe* resolution measurements.
A photo-diode box with seven channels and dual gain outputs is used to convert back the optical signal from the optical fibers to an electrical signal. As readout system a five boards, each of 4 channels FADCs from CAEN are used (7 channels connected to low gain, 7 to high gain and 4 for the reference PMTs). The FADCs have a bandwidth of 300 MHz with a 2 GSample/s sampling and a dynamic range of $\pm\,0.5\,\mathrm{V}$. It has a resolution of 0.25 mV/ADC count. The trigger for the readout system and for the laser are generated by an external pulse generator, with a frequency of 1 MHz for the laser and 1 kHz for the readout system. The functionality of the pixel, the gain, the linearity behavior and the *Sphe* resolution have been measured separately for all 1039 pixels.

3.3 Cluster characterization results

3.3.1 Optical transmission gain

For a sample of 20 pixels the variation of the gain of the optical transmission, which includes VCSEL and optical fiber, has been measured. The measurement has been done injecting a high pulse in the test pulse coaxial cable. This high pulse saturates the preamplifier, therefore, the pulse injected at the VCSEL level is the same for all the pixels. The optical fiber has been connected to a photodiode and the output pulses has been measured. The maximum variation of the gain of the optical transmission has been measured to be $\sim 35\%$. We believe that the VCSEL have the largest contribution in this.

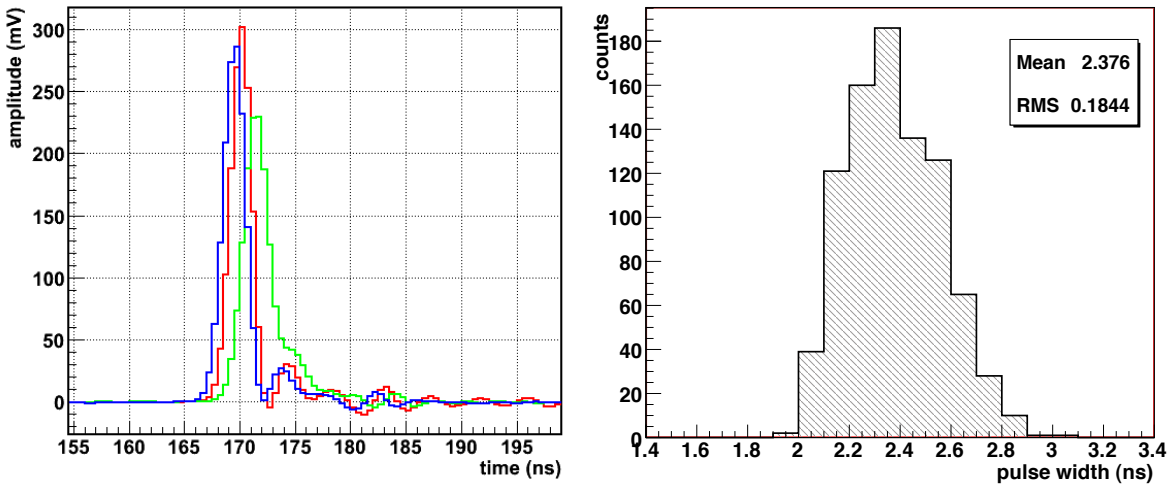

Fig. 3.7: Mean pulses from three different pixels on the left. Distribution of the pulse width of all the pixels on the right.

3.3.2 Pulse shape

One of the most important parameters in the response of PMTs is the width of its pulse. It is defined as the full width at half maximum (FWHM) of the output pulse. Since the Cherenkov pulse is only few nanosecond short, the PMT is required to be comparably fast. In figure 3.7 the mean pulses of three different pixels are shown on the left plot. One can notice how the pulse shape varies from pixel to pixel, nevertheless, the mean width averaged over all the pixels is $\sim 2.4\,\text{ns}$, as it is shown in the pulse width distribution in figure 3.7 on the right. It is well-known that the pulse width of the PMT is proportional to $1/\sqrt{HV}$; so the PMTs under higher voltage provide shorter pulses.

3.3.3 Flatfielding and Gain

In order to operate the whole camera it is important that all the pixels have the same response. This means that for the same light they have to provide all the same output charge. This procedure is called flatfielding. Gain of a pixel includes that of the PMT, of the preamplifier and of the VCSEL. Since gain varies with the applied voltage, a scan over several voltages is performed and the corresponding gain calculated.
A monitor PMT without VCSEL and optical fiber is used as reference. The applied voltage is set in order to have a gain of $3{\cdot}10^4$. All the pixels in the clusters are then exposed to a laser intensity corresponding to $\sim 100\,\text{phes}$. A scan over six different HV from 600 V to 1250 V is performed and the corresponding charge measured. The charge is calculated integrating the pulse over 5 ns. This is shown in figure 3.8 where the charge is plotted for different HV setting for 7 pixel of one cluster. The measurements are fitted by a power-law function $Q = aV^{\delta}$, where δ varies from ~ 3.8 to 4.0 for this cluster. Comparing the charge of the monitor PMT (shown as dash line in figure 3.8) with these curves, HV value for each pixel is calculated in order to have the same charge as in the monitor PMT. In this way all the pixels are flatfielded to the same

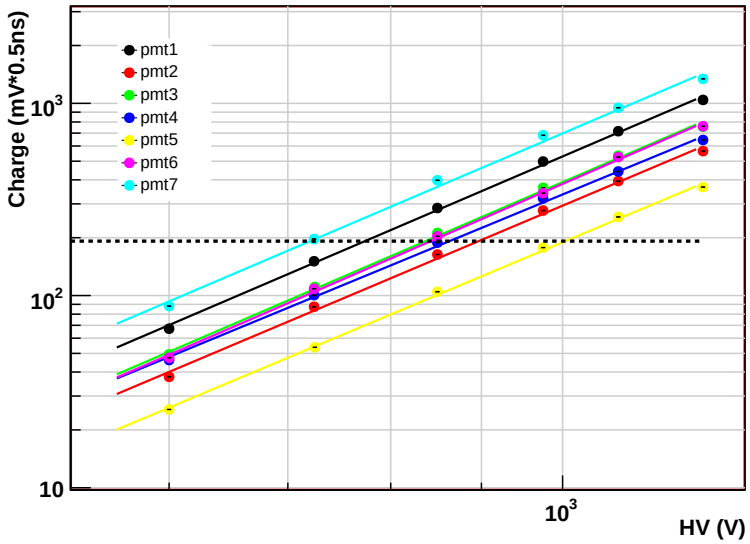

Fig. 3.8: PMT charge as function of the HV for 7 pixels of a cluster. The dash line represents the charge of the monitor PMT which correspond to a gain of $3{\cdot}10^4$.

output signal. The gain of all the PMTs at the flatfielded voltage is calculated in two different ways:

1. from the charge distribution:

$$G_Q = \frac{Q}{N_{phe} \cdot q_e \cdot R \cdot Ampl} \tag{3.4}$$

   where Q is the mean measured charge, $q_e = 1.6{\cdot}10^{-19}\,\mathrm{C}$ the electron charge, $R = 50\,\Omega$ the impedance of the FADC and $Ampl = (A_{preampl} + A_{optical})/2$ the amplification of the preamplifier and the attenuation of the optical fiber. The factor 2 came from the fact that the signal is split in two and the values of the amplifications are $A_{preampl} = 25$db and $A_{optical} =$ -20db. N_{phe} is the number of phe calculated as in 3.3, where the F-factor is computed from the $Sphe$ measurement (see section 3.3.5).

2. from the DC anode current:

$$G_{DC} = \frac{DC}{N_{phe} \cdot q_e \cdot \nu\eta} \tag{3.5}$$

   where η is the collection efficiency of the photoelectrons on the first dynode; DC is the measured PMT anode current and $\nu = 1$MHz the frequency of the input laser light pulses. N_{phe} is the number of phe calculated as in 3.3.

The distribution of the gain measured with the two methods is shown in figure 3.9. They are compatible with each other and their mean values are $\approx 3{\cdot}10^4$. Since the gain of the VCSEL is not known, the computed gain includes the gain of the PMT folded

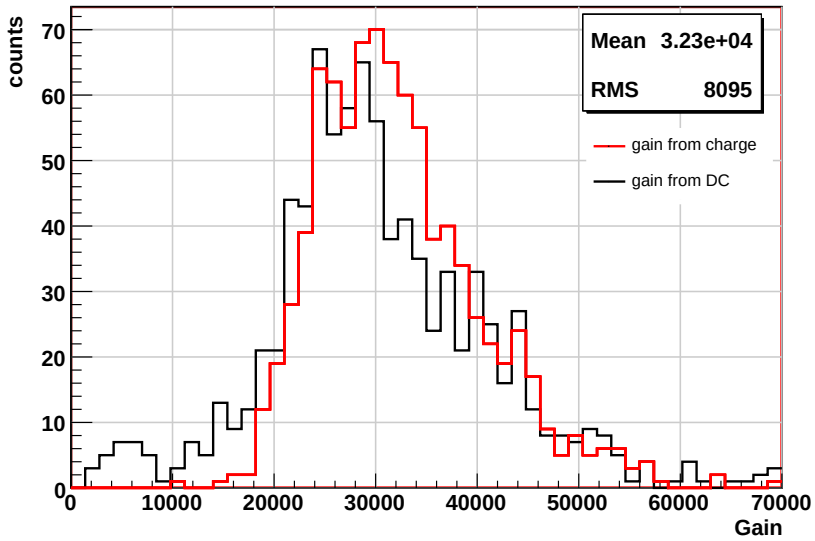

Fig. 3.9: Gain distribution for all PMTs at the flatfielded voltage. The red histogram shows the gain calculated from the charge, while the black histogram shows the gain calculated from the DC current

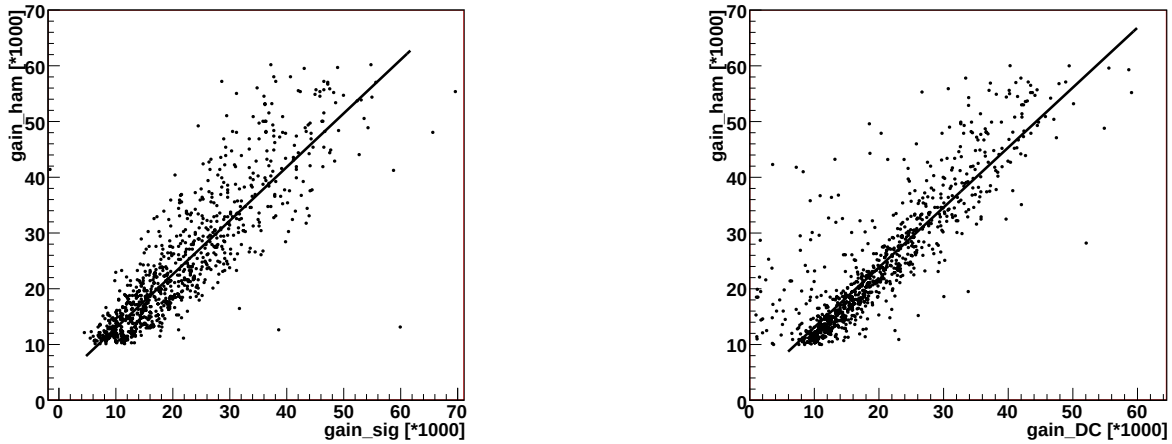

Fig. 3.10: Comparison of the measured gain at 850 V with the gain provided by Hamamatsu. On the left plot the measured gain is computed from the charge, while on the right plot it is computed from the DC current.

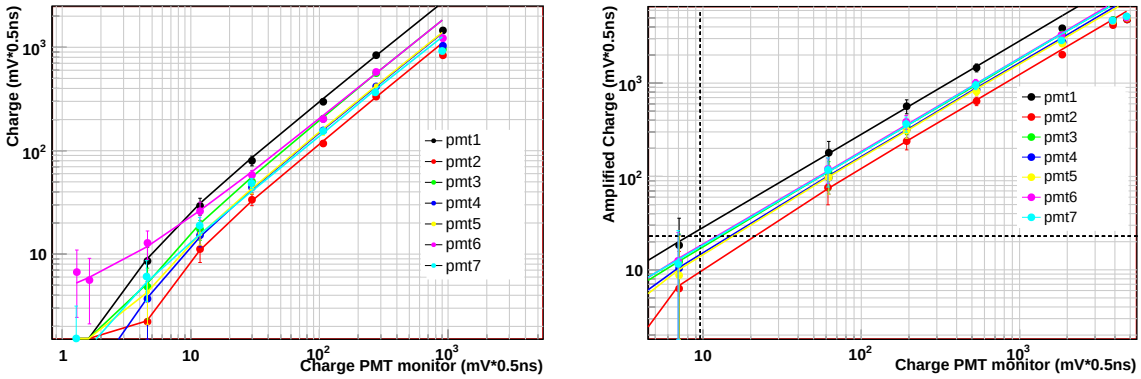

Fig. 3.11: Linearity curves for 7 pixels of a cluster on the left. On the right plot the signal of the pixels is amplified by 25db.

with the gain of the VCSEL. Given the values of the PMT gain at 850 V provided by the company, a comparison with our measurements is shown in figure 3.10. On the left plot the gain provided by the company is shown versus our measurement at 850 V from the charge distribution. On the right plot the comparison is done with the measurement from the PMT DC current. Even if in our measurements also the gain of the VCSEL is included, a linear correlation is present in both the plots. The spread from the linear fit is most probably due to the variation of the VCSEL gain.

3.3.4 Linearity and dynamic range

Measurements at different intensities of the input light have been performed in order to check the linearity of the pixels and to estimate the dynamic range. As already mentioned, a monitor PMT is used as reference. A relatively low HV of about 700 V has been applied to the monitor PMT in order not to saturate it. The flatfielded voltage has been applied to all pixels. In figure 3.11 on the left the charge of 7 pixels in a cluster is shown as a function of the charge of the monitor PMT. For small signals the curves deviate from linearity because of high pedestal noise. For large signals, at around 450 mV·0.5 ns some of the pixels start to saturate. On the right plot of figure 3.11 the same measurement is shown, with the usage of an additional amplifier (with 25 db amplification) in order to be able to measure small signals above the pedestal noise. At the largest signals the FADC is saturating before the pixels saturate. From these measurements (with and without an additional amplifier), the dynamic range is estimated to be $\sim$800 - 900 phes. In any case, the dynamic range of the whole camera is limited by the dynamic range of the Domino II read-out which is abut 600 - 700 phes.

3.3.5 Single photoelectron resolution

For the *Sphe* measurement the laser intensity has to be set very low. With the used setup, the level of the light intensity is set to measure a single photoelectron in the monitor PMT, which have been operated at a voltage of 1250 V.
The *Sphe* regime is determined using the Poisson statistics, with the probability of

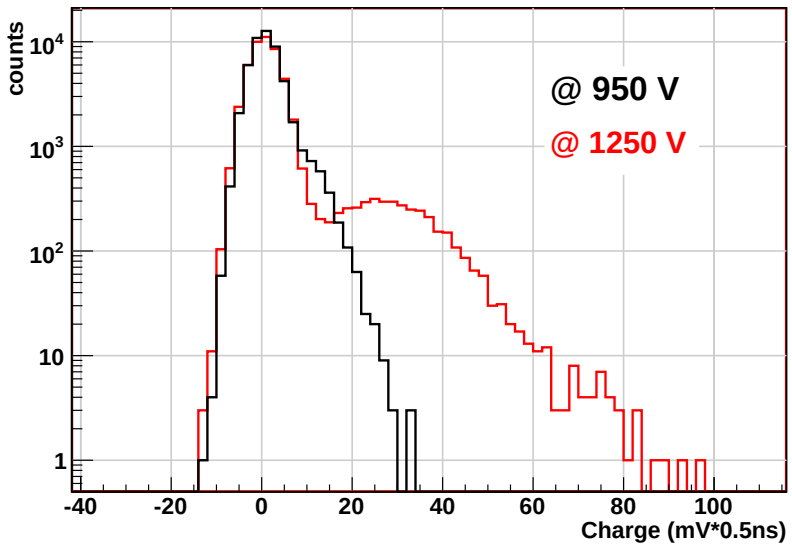

Fig. 3.12: *Sphe* distribution for two different HV setting of the PMT under test: In black the distribution is shown for 950 V (pedestal only), in red for 1250 V (essentially pedestal plus one phe).

having k phes for a mean value μ:

$$P(k,\mu) = \frac{\mu^k e^{-\mu}}{k!} \tag{3.6}$$

If we choose the value of μ to be 5%, the probability of having 2 phes is $\sim$2.5% of the probability of having 1 phe. Therefore, in the spectrum of the *Sphe*, 95% of the counts represent the pedestal, while 5% represent one phe.
This measurement has been carried out for all pixels at the maximum HV, in order to be able to distinguish the *Sphe* peak from the pedestal. As it is shown in figure 3.12 at 950 V the *Sphe* peak of the PMT under test is not discernible from the pedestal, while at higher HV ($\sim$1250 V) the *Sphe* peak is well defined with approximately $8\,\sigma_{ped}$ away from the pedestal peak, where the standard deviation of the pedestal is $\sigma_{ped} = 3.2\,\text{mV}\cdot 0.5\,\text{ns}$. The charge distributions of the *Sphe* and pedestal are determined integrating the FADC pulses over 5 ns.

The F-factor is calculated as:

$$F = \sqrt{1 + \frac{RMS^2_{Sphe} - RMS^2_{ped}}{(Q_{Sphe} - Q_{ped})^2}} \tag{3.7}$$

where RMS_{ped} and Q_{ped} are the RMS and the mean value of the pedestal, which is due to the electronic noise of the system. These values are calculated subtracting the Gaussian fit of the pedestal from the total distribution of the *Sphe* and calculating the mean value and the RMS of the remaining distribution. The *Sphe* and the pedestal

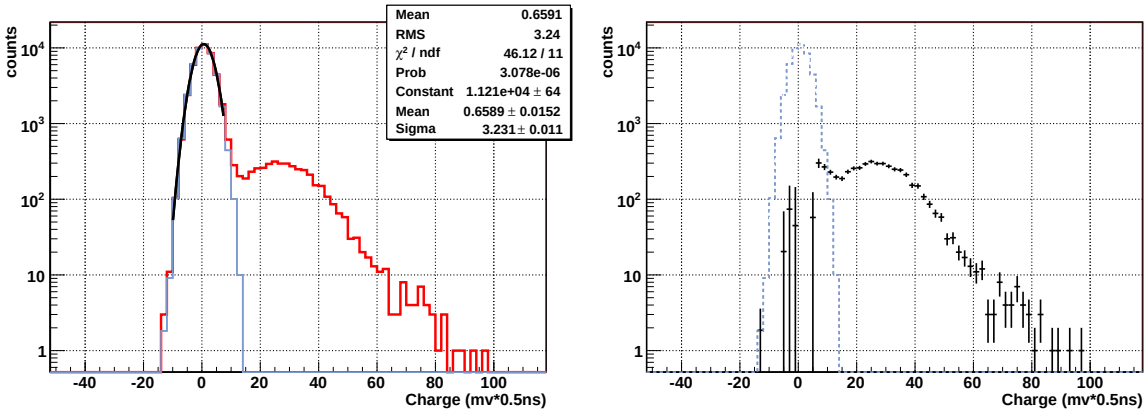

Fig. 3.13: Distribution of the *Sphe*. On the left panel: the total distribution is shown in red, while the distribution of the pedestal is in blue with the fit to it in black. On the right panel: the distribution of the *Sphe*, where the pedestal (shown in blue dash line) is subtracted.

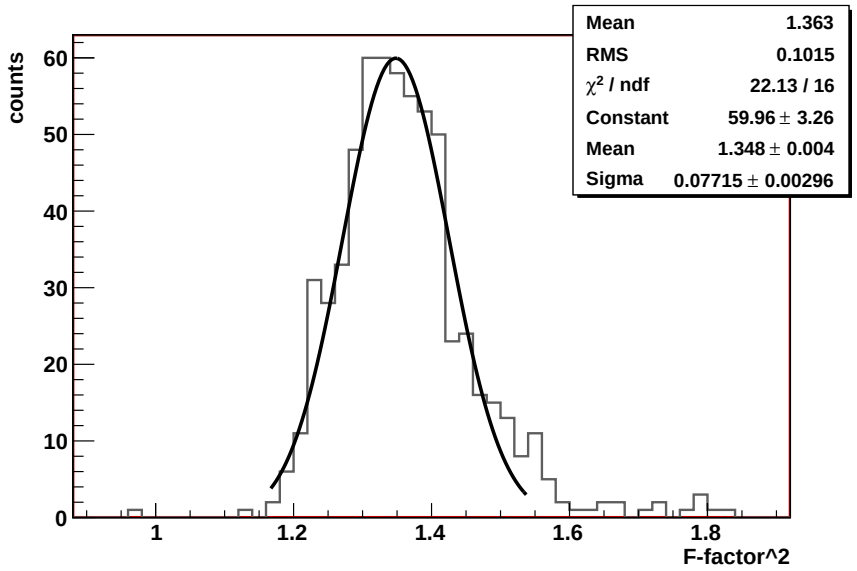

Fig. 3.14: Distribution of the F^2-factor computed for all pixels.

charge distributions are normalized by the number of events under the pedestal distribution peak integrated from -1 σ to +1 σ of the pedestal distribution.
The main difficulty in this measurement is subtracting the pedestal. Due to multiplication processes in the dynodes and back scattered electrons, the *Sphe* spectrum has large tail of low amplitudes. This makes the distribution asymmetric. In the spectrum shown in figure 3.13 (on the right) the black distribution representing the *Sphe* spectrum after the pedestal subtraction show a first peak at around 6 mV·0.5 ns, which is due to the back scattered electrons and multiplication processes.
Due to big uncertainties in the measurement, the estimation of the F-factor is very difficult and can vary considerable from PMT to PMT. In figure 3.14 the distribution of the F^2-factor for all the PMTs is shown. The computed distribution of the F^2-factor has a mean value of 1.36 and RMS of ~ 0.10.

All the measurements here described have been performed for all the clusters of the MAGIC-II camera. The PMTs with high QE (cathode blue sensitivity index > 12) and low gain (gain at 850 V $< 3.8{\cdot}10^4$) have been selected to be installed in the trigger region.
The preparation of the measurement setup and the tests took place between fall 2007 and summer 2008 and I was personally involved both in the cluster tests and in the commissioning of the camera. The installation of the entire camera in La Palma took place in summer 2008 and after that the commissioning. Since fall 2009 the MAGIC-II telescope and the stereo system are fully operational.

4

Analysis method for γ-ray point sources and for diffuse cosmic electrons with MAGIC

In this chapter the analysis methods used in this thesis are described. Since the standard analysis is optimized for point sources, I have developed a method to detect signal from diffuse sources, such as cosmic electrons and also to determine their energy spectrum. Both the methods are described here.
In this chapter, I describe the observation techniques and the entire analysis chain. At the end an overview of the simulation programs used and a comparison between simulated and real data is given.

4.1 Data Taking and observation modes

IACTs primarily are used for the observation of gamma-ray sources during dark, clear nights without moon. MAGIC with its 6-stage PMTs, which have lower gain, is able to operate under moderate moonlight too. For MAGIC, the average dark night duty cycle is about 1000 h per year. The capability of operating under moonlight conditions increases the observation time by about 300 h per year.
In both conditions, to ensure a safe operation of MAGIC, the following conditions must be fulfilled:

- Humidity $< 90\%$
- Wind speed $< 40 km/h$
- Average PMT current $< 7 \mu A$
- Individual PMT current $< 20 \mu A$

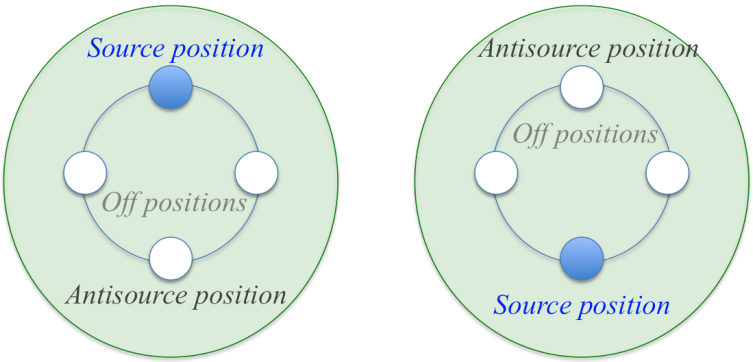

Fig. 4.1: Illustration of the wobble observation mode. The source is at the center of the blue circle, while white circles indicate the region from which the background is estimated. Every 20 minutes the source position and the anti-source position swaps places.

- Zenith angle $> 1.5^o$

Standard data taking procedure includes:

- Pedestal Runs. These runs contain 1000 events, taken with random trigger, which are used to calculate pedestal offsets of the read-out and pedestal RMS, to estimate the NSB level.
- Calibration Runs. These runs contain 4096 events triggered by a calibrated light pulser (from 10 UV LED for MAGIC-1 and from a laser with $\lambda = 355$ nm for MAGIC-II). These events are used to calculate conversion factors from FADC counts into the number of photoelectrons and arrival time offsets.
- Data Runs. These runs contain events triggered by the telescope while pointing to a preselected sky area to be studied. They contain also interleaved calibration and pedestal events, continuously recorded at a rate of 25 Hz. The interleaved calibration events are used to correct for possible gain changes of the electronics during the night, caused by temperature changes and mode hopping of the VCSELs.

Observational data are taken in two different observation modes: *On-Off* and *wobble* mode. In *On-Off* mode the target object is tracked pointing directly to the sky position of the source, such that the source is always in the camera center. Such data are called *On*-data. Additional data are needed to estimate the background. In the *On-Off* mode they are taken by observing a region without known γ-ray sources. They are called *Off* data, assuming similar conditions as the *On* observation in terms of zenith angle, sky brightness, discriminator thresholds, etc.
In *wobble* mode, the telescopes are not pointing directly at the source, but alternately (changing every 20 minutes) at two positions opposite each other and 0.4^o away from the source. In this way, simultaneous measurements of signal and background are provided. In figure 4.1, a sketch of the wobble mode shows how the source and the off positions swap places. Currently, most MAGIC data are taken in *wobble* mode,

with the advantage that simultaneous acquisition of *On* and *Off* reduces the systematic effects due to different conditions (NSB levels, discriminator thresholds, weather conditions, etc.). On the other hand, the trigger acceptance is reduced by 15-20 % depending on the energy and further cuts in the analysis , because of the offset of the source.
In the case of cosmic electrons, the observation mode is irrelevant, as they are completely diffused. Therefore, I will use available data independently of the observation mode.

4.2 The MAGIC analysis and reconstruction software

The MAGIC data are processed by the MAGIC Analysis and Reconstruction Software (MARS), which has been developed to perform a complete and robust analysis of the signals. It has been written in C++ language and is based on the ROOT framework [3].
The MARS package includes several programs that perform different steps of the analysis. I developed a new part (*electronflux* program) for the analysis of diffuse electron showers, for extracting the signal of electrons from the background and estimating their energy spectrum.
The main analysis programs which will be explained in details in the next sections are:

- *Callisto:* conversion from FADC counts into number of photoelectrons (phes) for each pixel, (section 4.2.1).
- *Star:* cleaning of the images to remove the noise, and parametrization of the recorded shower images, separately for the two telescopes (section 4.2.2).
- *SuperStar:* Reconstruction of the stereo parameters, combining the images of the two telescopes, (section 4.2.3).
- *Osteria:* training of the decision trees (Random Forest - RF) that will be used for electromagnetic/hadronic separation and energy estimation, (section 4.2.4).
- *Melibea:* application of the RF trained in *Osteria* to a set of MC sample, real data and background sample, to calculate the *Hadronness* parameter and estimate the energy for each event, (section 4.2.5, 4.2.6).
- *Electronflux:* calculation of the effective time of the observation, determination of the effective acceptance and the number of excess events. At the end, the energy spectrum is derived, (section 4.2.7, 4.2.8). *Electronflux* is a modified version of the program *Fluxlc* which is used for the analysis of point sources.
- *Unfolding:* recover of the true energy distribution from the estimated one to correct the energy spectrum.

A scheme of the analysis chain, as shown in figure 4.2, helps to understand the complete analysis procedure and the functions of the programs used.

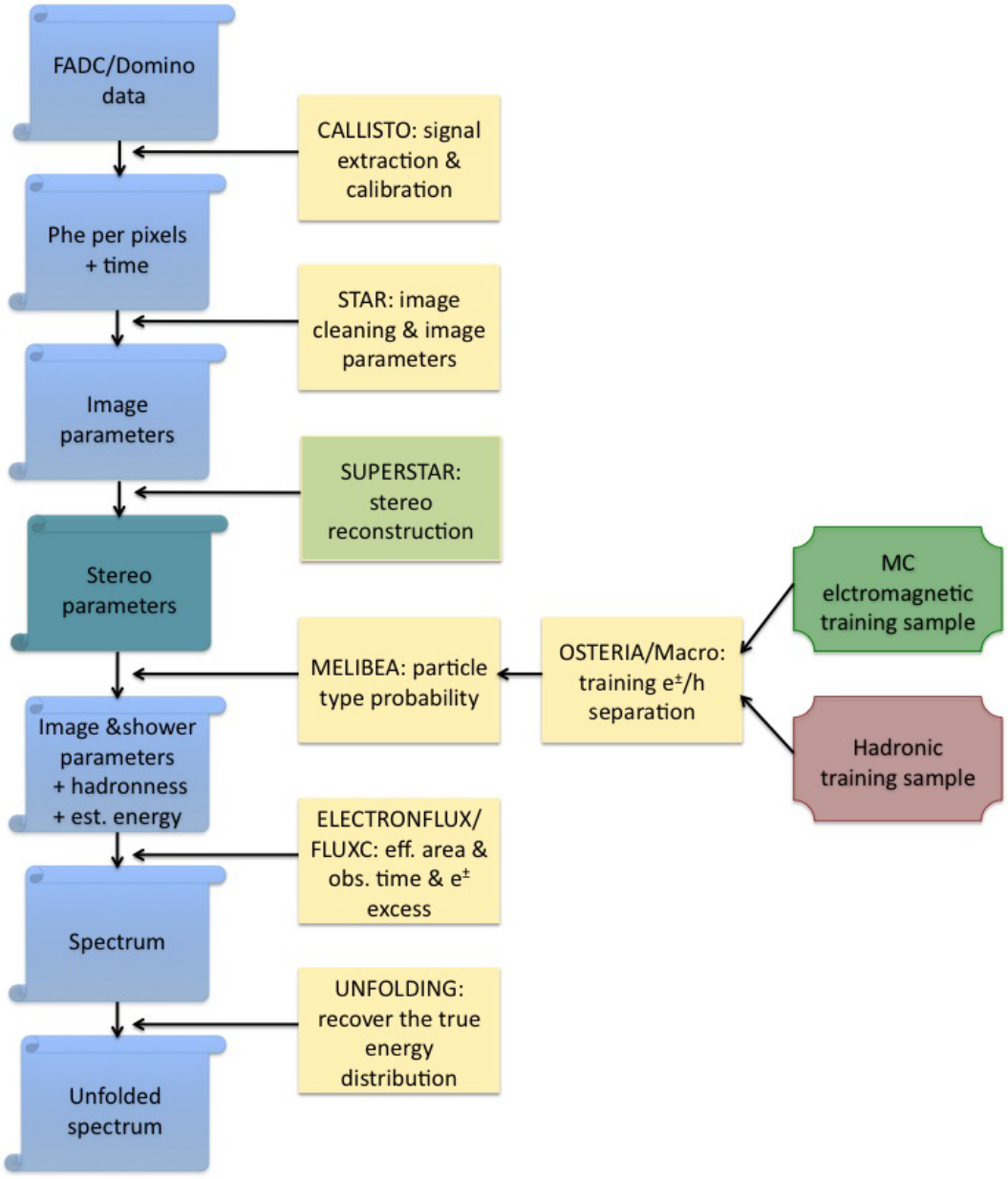

Fig. 4.2: The MAGIC stereo analysis chain from the raw data to the spectrum determination. In the case of single telescope analysis the procedure is the same but the stereo reconstruction. The electromagnetic and hadronic training samples are also processed up to superstar (or star for single telescope).

4.2.1 Charge reconstruction and calibration

From the data recorded by the DAQ, the signal has to be extracted and calibrated. At this level, the data contain not only Cherenkov photons, but also fluctuations of NSB (including light from close optical sources) and electronic noise from the readout chain. These offsets are measured by pedestal events taken at the beginning of the observation and by interleaved pedestal events and subtracted from the signal events. The signal is then extracted from the FADC samples, and its charge obtained by integrating over a preset number of FADC samples. The method used for MAGIC-I is based on an interpolation of the FADC counts by a cubic spline (for details see [16]) and a successive integration over 9 ns (18 FADC slides) in case of large pulses and over ~ 3.5 ns (7 FADC slides) for small pulses. In the case of MAGIC-II, instead, the charge is obtained integrating over 4 ns (8 ring sampler slides) around the peak of the pulse.
The arrival time of each event is also calculated and defined as the position of the rising edge of the pulse at 50% of the peak value.
After the pulse amplitude is determined, the calibration is performed by converting the number of ADC counts into the equivalent number of photoelectrons using a calibration constant for each individual pixel. The calibration constants are calculated from dedicated calibration runs taken before the observation and from interleaved calibration events.

4.2.2 Image Cleaning and Image Parameters

After calibration and extraction of the signal in each pixel, a procedure called *Image Cleaning* is applied. The image cleaning procedure discriminates pixels which belong to the shower image and pixels which contain only background noise. Different levels of cleaning can be applied depending on the data. Currently the cleaning level in photoelectrons used is *6/3-time* for MAGIC-I and *9/4.5-time* for MAGIC-II. This means, for example in the case of *6/3-time*, that pixels with more than 6 phes belong to the shower and are called core pixels, and pixels with at least 3 phes, neighboring at least to one core pixel, are also belonging to the shower. In addition the arrival time of the signal in each individual pixels is used to define if the pixel signal belongs to the shower image. In fact, while background noise pulses are uniformly distributed in time, the single photons of the showers arrive in a short time interval of few nanoseconds. Thus, the mean of the arrival times of the core pixels is calculated and the arrival time in each pixel belonging to shower image can deviate at most of 4.5 ns from the shower core arrival time. In addition the time difference between adjacent pixels has to be less than 1.5 ns. With these conditions more pixels are rejected from the shower compared to the image cleaning without the time conditions, but a lower phe cleaning level can be achieved. In figure 4.3, air shower images on the cameras before and after the cleaning process are shown.

The images of electromagnetic showers can be parametrized by the so-called Hillas parameters (of the 'Hillas ellipse'), as was first proposed by Hillas [101]. These are the second moments of the shower light distribution. The major axis of these ellipses

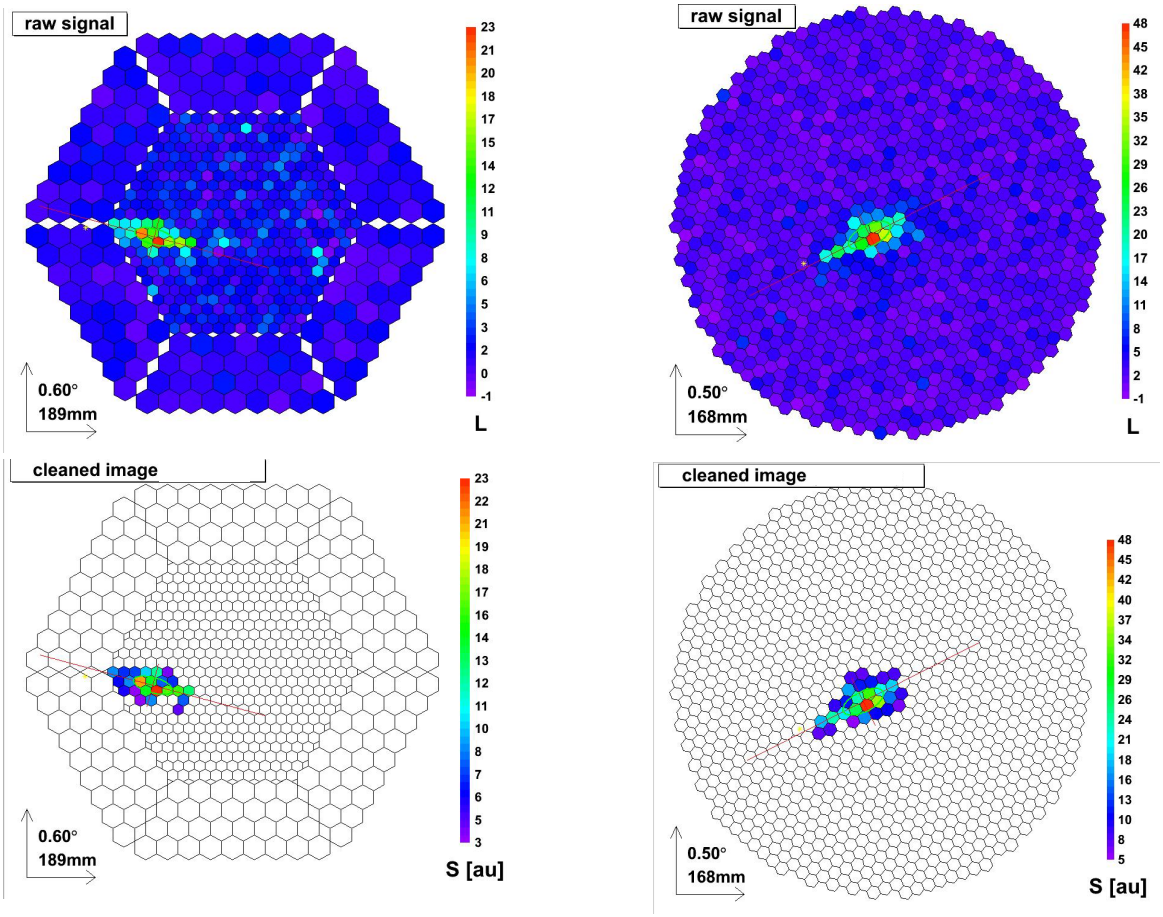

Fig. 4.3: Examples of two air shower events before (upper plots) and after (lower plots) image cleaning, in the two cameras (MAGIC-I on the left, MAGIC-II on the right).

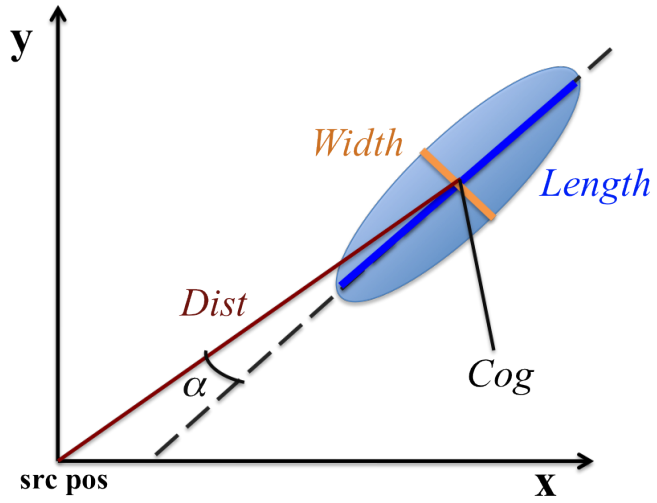

Fig. 4.4: Scheme of the parametrization of the shower image. The Hillas ellipse is shown in blue, with the minor axis as the *Width* and the major axis as the *Length*. The *Dist* and the α are also shown together with the *CoG*.

is related to the longitudinal development of the showers and the minor axis to the lateral ones (see fig 4.4). A detailed description of how the parameters are calculated can be found in the note [147]. Here I am going to describe the Hillas parameters, together with additional parameters, which will be used later in the analysis:

- *SIZE:* total number of photoelectrons in the shower after image cleaning.
- *CoG:* center of gravity of the charge distribution of the image, calculated from the first moment of the charge distribution.
- *WIDTH:* root mean square of the charge distribution along the minor axis of the image. It is the second moment of the transverse charge distribution.
- *LENGTH:* root mean square of the charge distribution along the major axis of the image. It is the second moment of the longitudinal charge distribution.
- *ALPHA (α):* clockwise angle from the longitudinal axis of the shower to the connection line between the source position in the camera and the center of gravity of the image.
- *CONC(n):* ratio between the light contained in the n pixels with the strongest signal and the total size.
- *LEAKAGE:* ratio between the light contained in the outermost pixel ring in the camera and the total size. The higher the ratio, the more likely truncated the image is. This parameter is a measure of the part of the shower which leaks outside the camera.
- *RMS TIME:* root mean square of the arrival times of pixels surviving the image cleaning.
- *TIME GRADIENT:* slope of the linear function fitted to the arrival time in the space coordinate along the major axis. It measures how fast the arrival time changes along the major axis of the image.
- *DIST:* distance between the camera center and the center of gravity of the image.

All these parameters are used for the electromagnetic/hadronic separation. In section 4.3.3 I will show a comparison of these parameters for electromagnetic and hadronic showers.

4.2.3 Stereo Reconstruction

The stereo parameters are calculated from the single telescopes parameters.
The intersection point of the two major axis of the images in the two cameras provides the location of the source as it is shown in figure 4.5 on the left. The location of the shower on ground is instead obtained by intersecting the major image axes from the telescope positions on the ground (fig.4.5 on the right).
Hence, the main parameters reconstructed and used in this analysis are:

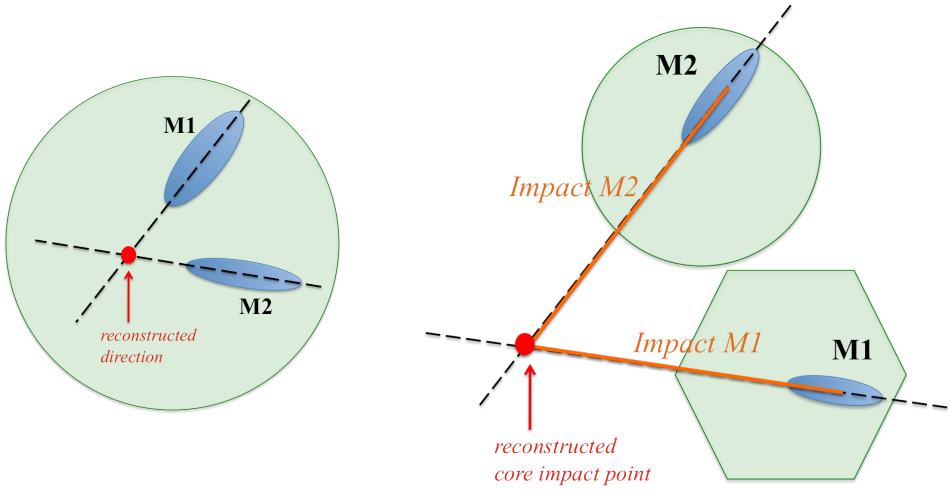

Fig. 4.5: Reconstruction of the stereo parameters. In the left plot the reconstructed arrival direction is shown. In the right plot, the reconstruction of the impact point on the ground is shown seen from above.

- *IMPACT:* distance on the plane perpendicular to the shower direction between the telescope position and the shower direction.
- *HEIGHT:* height of the shower maximum from the ground level.
- *DIRECTION:* incident direction obtained by geometrical reconstruction.

4.2.4 Signal/Background Separation

Once the images of the showers are delineated, the discrimination between different primary particle types is needed to be able to identify the background. Hadronic events are in fact the main and overwhelming background for the IACTs. Even for a strong source like the Crab Nebula, the gamma trigger rate is 1/1000 the hadron trigger rate. The signal to noise ratio is so small that a very effective background suppression is needed. A first rejection of the hadrons is achieved on the trigger level. The further separation of gammas and electrons from the dominant background of hadrons is called electromagnetic/hadronic separation and is the most important issue for IACTs.
In order to characterize and suppress the hadronic background a so-called Random Forest (RF) classification method [43] is trained in *Osteria* and applied in *Melibea*. This method is a multidimensional classification technique trained with two different sets of data. The training sample representing electromagnetic showers are MC electron or gamma showers, while the training sample representing the background are MC hadron showers or showers from the real data[1]. The method works as follows. A classification tree of the forest is grown from the two samples on the basis of the image parameters. Subsequently, one image parameter is selected randomly and a cut on this

[1]It is obvious that real data contain a small admixture from cosmic electrons, diffuse and isotropic gamma showers and also showers with a dominating π^0.

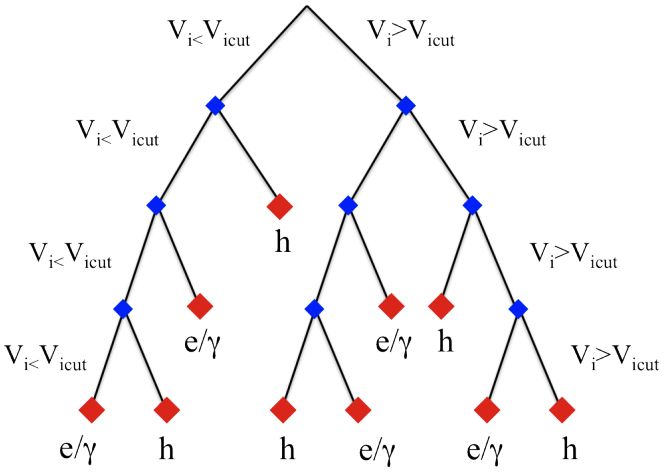

Fig. 4.6: Scheme of a RF tree. The image parameters chooses are represented by V_i and their values compared with V_{cut}. From this comparison the event follows the left or the right path. The red points represent the termination nodes in which the classification ends.

parameter that minimizes a parameter called Gini index is applied. The Gini index is defined as:

$$Q_{Gini} = 2\left(\frac{N_{signal}^{left} \times N_{bg}^{left}}{N_{tot}^{left}} + \frac{N_{signal}^{right} \times N_{bg}^{right}}{N_{tot}^{right}}\right) \tag{4.1}$$

where $N_{signal}^{left(right)}$ and $N_{bg}^{left(right)}$ are the number of the signal and background events on the left (below) or right (above) side of the cut value. $N_{tot}^{left(right)}$ is the number of the total events on the left or right side. A predefined number of nodes determines the number of cuts to be applied. This procedure, which is shown in figure 4.6 is repeated until in each node the maximum number of allowed events is reached or the maximum number of predefined nodes is reached. At the end of the classification tree, a value $H = \frac{N_{bg}^{end}}{N_{bg}^{end}+N_{signal}^{end}}$ is calculated. It spans from 0 to 1 and represents the probability of each event to be more hadron-like (=1) or electron-like (=0). Typically 100 trees are used in the RF and the final *Hadronness* is the average of the value H over all the trees. In order to avoid over-training effects and biases in the results, independent data samples are used for training and for applying the classification and calculating the effective acceptance.

The main difference between electron- or gamma-initiated showers and hadron initiated showers is the geometrical image shape and the time spread of the showers. Due to longer interaction length and larger transverse momentum of the hadronic interaction, the hadronic showers show larger fluctuations in their images than do the electromagnetic showers[2]. Images produced by hadronic shower are longer, wider and more irregular than those of the electromagnetic showers. Hence, parameters such as *Width* and *Length*, which determine the shape of the image, differ for the two particle types. Moreover, the *Conc* value is expected to be larger in electromagnetic showers than in hadronic ones. The parameters used in the Random Forest training to dis-

[2]Note that hadronic showers contain also electromagnetic subshowers

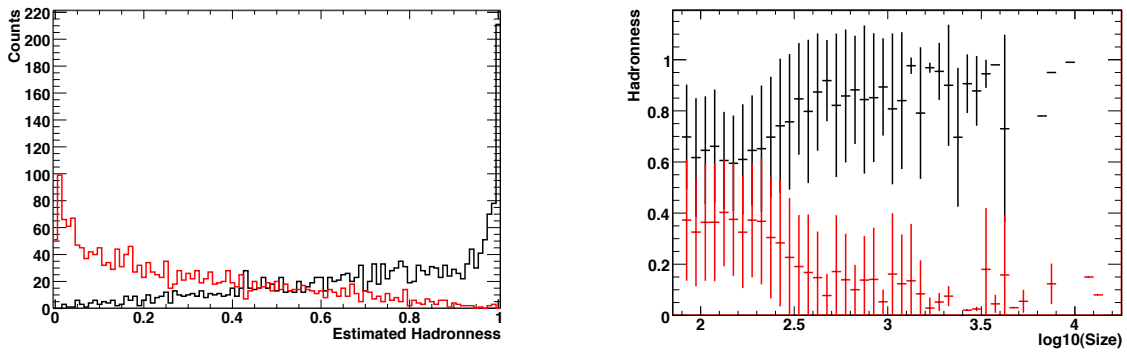

Fig. 4.7: Distributions of the *Hadronness* parameter. The red data points refer to MC electrons; the black data points refer to real data of the dominant hadronic background. The right figure shows the hadronness as function of Size. The separation is well defined in the region where the distributions of the two samples do not overlap.

tinguish between the two particle classes for the **single telescope** analysis are listed below:

- *Size*
- *Width*
- *Length*
- *log10(Size)/(Width×Length)*
- *Conc1*
- *RMS Time*

The **stereo system** introduced in 2008 improves the electromagnetic/hadronic separation further. It provides a better angular and energy resolution, a better determination of the *Impact* parameter and a determination of the height of the shower maximum (*Height*). The estimation of the *Height*, in fact, provides an additional powerful tool to discriminate showers from different particle types. Hadronic showers interact deeper in atmosphere than electromagnetic showers. In fact, the mean free path for a GeV proton in atmosphere is $\approx 80\,\mathrm{g\,cm^{-2}}$, while for electrons is $\approx 37\,\mathrm{g\,cm^{-2}}$ [69]. Therefore for the RF training in the standard stereo analysis the following parameters are used:

- *Size M1*
- *Size M2*
- *Zenith*
- *Width M1*
- *Width M2*
- *Length M1*

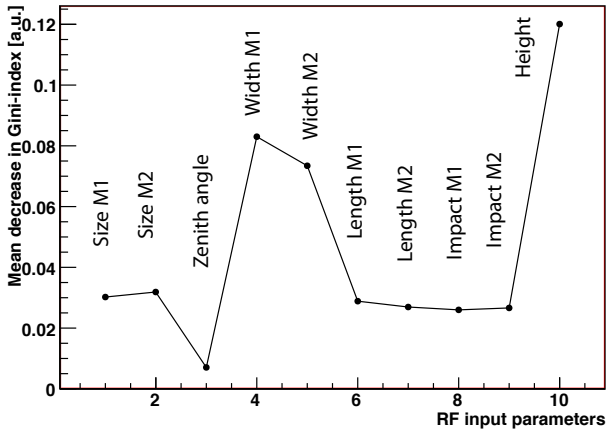

Fig. 4.8: Mean decrease of the Gini index value for each parameter used in the training, in arbitrary unit.

- *Length M2*
- *Height*
- *Impact M1*
- *Impact M2*

where $M1$ and $M2$ refer to the two telescopes MAGIC-I and MAGIC-II. A pre-cut allowing only 1 image *Island* is applied before the training. The *Zenith* angle is used to divide the sample in differet angle bins.
In figure 4.7, on the left panel, the distribution of the *Hadronness*, which is determined through the RF, is shown. The training has been done such that the electron distribution peaks at 0 (red curve), and the hadron distribution peaks at 1 (black curve). The distributions of the mean *Hadronness* and its RMS as function of *Size* is shown on the right plot in figure 4.7. The *Hadronness* is strongly dependent on *Size*.
In figure 4.8 the goodness of each parameter used in the training is represented by mean decrease in the Gini index, which is averaged over all nodes and all trees of the RF. The more a parameter decreases the Gini index, the more effective it is in the training. One can notice that, in case of the stereo analysis, $Width$ and $Height$ parameters are the most powerful parameters used to distinguish electromagnetic showers from hadronic showers.
The obtained RF classification is applied to all the data and the MC events in order to assign to each event a certain value of *Hadronness*.

4.2.5 Shower Reconstruction

For the shower reconstruction the following parameters are estimated:

- θ^2*:* θ is the angular distance between the position of the studied source and the estimated position.

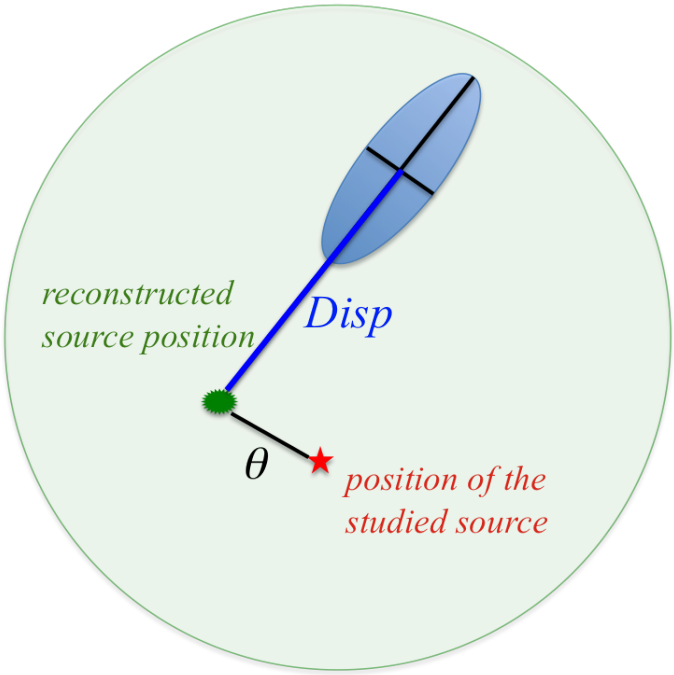

Fig. 4.9: Scheme of the reconstruction of the *Disp* and θ parameters.

- *DISP:* angular distance between the reconstructed source position in the camera (assumed to lie on the major axis of the Hillas ellipse) and the center of gravity of the shower image.

These parameters are shown in figure 4.9. *Disp* is also estimated by the RF method. *Disp* is also used to estimate the *Direction* and the particle energy.
Like the *Alpha* parameter, θ^2 can not be used in the analysis of cosmic electrons, because electrons being diffuse, are not pointing back to a single point source.

4.2.6 Energy Estimation

Together with the showers geometry, the shower energy is reconstructed. The image *Size* is roughly proportional to the initial energy of the primary particle which initiates the shower. In figure 4.10 the reconstructed energy versus the mean *Size*, in the case of the stereo analysis and for a sample of MC electrons, is shown. In a rough approximation, for zenith angles below 30^o, 300 phes correspond to $\sim$300 GeV.

For the **single telescope** analysis the energy estimation is performed by a RF method. The parameters used for the RF training are: *Size*, *Width*, *Length*, *log10(Size)/(Width×Length)*, *Conc1*, *Leakage*, *Disp* and *Zenith* angle.
For the **stereo system**, instead, the energy for each telescope is reconstructed using a predefined look-up table filled with MC events, based on *Size*, *Impact*, *Height* and *Zenith* angle. The average of the two energy estimations of each telescope event provides the final reconstructed energy.

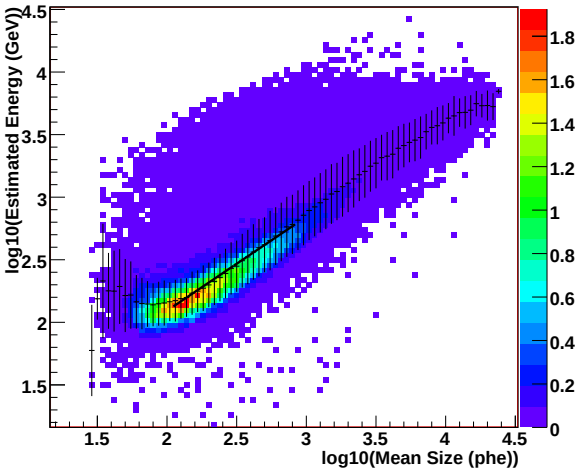

Fig. 4.10: Estimated energy versus mean *size* for the stereo analysis.

In the reconstruction of the energy, the *Zenith* angle is used. Light from showers observed at larger zenith angles travels, in fact, a farther distance and passes through more air, thus the absorption is higher and the image is smaller.
The energy resolution is defined by the standard deviation of the Gaussian fit to the relation $\frac{E_{est}-E_{true}}{E_{est}}$. The mean value of the Gaussian fit defines the energy bias. The energy resolution as a function of the energy is shown in figure 4.11 on the left. The mean energy resolution for a single telescope is $\sim 25\%$ in case of diffuse electrons, while it is below 20% for the stereo system.
The energy bias as a function of the energy is shown in figure 4.11 on the right. The biases are due to the fact that the response of the detector is not linear, in particular at the energy thresholds and at high energy where the statistic is low. At low energy the bias is due to an overestimation of the energy, because only showers with upward fluctuations pass the trigger criteria. At high energy, instead, it is due to an underestimation of the energy, primary due to the fact that the images are truncated in the camera. These effects are more accentuate in the case of single telescope.

4.2.7 Signal Detection for point-like source gammas and diffuse electrons

In this section the two different methods for detecting point-like source gammas and diffuse electrons are described.
In the analysis of VHE γ-ray point sources, one of the most important parameters is the arrival direction of the shower. The arrival direction is expressed by the *Alpha* or θ^2 parameter. In this case either the *Alpha* or θ^2 parameter can be calculated and used to distinguish the signal sitting on top of the hadronic background which is part of the data taken. The background can be estimated and subtracted using the recorded data as described in 4.1, according to the observation mode.
In the case of diffuse electrons, it is not possible to define a preferred shower direction and it is not possible to extract the background from the data itself, using *Alpha* or θ^2

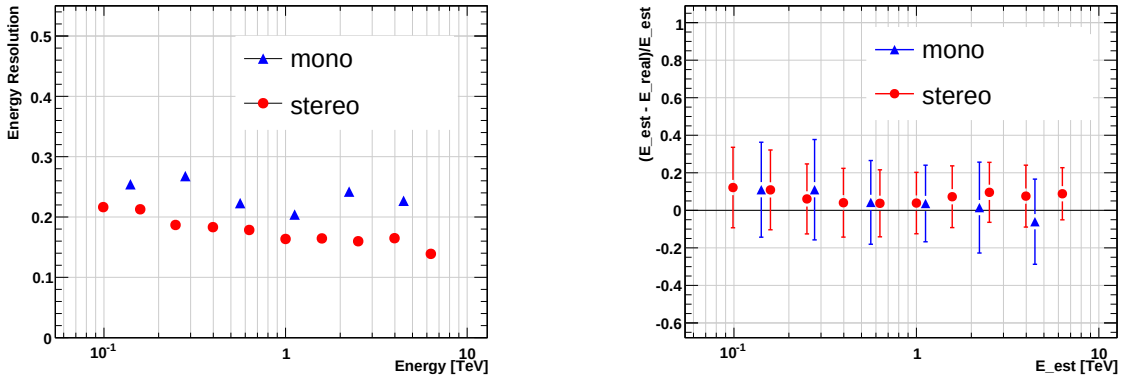

Fig. 4.11: Energy resolution for MC diffuse electrons after the cuts for Stereo and Single telescope on the left plot. On the right one the mean biases are displayed. The error bars reprensent the RMS of the distributions of the biases.

parameters.
Therefore, it is necessary to use another method to estimate the background and to determine the signal. The background can not be measured for diffuse sources and must be estimated from MC simulations. The parameter used to determine the signal in this case is the *Hadronness* (the result of the RF). The diffuse electron signal peaks around *Hadronness* = 0. The MC hadrons reflect the shape of the *Hadronness* distribution but without electron signal, and the distribution has a peak around *Hadronness*=1.
The two different approaches I used to determine the point-like gamma and the diffuse electron signals are described in the following: the ***point-source*** (θ^2) and the ***diffuse-source*** (*Hadronness*) approach. The *diffuse-source* method can be also applied to point-like γ-ray sources. In this way the method can be cross-checked.
For each of the two methods the following procedure is applied:

1. Apply selection cuts.
2. Determine the θ^2 or *Hadronness* distribution for data and background, define a signal region and normalize the two distributions by the number of events in a defined non signal region.
3. Count events in the signal region (N_{on}).
4. Count background events in the signal region (N_{bg}).
5. Determine the number of excess in the signal region ($N_{excess} = N_{on} - N_{bg}$).
6. Determine the significance of the excess.

Point-source approach (θ^2)

In the *Point-source* approach, a cut in *Hadronness* is applied in order to reduce the background. For every event that survives the cut, the θ^2 value is calculated. The θ^2 distribution is plotted for the ON and OFF data, and the two distributions are normalized to each other in the non signal region (for example between $\theta^2 = 0.15\,\mathrm{deg}^2$

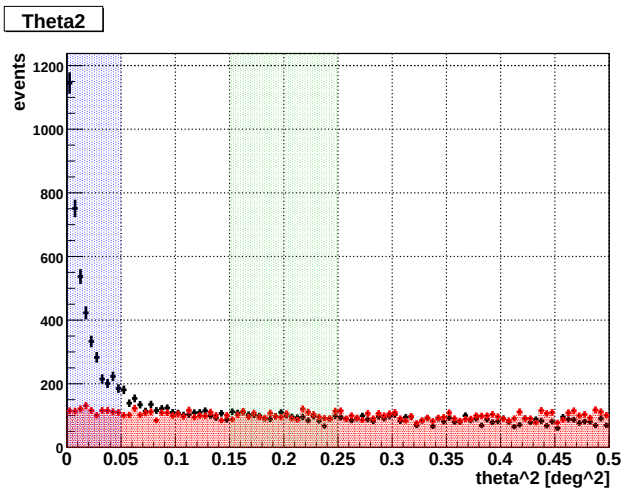

Fig. 4.12: θ^2 distribution for a Crab data sample. The ON data are shown in black, while the OFF data in red. The blue shaded area defines the signal region, while the green area denotes the background region in which the on and off histograms are normalized to each other.

and $\theta^2 = 0.25\,\mathrm{deg}^2$). The signal region (which can differ as a function of energy) is defined by a θ^2 cut, to keep more than 70% of gamma events. The number of excess events is then calculated subtracting the number of OFF events from the number of ON events in the signal region. In figure 4.12 an example of θ^2 distribution for a set of Crab Nebula data is shown. The signal region is shown as blue shaded area, while the non signal region is shown in the green area. The black points represent the ON events, while the red points the background events.

The probability that the excess is only a background fluctuation is defined by the significance. The significance of the signal is computed assuming that both ON and OFF events follow a Poissonian distribution. In this analysis the formula 17 from Li&Ma [99] is used to calculate the significance of the excess:

$$S = \sqrt{2}\left(N_{on}\ln\left[\frac{1+\alpha}{\alpha}\left(\frac{N_{on}}{N_{on}+N_{off}}\right)\right] + N_{off}\ln\left[(1+\alpha)\left(\frac{N_{off}}{N_{on}+N_{off}}\right)\right]\right)^{1/2} \tag{4.2}$$

where N_{on} and N_{off} are the numbers of ON and OFF events in the signal region. The factor $\alpha = t_{on}/t_{off}$ is the normalization expressed as the ratio between the effective time of the ON and the OFF samples, which implies $N_{bg} = \alpha N_{off}$.
For example, $S = 3\sigma$ means that a signal measured has a probability of (100%-99.73%)/2 = 0.135% (because its the upper half of the Gaussian curve) to be a background fluctuation.

Diffuse-source approach (Hadronness)

In the *Diffuse-source* approach, as already mentioned, the source is diffuse and it is not possible to select a preferred direction. Therefore, θ^2 can not be used and the background must be estimated by MC simulations. Only cuts in the *Hadronness* allow to

reduce the background. The interval of the signal region is determined as the region in which are at least 60% of the MC electron events in the *Hadronness* distribution. The signal region differs for each energy bin, since the *Hadronness* is an energy dependent quantity (see fig. 4.7 on the right panel). The background distribution is determined by the MC proton events which represent the major component of hadrons, as observed in the cosmic ray spectrum. The difficulty of this method is that the MC events have to describe perfectly the reality. Any deviation will result in a faulty background subtraction. Hadronic interactions, however, are difficult to simulate with high precision: many types of interactions compete, and not all details of cross sections are known, particularly at high energies.
The MC simulations have been performed with a different energy spectrum[3] of $E^{\Gamma_{sim}}$ (with Γ_{sim} = -2.0 or -1.78) compared to the real cosmic-ray spectrum of $E^{\Gamma_{real}}$, the *Hadronness* distribution has to be corrected. Thus, to each event i of the *Hadronness* distribution a weight factor of $w_i = E_{true}^{(\Gamma_{real}-\Gamma_{sim})}$ is assigned; E_{true} is the simulated energy. In this case, while the uncertainties on the ON data are poissonians, the uncertainties on the MC protons are defined as $\Delta N_{pr} = \sqrt{\sum_i w_i^2}$, the square root of the sum of the weights in the considered bins of the *Hadronness* distribution. The normalization factor $\alpha = \frac{n_{on}}{n_{pr}}$ is the ratio between the numbers of ON and MC proton events in the non signal region (for example between $Hadronness = 0.2$ and $Hadronness = 0.6$) which implies $N_{bg} = \alpha N_{pr}$. According to the electron simulation a small fraction of electrons will have a rather high hadroness in this non signal region. Because of the small background this will be neglected and later added to the systematic error. Thus, since the uncertainties on the proton events are not poissonians, the significance can not be calculated as in the formula 4.2.
Here, the significance is defined as:

$$S = \frac{N_{excess}}{\Delta N_{bg}} = \frac{N_{on} - \alpha N_{pr}}{\alpha \left[\Delta N_{pr}^2 + N_{pr}^2 \left(\frac{1}{n_{on}} + \frac{\Delta n_{pr}^2}{n_{pr}^2}\right)\right]^{1/2}} \tag{4.3}$$

In the figure 4.13 an example of *Hadronness* distribution for a set of Crab data is shown. The signal region, shown as blue shaded area, while the non signal region is shown in the green area. The black points represent the ON events, while the red points the background events. Comparing this distribution with the θ^2 distribution in figure 4.12 it is clear that for point-sources the background suppression is much more effective. Nevertheless in chapter 5, it will be shown that the two approaches give consistent and compatible results in the case of gamma point-like sources, and the *diffuse-source* approach can be used for the study of diffuse electron signals albeit with somewhat larger errors.

In general, the performance of an analysis method (or an experiment) is characterized by its sensitivity. The sensitivity of IACTs is usually defined as the minimum flux level measured with $5\,\sigma$ significance in 50 hours of observation. The sensitivity of the two different analysis methods will be compared in chapter 5, by applying them to a Crab Nebula data sample.

[3] to increase the statistics at high energy.

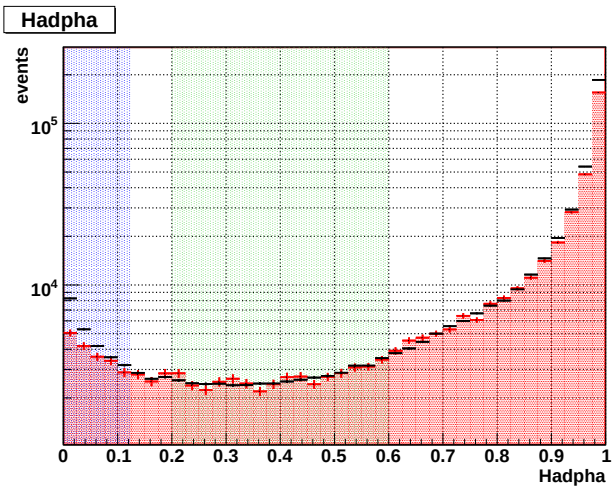

Fig. 4.13: *Hadronness* distribution for a Crab data sample. The ON data are shown in black, while the proton events in red. The blue shaded area defines the signal region, while the green area denotes the background region in which the on and proton histograms are normalized to each other. It can be seen that the MC simulations describe the*Hadronness* distribution of real hadronic events rather well.

4.2.8 Spectrum determination

The final step of the analysis is the calculation of the flux and the determination of the spectrum. The differential energy spectrum for a point source is defined as the number of gammas N, of a given energy E per effective observation time t and effective collection area A:

$$\frac{dF}{dE}_{pointlike-\gamma} = \frac{dN}{dEdAdt} \tag{4.4}$$

In the case of diffuse electrons, the dependence of the solid angle Ω has also to be taken into account, therefore:

$$\frac{dF}{dE}_{diffuse-electrons} = \frac{dN}{dEdAd\Omega dt} \tag{4.5}$$

The effective collection area is the artificial area on ground in which air showers are all detected with full efficiency[4] by the telescope and depends on the incident energy, trigger efficiency and zenith angle. At large zenith angles and high incident energy the light pool of Cherenkov showers and thus, the effective area, is bigger.
The effective collection area for γ-ray point sources is computed from MC-γ simulations, as:

$$A(E, Zd) = A_{sim}\frac{N(E, Zd)}{N_{sim}(E, Zd)} \tag{4.6}$$

where $N_{sim}(E, Zd)$ is the number of simulated gammas with an energy E and a zenith angle Zd, incident on an area A_{sim}. $N(E, Zd)$ is the number of events triggering the telescope and surviving all the cuts applied in the analysis. In case of diffuse electrons

[4]if in a given area one detects 50% of the showers then the effective area is only half of the given area.

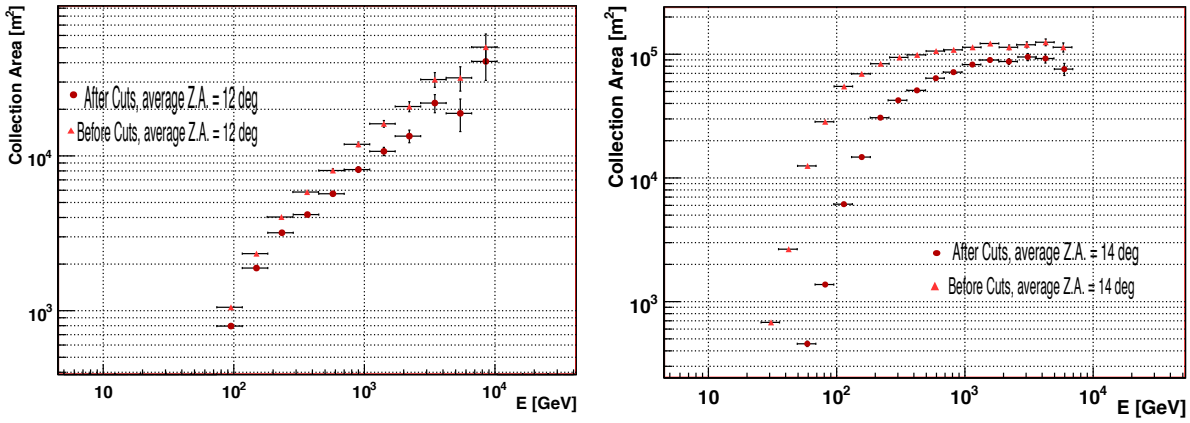

Fig. 4.14: An example of the effective area distributions as a function of the reconstructed energy, before and after the cuts. The left figure shows the acceptance per unit of solid angle of the MAGIC-I camera for electrons as a function of energy. The right figure shows the effective collection area as a function of energy for gammas from a point-like source.

it is more appropriate to talk about $Acceptance = A(E, Zd) \times \Omega$, which depends on the simulated solid angle Ω. The *Acceptance* is calculated using MC electrons. On the left plot of figure 4.14 , the *Acceptance* for electrons, expressed per unit of solid angle (in order to compare with gammas), is shown as a function of the estimated energy for zenith angles lower than 30 deg, before and after the analysis cuts. On the right plot, the effective area for gammas from a point-like source is shown. The trend of the distribution continuously increasing for electrons is related to the fact that they are diffuse. Therefore the trigger efficiency at decreasing energy is lower for showers with large impact and high inclination angle, compared to point-like sources and, thus the effective area becomes smaller. In fact, the impact parameter of electrons ($\sim 650\,\mathrm{m}$) that still trigger the telescope is more than twice larger than in the case of gammas from a point-like source at the center of the camera ($\sim 300\,\mathrm{m}$).
In order to compute the differential flux and the spectrum, the number of excess events and the effective area (from MC) have to be calculated.
Moreover, to correct for the energy biases and resolution, an **Unfolding** procedure is applied. The measured energy distribution is a convolution of a distribution in the true energy with a migration matrix M_{ij} (M). This migration matrix, which represents the detector response, describes the migration of events from bins of estimated energy to bins of true energy:

$$Y = M \cdot S \quad or \quad Y_i = \sum M_{ij} \cdot S_j \tag{4.7}$$

Where Y_i (elements of Y) and S_j (elements of S) are the number of events in bin i of estimated energy and in bin j of true energy respectively. The unfolding procedure aims to invert the matrix in order to recover the true distribution from the estimated one. Since M is not of the type $n \times n$, the equation 4.7 can not be so easily inverted. Therefore the true distribution is derived by different methods, through a procedure of regularization. It implies a following definition for the χ^2:

$$\chi^2 = \frac{w}{2} \cdot \chi_0^2 + Reg(S) \tag{4.8}$$

where χ_0^2 is the χ square between Y and $M \cdot S$, $Reg(S)$ is the regularization term and the weight w the regularization parameter. There are different methods to determine $Reg(S)$ [148]. The ones used in this thesis are: Bertero's method [38], which consists in calculating a solution iteratively; Schmelling's method [134], in which the X^2 is mimimized using MINUIT; Tikhonov's method [140], in which $Reg(S)$ is calculated as a sum of second derivatives of the unfolded distribution and the χ^2 is minimized using MINUIT.

My contribution to the development of the new analysis method

In order to be able to perform the diffuse electrons analysis, the standard software used by the MAGIC collaboration had to be further developed. Here the main tasks I developed are summarized:

- Introduction of weights over the *Hadronness* distribution for the MC background events (to correct for the real cosmic-ray spectrum) and successive recalculation of the uncertainties.
- Determination of the electron excess from the *Hadronness* distribution by subtracting MC-background simulations, and calculation of the significance.
- Calculation of the *Acceptance* with a solid angle dependence, for the determination of the energy spectrum.

4.3 Monte Carlo Simulations and Comparison with Real Data

In ground-based gamma astronomy one cannot calibrate a telescope in a test beam. Therefore the MC method has to be used to predict the performance. Simulations based on Monte Carlo (MC) method have been used to optimize and to calibrate the new analysis software of the MAGIC telescopes and evaluate the performance. They are used to calibrate the energy scale and determine the incident particle's energy and flux. Moreover, in the present work, MC simulations of hadronic cosmic rays are used to characterize the background in the case of diffuse sources. As already mentioned, MC simulations of air showers are absolutely crucial for understanding and analysing IACT data.
In these simulations, primary particles are generated and the development of their showers is tracked in the atmosphere. Further, the response of the telescopes are simulated to detect these showers.
After a description of the simulation programs used for MAGIC in section 4.3.1, in section 4.3.2 I am going to present the MC production made for the present study together with the comparison with real data.

4.3.1 Simulation software for MAGIC

The MC simulation for MAGIC is divided into three stages. Electron, gamma and hadron initiated showers are simulated with CORSIKA 6.501. Later, *Reflector* and

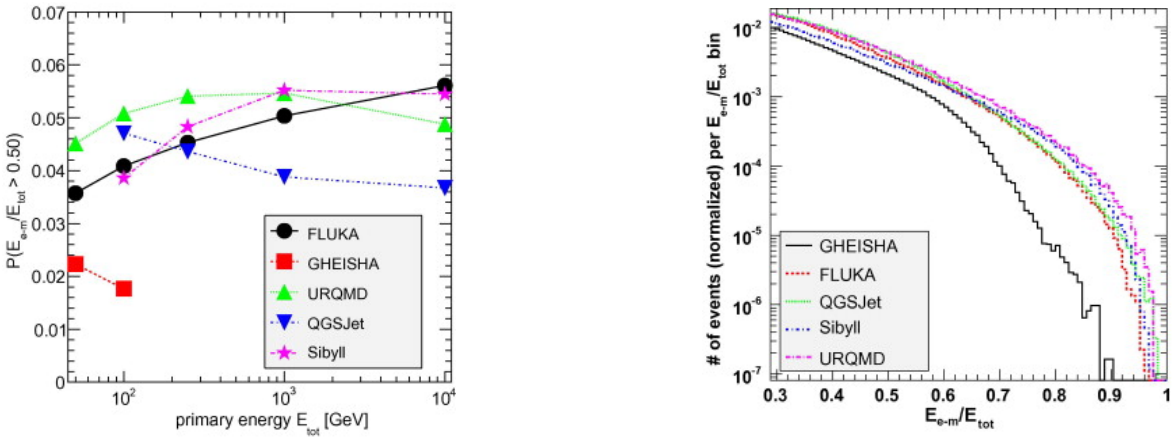

Fig. 4.15: On the left plot: probability that more than 50% of the primary energy deposited in the electromagnetic part in proton-nitrogen collisions for different interaction models and primary energies. On the right plot: energy deposited in the electromagnetic components (γ, $e^{\pm}$, π^0, η) in the interaction of 100 GeV protons with nitrogen, for the same interaction model: FLUKA [2], GHEISHA [67], URQMD [36], QGSJet [119] and Sibyll [63]. Figures are taken from [104].

Camera programs simulate the response of the reflector and the camera and read-out of the telescopes by using measured parameters of the different detector components (mirror reflectivity PMT QE....).

CORSIKA

CORSIKA (COsmic Ray SImulations for KAscade) is a MC program to simulate the atmospheric cascade initiated by primary particles such as photons, nuclei and any other particles. It was developed at the Forschungszentrum Karlsruhe for the KASCADE experiment [80], [81].
CORSIKA simulates the transport of particles in the atmosphere and their interaction with air nuclei as well as their decays. All secondary particles produced are tracked down to low energy when they produce no more Cherenkov light. Parameters such as, for example, particle type, energy, direction, arrival time, location of the shower that reaches the selected observation level are calculated and stored. In addition, Cherenkov photons produced by charged particles are also calculated by a modified version of the program.
There are several atmospheric models implemented in CORSIKA. The one used in MAGIC (MagicWinter atmosphere) contains a mixture of N_2 (78.1%), O_2 (21.0%) and Ar (0.9%). The density variation of the atmosphere with altitude and time of the year is also taken into account and optimized for the MAGIC site.
All the physics processes involved in the shower development are taken into account in the simulations:

- *Particle tracking through the atmosphere.* Propagation of particles between two interactions accounts for ionization losses, deflection by the Earth's magnetic field and Coulomb multiple scattering.

- *Hadronic interactions and decay of unstable particles.* The largest uncertainty of these simulations comes from the limited knowledge concerning the hadronic interactions at TeV energies. Since at TeV energies and in the forward direction experimental data on the cross sections do not exist yet, they have to be extrapolated from current measurements [5]. Several models are in use to describe hadronic interactions and they are divided in low-energy and high-energy models. The transition energy between low and high energy models depends on the model combination and varies from 50 GeV to 1 TeV. In this work for the low-energy interaction, the FLUKA model [2] has been used, in combination with the high-energy QGSJet-II model [119]. Since only one combination has been used, for completeness a comparison of different models is presented, taken from the literature [104]. On the left plot of figure 4.15, the probability that more than 50% of the primary energy is deposited in the electromagnetic component, as a function of energy, is displayed. The differences in the amount of energy deposited at 500 GeV between different models is $\sim$30%. The same difference can be seen on the right plot of figure 4.15, where the energy deposited in the electromagnetic components in proton-nitrogen interaction is displayed, for a fixed energy of 100 GeV, and different models. The fact that the models differ from each other is certain to influence the electron spectrum.

  Many of the particles generated in high energy hadronic interactions are unstable. Particles such as for example π^0, or other mesons have such a short lifetime that a possible interaction with air molecules before their decay is neglected. On the other hand, more stable particles are neutrons, which decay likely only after penetrating the whole atmosphere.

- *Electromagnetic interactions.* Unlike the hadronic interactions, electromagnetic interactions are few and well understood. The interaction of electrons, positrons and photons are simulated in CORSIKA using the EGS4 model [116]. Bremsstrahlung, multiple scattering and annihilation processes are taken into account for electrons, while Compton scattering, electron-positron production and photoelectric reactions are considered for γ-rays.

- *Cherenkov radiation.* In the modified CORSIKA version used for Cherenkov telescopes, also the Cherenkov photons produced in air are calculated and the transport through the atmosphere calculated. The program stores also the arrival times, direction at the telescope and the height of production.

Simulation of the atmospheric effects and the reflector response

At the second step of the simulations the absorption of the Cherenkov photons by the Ozone, together with the Rayleigh and Mie scattering are taken into account. The Cherenkov photons that hit the reflector dish and are reflected into the camera

[5] Recently the LHC reached energies up to few TeV, so in the near future data might become available from fixed target experiments providing cross-sections, multiplicities etc in the so-called forward direction.

are saved, to be used in the last step of the simulation chain. Parameters such as aluminum absorption and mirror reflection are considered when calculating photon numbers hitting the camera plane. A Gaussian spread is added on the position of the reflected photon on the camera plane and simulates the point spread function (PSF). As already mentioned in chapter 2, the parabolic shape of the mirror dish allows to keep the information about the time profile of the Cherenkov photons produced in the showers. In addition the positions of these photons in the camera coordinate are saved, as well as the wavelength of each photon. In case of electrons and hadrons, it is possible to define a view cone angle in which the same particles are used a certain defined number of times only with different incident angles. This allows to simulate not only particles from point sources, but also diffuse particles. Detail on the *Reflector* program and how to use it can be found in the note [112].

Simulation of the Camera Response

Once the photons hit the camera plane, the *Camera* program simulates the response of the photomultipliers, as well as the trigger and the data acquisition systems. Pulse shapes, noise levels and gain fluctuations obtained from real data have been used in the program, as well as the QE values of the PMTs for different wavelengths to make the simulations as realistic as possible. At this stage of the simulation the noise due to NSB is also included. The NSB is simulated by a program (*Starrespo*), which generates a set of random signals in the PMTs equivalent to those found in real data. Detail on the *Camera* program and how to use it can be found in the note [113].

4.3.2 Monte Carlo simulations of electromagnetic and hadronic showers

MC simulations produced for this work consist of diffuse electrons, protons, helium and gammas. Electron and proton shower simulations are used in the analysis of the electron spectrum, while diffuse helium and gamma showers are used for some tests and performance studies. The parameters that have been used to simulate the particle showers are listed in table 4.1. There are two different samplers of protons, produced in different periods: sample a) and sample b). The latter was introduced to enlarge the impact parameter and the view cone of the previous production a). A power law spectrum harder than the real one has been used in the energy distribution in order to avoid poor statistics in the high energy region. The last row of the table shows the percentage of events that trigger each telescope. This value depends on the impact and view cone angle used. The energy range has been chosen to be up to few tens of TeV in order to study the electron spectrum up to a few TeV. The wavelength range of the simulated Cherenkov photons is between 290 and 900 nm.
All the parameter values needed to steer the production of air showers are listed in the so called *input cards*. The parameters are set by the user, and are used by the three programs (CORSIKA, *Reflector* and *Camera*). The *input cards* with the parameters used in this work can be found in the appendix B.
In order to be able to use together all the simulations produced, a selection in energy and zenith angle has been made in such a way that all the MC productions are in the

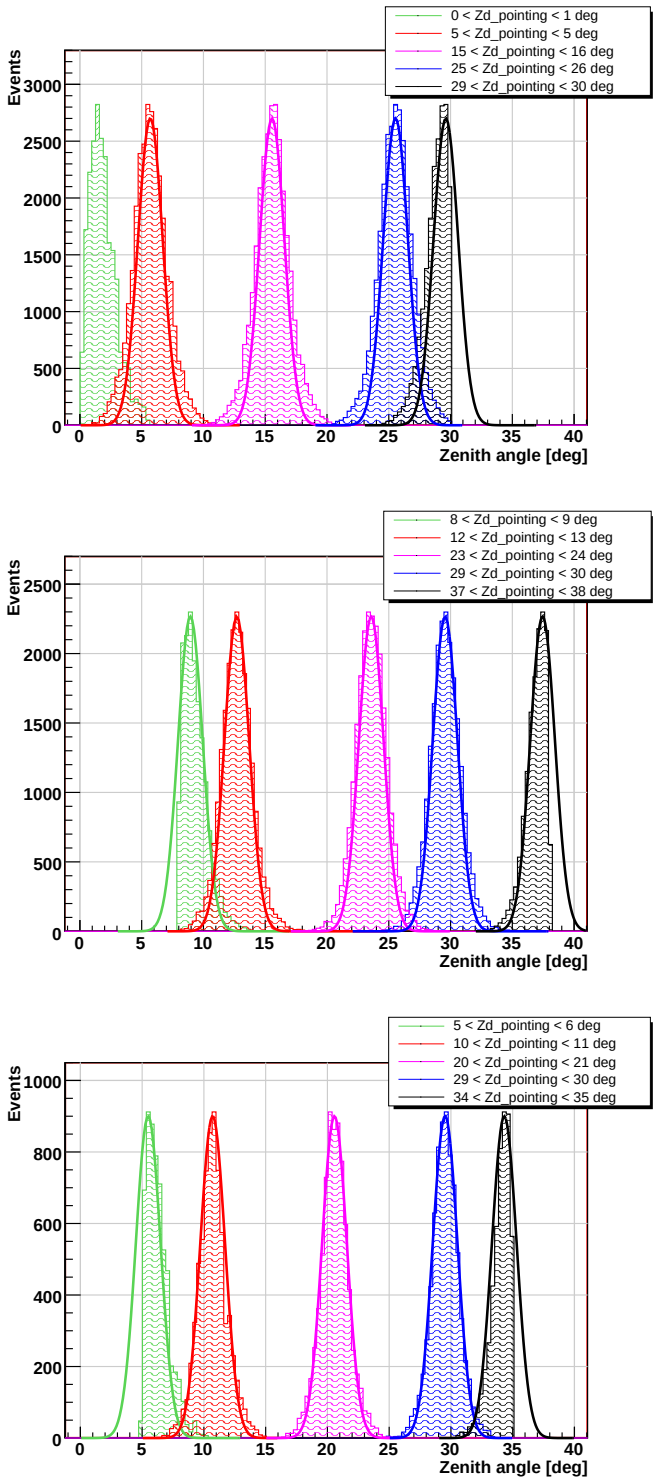

Fig. 4.16: Distributions of the zenith angles for different pointing position of the telescopes. On the top plot: the proton simulations sample a) in table 4.1. On the middle plot: the proton simulation sample b). On the bottom plot: electron simulations.

Particle	e^-	p a)	p b)	He	diffuse γ	point γ
Energy range (TeV)	0.07-7	0.03-30	0.07-20	0.07-20	0.01-30	0.01-30
Zenith angle (deg)	5-35	0-30	8-38	8-38	5-30	5-35
Impact (m)	650	850 (600×600)	1200	1200	400	400
View cone radius (deg)	4.5	5	6	6	1.5	no
power law spectrum	-2	-1.78	-2	-2	-1.6	-1.6
# events simulated	7×10^7	7×10^7	2×10^9	3.7×10^8	3×10^7	2×10^6
average trigger rate (%)	0.4	0.2	0.04	0.03	6	8

Table 4.1: Relevant parameters of the simulated showers for electrons, protons, helium and gamma. There are two different samples of MC protons listed separately, since they were produced at different periods.

same ranges. Figure. 4.16 shows the distributions of zenith angle for different pointing positions of the telescopes. The upper panel is for the production of protons a), the middle panel for proton production b) and the bottom for electrons. The selection of the zenith angle has been done in such a way to lose less than 1% of the events in each pointing position bin. Thus, for the proton production a) the selected zenith range is between 3-27 deg, for proton production b) and helium between 11 - 35 deg and for electrons between 8 - 32 deg. Therefore, the analysis of electron signals has been performed in the zenith angle between 11 - 27 deg, where the distributions from all the productions overlap.

4.3.3 Comparison between MC simulations and real showers

Very good agreement between the simulations and the real data is needed in the *Hadronness* range where neither electrons nor helium are expected in order to be able to subtract the background and determine the signal. A wrong background subtraction leads to a wrong flux measurement. Therefore it is important that the MC in the non-signal region in the *Hadronness* distribution describe well the data. In order to demonstrate the good agreement between electromagnetic shower simulations and data, MC γ-rays and data from the Crab Nebula are used. They have the advantage, compared to electrons, that γ-ray data are obtained with θ^2 cuts around the source position of $\sim 0.2\,\mathrm{deg}^2$. In figure 4.17 the *Hadronness* distributions of the excess from the Crab Nebula data are compared with the gamma excess in different *Size* bins. We notice that in the range between 200 and 1500 phes the two distributions agree very well, while at very high *Sizes* there are minor discrepancies. More plots can be found in the appendix A, where the comparison of the *Width*, *Length*, *Impact* and *Height* are shown.

In order to demonstrate, instead, the good agreement between hadron simulations and hadron data, MC protons, MC helium and a sample of measured extragalactic data in the *Hadronness* range between 0.4 and 0.8 are used. Here I am going to present the comparison simulations-data of the parameters used in the RF. The real data used

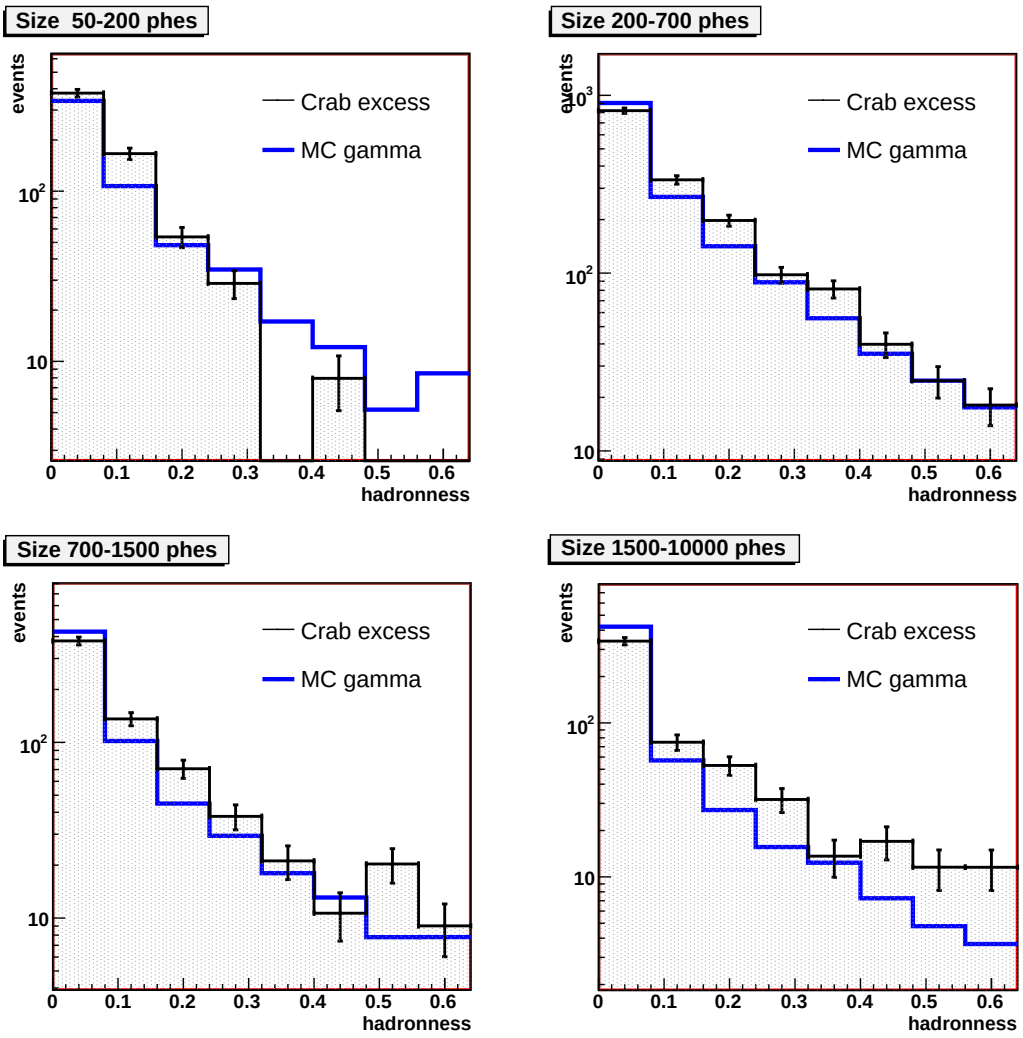

Fig. 4.17: *Hadronness* distributions in size bins for MC gamma and excess events from the Crab Nebula.

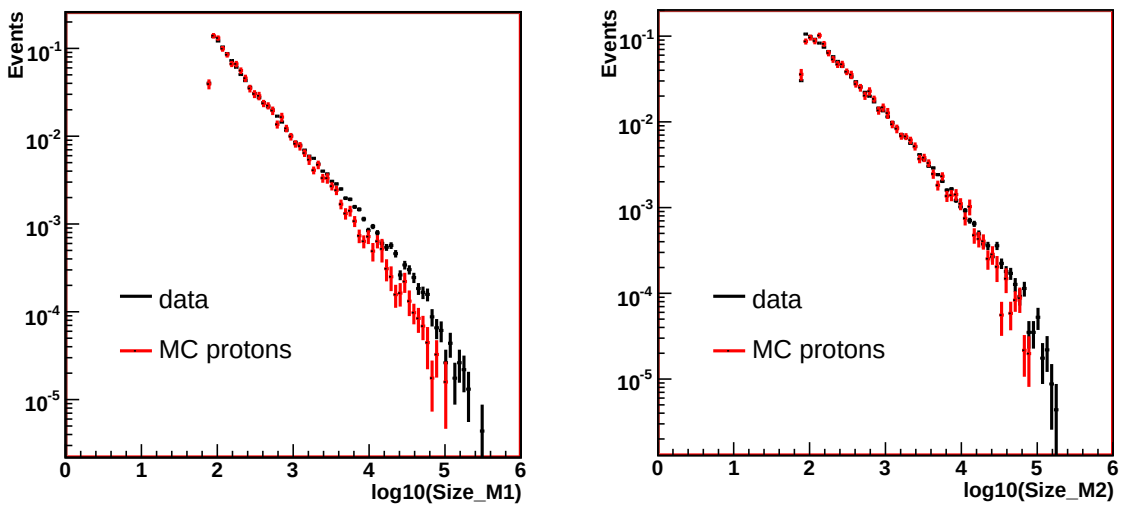

Fig. 4.18: Size distributions in the two telescopes (MAGIC-I on the left and MAGIC-II on the right) for a set of data and a sample of MC protons. A cut in the distance from the center of the camera (~ 1 deg) is applied in order to consider only the trigger region, where the PMTs have all the same size.

for comparing with MC samples were taken in December 2009, from an observation a region in the sky with no γ-ray sources in the FoV. The samples are compared in a zenith angle range between 14^o and 24^o and cuts in the number of *Islands* (<2) and *Leakage* (<0.2) are applied. The MC events have been weighted to reproduce the real energy spectrum, as discussed in 4.2.7. In figure 4.18 the *Size* distributions of protons and hadron data, normalized by the number of events, are displayed for MAGIC-I on the left and MAGIC-II on the right. The observed distributions agree very well with the expectations in the case of MAGIC-II, where a correction due to cross talk between channels in the read-out electronics is applied. In case of MAGIC-I, for high sizes, the protons do not reproduce faithfully the data, possibly due to systematics in the simulations. In both cases, at large *Size*, the MC proton statistic is limited by the maximum simulated energy of 30 TeV.
Since the parameters used here depend on energy, the comparison is done for different *Size* values. Comparing the *Width* distribution of hadron data with MC proton in different *Size* bins, one can get an estimation of how accurate the simulation of the PSF of the telescopes is. In figure 4.19 and 4.20 the *Width* distributions for data are compared with the *Width* distributions for MC proton for two different values of PSF, in different *Size* bins. The distributions are normalized to the number of events. In the distributions of the MC the big discrepancies are due to low statistic. Since, above 200 phes, the data distributions are enclosed between the two MC proton distributions, one can conclude that PSF values between 10.6 mm and 11.4 mm for MAGIC-I and between 10.6 mm and 12.6 mm for MAGIC-II reproduce well the response of the telescopes. Therefore in this work we use PSF values of 11.4 mm for MAGIC-I and 12.6 mm for MAGIC-II, respectively. In figure 4.21 the *Width* and

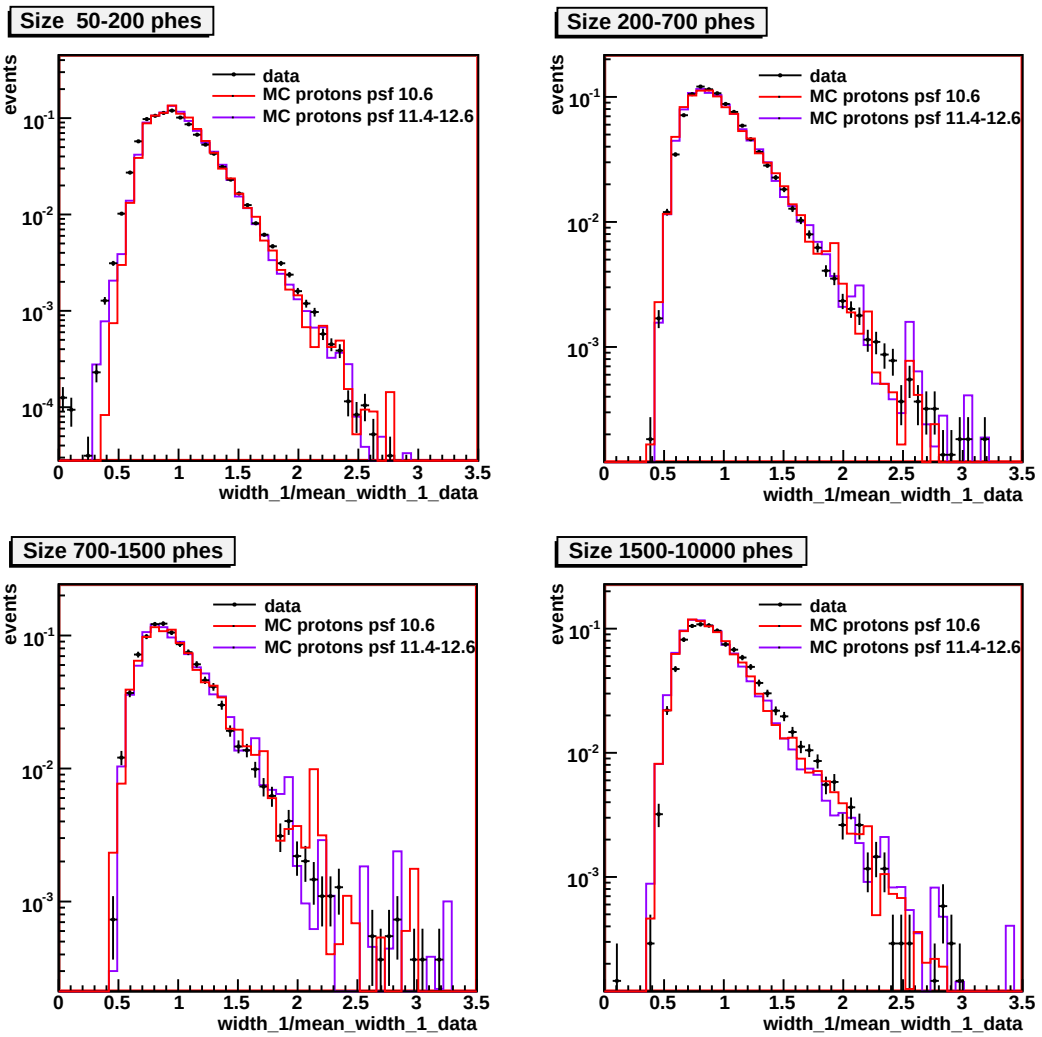

Fig. 4.19: MAGIC-I width distributions in size bins for MC protons with different PSF compared to real data.

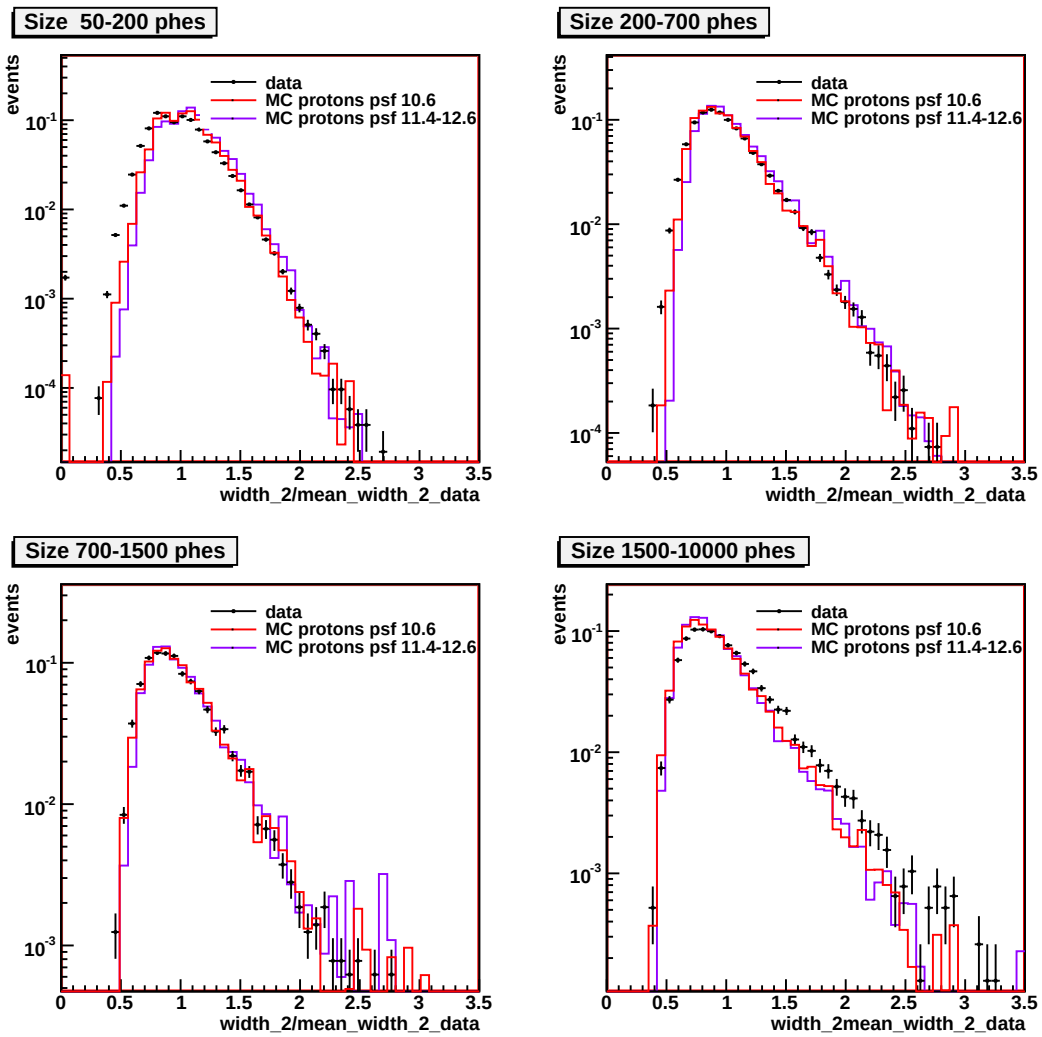

Fig. 4.20: MAGIC-II width distributions in size bins for MC protons with different PSF compared to real data.

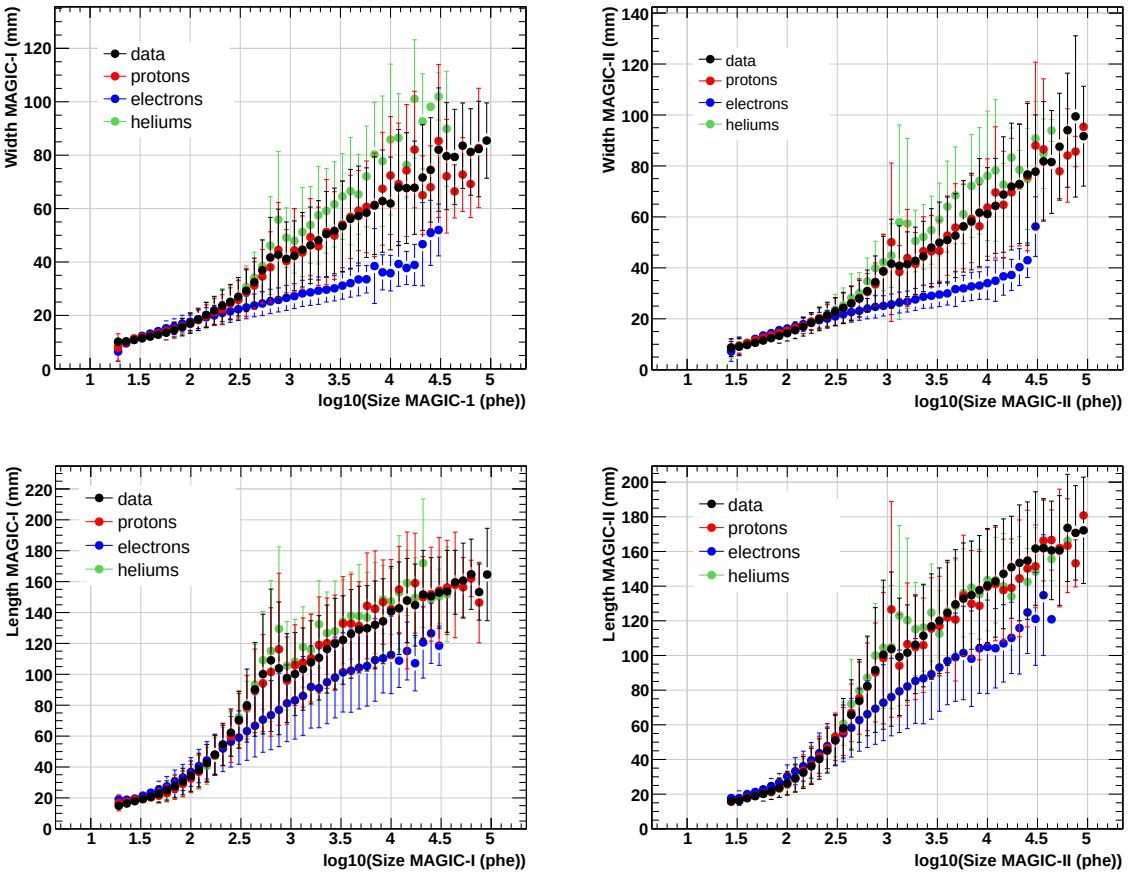

Fig. 4.21: Distributions of the mean width and mean length of the images for the two telescopes as a function of the respective sizes. The error bars represent the RMS of the distributions.

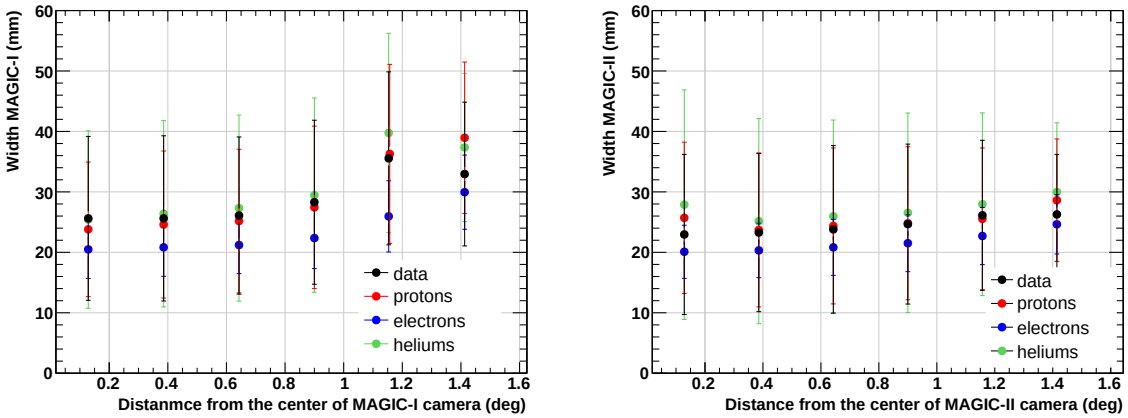

Fig. 4.22: *Width* of the images as a function of the distance from the center of the camera for the two telescopes. Data are shown in black, protons in red, electrons in blue and helium in green. On the left plot, MAGIC-I data are shown and the transition from the smaller pixels to the bigger ones is visible as a clear increase of the width after 1^o. The error bars represent the RMS of the *Width* distrubution.

Length of the images as a function of *Size* are then compared for different particle showers. Electron showers have a smaller *Width* while helium showers have a bigger one compared to data. At a *Size* around 10^3 phe the peak present in the data and in the hadrons is due to muons. This peak, in fact, represents the maximum intensity of Cherenkov light produced by a single particle detected by the MAGIC telescopes.

Figure 4.22 shows the *Width* of the images for different particles showers in the two telescopes as a function of the distance from the center of the camera. While for MAGIC-II the *Width* is constant all over the camera, in the case of MAGIC-I, the transition between smaller pixels and bigger ones is clearly visible. The *Height* as a function of *Size* is shown in figure 4.23. A lower *Height* for hadrons with respect to electrons demonstrates that they penetrate deeper in the atmosphere. At higher sizes, hence at higher energies, hadrons behave more similar to electrons. The *Height* can not be measured by a single telescope, but can only be measured with a stereo system.

The *Hadronness*, computed with the parameters here compared, is shown in different size bins in figure 4.24. The blue distributions represent the MC electrons, the red distributions the MC protons and the green ones the MC helium. The distributions are normalized to the number of events. We see that the discrimination power of this parameter increases with energy: the peak at zero for electrons becomes sharper with increasing energy, while the hadron level decreases with energy. It is interesting to note that helium contributes essentially at large *Hadronness* values. At *Size* above 200 phes, the electromagnetic/hadronic separation is more effective than for protons, thus, for helium, the *Hadronness* distribution at low values (signal region) is flatter. Therefore the contribution of helium in the signal region is at most only a few percent of protons. This will lead to a systematic error contribution of less than 5% in the spectrum when ignoring the MC helium in the analysis.
While there are several parameters used to distinguish electrons from hadron-initiated

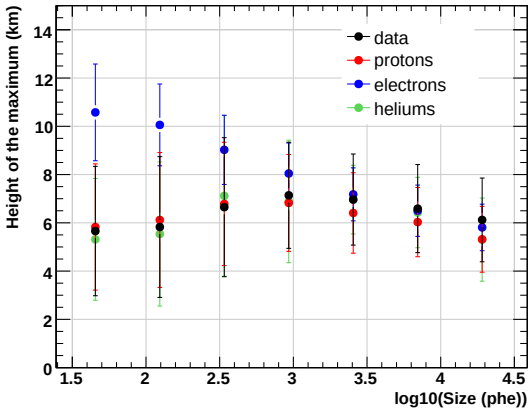

Fig. 4.23: Distributions of the *Height* of the maximum as a function of *size*. The error bars represent the RMS of the *Height* distrubution.

showers, it is extremely difficult to distinguish between electron and γ-initiated showers. From theoretical predictions, the contribution of the diffuse extragalactic γ-ray signals to the cosmic electron flux is very low. Nevertheless it is interesting to investigate the differences. The images from the two particle types appear to be very similar, thus the only useful parameter to distinguish them is the depth of the shower maximum (X_{max}). X_{max} occurs on average half a radiation length higher in the atmosphere for electrons. In figure 4.25, the depth of the shower maximum is shown, calculated from the reconstructed height of the maximum. The blue line represents the electrons, the pink one the γ-rays and the black points represent the real data from electromagnetic showers. As one can see from the plot here shown, it is very difficult to distinguish between the two origins.

The Monte Carlo simulations have been shown to reproduce the experimental data. Thus the proton simulations can be used to estimate the level of background of electron signals. Additional plots of the parameters used in the analysis and their comparison with real data can be found in the appendix A.

4.4 Systematic uncertainties

Together with the derivation of the spectrum, the uncertainties are an important part of the result. Besides statistical uncertainties, the systematic uncertainties on the integral flux and on the energy estimation contribute to enlarge the errors of the energy spectrum. The systematics are related to the impossibility to calibrate the instruments in an absolute scale and to the uncertainties in the hadronic models, which contributes to the flux. MC hadrons are in fact used to subtract the background. It is very difficult to estimate accurately the systematic uncertainties. Here I am trying to investigate them listing the main sources. Part of the study is based on previous works: [120], [23] and [16].

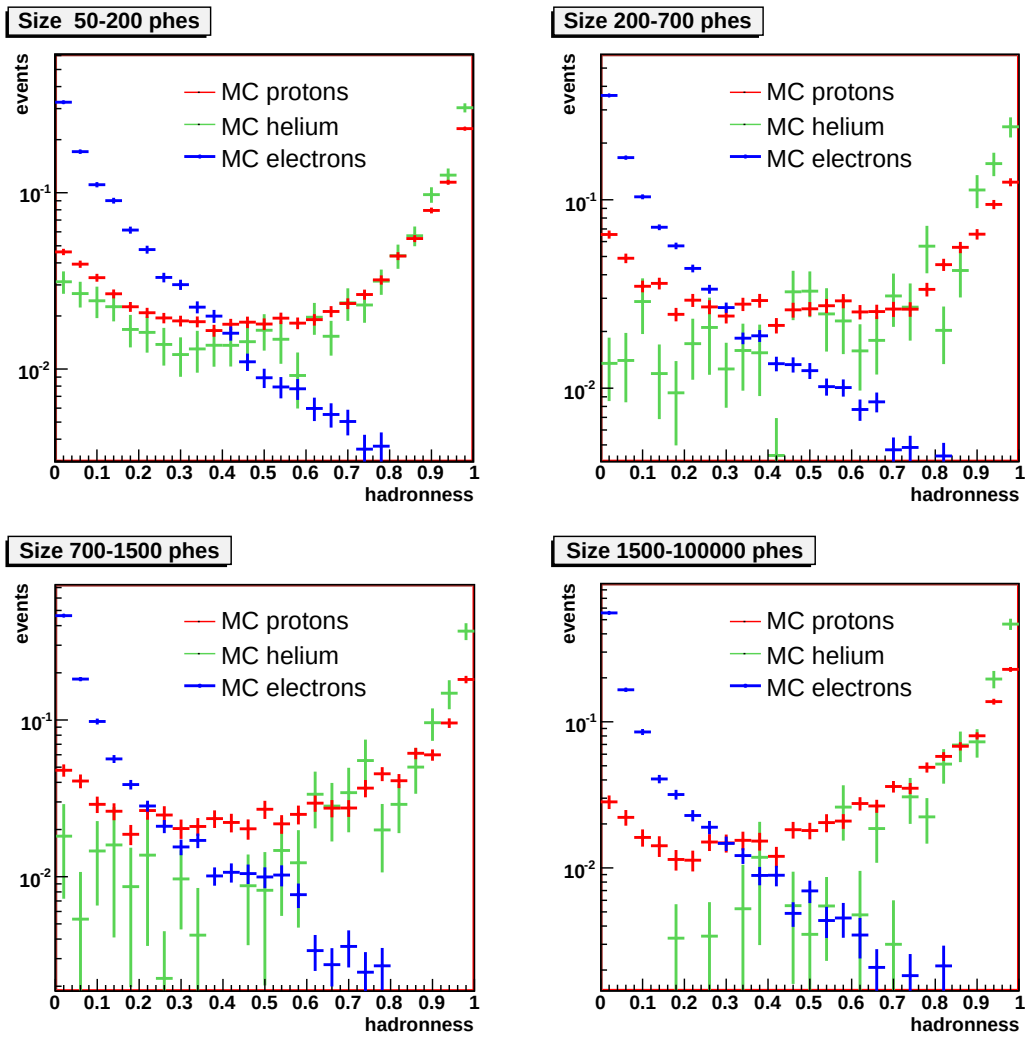

Fig. 4.24: *Hadronness* distributions in size bins for MC electrons, MC protons and MC helium .

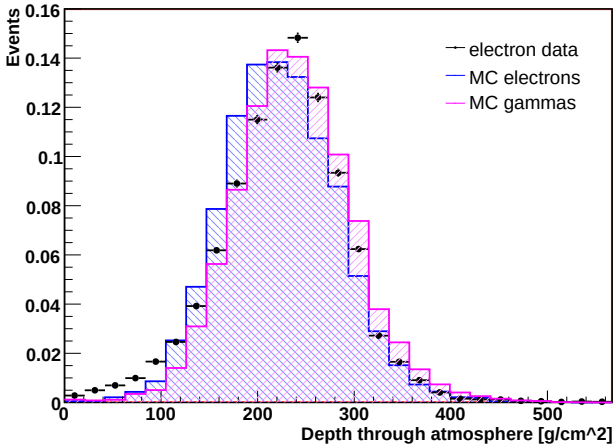

Fig. 4.25: Distributions of the depth through the atmosphere converted from the *Height* for MC electrons, MC diffuse gamma and electron data.

Effects on the energy scale

- Parametrization of the atmosphere in MC simulations: 3%.
- Variation of atmospheric transmission due to Mie-scattering: 5%.
- Incomplete NSB simulation (MC assume uniform NSB): 4% below 100 GeV, less than 1% above 300 GeV.
- Reflectivity of the mirror dish: 7%.
- AMC system errors: 3%.
- Day to day reflectivity changes: 2%.
- Aging of the coating enhancing the UV-sensitivity of the MAGIC-I PMTs: 3%.
- Uncertainty in the quantum efficiency of the PMTs: 10%.
- Uncertainties of the light collection efficiency of the first dynode in the PMT: 5 - 10%.
- Uncertainty in the reflectivity of the foil used for the light catchers: 3%.
- Uncertainty in the photoelectron collection efficiency of the PMT: 5 - 10%.
- Gain fluctuations of PMTs: 10%.
- Use of Poisson distribution (F-factor method) to calibrate the signal: 10%.
- Uncertainties in discriminator threshold: 5 - 10%.
- Signal drift in camera due to temperature drifts (including QE, amplifier and optical transmitter drifts): 2%.

- Precision in the camera flatfielding: 2%.
- Discrepancies between simulated showers and real showers: 20% below 300 GeV, 10% above 300 GeV.
- Errors in the stereo parameters calculations: 5%.
- Non-linearity in the analog signal chain and in the DRS2 chip: uncertainty of 0.04 in the spectral index.
- Uncertainties of the unfolding procedure: 0.1 in the spectral index.

Effects on the flux normalization

- Uncertainty on the optical PSF which effects the trigger efficiency: 5%.
- Losses due to the protective Plexiglas in front of the PMTs: 3%.
- Variation of the number of PMTs switched off: 2%.
- Trigger inefficiencies: 10% below 150 GeV, 3-5% above 500 GeV.
- Failures of the FADC acquisition system of MAGIC-I and DRS2 of MAGIC-II: 2%.
- Differences in the analysis methods (signal extraction, image cleaning, RF training): 3%.
- Event reconstruction (errors in the Hillas parameters calculations): 8%.
- Camera inhomogeneity: 4%.
- Uncertainties due to the hadronic interaction model used: 25 - 30%, [64].
- Lack of simulations of heavy elements for the background estimation: 5%.

The overall systematic errors in the energy scale are estimated to be more than 30%, if we sum up variances [120].
We have some additional information: for MAGIC-I, an energy calibration is done with the analysis of the muons events. Hillas parameters of the muon images are compared with the MC muon simulations. This calibration leads to a $\sim$25% mis-match between real data and MC in energy scales. In this context the uncertainties due to weather changes and instabilities are not taken into account. For MAGIC-II, a relative comparison with MAGIC-I concludes that there is an increase of 10% in the size of the images, due to a 10% - 15% better photon-efficiency.
Due to all these systematics, the energy is likely underestimated, since most of the effects result in a loss of Cherenkov photons.
The error on the flux normaization is estimated to be $\sim$15% in case of the standard *point-source* analysis and $\sim$30% in case of *diffuse-source* analysis, where the uncertainties of the hadronic interaction model used affect the background estimation.

Based on the work of [23], the systematic error on the slope of the energy spectra for γ-ray sources is ± 0.15. We can assume a minimum value of systematic error on the spectral index for diffuse cosmic electrons to be ± 0.15, the same as for γ-ray sources.

The whole analysis described so far has been applied to different sets of data in order to demonstrate the method (in chapter 5) and to measure the diffuse cosmic electron signals (in chapter 6).

5 Performance of the MAGIC Stereo System

The MAGIC stereo system was commissioned in 2009. In this chapter the performance of the stereo system is investigated. Since the calibration of the system can not be done in the laboratory with a test beam, as explained in the previous chapter, in VHE γ-ray astrophysics it is common to determine the sensitivity by measuring of a strong, steady source. Normally one uses the Crab nebula as a reference source.
In the first part of this chapter the Crab Nebula data used for this study are presented and the telescope performance is derived. Moreover, in order to demonstrate the technique and the performance of the method developed for the study of cosmic electrons, the *diffuse-source* method is applied on data of the Crab Nebula. It is compared with the standard *point-source* method both for single MAGIC-I telescope and stereo analysis.

5.1 The Crab Nebula data sample

The data used for the performance study are based on Crab Nebula observations. The Crab Nebula is a pulsar wind nebula in the constellation of Taurus, located at a distance of $\sim 2\,\mathrm{kpc}$. The nebula formed after a supernova explosion in 1054. This cosmic event was observed and documented by many astronomers worldwide, for example by Chinese [107], Indian and Korean astronomers. The nebula contains in its center a pulsar, well studied at lower energy and recently also detected in the VHE range by MAGIC [26]. The Crab Nebula is the strongest continuous source of X-rays and γ-rays in the sky [22]. For this reason it is considered as the standard candle of gamma-astronomy

and it is used as calibration source to study the telescope performance and test the consistency of different analysis methods[1].

	obs. period	obs. time (hour)	Zenith range
MAGIC-I	01/2008	10	15^o - 25^o
MAGIC-Stereo	10-11/2009, 01/2010	17	11^o - 27^o

Table 5.1: Crab Nebula data sample details for mono and stereo observations.

Observation of the CRAB nebula with the MAGIC-I telescope

A total of ∼10 hours of Crab Nebula data taken with the MAGIC-I telescope in January 2008 are used for this analysis (in table 5.1 the observations are summarized). Data are selected in the *zenith* angle range between 15^o and 25^o, with the restriction that the rate variations are in the range of $\pm\,15\%$ of their mean value. Concerning the weather conditions, limits on the humidity (below 60%) and the so-called cloudiness[2] (below 40%) levels are set in order to ensure good quality data. After the selections, a total of 6.6 hours were analyzed. Additional cuts applied to the data in the analysis are: $Leakage$ <0.2, $Island$ <2 and $Size$ >100 phes.

Observation of the Crab nebula with the MAGIC stereo system

A total of ∼ 17 hours of Crab Nebula data taken in the *zenith* angle range between 11^o and 27^o in stereo mode in October, November 2009 and January 2010 are used (in table 5.1 the observations are summarized). The selection was made in the same way as for MAGIC-I: rates being $\pm\,15\%$ of the mean values, humidity below 60% and cloudiness below 40%. After the selection a total of 10 hours were analyzed. Further, additional cuts applied in the analysis are: $Leakage$ <0.2 and $Island$ <2 for both telescopes, with $Size$ >100 phes for MAGIC-I and $Size$ >200 phes for MAGIC-II. The reason for using a higher $Size$ cut for MAGIC-II is related to a non perfect matching between MC and data at low $Sizes$ (see fig. 4.20). The origin of the mis-match is not yet understood. As MAGIC-II is more sensitive than MAGIC-I the images of the same showers have a higher number of photoelectrons (it should also be noted that the mirrors of MAGIC-I were already degraded after about 7 years exposure to the atmosphere and that the PMTs of MAGIC-II have a higher QE).

[1] Up to late 2010 the Crab Nebula was considered as a so-called 'standard candle' for VHE gamma astronomy because the source seemed to be extremely stable. Recently, quite some rapid flux changes have been observed by Agile and Fermi between ∼ 100 MeV and ∼ 200 GeV. During the time of the calibration for this study the source was still in a stable state.

[2] The cloudiness is an empirical parameter derived from the temperature of the sky measured by a radiometer in the 8-14 micron wavelength band.

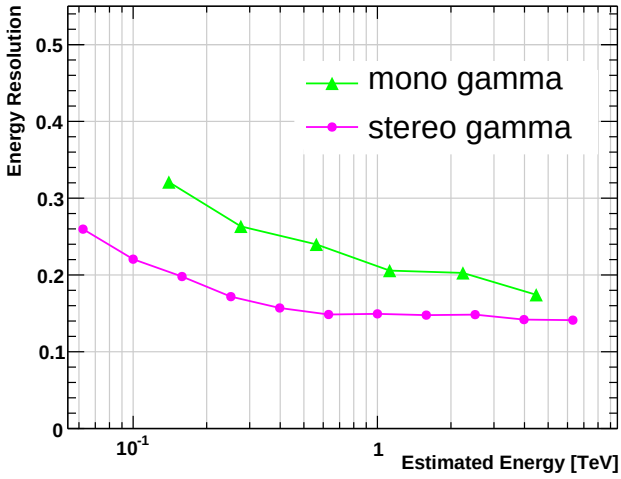

Fig. 5.1: Relative energy resolution of MC gammas after the cuts for both MAGIC-I (in green triangles) and MAGIC-stereo (in pink circles).

5.2 Performance of the single telescope and the stereo system for point-like sources

The most important MAGIC performance here investigated are:

- Energy resolution
- Angular resolution
- Electromagnetic/Hadronic separation
- Sensitivity
- Spectral analysis

5.2.1 Energy resolution

The energy of the primary particle is estimated by means of MC simulations. Therefore, a good agreement between MC and real showers is essential for the estimation of the energy. Figure 5.1 shows the energy resolution (defined in section 4.2.6) as a function of energy for gammas from point sources, for observations with MAGIC-I and with the stereo system. An energy resolution better than 15% is achieved with the stereo system, above 400 GeV. The stereo system provides a better energy resolution because the 3D-parameters of the shower are better reconstructed. Two new parameters, the *Impact* and the *Height* of the shower maximum, inaccessible in case of single telescope observation, allow a better reconstruction.

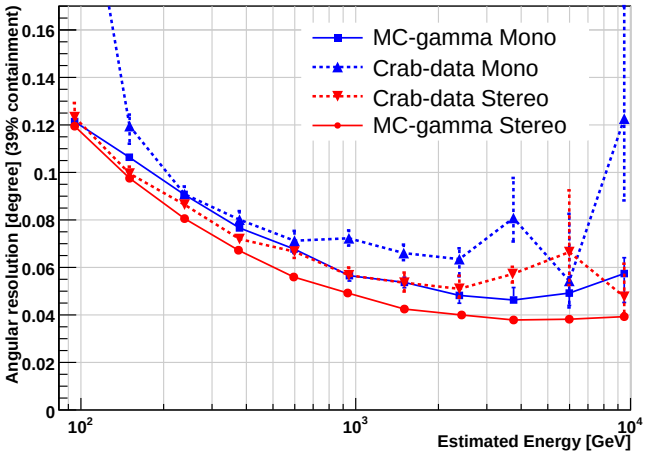

Fig. 5.2: Angular resolution of the MAGIC stereo mode (red) compared with the MAGIC-I telescope (blue) for MC gamma in solid lines and Crab Nebula data in dashed line.

5.2.2 Angular resolution

The angular resolution is defined as the confinement radius in which 39% of all reconstructed events are contained. This radius is determined from the θ^2 distribution of point source. Only events with θ^2 <0.2 are considered. In addition the following cuts have to be fulfilled: *Hadronness* <0.2, *Leakage* <0.2 and *Island* <2, for *zenith* angles below 30^o. With the stereo information, the direction of the primary particle is much better reconstructed compared to a single telescope information. Figure 5.2 shows the improvements in the angular resolution as function of energy for the stereo system compared to MAGIC-I alone, both for MC γ and Crab Nebula data events. The improvement of the angular resolution for real data is estimated to be $\sim$30% in the total energy range. At around 300 GeV the angular resolution improves from $\sim 0.09^o$ to $\sim 0.07^o$, in good agreement with the MC simulations.
In figure 5.2 the differences between real data and MC might be due to a mis-pointing or to the fact that the *Disp* is trained only with MC events, therefore small discrepancies between MC events and real data can introduce differences in the angular resolution. The angular information is very important in the case of γ-ray point source studies, because it is used to discriminate and extract the signal from the background.
In the case of diffuse electrons, instead, the distribution of the arrival directions is completely uniform and it is not a relevant information.

5.2.3 Gamma/hadron separation

The γ/hadron separation is essential for measuring signals. The *Hadronness* distribution is shown in figures 5.3 for MC gammas and MC protons, for a reconstructed energy above 150 GeV, for MAGIC-I (left) and for the stereo system (right). The *Hadronness* distribution of gammas peaks at 0, while the distribution of protons peaks at 1. For a quantitative estimate one can calculate the so-called quality factor $Q = \frac{f_\gamma}{\sqrt{f_{pr}}}$, with f_γ and f_{pr} the fraction of γ and protons events surviving a preset cut in *Hadronness*

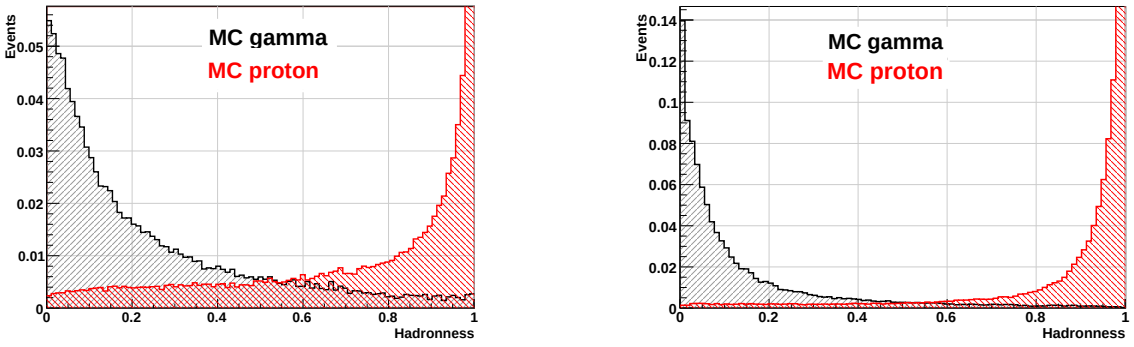

Fig. 5.3: *Hadronness* distribution for gamma in black and proton in red for a reconstructed energy above 150 GeV for MAGIC-I (left) and Stereo analysis (right).

and thus gives also an information about the background rejection. The *Hadronness* cut which keeps 60% of the gamma events give $Q = 2.3$ for the MAGIC-I analysis and $Q = 4.7$ for the stereo one. Therefore, the improvement in the background rejection, from the single-telescope to the stereo, is a factor 4.

5.2.4 Sensitivity

The improved performance in energy reconstruction and γ/hadron separation of the stereo-mode compared to the single-telescope mode translates into a better sensitivity of the system. Moreover the improved angular resolution reduces the background for point sources, with a subsequent improved in the sensitivity for this kind of sources. For illustrative purposes, in figure 5.4 on the two upper plots, the θ^2 distribution is shown for a sample of Crab Nebula data and background for single-telescope (MAGIC-I) mode (on the left) and stereo mode (on the right) in the lower energy limit, between 80 and 100 GeV. In the stereo analysis the higher background suppression allows one to go to lower energies with better sensitivity. From the two upper plots in figure 5.4, in which the same cuts are applied, one can notice that the differential sensitivity, for an average energy of $\sim$90 GeV, in the stereo analysis is five times better than in single telescope analysis (the analysis shown here is not optimized in the case of the single telescope). At higher energies, between 300 and 500 GeV, as it is shown in the two lower plots of figure 5.4, as an example, the improvement is reflected more in the background reduction. On the other side, the good γ/hadron separation of the single telescope analysis at these energies leads to a better significance compared to lower energies. For the integral sensitivity, the improvement is shown in figure 5.5, where the achieved integral sensitivity for MAGIC-I (blue line) is compared with the expected one for the stereo system (red line) and the so far achieved for the stereo (black points) with 5 hours of Crab Nebula data taken in October 2009. Basic cuts are applied: *Leakage* <0.2 and *Island* <2 for *zenith* angles below 30^o. Cuts in *Hadronness* and θ^2 depending on energy are optimized on the other 5 hours of Crab Nebula data from the same period. The sensitivity scales with the square root of the observation time. The stereo system provides $\sim$2 - 3 times better sensitivity than MAGIC-I alone. Above few TeV instead, the stereo performance is limited by a smaller trigger region of the

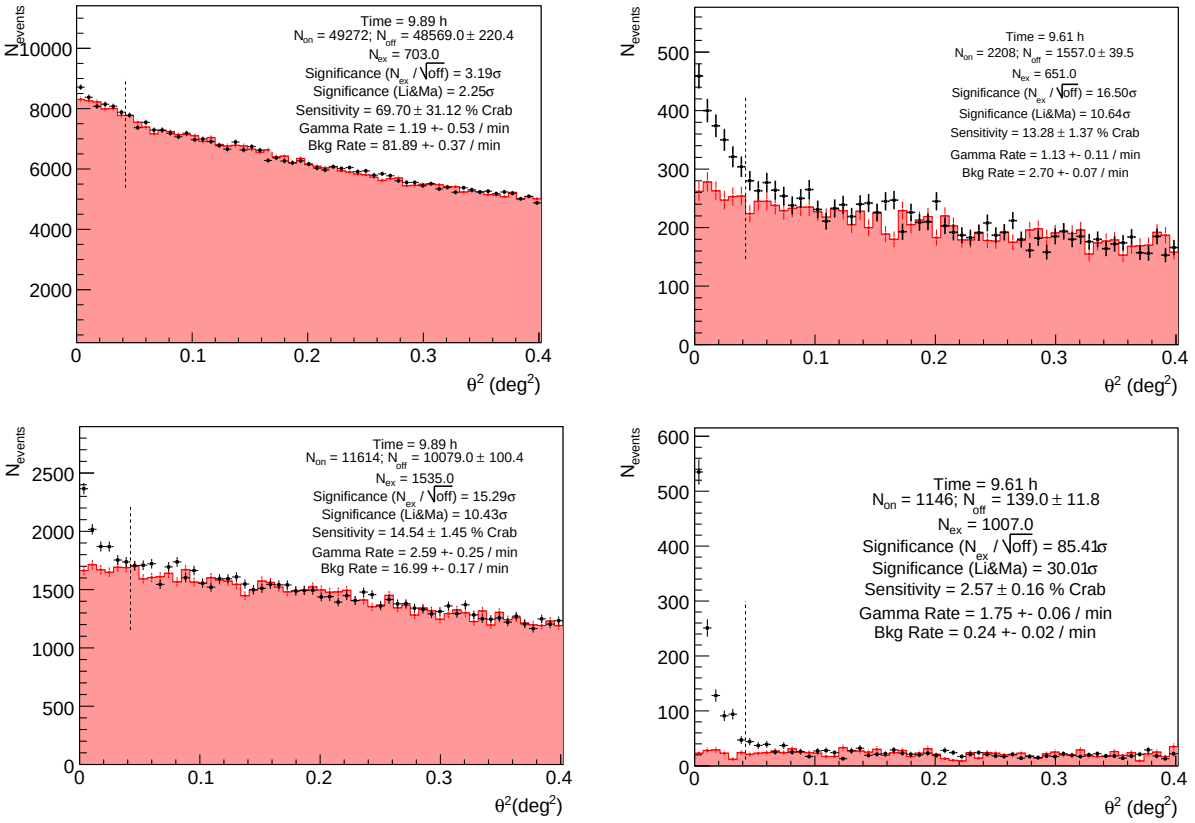

Fig. 5.4: θ^2 distribution for the Crab Nebula in black and for the background in red in the energy range between 80 and 100 GeV for MAGIC-I analysis on the left and for the stereo analysis on the right in the two upper panels. In the two lower panels the same plots are done for the energies between 300 and 500 GeV.

MAGIC-I camera. The best sensitivity for MAGIC-I reaches 1.6% of the Crab Nebula flux, above 300 GeV. With the current stereo system, instead, one is able to detect point sources with flux levels of less than 1% of the emission of the Crab Nebula (see fig. 5.5).

5.2.5 Spectral analysis

The performance shown so far refers to the analysis of point sources. In particular γ/hadron separation and angular resolution of the stereo analysis lead to a more efficient background rejection compared to a single-telescope (MAGIC-I) mode. In figure 5.6 the spectrum of the Crab Nebula is derived from observations carried out in October, November 2009 and January 2010 with the stereo system. The analysis is performed selecting events with *Leakage* <0.2 and *Island* <2 in the *zenith* angle range between 11^o and 27^o. The background is rejected mainly with cuts on the *Hadronness* which are optimized on a different set of Crab Nebula data. The derived spectrum is fitted by a power law:

$$\frac{dF}{dE} = f_0 \left(\frac{E}{1TeV} \right)^{\Gamma} \tag{5.1}$$

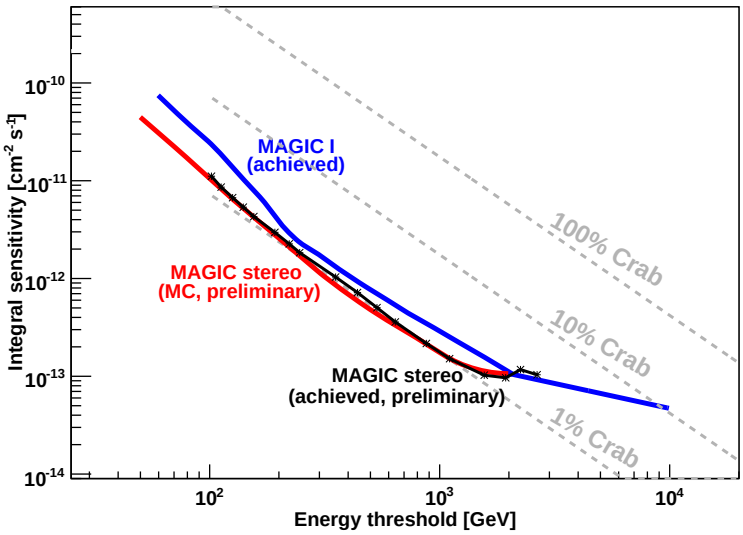

Fig. 5.5: Minimum flux level achieved in the stereo analysis (black points) compared to the expected stereo one (red) and to the achieved one for MAGIC-I alone (blue)

In figure 5.6 the spectrum of the Crab Nebula is shown for three different unfolding methods (Bertero [38], Tikhonov [140] and Schmelling [134] discussed in section 4.2.8). The points obtained with the different methods agree very well and are consistent with the previous measurements of MAGIC-I [22] (turquoise dashed line), HEGRA [11] (green dashed line) and H.E.S.S. [12] (grey dashed line).
Due to the better sensitivity of the stereo system compared to that of a single telescope, less observation time is needed to detect a source. The improved signal/background ration results in smaller error bars in the spectrum. Also, the better γ/hadron separation translates in a lower energy threshold.

5.3 Performance of the stereo system for diffuse sources

In this section the performance of the analysis methods is investigated. The *point-source* and the *diffuse-source* approaches, described in section 4.2.7, for the determination of the energy spectrum, are compared for both the single-telescope (MAGIC-I) and the stereo analysis.

5.3.1 Energy resolution

The energy resolution in the case of diffuse sources is computed without any θ^2 cuts. In figure 5.7 the energy resolution in case of diffuse electrons is shown both for MAGIC-I and the stereo system. Above 400 GeV the energy resolution is $\sim$16% for the stereo system, and larger than 20% for the MAGIC-I analysis alone. In the same plot (fig. 5.7), the energy resolution for diffuse gammas in stereo mode observation is also shown. A better energy resolution for gammas than for electrons is related to the fact that

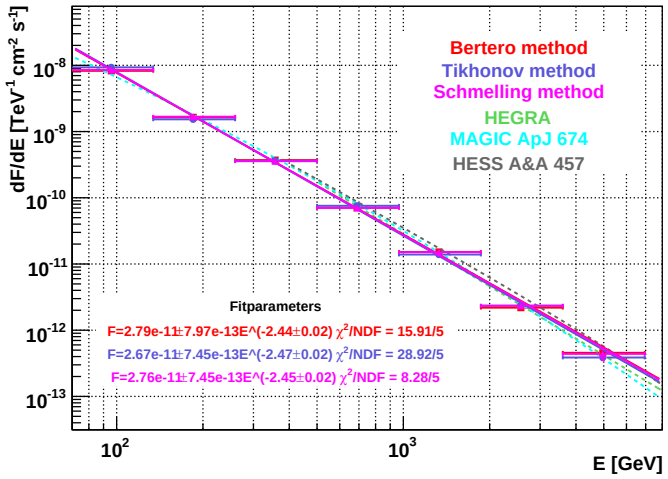

Fig. 5.6: Measured differential Crab spectra derived from the three different unfolding methods: in red the Bertero method, in blue the Tikhonov method and in pink the Schmelling method. Previous measurement are also shown: MAGIC-I [22] (turquoise dashed line), HEGRA [11] (green dashed line) and H.E.S.S. [12] (grey dashed line).

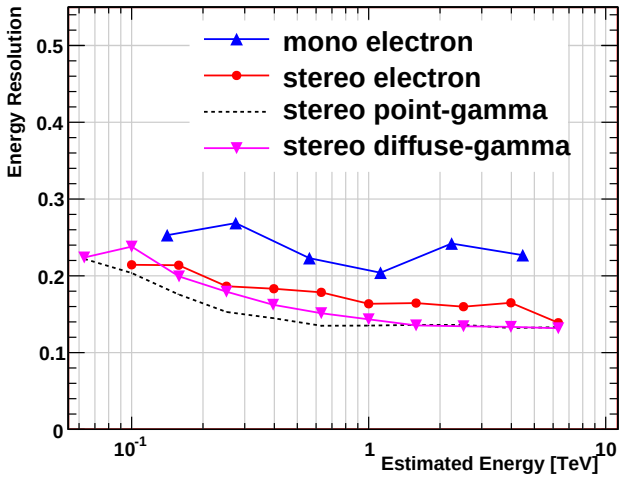

Fig. 5.7: Energy resolution for diffuse MC electron events after the cuts for both MAGIC-I (in blue) and MAGIC-stereo (in red). In addition the energy resolution of diffuse MC gamma events for MAGIC-stereo (in pink) and as a reference the energy resolution of point source MC gamma events for MAGIC-stereo is shown as dash line.

gammas are simulated in a smaller solid angle (semi-aperture angle=1.5^o) compared to electrons (semi-aperture angle = 4.5^o).

5.3.2 Sensitivity

In the analysis of diffuse sources, the sensitivity is strongly dependent on how well the MC simulations describe the background. Moreover, having a large enough amount of MC simulations, will reduce considerably the fluctuations on the background.
One can compute the best sensitivity in 50 hours of observation with a 5 sigma detection, using data from the Crab Nebula. In the simple approximation, the significance in 50 hours is expected to be:

$$\sigma_{50} = \frac{N_{excess}}{\sqrt{N_{bg}}} \cdot \sqrt{\frac{50h}{t_{obs}}} \tag{5.2}$$

where N_{excess} is the number of excess events collected during the observation time t_{obs} and N_{bg} the number of MC background events, normalized by the same time t_{obs}. The *diffuse-source* analysis method yields an integral sensitivity above 300 GeV of $flux_{min} = 2.3{\cdot}10^{-11}\,\mathrm{cm}^{-2}\mathrm{s}^{-1}$ ($\sim 10\%$ of the Crab Nebula flux) for γ-ray point sources and stereo analysis. In figure 5.8 the *Hadronness* distributions for the Crab Nebula events and for the background are shown in the energy range between 300 and 500 GeV for the single MAGIC-I telescope and stereo analysis. Again, the higher significance of the stereo analysis leads to a better sensitivity than for the single telescope. Different cuts are applied in single telescope and stereo analysis, since the *Hadronness* distributions differ and depend on the training. In fact, different parameters are used in the RF, as explained in 4.2.4.
In case of diffuse cosmic electrons, the integral sensitivity above 300 GeV, which can be measured by MAGIC, is $flux_{min} = 1.8{\cdot}10^{-8}\,\mathrm{cm}^{-2}\mathrm{s}^{-1}\mathrm{sr}^{-1}$ (in a simulated solid angle of $\Omega = 0.019\,\mathrm{sr}$). The cosmic electron flux measured by Fermi [5] above 300 GeV is $flux_{electrons} = 8{\cdot}10^{-8}\,\mathrm{cm}^{-2}\mathrm{s}^{-1}\mathrm{sr}^{-1}$, which is 4 times higher than the minimum flux measurable by MAGIC.

5.3.3 Spectral analysis

In case of the standard *point-source* analysis cuts in *Hadronness* and θ^2 are applied in each energy bin such that 60% of the gammas survive.
In case of the *diffuse-source* analysis the background events are determined by the simulations of protons. In case of the single telescope analysis, also cuts in distance of the centroid of the image from the center of the camera are applied, in order to select only the region of the source and to reduce the background. In case of the stereo analysis, the background is already reduced thanks to the stereo trigger. Again, *Hadronness* cuts are applied in each energy bin such that 60% of the gammas survive, both for the single telescope and the stereo analysis.
In the upper plot of figure 5.9 the differential spectra obtained by the two methods are compared for the single MAGIC-I telescope analysis. A power law fit is used in both

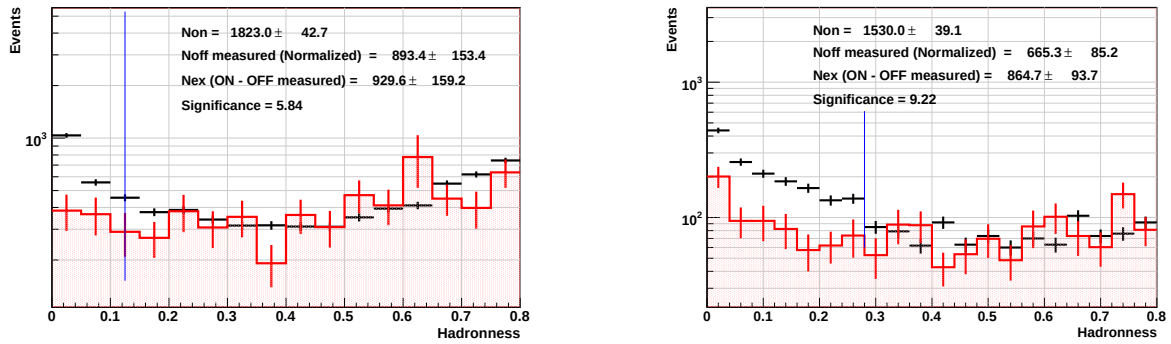

Fig. 5.8: *Hadronness* distribution for the Crab Nebula in black and for the background in red in the energy range between 300 and 500 GeV for MAGIC-I telescope analysis on the left and for the stereo analysis on the right. Different cuts are applied in single telescope and stereo analysis, since the *Hadronness* distributions differ and depend on the training.

approaches, which lead to the differential spectra:

$$\left(\frac{dF}{dE}\right)_{point} = (3.62\pm0.15_{(stat)}\pm0.54_{(syst)})\cdot10^{-11}\times\left(\frac{E}{1TeV}\right)^{-2.31\pm0.04_{(stat)}\pm0.2_{(syst)}} TeV^{-1}cm^{-2}s^{-1}$$

$$\left(\frac{dF}{dE}\right)_{diffuse} = (3.44\pm0.24_{(stat)}\pm1.03_{(syst)})\cdot10^{-11}\times\left(\frac{E}{1TeV}\right)^{-2.30\pm0.11_{(stat)}\pm0.2_{(syst)}} TeV^{-1}cm^{-2}s^{-1}$$

In the lower plot of figure 5.9 the differential spectra obtained by the two methods are shown for the stereo analysis. A power law fit used in both approaches, lead to the differential spectra:

$$\left(\frac{dF}{dE}\right)_{point} = (2.79\pm0.08_{(stat)}\pm0.42_{(syst)})\cdot10^{-11}\times\left(\frac{E}{1TeV}\right)^{-2.44\pm0.02_{(stat)}\pm0.15_{(syst)}} TeV^{-1}cm^{-2}s^{-1}$$

$$\left(\frac{dF}{dE}\right)_{diffuse} = (2.72\pm0.22_{(stat)}\pm0.82_{(syst)})\cdot10^{-11}\times\left(\frac{E}{1TeV}\right)^{-2.68\pm0.05_{(stat)}\pm0.15_{(syst)}} TeV^{-1}cm^{-2}s^{-1}$$

The systematic errors on the flux normalization are calculated at the level of 15% in case of *point-source* analysis and 30% in case of *diffuse-source* analysis, as estimated in section 4.4. The systematic error on the spectral slope for the stereo analysis, also explained in in section 4.4, is based on the work of [23]. In the case of the single telescope analysis, instead, the systematic error on the spectral slope is higher than the stereo, as computed in [120].
The spectrum determined with the *diffuse-source* method is consistent and in agreement with the standard one, confirming that the *diffuse-source* method is reasonably reliable and can be used in the present work to determine the cosmic electron spectrum. In addition, the stereo system with both the analysis method allows to reach energies lower than 100 GeV, while with a single telescope, with the *diffuse-source* method, the excess at $\sim$100 GeV is not significant. The spectral slope derived with MAGIC-I and with the stereo system differ from each other because the stereo data span a wider range of energies than MAGIC-I data.

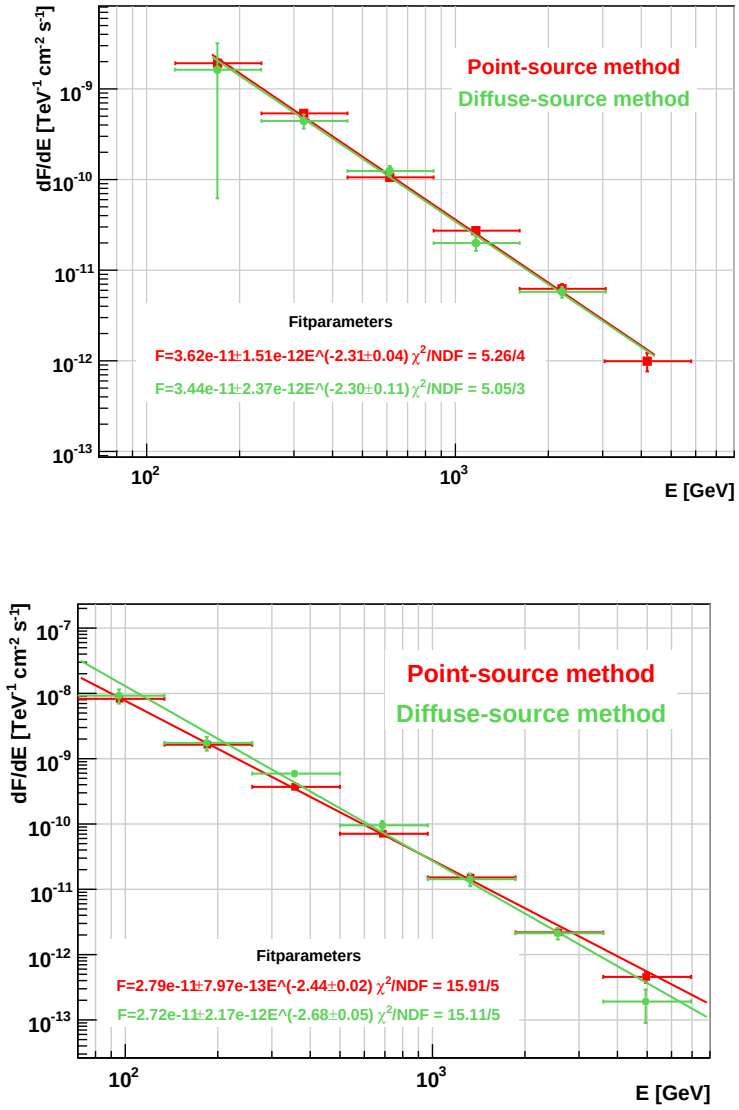

Fig. 5.9: Measured differential Crab spectra derived from the two methods: in red the standard *point-source* method and in green the new developed *diffuse-source* method. On the top: **Single telescope (MAGIC-I) analysis**. On the bottom: **Stereo analysis**.

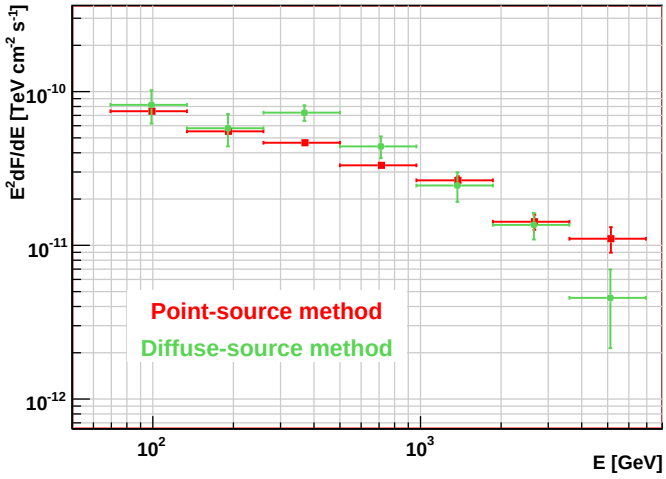

Fig. 5.10: Measured differential Crab spectra derived from the two methods multiplied by E^2: in red the standard *point-source* method, in green the new developed *diffuse-source* method.

In case of the stereo analysis the spectrum derived with the *diffuse-source* method is slightly steeper, but still within the errors, than the one derived with the *point-source* method. In figure 5.10 the spectrum is multiplied by E^2 and at around 400 GeV a feature in the spectrum is visible in case of *diffuse-source*. Differently from single telescope analysis, in which a cut in distance of the centroid of the image from the center of the camera is applied, in the stereo analysis such a cut is not applied. This means that while the hadronic background is rejected by the stereo trigger, a contamination from the electron background might still be present, which would increase the flux and steepen the spectrum.

6

Cosmic Electron Measurements and results

In this chapter the analysis of cosmic electrons and the resulting spectrum from MAGIC data are presented. In the first part I will describe the analysis using data recorded only with the MAGIC-I telescope, while in the second part the search for cosmic electrons with the MAGIC stereo system (shortcut MAGIC stereo) will be described.
Data used in these analyses come only from observations of selected extragalactic sky areas (see below for the coordinates), in order to minimize the contribution from the diffuse γ-ray emission which comes mainly from the Galactic plane. γ-rays are in fact extremely difficult to distinguish from electrons. In addition sky areas containing known γ-ray sources are excluded from the analysis. A standard γ-ray analysis has been carried out beforehand in order to ensure the absence of any significant γ-ray signal.

6.1 The MAGIC-I search for cosmic electrons

6.1.1 Data sample and applied selection criteria

The data sample used for the single MAGIC-I telescope analysis is from the observation of the region of 2E1415+2557, which is an HBL located at RA: 14h 17m 56.7s and DEC: +25d 43' 26", at a redshift z = 0.237. This region is highlighted in the full-sky plot in figure 6.3 with the black rectangle. Prior, it has been found out that no gamma emission has been detectable at or around this source.
The observations were carried out in March and April 2008. The target has been observed in wobble mode in zenith angle range between 3^o and 28^o. In table 6.1 the data used to measure the electron spectrum are listed day by day.

Date	Events (k)	obs. time (min)
2008-03-02	90	9
2008-03-07	1092	89
2008-03-08	1030	90
2008-03-09	933	75
2008-03-10	423	35
2008-03-11	1098	91
2008-03-29	228	19
2008-03-30	181	16
2008-04-01	147	12
2008-04-02	219	17
2008-04-05	186	14
Total	5627	467

Table 6.1: Observation details of the data sample used for the electrons analysis.

Quality cuts are performed in order to reject bad weather data. Changes in the atmosphere influence the trigger rate and the total flux normalization. Therefore, runs with unstable trigger rates are rejected, keeping the events with rates within $\pm 15\%$ of the average one. In addition, runs with too high humidity (above 60%) and cloudiness (above 40%) values (see section 4.1) are rejected. The Hillas parameters are also checked to be within 5% of the average. Some days have been completely removed due to bad weather conditions.
After these quality cuts, ~ 7 hours of data have been analyzed. The zenith angle range is limited by the simulations of protons and has finally been reduced to 5^o - 20^o.

6.1.2 Event reconstruction and excess determination

The data analysis was carried out as described in section 4.2. An image cleaning with a threshold of 6 phes for core pixels and 3 phes for boundary pixels was applied. After the calculation of the Hillas parameters, the RF for electron/hadron separation was trained using MC electrons and ~ 6 hours of data as hadron sample. For the additional hadron sample also data from 2E1415+2557 was taken, but a different set of data, in order to avoid biases in the analysis.

In figure 6.1 the *Hadronness* distribution of the observed events is plotted together with the normalized distribution of the background for four energy ranges. The normalization of the background distribution is done in *Hadronness* parameter range between 0.2 and 0.6, where basically only a proton background signal is expected. The electron signal is expected to show up at lower *Hadronness* values with only a very small admixture in the 0.2 - 0.6 *Hadronness* range.
For the background rejection I applied the following cuts: *Leakage* <0.2, *Island* <2, distance of the centroid of the image from the center of the camera <300 mm, for events with *Size* >100 phes. A *Leakage* cut is applied in order to remove showers

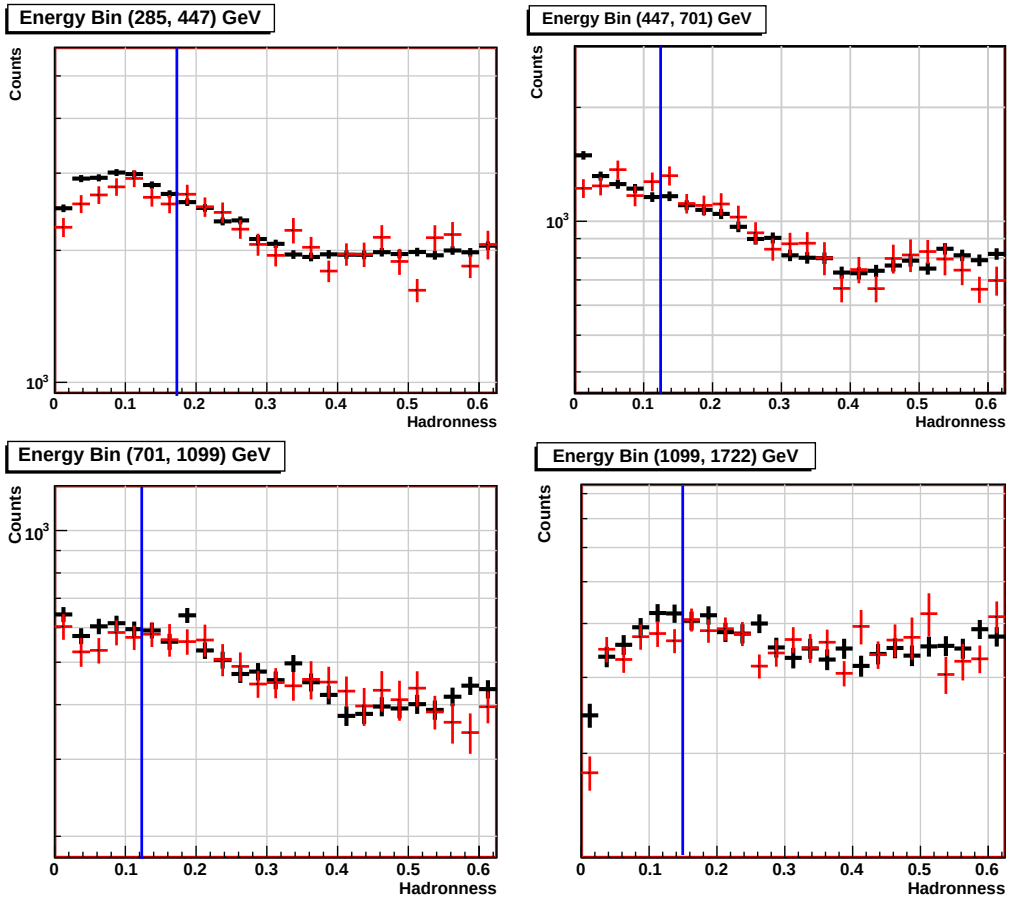

Fig. 6.1: Distributions of the *Hadronness* parameter for data in black and MC protons in red for the four energy bins that are used for the determination of the spectrum. The distributions are shown in the range between 0 and 0.6. The blue line determines the upper *Hadronness* cut values for the selected signal regions. One can see a small excess in every energy bin above the background.

with truncated images (i.e. a part of the image is outside the camera). These showers are in fact difficult to reconstruct, a stable *Hadronness* value cannot be calculated. Unlike for point sources, in the analysis of diffuse sources, applying a *Leakage* cut is of particular importance, because the images are spread over all the camera and many of them are truncated. The upper cut in *Hadronness* is chosen at a value for which 60% of MC electrons will survive. Figure 6.1 shows the electron excesses with a significance of $2\text{-}3\,\sigma$ in each energy bin. The details are listed in table 6.2.
Although the significance is not very high, a tentative spectrum can be determined.

6.1.3 Electron energy spectrum

The differential electron energy spectrum is shown in figure 6.2. The spectrum can be well fitted by a power law ansatz:

$$\frac{dF}{dE} = (1.03 \pm 0.36_{(stat)} \pm 0.31_{(syst)}) \times 10^{-7} \times \left(\frac{E}{1TeV}\right)^{-2.97\pm0.61} GeV^{-1}m^{-2}s^{-1}sr^{-1}$$

<E (GeV)>	N_{ON}	N_{bg}	N_{exc}/N_{bg}	Sigma	E^3dN/dE ($GeV^2m^{-2}s^{-1}sr^{-1}$)
353.7	13771±117	12769.5±444.5	8%	2.3	113.7±52.3
554.3	4417±66	4005.8±203.2	10%	2.0	84.1±43.8
868.8	2036±45	1733.2±102.5	17%	2.9	106.2±39.5
1361.6	1430±38	1262.7±70.4	13%	2.4	109.9±52.9

Table 6.2: This table list the stand-alone MAGIC-I telescope results. For each energy bin (where the mean energy value is listed) the number of ON and Background events, the excesses over the background, the significance of the excesses and the E^3dN/dE are given.

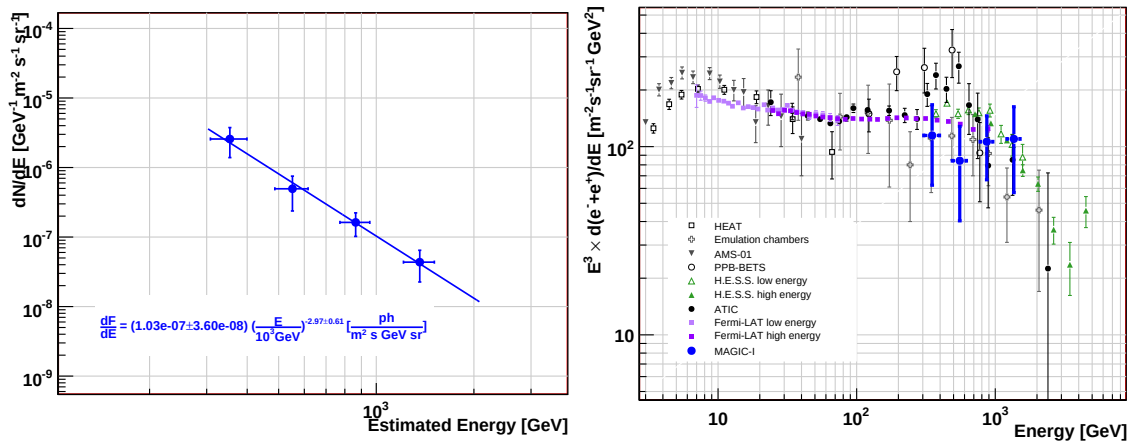

Fig. 6.2: On the left panel the electron spectrum from stand-alone MAGIC-I telescope analysis is shown. On the right one the spectrum multiplied by E^3, overlayed onto the measurements from other experiments, is shown.

in the energy range from 300 GeV to ∼1.5 TeV. The quoted systematic errors are calculated at the level of 30% on the flux normalization as estimated in section 4.4. Although the points in the spectrum are not of high significance, the electron flux is compatible with measurements of other instruments, as shown on the right plot of figure 6.2.
For any solid interpretation and conclusion, higher significance and better energy spectrum determination are needed. With a better sensitivity and higher background rejection, the analysis performed with the stereo system provides such an improvement.

6.2 The MAGIC stereo search for cosmic electrons

With the introduction of a second telescope, as described in chapter 5, the sensitivity of the MAGIC observatory is considerably improved.

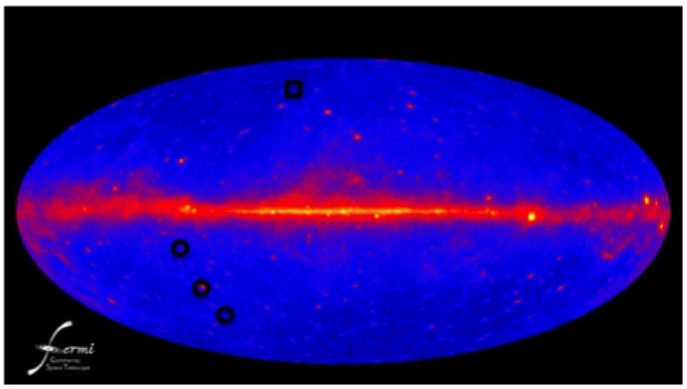

Fig. 6.3: Image of the sky seen by the Fermi satellite. The three black circles highlight the sky areas used for the cosmic electron searches with the MAGIC stereo analysis. The black rectangle highlights the sky area used for the stand-alone MAGIC-I analysis.

Below the analysis of some data taken during the first year of the stereo operation is presented.

6.2.1 Data sample and applied selection criteria

Data used for the stereo analysis are from the observation of three different regions in the sky, which are highlighted in the full-sky plot in figure 6.3 with the black circles. The observations were carried out in December 2009, June 2010, October 2010 and November 2010 (see table 6.3). The targets were observed at zenith angles from 14^o to more than 30^o , but the events have been selected from the zenith angle range between 14^o and 27^o, i.e. matching that of the simulations.
Quality selection cuts have been performed to reject days with bad weather. The following conditions have been applied: trigger rates within the range of $\pm\,15\%$ of the average, humidity below 60%, cloudiness below 40% and number of identified stars[1] above 30. After the selection ~ 14 hours of good data are have been analyzed.

6.2.2 Event reconstruction and excess determination

The events are cleaned using a threshold of 6 phes for core pixels and 3 phes for boundary pixels for the MAGIC-I telescope data. For the MAGIC-II telescope data the following cleaning levels have been used: a threshold of 9 phes for core pixels and 4.5 phes for boundary pixels. Higher cleaning for the MAGIC-II telescope data is needed because of a higher photon to phe efficiency and a higher noise level in the read-out chain compared to MAGIC-I read-out. A priory, a search for a gamma-point source has been carried out to verify that no gammas contaminated the sample. It should also be noted that no gamma-rays are expected from 3C454 above a *Size* 100 phes because the high redshift and the suppression of higher energy gamma rays due to interaction with the cosmic low energy photon fields (The so-called extragalactic background light).

[1] An optical picture of the observed region in the sky is taken with a CCD camera. The number of visible stars is compared with the number of known stars in that region.

Target	RA	DEC	redshift
3c454.3	22h 50m 34.7s	+18d 48' 40"	0.859
BLLac	22h 02m 43.3s	+42d 16' 40"	0.0686
1FGLJ2347.3+0710	23h 47m 19.7s	+07d 10' 26"	unknown
	Date	Events (k)	obs. time (min)
3c454.3	2009-12-06	457	55
3c454.3	2009-12-08	245	30
3c454.3	2009-12-10	280	36
3c454.3	2009-12-11	231	30
BLLac	2010-06-15	300	46
BLLac	2010-06-17	310	45
1FGLJ2347.3+0710	2010-10-06	441	56
1FGLJ2347.3+0710	2010-10-10	854	110
1FGLJ2347.3+0710	2010-10-11	870	112
1FGLJ2347.3+0710	2010-10-13	944	116
1FGLJ2347.3+0710	2010-11-01	600	79
1FGLJ2347.3+0710	2010-11-04	370	61
1FGLJ2347.3+0710	2010-11-25	467	62
	Total	6372	838

Table 6.3: The table lists the observation details of the data sample used for the stereo analysis of electrons.

Electron/hadron separation is trained in RF by using MC electrons and a sample of MC protons. At the time in which the stereo analysis was performed, more MC protons became available with respect to the time in which the MAGIC-I analysis was performed. They could, therefore, be used as a training sample. This ensures absence of contamination of electromagnetic showers in the hadron sample compared to the usage of observed data sample.
A part of the background is rejected by the following cuts: $Leakage$ <0.2, $Island$ <2 and 10 m< $Impact$ <300 m for both telescopes, for MAGIC-I $Size$ >100 phes and MAGIC-II $Size$ >200 phes. The decision for the $Impact$ cut is motivated by the need to keep the best reconstructed electron events, which are contained in the Cherenkov pool. Figure 6.4 shows that most of the detected events are contained in a radius of ∼300 m, with a peak of the distribution at ∼130 m. A higher $Size$ cut applied to the events recorded with MAGIC-II telescope is also motivated by a mis-match of the $Width$ between data and MC protons, as shown in figure 4.20 and discussed there.

The total $Hadronness$ distribution of the observed events is plotted together with the normalized distribution of background events in figure 6.5. The normalization is done in the $Hadronness$ range between 0.4 and 0.8. In total, 5383 electron excess events are seen with a significance of 8.08 σ in the energy range between 150 GeV and 2 TeV. Definition of the signal region, by means of a cut in the $Hadronness$ parameter, is chosen by requiring an acceptance for MC electrons of 60%. In figure 6.6, the $Hadronness$

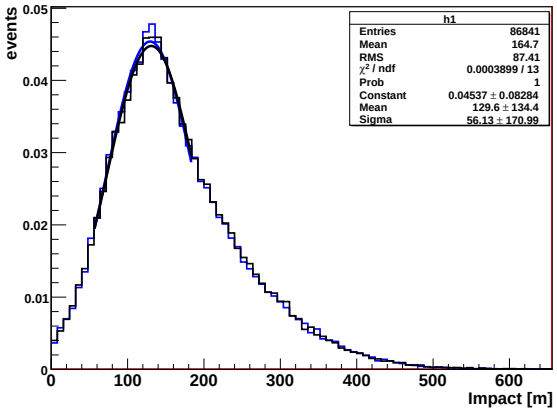

Fig. 6.4: Distribution of the Impact parameter for the MAGIC-I data in blue and the MAGIC-II data in black.

distributions for different energy ranges are shown, and the details of the analysis are summarized in table 6.4. For each energy bin the number of ON and Background events are given, as well as the number of excess events over the background, the number of excess events over the total number of particles and the significance of the excess. For consistency, a comparison of excess events with MC electron events is given in figure 6.7, where the *Hadronness* distribution is plotted for different energy bins, for *Hadronness* values smaller than 0.5. The distributions are normalized by the number of excess events in each energy bin. One can notice that the distributions of the excess is well in agreement within errors with the distributions of the MC electrons. A statistical test of compatibility in shape between the two distributions is done using the Kolmogorov test. A probability that the excess events follow the distribution of the MC electrons is found to be more than 70% in each energy bin.
The spectrum is derived from the excess events measured with the MAGIC stereo system.

6.2.3 Electron energy spectrum

The obtained differential energy spectrum is unfolded using three different methods (Bertero, Tikhonov and Schmelling, see section 4.2.8), and is shown in figure 6.8. The spectrum spans from $\sim 100\,\mathrm{GeV}$ to $\sim 2\,\mathrm{TeV}$ and is fitted by a power law which gives the following results for the three different methods:

$$\left(\frac{dF}{dE}\right)_{Bertero} = (1.47\pm0.21_{(stat)}\pm0.44_{(syst)})\times10^{-7}\times\left(\frac{E}{1TeV}\right)^{-3.00\pm0.12} GeV^{-1}m^{-2}s^{-1}sr^{-1}$$

$$\left(\frac{dF}{dE}\right)_{Tikhonov} = (1.44\pm0.22_{(stat)}\pm0.43_{(syst)})\times10^{-7}\times\left(\frac{E}{1TeV}\right)^{-3.12\pm0.12} GeV^{-1}m^{-2}s^{-1}sr^{-1}$$

$$\left(\frac{dF}{dE}\right)_{Schmelling} = (1.25\pm0.20_{(stat)}\pm0.37_{(syst)})\times10^{-7}\times\left(\frac{E}{1TeV}\right)^{-3.25\pm0.12} GeV^{-1}m^{-2}s^{-1}sr^{-1}$$

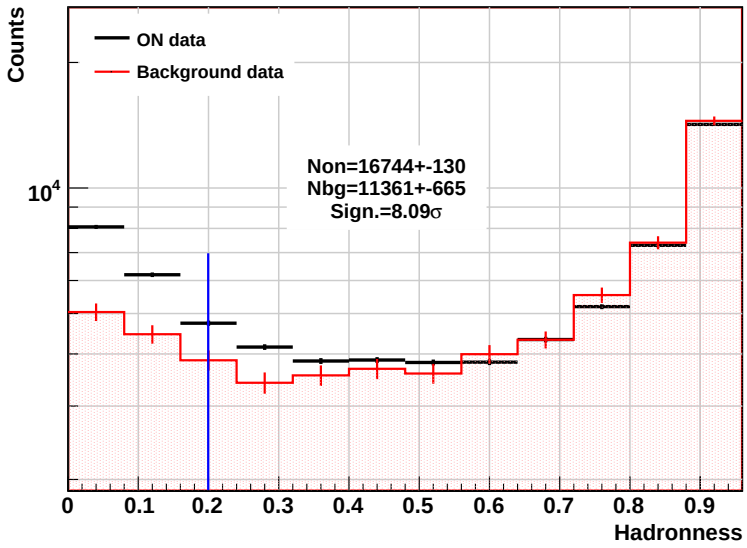

Fig. 6.5: Total Hadronness distributions of the ON events (in black) and background events (in red) for energy between 150 GeV and 2 TeV.

<E (GeV)>	N_{ON}	N_{bg}	N_{exc}/N_{bg}	$N_{exc}/N_{ON_{tot}}$	Sigma
205.5	10460±102	7712.3±457.4	36%	5.0%	6.0
325.5	7452±86	4915.8±333.8	50%	6.0%	7.6
515.5	4243±65	2875.1±229.1	47%	4.5%	5.9
817.5	2142±46	1531.1±141.9	40%	2.5%	4.3
1296.0	1146±34	756.2±88.2	50%	2.0%	4.4
2054.5	704±26	603.4±69.0	16%	0.75%	1.5

Table 6.4: This table lists the stereo analysis results. For each energy bin (where the mean energy is shown) the number of ON and Background events are given, also the excesses over the background, the number of excess events over the total number of measured particles ($N_{ON_{tot}}$) and the significance of the excesses are given.

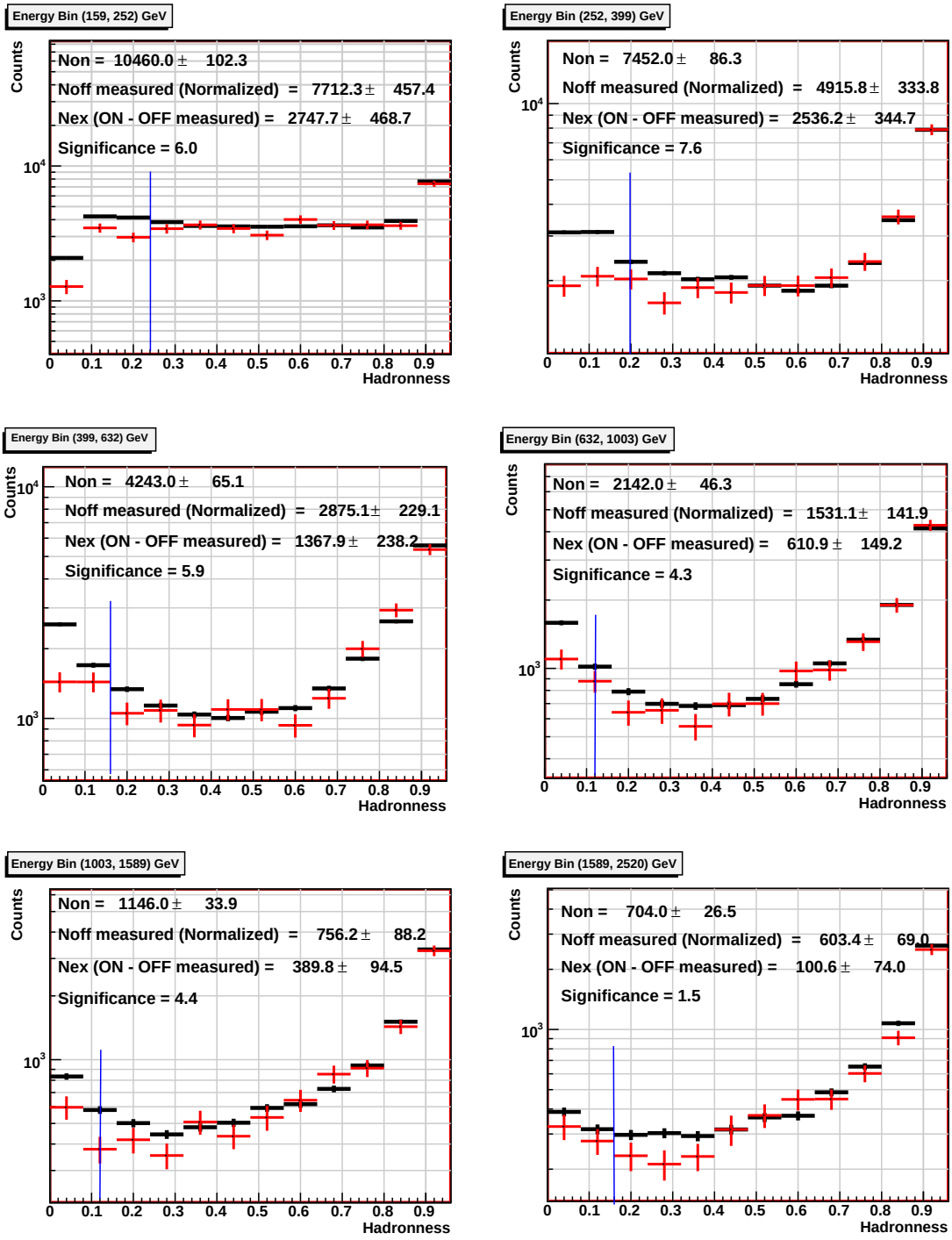

Fig. 6.6: Hadronness distributions in six consecutive energy bins of ON events (in black) and for simulated proton background events (in red). Cut in *Hadronness* are applied in order to keep 60% of the electron events in each energy bin

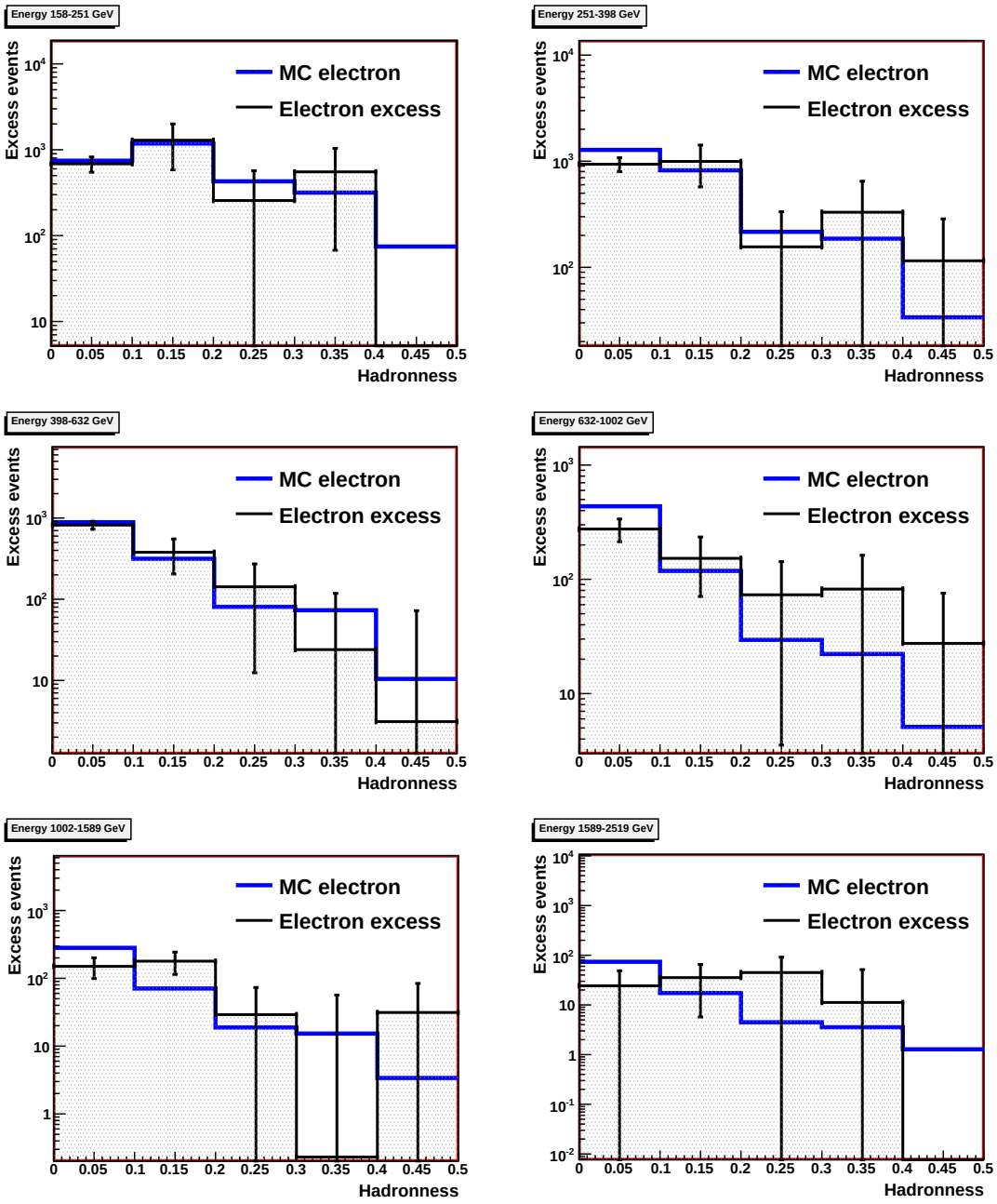

Fig. 6.7: Hadronness distributions in energy bins of the excess events (in black) compared with MC simulated electron events (in blue). The distributions are normalized by the number of excess events.

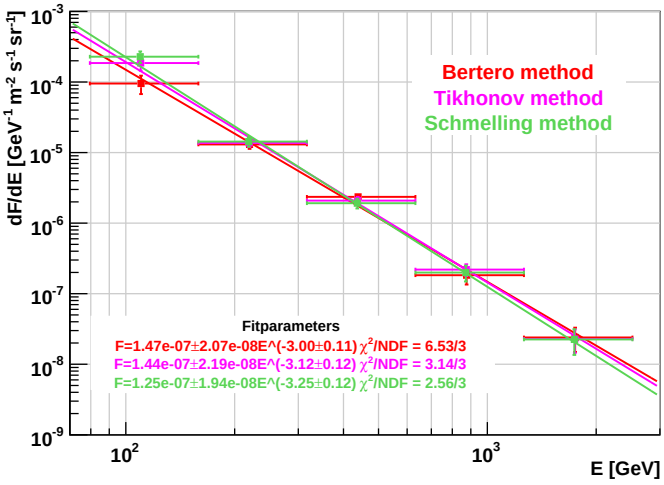

Fig. 6.8: Electron spectrum from the MAGIC stereo analysis using three different unfolding methods: Bertero (in red), Tikhonov (in pink) and Schmelling (in green). The horizontal bars are reflecting the energy bin width.

The three methods agree very well for energies above $\sim 200\,\mathrm{GeV}$. At around 100 GeV the calculated flux varies considerably depending on the method. The large uncertainties on the first point in the spectrum are related to the fact that the detection efficiency at low energy is low and the migration of the events from higher energy to lower energy in the unfolding procedure contains large uncertainties. Therefore different unfolding algorithms result in different spectra.
I decided to use the Bertero method as final unfolding procedure because of its stability and robustness. Also, it is widely used in the MAGIC collaboration.
In figure 6.9 the MAGIC electron spectrum is compared with the measurements from other experiments. It is shown in the form of $E^3 \frac{dF}{dE}$. The MAGIC spectrum shows some overlap with the direct measurements of ATIC, Fermi PPB-BETS and emulsion chambers and it is in agreement within errors with both the ATIC and Fermi measurements. At higher energies the MAGIC spectrum overlaps with the measurements of H.E.S.S. and, inspite of large uncertainties, they are well in agreement.

Systematic uncertainties

The electron energy spectrum determined in this work suffers from large systematic uncertainties. In section 4.4 a list of possible systematic errors is given. It is important to underline that the analysis of diffuse sources strongly depends on the MC simulations that reproduce the background. Thus, compared to the standard analysis of point sources, larger systematic errors are induced by the simulation uncertainties. In particular the lack of simulations of heavier chemical elements leads to a $\sim 5\%$ error on the computation of the spectrum, as discussed in section 4.3. On the top of that the hadronic interaction model used in the simulations increase the uncertainties of about 25 - 30%. Therefore, the systematic errors on the flux normalization are esti-

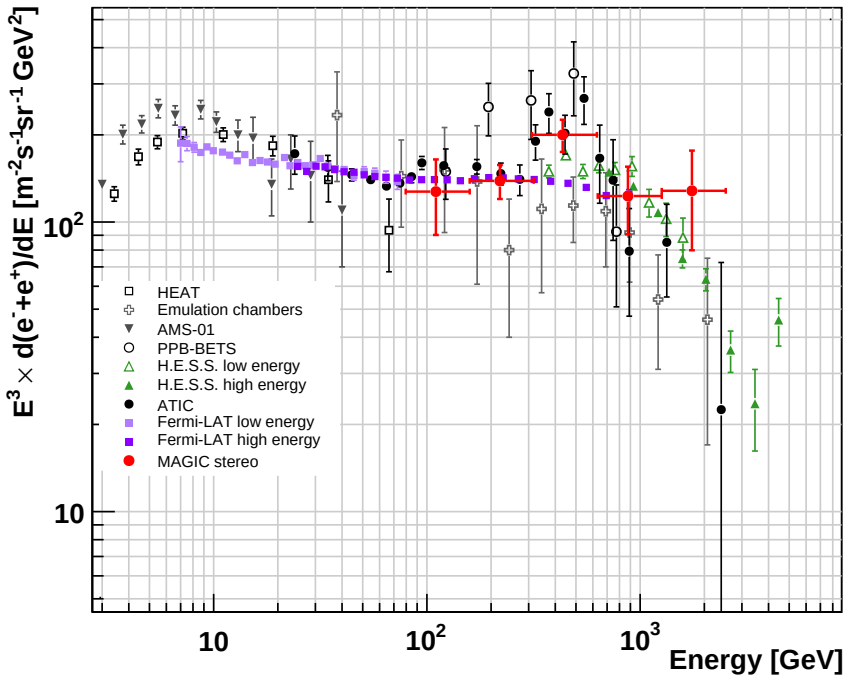

Fig. 6.9: The electron energy spectrum, measured with the MAGIC stereo system, multiplied by E^3 is shown including the measurements from other experiments.

mated to be at the level of 30% as estimated in section 4.4. The systematic errors on the spectral slope are more difficult to estimate, since they need large MC samples with different parameter settings. A minimum value expected is ± 0.15, the same as for γ-ray sources. In addition, a partial estimation is given comparing results from different unfolding methods, which produce a spread in the spectral index of ± 0.125. The total systematic uncertainties on the spectral index are still under study and could not be complitely established for this thesis.

Interpretation of the cosmic electron energy spectrum

Despite the fact that the MAGIC points can be well fitted by a single power-law function, the trend of the spectrum may give a hint for a possible excess between ~ 300 and ~ 600 GeV, which is higher than that measured by Fermi. This could confirm the peak measured by ATIC, but in fact this feature is not significant and can just be due to statistical fluctuation.
Nevertheless, the MAGIC cosmic electron spectrum shows an excess compared to the conventional background propagation that can be explained in terms of acceleration of particles in some nearby sources. For example this can be seen in figure 6.10, where a calculation of the contribution of sources (such as pulsars), with distances closer than 1 kpc and older than 10^5 y, is added to the galactic electron background component [7]. Given the large uncertainties in the total flux due to systematic errors, the MAGIC

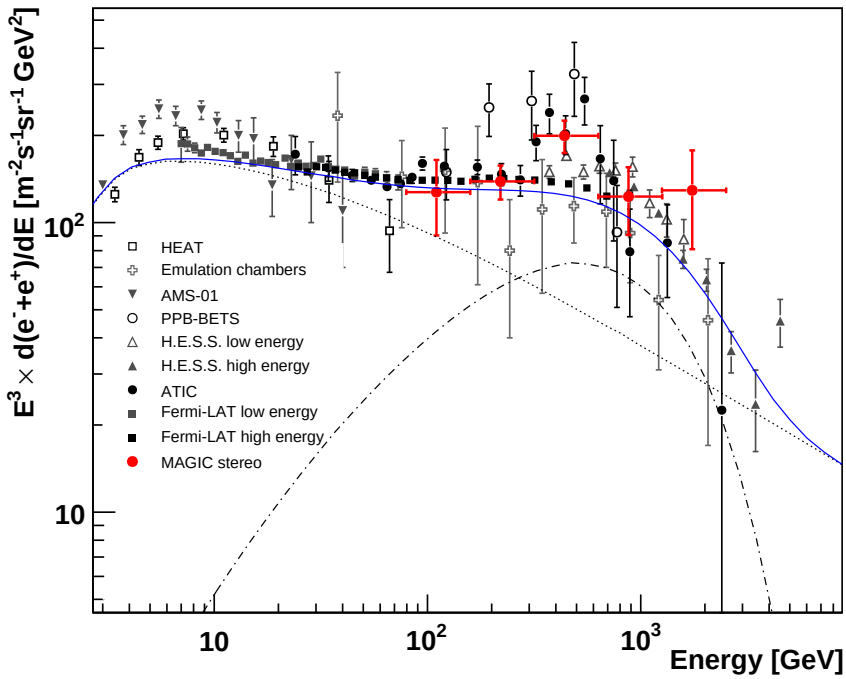

Fig. 6.10: Electron spectrum ($E^3(\frac{dF}{dE})$) measured with the MAGIC stereo system (red points) compared to the conventional GALPROP model [129]. The galactic electron background component is shown by the black-dotted line; An extra component with injection index $\Gamma = 1.5$ and exponential cut-off is shown by the dashed line; the contribution of both background component and extra component is shown by the blue line [7].

cosmic electron spectrum is in agreement with this model.
At the same time, other interpretations can not be ruled out, as for example models suggesting the reacceleration of secondary electrons in SNR (discussed in section 1.3.2), or interpretations invoking contributions from dark matter particles (discussed in section 1.3.4).

Possible other contributions to the cosmic electron flux

In the cosmic electron flux measured with MAGIC, contributions from CRs and γ-rays may also introduce errors. In fact, the analysis method used is not able to perfectly describe the *Hadronness* distribution of the background and thus to reject 100% of the background. Possible other contributions to the electron flux are listed below:

- Signal from hadron electromagnetic sub-showers, mainly due to π^0. Early in the development of the shower, a large fraction of energy might be transferred to a single π^0. The energetic π^0 decays into two gammas, which generate an unresolved electromagnetic shower. The only way to discriminate these showers is using a cut in the number of *Islands*, in order to reject multiple showers.

- Signal from diffuse extragalactic γ-rays. While a contribution from the diffuse galactic γ-rays is excluded, because the observed target are far from the galactic plane, an extragalactic γ-ray contribution cannot be excluded.
  As already discussed in section 1.3.1, in the TeV energy region no measurements of extragalactic γ-rays are available. However, extrapolations based on the Fermi measurements [6],[93], show a drop in the γ-ray flux due to absorption processes. Therefore, the contribution from the extragalactic γ-rays in the energy range between 100 GeV and few TeV is negligible.

6.3 Challenges and difficulties

This study of cosmic electrons has been challenging in many aspects and had to fight with some difficulties. Some of the problems are listed below.

- In the first year of the stereo operation, a large fraction of the observation time has been dedicated to the search for strong γ-ray sources to perform several technical tests and to confirm the results achieved with the MAGIC-I telescope. It was difficult to find enough good target candidates for the cosmic electrons study. In addition the requirement of a small zenith angle range simulated in the MCs limited the amount of useful data.

- In the Digital Ring Sampler (DRS-2) based readout of MAGIC-II, a crosstalk between channels was identified, leading to a widening of, for example, the $Width$ of the images and causing a mis-match between the simulations and the data. Thus, a correction had to be applied in the data.

- The electronic noise level of the DAQ of the second telescope appeared to be higher than the one of MAGIC-I DAQ. Thus, a higher cleaning level for MAGIC-II was required in order to provide high quality data.

- More recently, some non-linearity problems have been found in the electronic chain. This problem is still under investigation and it is not yet clear how it influences the results.

All these difficulties made the study of the cosmic electrons even more challenging. Therefore, in the near future, more precise results can be expected.

Tausend Pfade giebt es, die nie noch gegangen sind; tausend Gesundheiten und verborgene Eilande des Lebens.
Unerschöpflich und unentdeckt ist immer noch Mensch und Menschen-Erde.

Also sprach Zarathustra – Friedrich Wilhelm Nietzsche

7 Conclusions and Outlook

In this thesis I presented the work done during my PhD studies. During the first year I was responsible for the evaluation, selection and characterization of the photosensors of the MAGIC-II camera. The PMTs with the highest quantum efficiency with low gain (gain $< 3.8{\cdot}10^4$ at 850 V) have been selected to be installed in the trigger region. The remaining ones were installed in the outer part of the camera. The performance of all the pixels[1] has been investigated: a procedure of flatfielding sets all the pixels for the same input light to the same output charge; after that, the time response, linearity and resolution of single photoelectron have been studied.
The whole camera was then installed in La Palma in the summer of 2008. After the installation I was involved in the commissioning of the telescope.
Since the introduction of the MAGIC-II telescope, MAGIC became a system operating in stereoscopic mode. The stereo system improves the sensitivity, which is particularly important for the detection of faint γ-ray sources or of the low cosmic electron flux. Indeed, the main part of my PhD studies was devoted to the analysis of the spectrum of cosmic electrons and positrons, as observed with the MAGIC telescopes. This study was motivated by the interest of investigating unexpected features in the cosmic electron spectrum measured above 100 GeV by some experiments. These features could point out to the presence of possible, still unknown sources of cosmic electrons. A 'hump' in the electron spectrum between 300 and 800 GeV found by ATIC (see fig. 7.1) was not confirmed by Fermi. This created a controversial situation which was very appealing and therefore I decided to investigate it.
Since this study was being performed for the first time within the MAGIC experiment, I had to develop new analysis tools to detect leptonic signal from diffuse sources and to determine its energy spectrum. The method is based on the identification of electrons via the shape of the air shower (without any arrival direction information) recorded by the telescopes. The electron signal has to be extracted from the overwhelming

[1] A pixel includes a PMT, a socket with an HV generator, a preamplifier, a coaxial cable for test pulse and a VCSEL

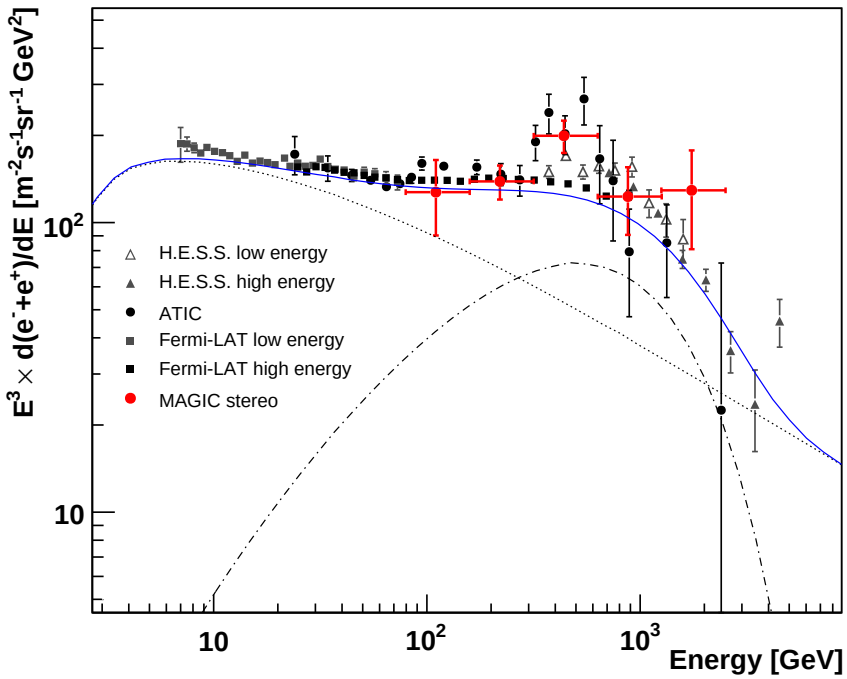

Fig. 7.1: The spectrum of cosmic electrons from MAGIC (red points), Fermi [7], H.E.S.S. [14], [13] and ATIC [49]. The conventional GALPROP [129] model for the galactic electron background component is shown by the black-dotted line; An extra component with injection index $\Gamma = 1.5$ and exponential cut-off is shown by the dashed line; the contribution of both background components and the extra component is shown by the blue line [7].

background of hadronic cosmic rays, which has to be estimated by MC simulations. The method has been verified to work by obtaining the expected spectra, when applied to data from the Crab Nebula, but ignoring the point source constraint used in the classical analysis. The results are in good agreement with the standard point source analysis method. Performance studies were carried out both with data recorded with the stand-alone MAGIC-I telescope and with the stereo system, using a sample of Crab Nebula data. A considerable improvement in sensitivity, angular resolution and energy resolution is achieved by the stereo observations.
The main challenge of this study is the subtraction of the background estimated by MC proton simulations, which are very time consuming. Due to limited MC statistics, the statistical errors on the electron spectrum are quite large. Also part of the systematic uncertainties are due to simulations, because of the poor knowledge of the cross-section of the hadronic interaction at TeV energies. Additional uncertainties are due to changes in the atmospheric conditions and due to the calibration accuracy of the instrument.

The cosmic electrons were studied both with the MAGIC-I telescope and the MAGIC stereo system. The cosmic electron spectrum measured with the MAGIC stereo system is derived in the energy range from $\sim 100\,\mathrm{GeV}$ to $\sim 2\,\mathrm{TeV}$ (shown in fig. 7.1). The

spectrum follows a power-law:

$$\frac{dF}{dE} = (1.47 \pm 0.21_{(stat)} \pm 0.44_{(syst)}) \cdot 10^{-7} \times \left(\frac{E}{1TeV}\right)^{-3.00\pm0.12_{(stat)}} GeV^{-1}m^{-2}s^{-1}sr^{-1}$$

with 30% of systematic errors on the flux normalization and a minimum systematic spread of ± 0.15 in the spectral index, extrapolated from γ-ray point source analysis. Since MAGIC can not distinguish particle charges, the measured electron flux contains both species (electrons and positrons).
At around 200 GeV the current study revealed a fraction of cosmic electrons of 5% of the total CR flux triggered by MAGIC. It is important to remark that a substantial part of the hadronic cosmic rays is rejected on hardware level by the trigger. At around 2 TeV the fraction of cosmic electrons decreases instead to 0.75%.
The spectrum agrees well with the indirect measurements from H.E.S.S. ([14], [13]). The lower energy threshold of MAGIC allows us to measure the spectrum down to 100 GeV, as opposed to 300 GeV of H.E.S.S. The measurement also agrees with those by Fermi and ATIC, as can be seen in figure 7.1. The feature of the electron spectrum measured by ATIC ([49]) between 300 GeV and 800 GeV can neither be confirmed nor excluded by MAGIC, due to large uncertainties.
Considering that very high energy electrons lose energy via synchrotron radiation and inverse Compton scattering, the measurement of the cosmic electron spectrum with MAGIC suggests the presence of local (d$<$ 1 kpc) cosmic electron accelerators. Models, presented in [7], which consider contributions from pulsar sources, seem to fit quite well the observations, as shown in figure 7.1. At the same time, interpretations in terms of contributions from nearby and recent SNRs or models invoking contributions from dark matter particles can not be ruled out.

In the near future many improvements are foreseen in the cosmic electron study that will help to increase statistics in the flux measurements and in a better understanding of the cosmic electron origin and propagation. Below some prospects are given:

- Larger MC and data statistics will reduce the statistical errors on the spectrum measured by MAGIC. Consequently, stronger grounds on astrophysical sources or dark matter theories will be given. In addition, in the context of indirect DM searches it would be interesting to interpret new data in light of the results from LHC or direct-detection experiments.

- Future IACT experiments, such as CTA, with larger effective area, larger FoV and better sensitivity, will be able to resolve features in the cosmic electron spectrum.

- Separating positrons and electrons would be of particular interest and would provide strong grounds to any interpretation attempt. A project called "Moon shadow" [54], in which I am also involved, is currently ongoing: the geomagnetic field deflects in opposite directions particle with opposite charges; with the shield of the Moon, MAGIC is then able to separate the particle charges. MAGIC is

particularly suited to observe in the vicinity of the Moon thanks to operation of its PMTs under low-gain. Such observations started recently and we expect first results soon.

In addition, the analysis technique developed for this study are applicable also to the study of extended γ-ray sources, or even completely diffuse γ-rays. The diffuse galactic γ-ray background can be studied by performing scans across the galactic plane. In this case its background, made of CR, electrons and diffuse extragalactic γ-rays, can be estimated directly from the extragalactic observations.

A
Supplementary figures

In this appendix the parameters which are used in training the RF and in the analysis are compared for MC and real data.
In figures A.1, A.2, A.3, A.4, A.5, A.6, A.7 the comparison of the parameters $Width$, $Length$, $Impact$ and $Height$ for different $Size$ bins are shown respectively for MC pointlike gamma and data from the Crab Nebula. The following cuts are applied: $zenith$ <30^o, $Leakage$ <0.2, $Island$ <2, $Hadronness$ <0.2 and θ^2 <0.02 deg^2.
The distributions of the MC gamma in blue and the distributions of the real data in black are normalized to the number of events. Within the errors, the distributions obtained from the real events match reasonably the ones from the simulations. At $Size$ below 200 phes, in the distribution of the $Height$, the mismatch between real data and gamma simulations, clearly seen at ∼4 km, is due to the muon events fraction present in the real data. In fact at low $Size$ the γ/hadron separation is poor and a large contribution from the hadron products is expected.

In figure A.8 the distribution of the $Height$ of MC electrons is compared with the one of MC diffuse gammas in four $Size$ bins. The following cuts are applied: $zenith$ <30^o, $Leakage$ <0.2, $Island$ <2. As already mentioned in this thesis, electrons interact higher in atmosphere than gammas. This is particularly visible at low energies. In general the resolution of MAGIC is poor to be able to discern electron from gamma from the $Height$ of the shower maximum. The $Height$ parameter is, instead, more powerful to distinguish electromagnetic showers from hadronic one. In figure A.9 in fact, for the same cuts, the $Height$ distribution is compared for MC electrons, MC protons, MC helium and real hadronic data.

In figure A.10 the $Conc1$, $Leakage$, $Impact$ and $RMSTime$ parameters are shown as a function of $Size$ both for MAGIC-I and MAGIC-II. The black points represent real hadronic data, the red ones the MC proton, the blue ones the MC electrons and the green ones the MC helium.

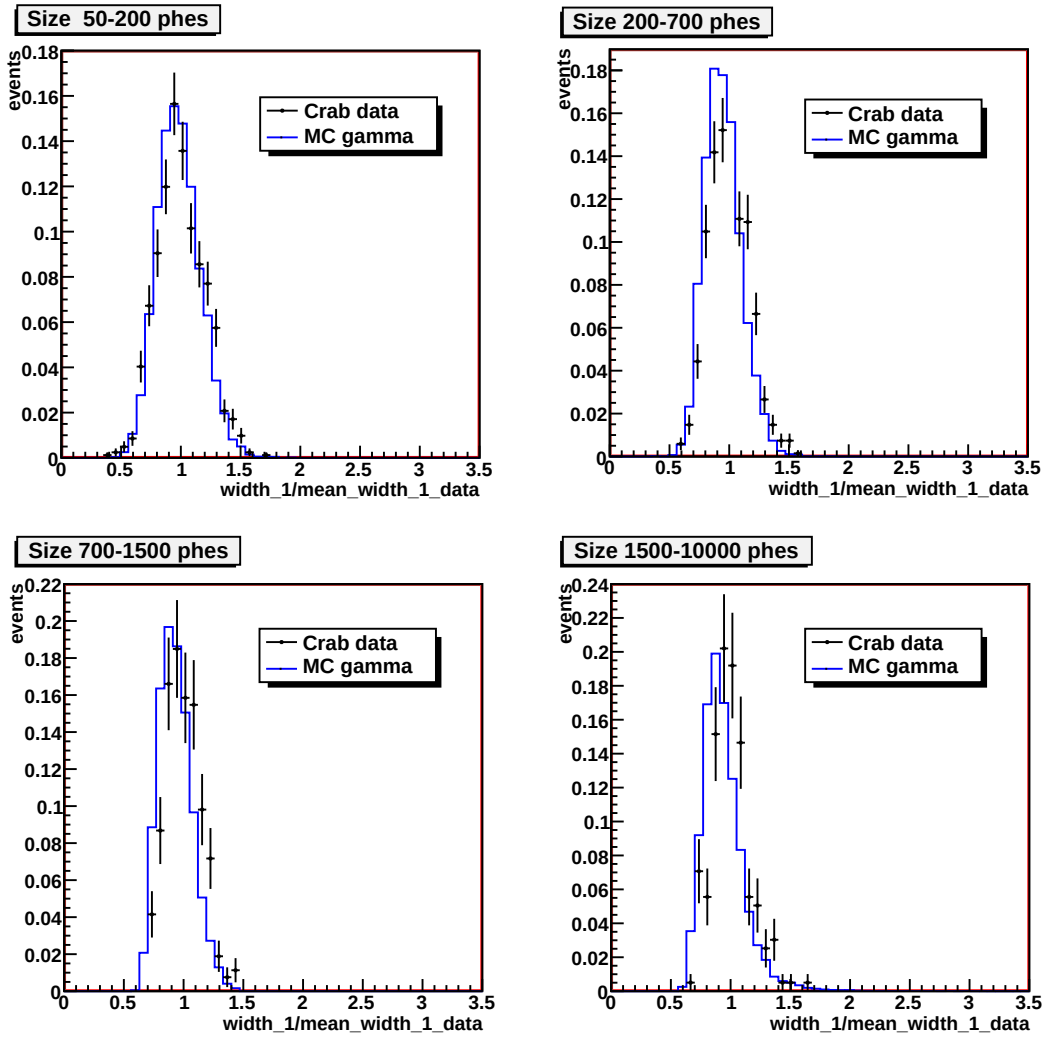

Fig. A.1: *Width* distributions (expressed as the *Width* divided by the mean *Width* of the data) of MAGIC-I images in different *Size* bins. Black: Crab data; blue: MC gammas.

In figures A.11, A.12, A.13, A.14, A.15 and A.16 the agreement between real data and MC protons and helium is shown in the *Width*, *Length* and *Impact* parameter distributions in *Size* bins, for both the telescopes.

In fig.A.17 the *Hadronness* distributions for different image cleaning is shown for a set of MC protons. This to show that in this analysis using different cleaning than the standard one (which is 6-3 for MAGIC-I and 9-4.5 for MAGIC-II) would not affect the electron/hadron separation and the background suppression.

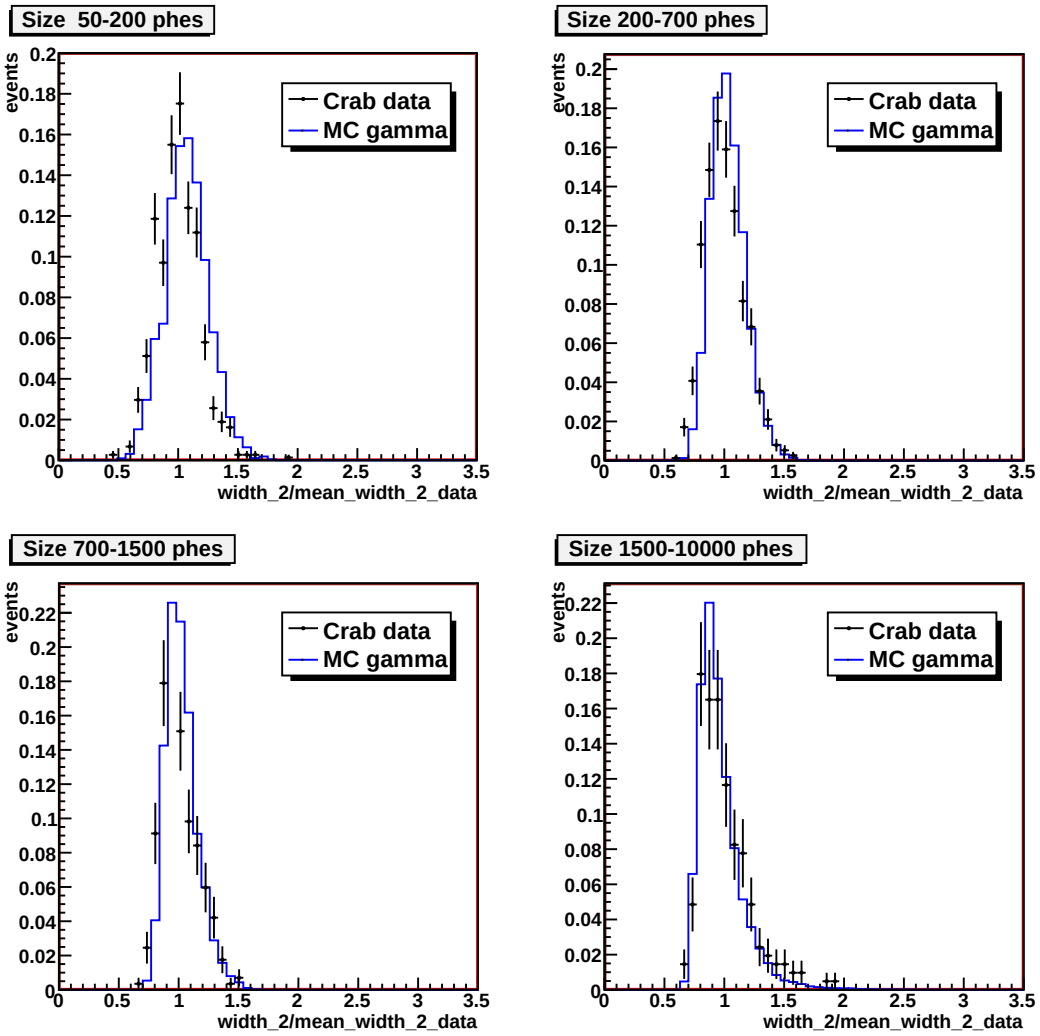

Fig. A.2: *Width* (expressed as the *Width* divided by the mean *Width* of the data) distributions of MAGIC-II images in different *Size* bins. Black: Crab data; blue: MC gammas.

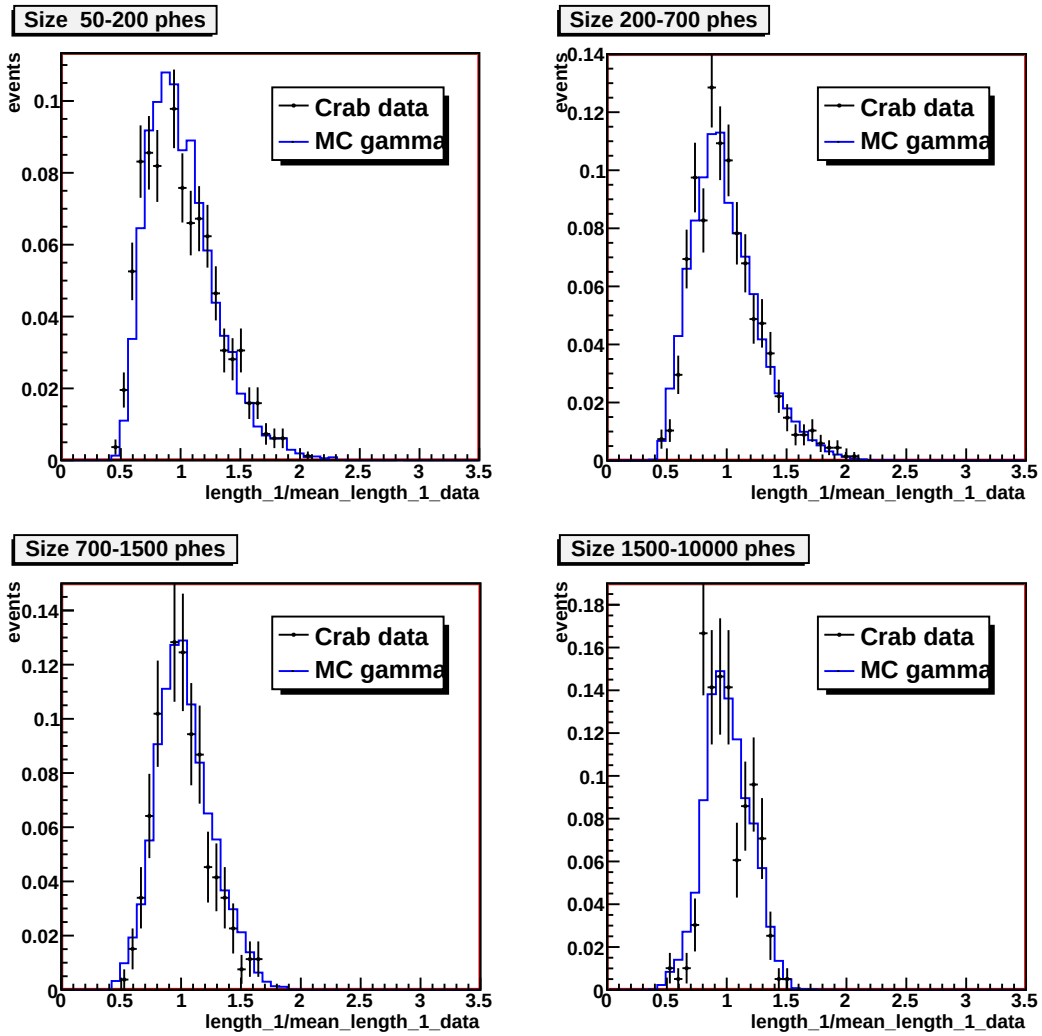

Fig. A.3: *Length* (expressed as the *Length* divided by the mean *Length* of the data) distributions of MAGIC-I images in different *size* bins. Black: Crab data; blue: MC gammas.

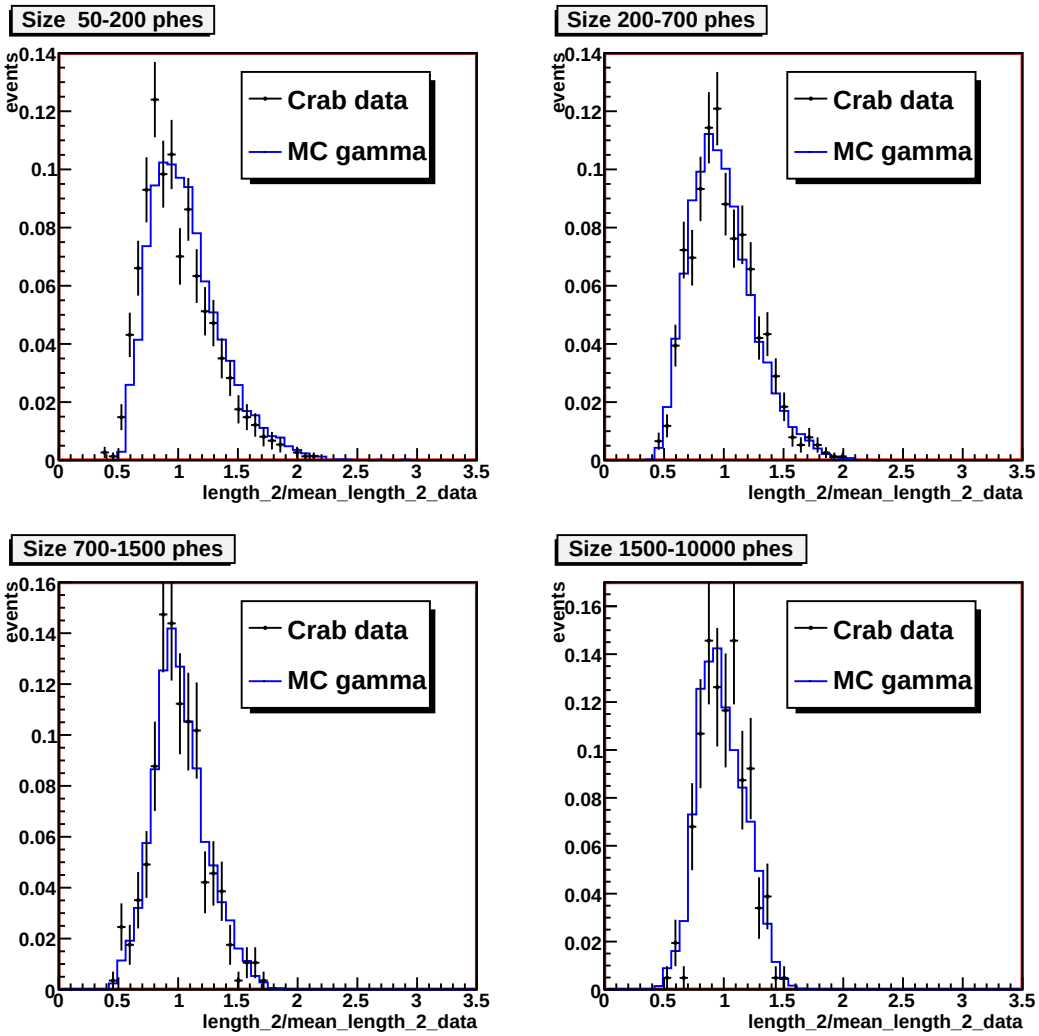

Fig. A.4: *Length* (expressed as the *Length* divided by the mean *Length* of the data) distributions of MAGIC-II images in different *size* bins. Black: Crab data; blue: MC gammas.

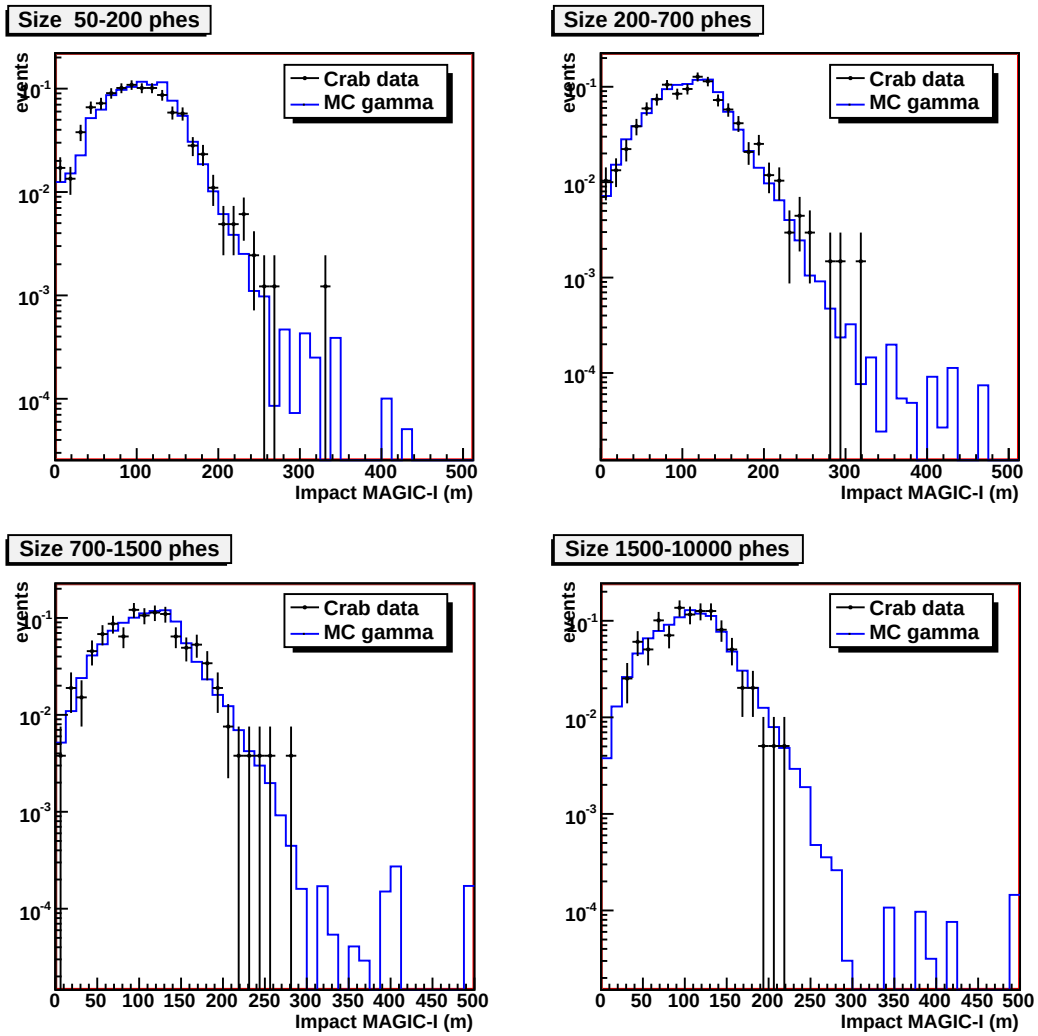

Fig. A.5: *Impact* distributions of MAGIC-I images in different *size* bins. Black: Crab data; blue: MC gammas.

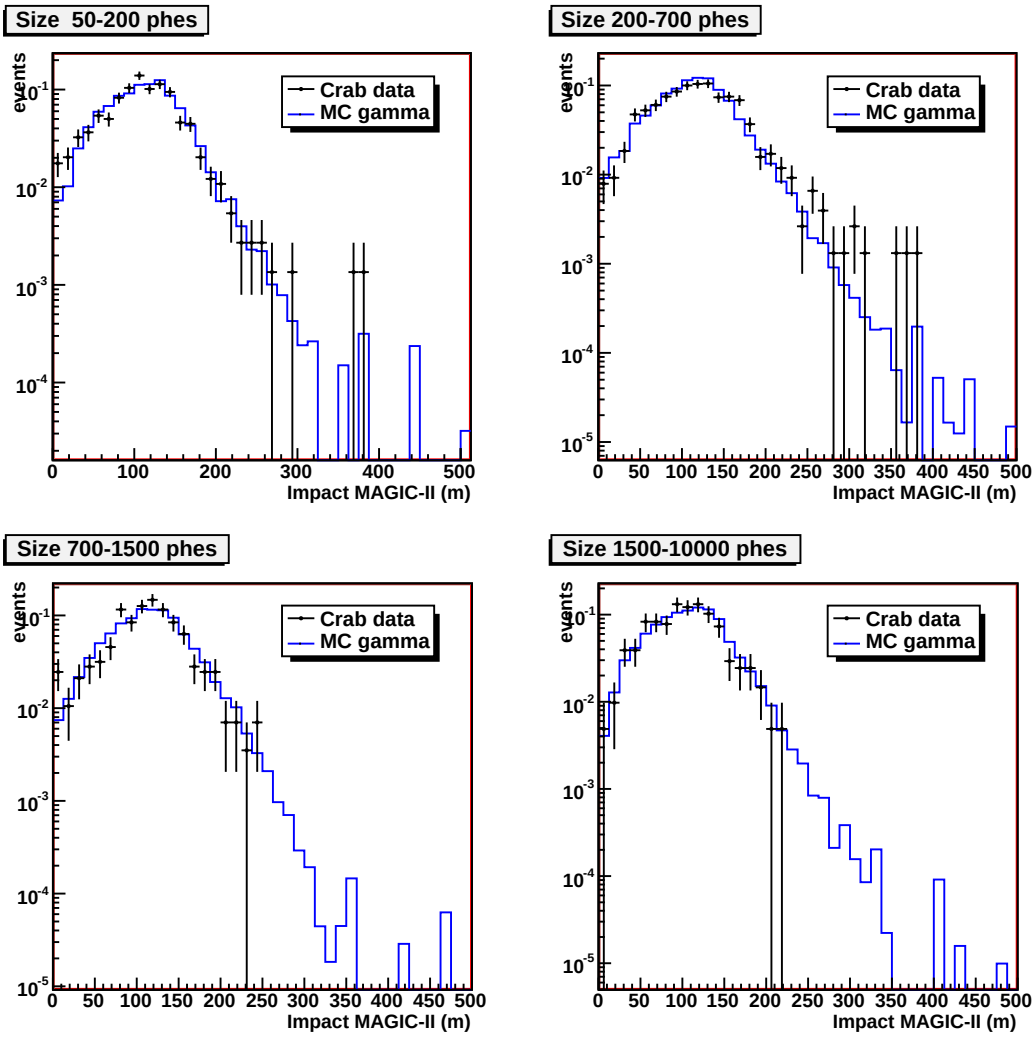

Fig. A.6: *Impact* distributions of MAGIC-II images in different *size* bins. Black: Crab data; blue: MC gammas.

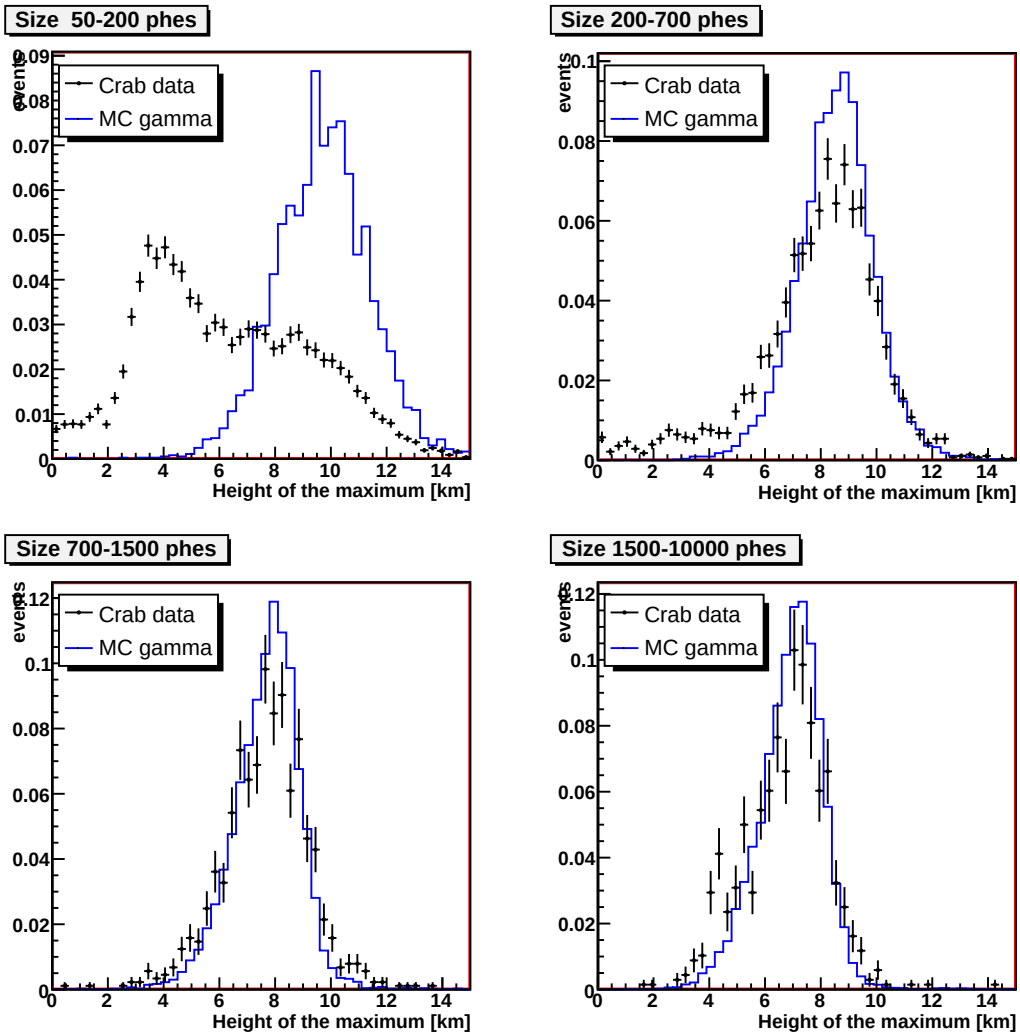

Fig. A.7: Distributions of the *height* of the shower maximum in *size* bins. Black: Crab data; blue: MC gammas. At low *size* mainly muons are effecting the data

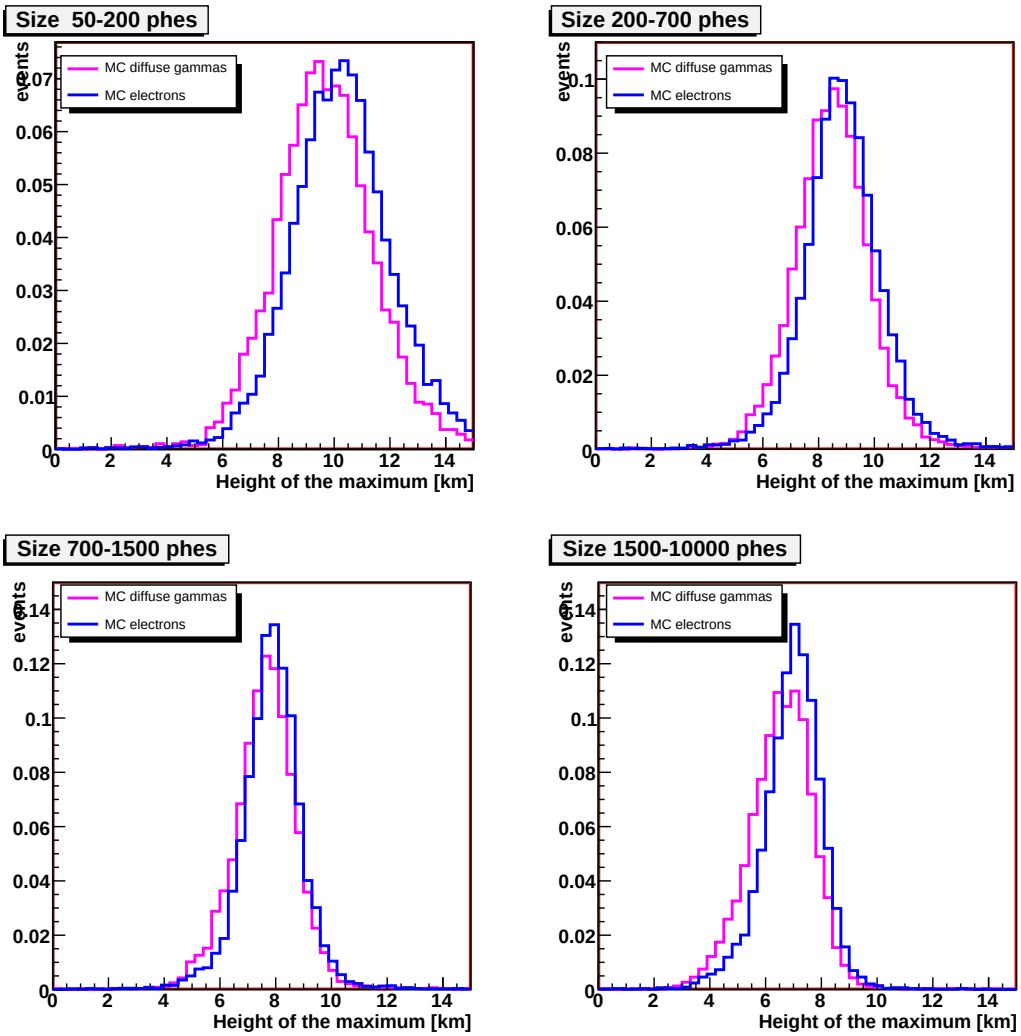

Fig. A.8: Distributions of the *Height* of the shower maximum in *size* bins. Blue: MC electrons; pink: MC diffuse gammas.

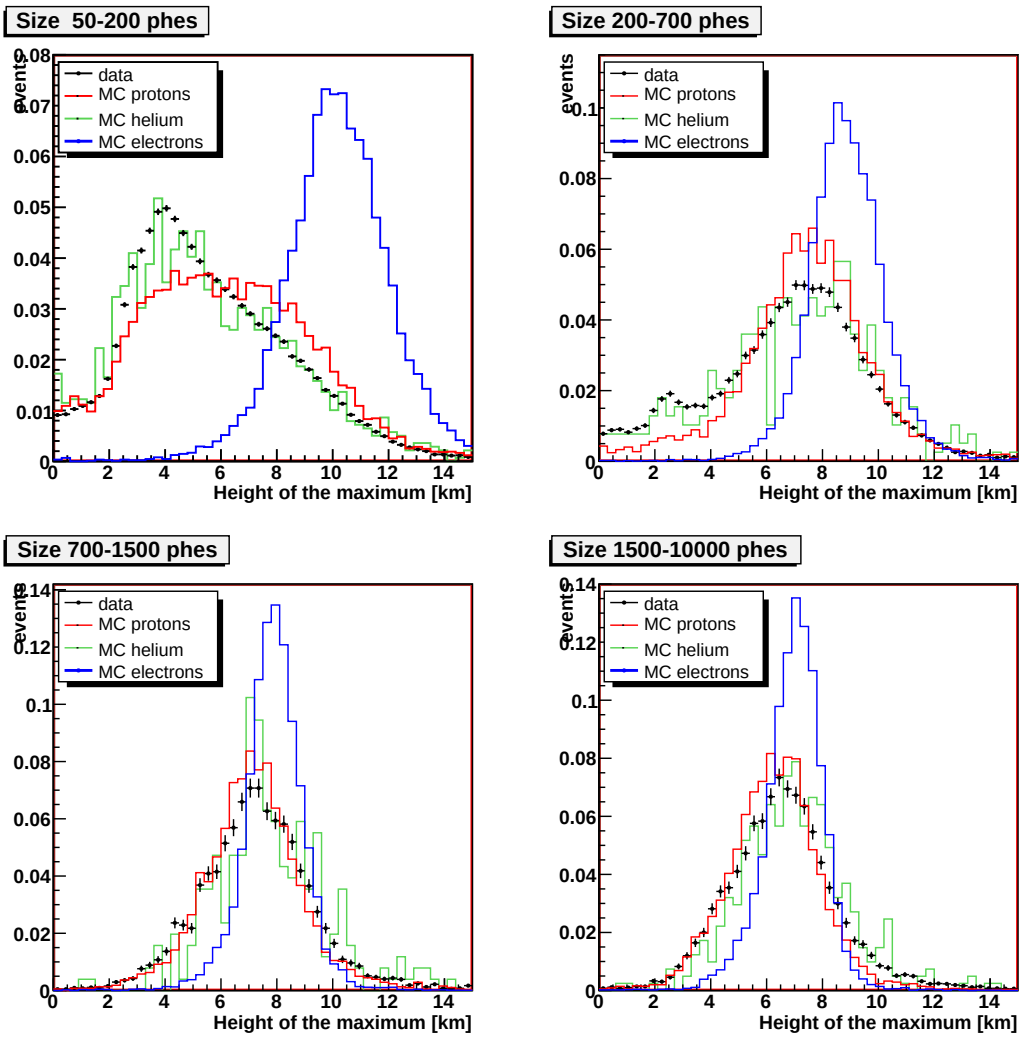

Fig. A.9: Distributions of the *Height* of the shower maximum in *Size* bins. Black: hadron data; red: MC protons; green: MC helium; blue: MC electrons. At low *Size* mainly muons are effecting the data

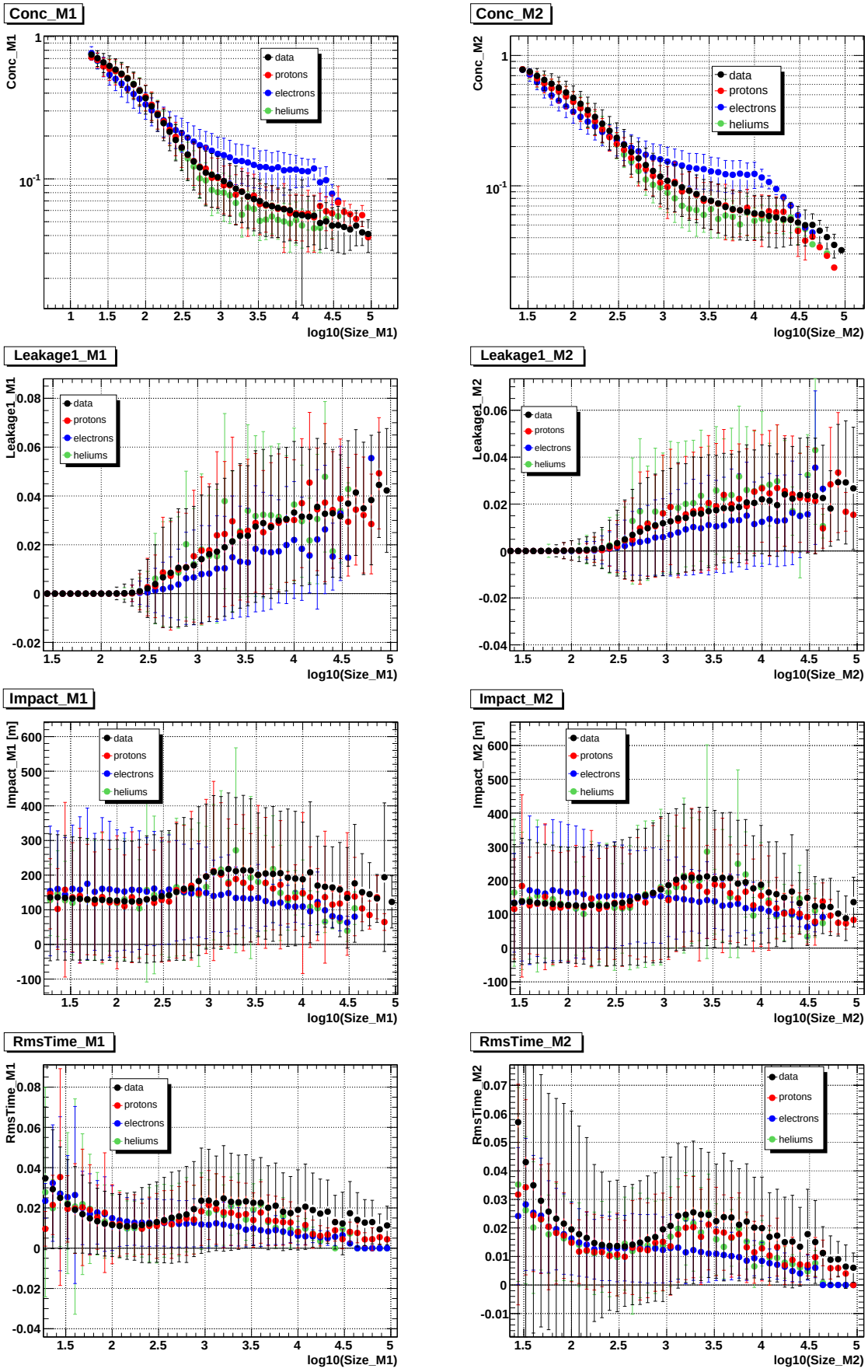

Fig. A.10: Distributions of Concentration, Leakage, Impact parameter and RMS Time of the images for the two telescopes as function of the respective sizes.

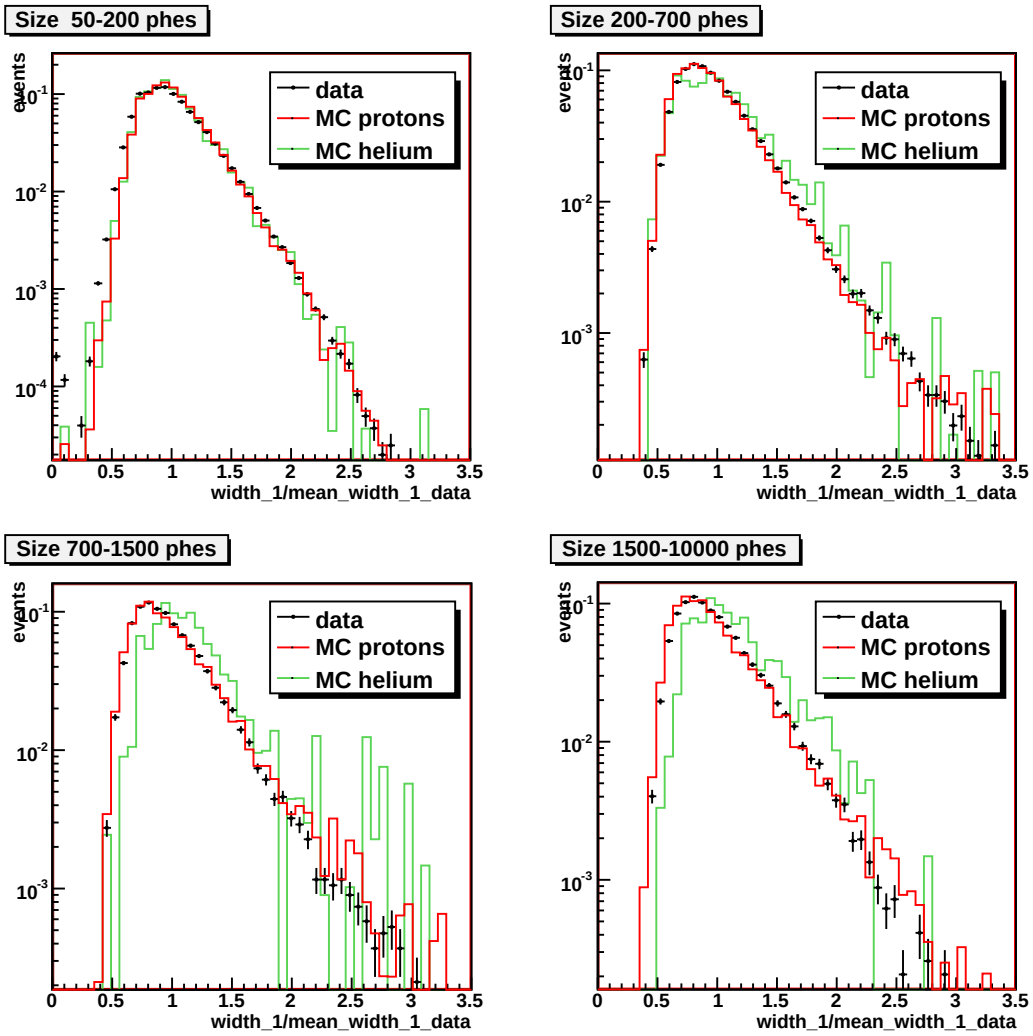

Fig. A.11: *Width* distributions of MAGIC-I images in different *size* bins. Black: hadron data; red: MC protons; green: MC helium.

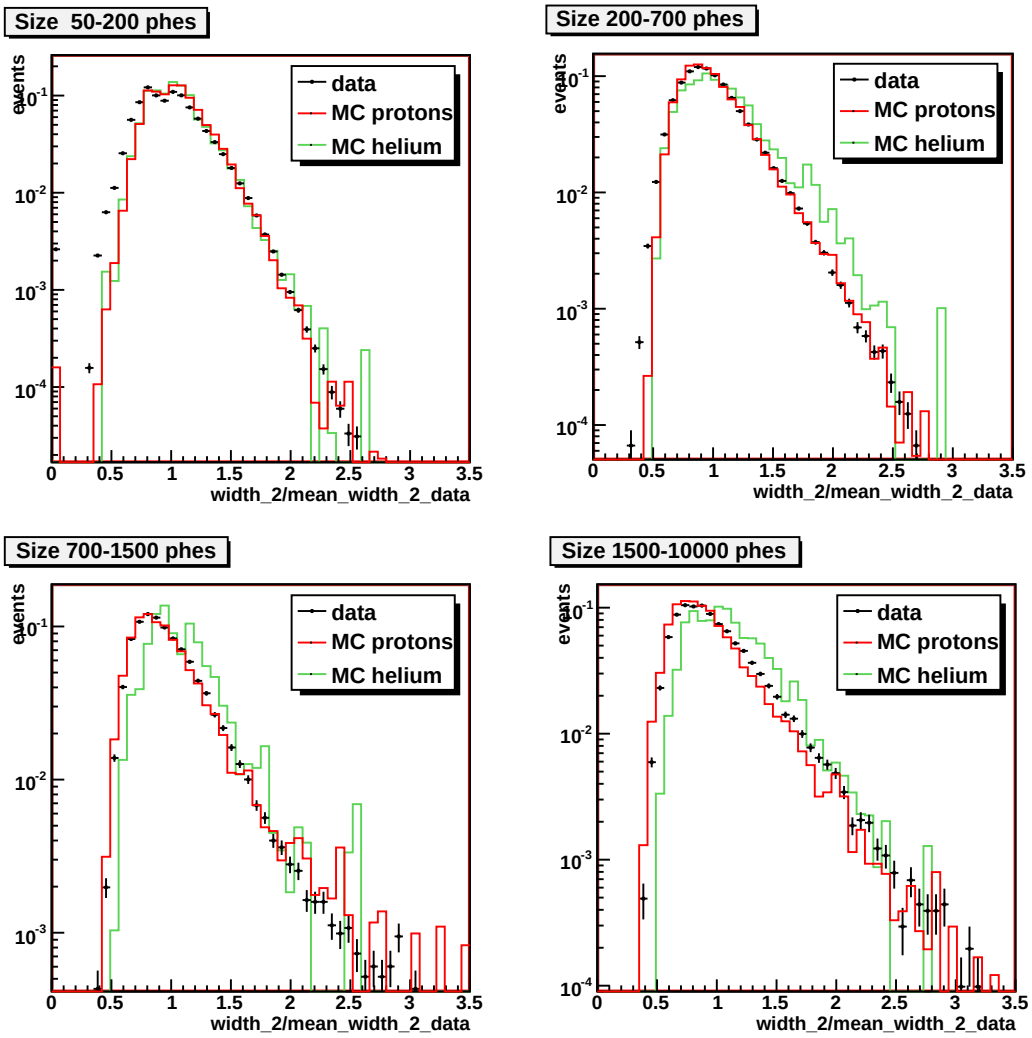

Fig. A.12: *Width* distributions of MAGIC-II images in different *size* bins. Black: hadron data; red: MC protons; green: MC helium.

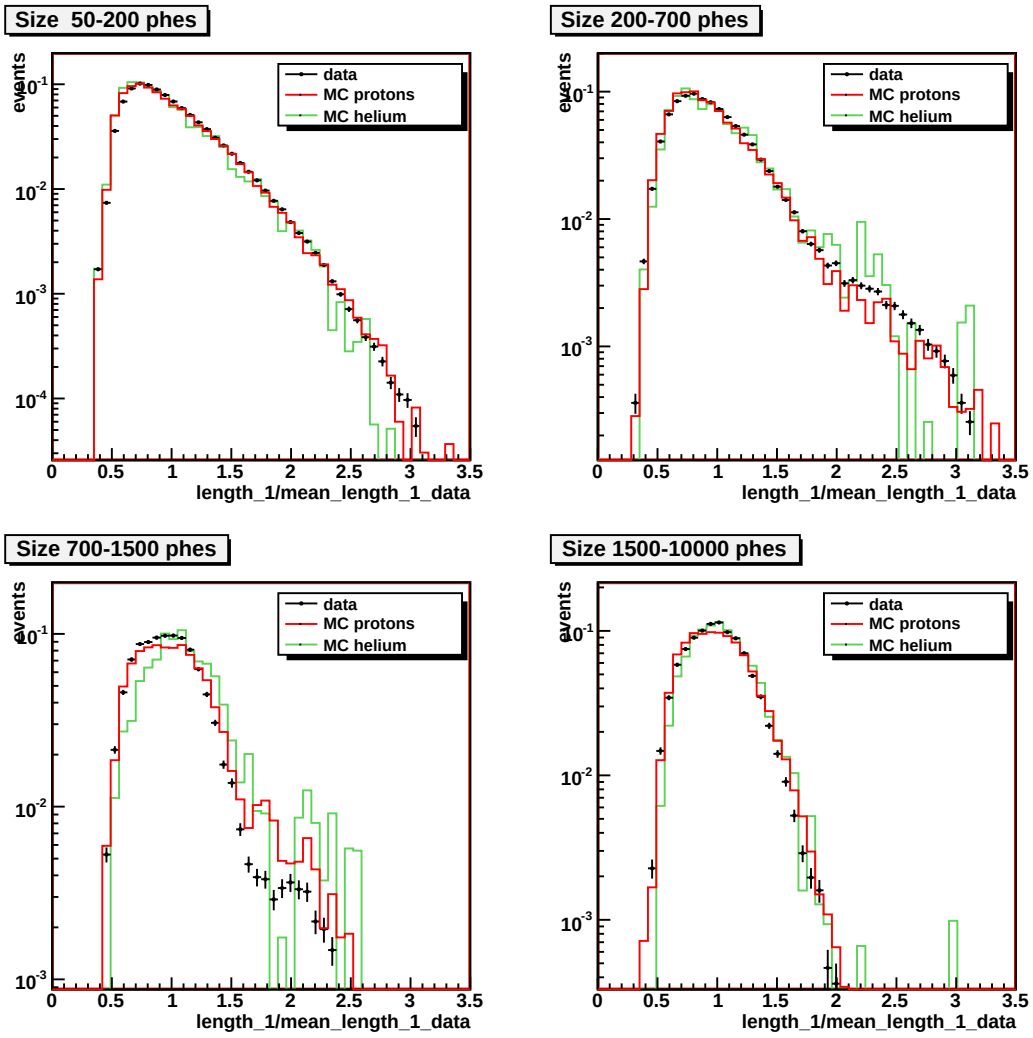

Fig. A.13: *Length* distributions of MAGIC-I images in different *size* bins. Black: hadron data; red: MC protons; green: MC helium.

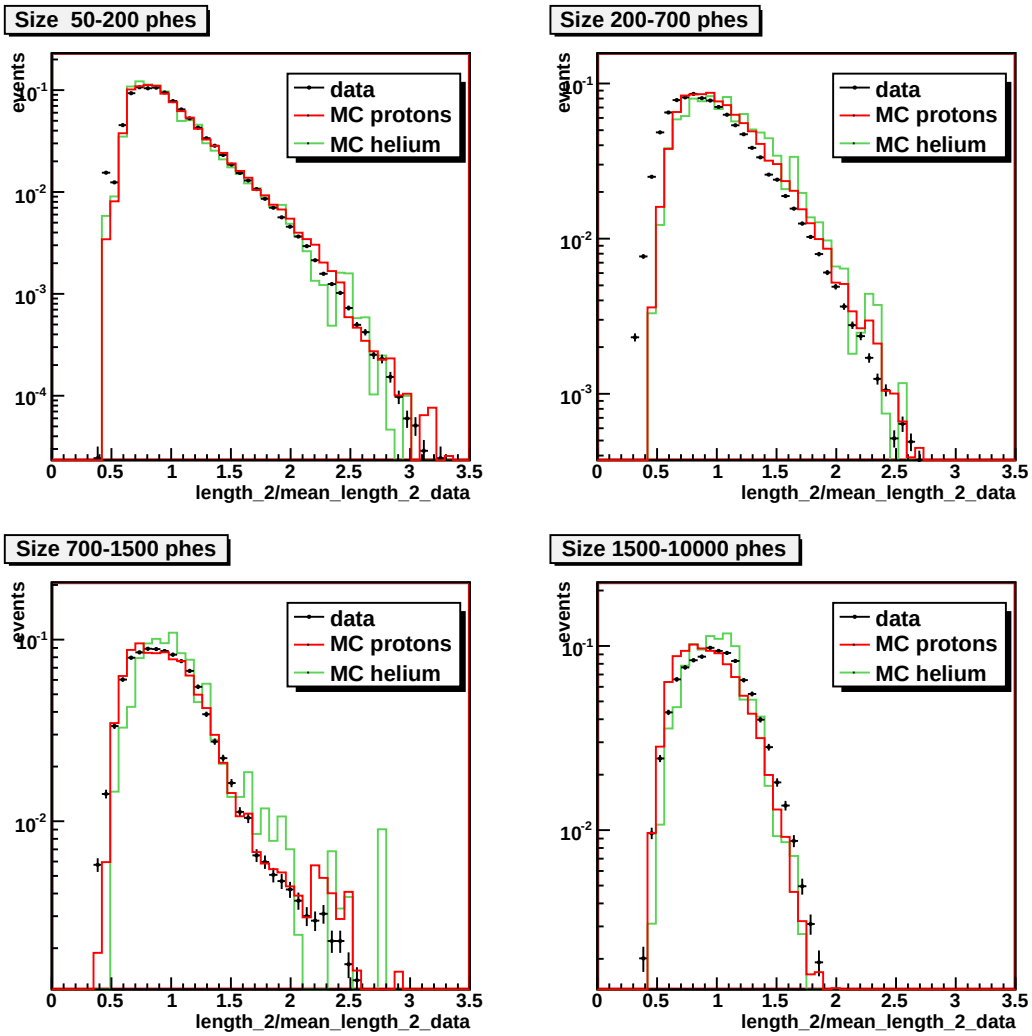

Fig. A.14: *Length* distributions of MAGIC-II images in different *size* bins. Black: hadron data; red: MC protons; green: MC helium.

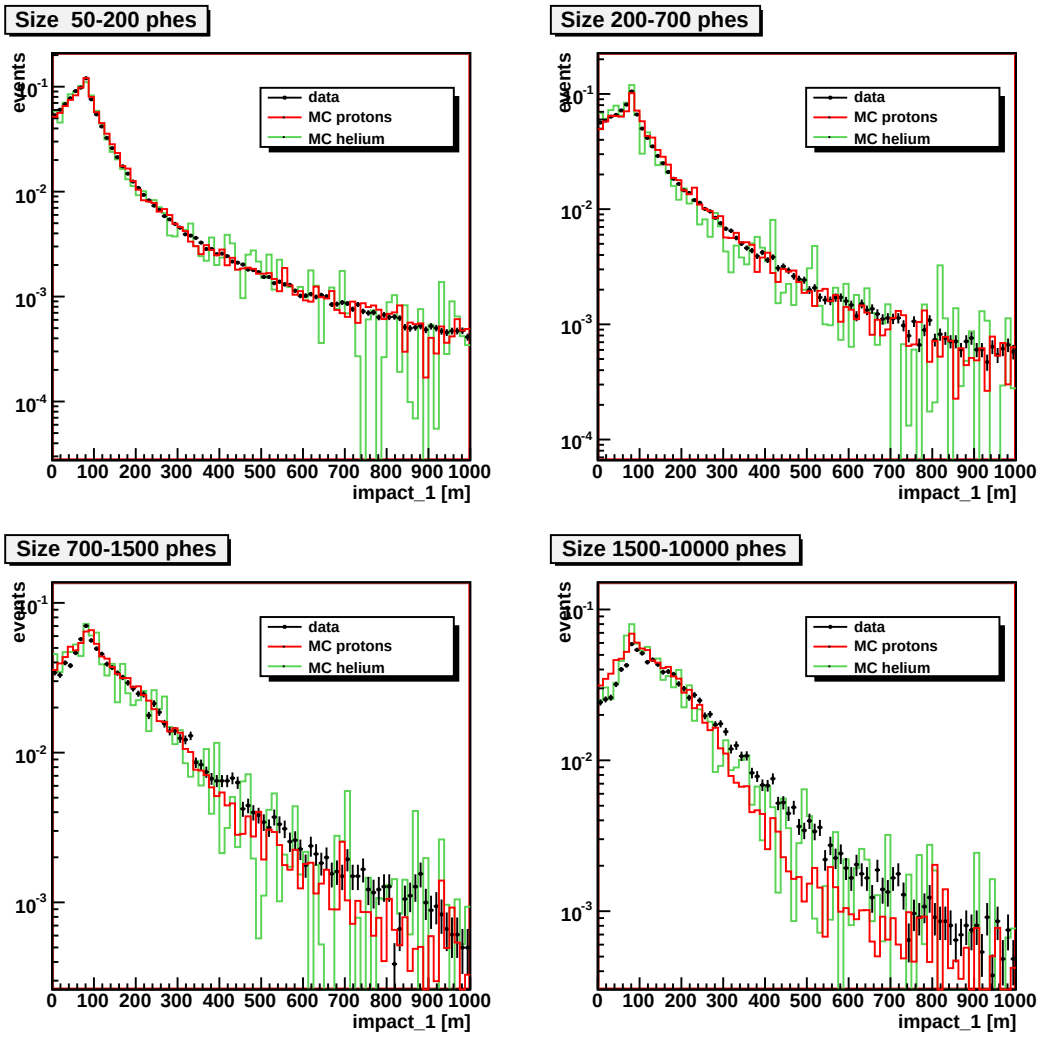

Fig. A.15: *Impact* distributions for MAGIC-I in different *size* bins. Black: hadron data; red: MC protons; green: MC helium.

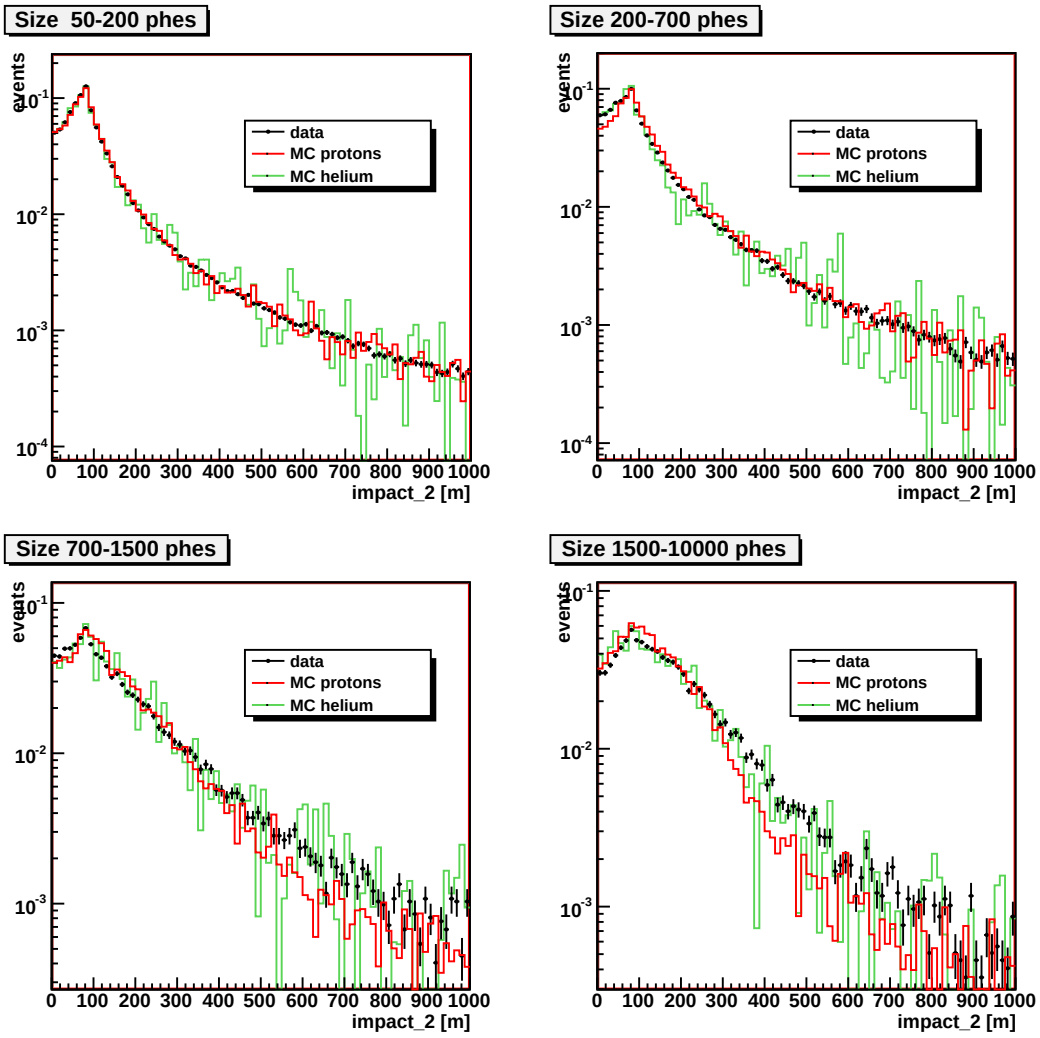

Fig. A.16: *Impact* distributions for MAGIC-II in different *size* bins. Black: hadron data; red: MC protons; green: MC helium.

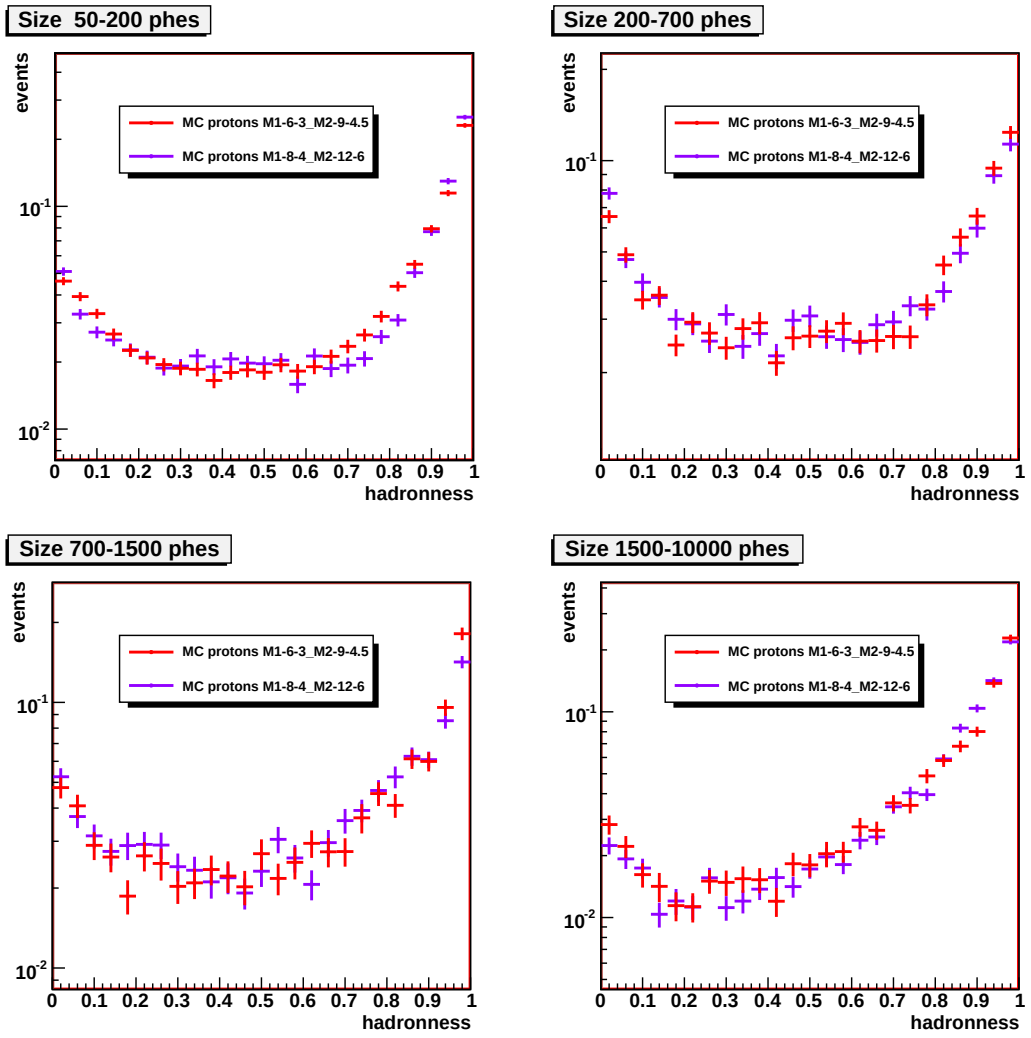

Fig. A.17: *Hadronness* distributions in size bins for protons MC samples for different cleaning. In red cleaning 6/3-time for MAGIC-I and 9/4.5-time for MAGIC-II. In violet cleaning 8/4-time for MAGIC-I and 12/6-time for MAGIC-II

B

Monte Carlo Simulations input cards

In this appendix the input cards used to simulate electrons, protons and helium are collected. These cards collect all the parameters used as input to run the programs and simulate the air showers. The values chosen are optimized for the study presented in this thesis in the energy range between few GeV and tens of TeV. In order are shown the *input cards* for the CORSIKA, *Reflector* and *Camera* program.

```
                ELECTRONS INPUT CARD

PRMPAR  3                          particle type
ERANGE  70.  7000.                  energy range
EVTNR   1                           number of first shower event
NSHOW   200                        number of showers to generate
ESLOPE  -2.0                        slope of primary energy spectrum
THETAP   5.  35.                    range of zenith angle (degree)
PHIP     0.  360.                   range of azimuth angle (degree)
QGSJET  T  0
QGSSIG  T
SEED 11350 0 0
SEED 11351 0 0
SEED 11352 0 0
OBSLEV  2200.E2                     observation level (in cm)
RADNKG  200.E2                      outer radius for NKG lat.dens.determ.
MAGNET  29.5  23.0                  magnetic field at LaPalma
ECUTS   0.3  0.3  0.02  0.02        e.cuts: had, mu, elec y fot
MUADDI  F                           additional info for muons
MUMULT  T                           muon multiple scattering angle
LONGI    T  10.  F   F              longit.distr. & step size & fit
MAXPRT   0                          max. number of printed events
ECTMAP  1.E4                        cut on gamma factor for printout
STEPFC   1.0                        mult. scattering step length fact.
DEBUG   F  6  F  1000000            debug flag and log.unit for out
CWAVLG  290.  900.                  Cherenkov wavelength band
CSCAT   20  0.  65000.             scatter Cherenkov events
CERSIZ  1.                          bunch size Cherenkov photons
CERFIL  T                           Cherenkov output to extra file
DATBAS  F                           write .dbase file
CERTEL  2
        3180.0  -2810.0 0.0 0.0 0.0 2000.0 1700.0  Location and size of the CTs
        -3180.0  2810.0 0.0 0.0 0.0 2000.0 1700.0
ATMOSPHERE   11 T                   MAGIC Winter atmosphere with refraction

                PROTONS INPUT CARD

PRMPAR  14                         particle type
ERANGE  70.  20000.                 energy range
EVTNR   1                           number of first shower event
NSHOW   600                         number of showers to generate
ESLOPE  -2.0                       slope of primary energy spectrum
THETAP   8.  38.                    range of zenith angle (degree)
PHIP     0.  360.                   range of azimuth angle (degree)
QGSJET  T  0
QGSSIG  T
SEED 12350 0 0
SEED 12351 0 0
SEED 12352 0 0
OBSLEV  2200.E2                     observation level (in cm)
RADNKG  200.E2                      outer radius for NKG lat.dens.determ.
MAGNET  29.5  23.0                  magnetic field at LaPalma
ECUTS   0.3  0.3  0.02  0.02        e.cuts: had, mu, elec y fot
MUADDI  F                           additional info for muons
MUMULT  T                           muon multiple scattering angle
LONGI    T  10.  F   F              longit.distr. & step size & fit
MAXPRT   0                          max. number of printed events
ECTMAP  1.E4                        cut on gamma factor for printout
STEPFC   1.0                        mult. scattering step length fact.
DEBUG   F  6  F  1000000            debug flag and log.unit for out
CWAVLG  290.  900.                  Cherenkov wavelength band
CSCAT   20  0.  120000.            scatter Cherenkov events
CERSIZ  1.                          bunch size Cherenkov photons
CERFIL  T                           Cherenkov output to extra file
DATBAS  F                           write .dbase file
CERTEL  2
        3180.0  -2810.0 0.0 0.0 0.0 2000.0 1700.0  Location and size of the CTs
        -3180.0  2810.0 0.0 0.0 0.0 2000.0 1700.0
ATMOSPHERE   11 T                   MAGIC Winter atmosphere with refraction
```

Fig. B.1: Input card used in CORSIKA to generate electrons and protons. The main parameters are displayed.

```
reflector 0.7
#
# Sample parameters file
#
verbose_level 1
#
# Seeds for random number generator:
seeds 1006030L 2006030L
#
telescopes_layout 1 2
telescope_position      3180.0  -2810.0
telescope_position      -3180.0  2810.0
# To reflect each event in the cer file several times with different orientations of
# the telescope, use the command:
# randomize_ct_orientation epsilon_min epsilon_max N_times.
# Each event will be reused N_times, pointing the telescope at random (isotropically) within a cone
# of semiaperture between epsilon_min and epsilon_max degree.
randomize_ct_orientation 0. 6.0 10
#
# Maximum number of events to be processed
max_events   10000000
#
# Some configuration files, and output file, for telescope 1:
#
ct_file           /afs/ipp/home/d/dborla/prog/MagicSoft/Simulation/Detector/Data/magic.def
reflectivity_file /afs/ipp/home/d/dborla/prog/MagicSoft/Simulation/Detector/Data/reflectivity.dat
axisdev_file      /afs/ipp/home/d/dborla/prog/MagicSoft/Simulation/Detector/Data/axisdev.dat
# Output file
output_file  /afs/ipp-garching.mpg.de/mpp/magic/mcdata/hadrons/rfl/Pr/Pr_za00to30_9_390_ct1_w0.rfl
#
# Some configuration files, and output file, for telescope 2:
#
ct_file          /afs/ipp/home/d/dborla/prog/MagicSoft/Simulation/Detector/Data/magic2.def
reflectivity_file /afs/ipp/home/d/dborla/prog/MagicSoft/Simulation/Detector/Data/reflectivity.dat
axisdev_file      /afs/ipp/home/d/dborla/prog/MagicSoft/Simulation/Detector/Data/axisdev.dat
#
output_file  /afs/ipp-garching.mpg.de/mpp/magic/mcdata/hadrons/rfl/He/006/heliums_stereo_production_7/
He_za00to30_9_390_ct2_w0.rfl
# Atmospheric model to be used in the absorption of C-photons for what regards to Rayleigh scattering:
atm_model     ATM_MagicWinter
#
#
cer_files
/afs/ipp-garching.mpg.de/mpp/magic/mcdata/hadrons/cer/Pr/004/protons_stereo_production_7/cer003891
/afs/ipp-garching.mpg.de/mpp/magic/mcdata/hadrons/cer/Pr/004/protons_stereo_production_7/cer003892
/afs/ipp-garching.mpg.de/mpp/magic/mcdata/hadrons/cer/Pr/004/protons_stereo_production_7/cer003893
/afs/ipp-garching.mpg.de/mpp/magic/mcdata/hadrons/cer/Pr/004/protons_stereo_production_7/cer003894
/afs/ipp-garching.mpg.de/mpp/magic/mcdata/hadrons/cer/Pr/004/protons_stereo_production_7/cer003895
/afs/ipp-garching.mpg.de/mpp/magic/mcdata/hadrons/cer/Pr/004/protons_stereo_production_7/cer003896
/afs/ipp-garching.mpg.de/mpp/magic/mcdata/hadrons/cer/Pr/004/protons_stereo_production_7/cer003897
/afs/ipp-garching.mpg.de/mpp/magic/mcdata/hadrons/cer/Pr/004/protons_stereo_production_7/cer003898
/afs/ipp-garching.mpg.de/mpp/magic/mcdata/hadrons/cer/Pr/004/protons_stereo_production_7/cer003899
/afs/ipp-garching.mpg.de/mpp/magic/mcdata/hadrons/cer/Pr/004/protons_stereo_production_7/cer003900
```

Fig. B.2: Input card used in the program *Reflector* to simulate the response of the reflector. The main parameters are displayed.

```
camera 0.85
# ------------------------------------------Common values for camera simulation-----------------------------------------
format_version 9
ct_num 2
ct_geom 14
project_name test
observation_mode OnOff
nsb_on
nsb_mean 0.20 10
seeds 16030 26030
write_McTrig
write_McFadc
data_file /afs/ipp-garching.mpg.de/mpp/magic/mcdata/hadrons/cam/Pr/005/protons_stereo_production_7/Pr_M1_za00to30_9_390_w0.dat
# ------------------------------------------------MAGIC-I simulation values-------------------------------------------------
qe_file 0 /afs/ipp-garching.mpg.de/home/d/dborla/prog/MagicSoft/Simulation/Detector/Data/qe-emi-coat.RFL.dat
lcoll_file 0 /afs/ipp-garching.mpg.de/home/d/dborla/prog/MagicSoft/Simulation/Detector/Data/LightCollection.dat
pmt_jitter_ns 0 0.3
chessboarding_jitter_ns 0 0
trigger_prop 0 3.0 0.25 1.0 2.0
trigger_delay 0 10.5
set_gain_fluct 0 -1
mirror_fraction 0 0.655
fadc_noise_from_file 0 /afs/ipp-garching.mpg.de/home/d/dborla/prog/MagicSoft/Simulation/Detector/Data/elecnoise_20070208.root
fadc_pedestal 0 2200.
sigma_xy_cm_spot 0 0.79
nsb_directory 0 /afs/ipp-garching.mpg.de/home/d/dborla/prog/MagicSoft/Simulation/Detector/StarResponse/StarLight_MUX/inner/
nsb_dir_outer 0 /afs/ipp-garching.mpg.de/home/d/dborla/prog/MagicSoft/Simulation/Detector/StarResponse/StarLight_MUX/outer/
fadc_type 0 2
fadc_prop 0 0 550. 2.3
fadc_outer 0 0 218. 2.3
fadc_GHz 0 2. 50 2 64 15 15
saturation_method 0 1
saturation_value 0 61000
trigger_single 0 4 4 2
misspoint_deg 0 0.4 0
input_file 0 /afs/ipp-garching.mpg.de/mpp/magic/mcdata/hadrons/rfl/Pr/006/protons_stereo_production_7/
Pr_za00to30_9_390_ct1_w0.rfl
root_file 0 /afs/ipp-garching.mpg.de/mpp/magic/mcdata/hadrons/cam/Pr/005/protons_stereo_production_7/
Pr_M1_za00to30_9_390_w0.root
# ------------------------------------------------MAGIC-II simulation values-------------------------------------------------
qe_file 1 /afs/ipp-garching.mpg.de/home/d/dborla/prog/MagicSoft/Simulation/Detector/Data/qe-hamamatsu-MAGIC2-
updated_scaled.RFL.dat
lcoll_file 1 /afs/ipp-garching.mpg.de/home/d/dborla/prog/MagicSoft/Simulation/Detector/Data/LightCollection-MAGIC2.dat
pmt_jitter_ns 1 0.4
chessboarding_jitter_ns 1 0
trigger_prop 1 3.0 0.25 1.0 2.3
trigger_delay 1 20.0
set_gain_fluct 1 -2
mirror_fraction 1 0.73
fadc_noise 1 20 20 0
fadc_pedestal 1 10000.
sigma_xy_cm_spot 1 0.79
nsb_directory 1 /afs/ipp-garching.mpg.de/home/d/dborla/prog/MagicSoft/Simulation/Detector/StarResponse/StarLight_DOM/
nsb_dir_outer 1 /afs/ipp-garching.mpg.de/home/d/dborla/prog/MagicSoft/Simulation/Detector/StarResponse/StarLight_DOM/
fadc_type 1 2
fadc_prop 1 0 150 3.5
fadc_outer 1 0 150. 3.5
fadc_GHz 1 2. 80 2 6 0 0
saturation_method 1 0
saturation_value 1 24000
trigger_single 1 4 4 2
misspoint_deg 1 0.4 0
input_file 1 /afs/ipp-garching.mpg.de/mpp/magic/mcdata/hadrons/rfl/Pr/006/protons_stereo_production_7/
Pr_za00to30_9_390_ct2_w0.rfl
root_file 1 /afs/ipp-garching.mpg.de/mpp/magic/mcdata/hadrons/cam/Pr/005/protons_stereo_production_7/
Pr_M2_za00to30_9_390_w0.root
end_file
```

Fig. B.3: Input card used in the program *Camera* to simulate the resins of the camera. The main parameters are displayed.

List of abbreviations

ADC	Analog to digital converter
AGN	Active galactic nucleus
AMC	Active mirror control
AMP	Amplifier
AMS	Alpha Magnetic Spectrometer
a.s.l.	above see level
ATIC	Advanced Thin Ionization Calorimeter
CANGAROO	Collaboration of Australia and Nippon for a GAmma Ray Observatory in the Outb
CCD	Charge coupling device
COG	Center of gravity
CORSIKA	COsmic Ray SImulations for KAscade
CR	Cormic ray
CU	Crab Units
DAQ	Data acquisition
DEC	Declination
DC	Direct current
DT	Discriminator threshold
EAS	Extensive air shower
EGRET	Energetic gamma ray experiment telescope
EM	Electro magnetic
FADC	Flash analogue to digital converter
FERMI	Fermi gamma ray telescope
FoV	Field of view
FWHM	Full width half maximum
GeV	Giga electron volt
GRB	Gamma ray burst
GZK-cutoff	Greisen Zatesepin Kuz'min cutoff
HBL	High frequency peaked BL Lac
HE	High energy
HEAT	High-Energy Antimatter Telescope
HEGRA	High energy gamma ray astronomy
H.E.S.S.	High energy stereoscopic system
HPD	Hybrid photo diode
HV	high voltage
IACT	Imaging atmospheric Cherenkov telescope
IC	Inverse Compton
IR	Infrared

IPRC	Individual pixel rate control
ISM	Inter stellar medium
keV	Kilo electron volt
KK	Kaluza-Klein paricle
kpc	Kilo parsec
L1	level one
LED	Light emitting diode
MAGIC	Major atmospheric gamma ray imaging Cherenkov (telescope)
MARS	MAGIC Analysis and Reconstruction Software
MC	Monte carlo (simulation)
MeV	Mega electron volt
MJD	Modified Julian date
MUX	Multiplexing 2GHz FADC read out
NDF	Number degrees of freedom
NN	Next neighbor
PAMELA	Payload for Antimatter Matter Exploration and Light-nuclei Astrophysics
PHE	Photoelectron
PIN	Positive intrinsic negative (diode)
PMT	Photo multiplier tube
PPB-BETS	Polar Patrol Balloon - Ballolon-borne Electron Telescope with Scintillating fibers
PSF	Point spread function
PWN	pulsar wind nebula
QE	Quantum efficiency
RA	Right ascension
RF	Random forest
SCCP	Slow control cluster processor
SNR	Supernova remnant
TeV	Tera electron volt
UHE	Ultra high energy
UL	Upper limit
UV	Ultra violet
VCSEL	Vertical cavity surface emitting laser
VERITAS	Very energetic radiation imaging telescope array system
VHE	Very high energy
WC	Winston cone
WMAP	Wilkinson Microwave Anisotropy Probe

List of Tables

List of Figures

Bibliography

[1] Extragalactic objects. http://magic.mppmu.mpg.de/ rwagner/sources/.

[2] FLUKA. http://www.fluka.org.

[3] ROOT. http://root.cern.ch.

[4] TANGO IN PARIS workshop, may 2009. http://irfu.cea.fr/Meetings/tangoinparis/.

[5] A. A. Abdo et al. Measurement of the Cosmic Ray e^++e^- Spectrum from 20 GeV to 1 TeV with the Fermi Large Area Telescope. *Physical Review Letters*, 102(18):181101–+, May 2009.

[6] A. A. Abdo et al. The Spectrum of the Isotropic Diffuse Gamma-Ray Emission Derived From First-Year Fermi Large Area Telescope Data. *Phys. Rev. Lett.*, 104:101101, 2010.

[7] M. Ackermann et al. Fermi LAT observations of cosmic-ray electrons from 7 GeV to 1 TeV. *Phys. Rev.*, D82:092004, 2010.

[8] M. Ackermann et al. Searches for Cosmic-Ray Electron Anisotropies with the Fermi Large Area Telescope. *Phys. Rev.*, D82:092003, 2010.

[9] O. Adriani et al. A new measurement of the antiproton-to-proton flux ratio up to 100 GeV in the cosmic radiation. *Phys. Rev. Lett.*, 102:051101, 2009.

[10] O. Adriani et al. An anomalous positron abundance in cosmic rays with energies 1.5-100 GeV. *Nature*, 458:607–609, 2009.

[11] F. Aharonian et al. The Crab Nebula and Pulsar between 500 GeV and 80 TeV: Observations with the HEGRA Stereoscopic Air Cerenkov Telescopes. *apj*, 614:897–913, Oct. 2004.

[12] F. Aharonian et al. Observations of the Crab Nebula with H.E.S.S. *Astron. Astrophys.*, 457:899–915, 2006.

[13] F. Aharonian et al. Energy Spectrum of Cosmic-Ray Electrons at TeV Energies. *Physical Review Letters*, 101(26):261104–+, Dec. 2008.

[14] F. Aharonian et al. Probing the ATIC peak in the cosmic-ray electron spectrum with H.E.S.S. *aap*, 508:561–564, Dec. 2009.

[15] F. A. Aharonian, A. M. Atoyan, and H. J. Voelk. High energy electrons and positrons in cosmic rays as an indicator of the existence of a nearby cosmic tevatron. *aap*, 294:L41–L44, Feb. 1995.

[16] J. Albert, E. Alium, H. Anderhub, and others (2008a). FADC signal reconstruction for the MAGIC telescope. *Nuclear Instruments and Methods in Physics Research*, 2008. A 594 407–419.

[17] J. Albert et al. MAGIC Upper Limits on the Very High Energy Emission from Gamma-Ray Bursts. *apj*, 667:358–366, Sept. 2007.

[18] J. Albert et al. Observation of VHE γ-rays from Cassiopeia A with the MAGIC telescope. *aap*, 474:937–940, Nov. 2007.

[19] J. Albert et al. MAGIC Observations of a 13-Day Flare Complex in M87 in February 2008. *Astrophys. J.*, 685:L23–L26, 2008.

[20] J. Albert et al. Multiwavelength (Radio, X-Ray, and γ-Ray) Observations of the γ-Ray Binary LS I +61 303. *apj*, 684:1351–1358, Sept. 2008.

[21] J. Albert et al. Upper Limit for γ-Ray Emission above 140 GeV from the Dwarf Spheroidal Galaxy Draco. *apj*, 679:428–431, May 2008.

[22] J. Albert et al. VHE Gamma-Ray Observation of the Crab Nebula and its Pulsar with the MAGIC telescope. *Astrophys. J.*, 674:1037–1055, 2008.

[23] J. Aleksic et al. MAGIC Stereo Crab Performance. 2011. Paper in preparation.

[24] E. Aliu et al. MAGIC upper limits on the VHE gamma-ray emission from the satellite galaxy Willman 1. *Astrophys. J.*, 697:1299–1304, 2009.

[25] E. Aliu and MAGIC Collaboration. Observation of Pulsed γ-Rays Above 25 GeV from the Crab Pulsar with MAGIC. *Science*, 322:1221–, Nov. 2008.

[26] E. Aliu and MAGIC Collaboration. Observation of Pulsed γ-Rays Above 25 GeV from the Crab Pulsar with MAGIC. *Science*, 322:1221–, Nov. 2008.

[27] R. Allahverdi, B. Dutta, K. Richardson-McDaniel, and Y. Santoso. A Supersymmetric B^- L Dark Matter Model and the Observed Anomalies in the Cosmic Rays. *Phys. Rev.*, D79:075005, 2009.

[28] AMS Collaboration, Aguilar, et al. The Alpha Magnetic Spectrometer (AMS) on the International Space Station: Part I - results from the test flight on the space shuttle. *physrep*, 366:331–405, Aug. 2002.

[29] C. Amsler et al. Review Of Particle Physics: Cosmic Rays. *Journal of Physics G*, 2009.

[30] J. Arons and E. T. Scharlemann. Pair formation above pulsar polar caps - Structure of the low altitude acceleration zone. *apj*, 231:854–879, Aug. 1979.

[31] A. Arvanitaki et al. Astrophysical Probes of Unification. *Phys. Rev.*, D79:105022, 2009.

[32] A. M. Atoyan, F. A. Aharonian, and H. J. Voelk. Electrons and positrons in the galactic cosmic rays. *prd*, 52:3265–3275, Sept. 1995.

[33] W. I. Axford, E. Leer, and G. Skadron. Acceleration of cosmic rays by shock waves. In *Nuclear Cosmophysics*, pages 125–134, 1978.

[34] K. J. Bae, J.-H. Huh, J. E. Kim, B. Kyae, and R. D. Viollier. White dwarf axions, PAMELA data, and flipped-SU(5). *Nucl. Phys.*, B817:58–75, 2009.

[35] J. Barrio et al. The MAGIC Telescope-Design study for the construction of a 17 m Cerenkov telescope for Gamma-Astronomy above 10 GeV. *MPI-PhE 98-05*, 1998.

[36] S. A. Bass et al. Microscopic models for ultrarelativistic heavy ion collisions. *Prog. Part. Nucl. Phys.*, 41:255–369, 1998.

[37] A. R. Bell. The acceleration of cosmic rays in shock fronts. II. *mnras*, 182:443–455, Feb. 1978.

[38] M. Bertero. Linear inverse and ill-posed problems. volume 75, pages 1–120. Academic Press, New York, 1989.

[39] X.-J. Bi, X.-G. He, and Q. Yuan. Parameters in a class of leptophilic models from PAMELA, ATIC and FERMI. *Phys. Lett.*, B678:168–173, 2009.

[40] A. Biland et al. The Active Mirror Control of the MAGIC Telescopes. In *International Cosmic Ray Conference*, volume 3 of *International Cosmic Ray Conference*, pages 1353–1356, 2008.

[41] R. D. Blandford and J. P. Ostriker. Particle acceleration by astrophysical shocks. *apjl*, 221:L29–L32, Apr. 1978.

[42] P. Blasi. The origin of the positron excess in cosmic rays. *Phys. Rev. Lett.*, 103:051104, 2009.

[43] R. K. Bock, A. Chilingarian, M. Gaug, F. Hakl, T. Hengstebeck, M. Jiřina, J. Klaschka, E. Kotrč, P. Savický, S. Towers, A. Vaiciulis, and W. Wittek. Methods for multidimensional event classification: a case study using images from a Cherenkov gamma-ray telescope. *Nuclear Instruments and Methods in Physics Research A*, 516:511–528, Jan. 2004.

[44] I. Bombaci. The maximum mass of a neutron star. *aap*, 305:871–+, Jan. 1996.

[45] D. Borla Tridon, F. Goebel, D. Fink, W. Haberer, J. Hose, C. C. Hsu, T. Jogler, R. Mirzoyan, R. Orito, O. Reimann, P. Sawallisch, J. Schlammer, T. Schweizer, B. Steinke, M. Teshima, and for the MAGIC Collaboration. Performance of the Camera of the MAGIC II Telescope. *ArXiv e-prints*, June 2009.

[46] D. Borla Tridon, T. Schweizer, F. Goebel, R. Mirzoyan, and M. Teshima. The MAGIC-II gamma-ray stereoscopic telescope system. *Nuclear Instruments and Methods in Physics Research Section A: Accelerators, Spectrometers, Detectors and Associated Equipment*, In Press, Corrected Proof:–, 2010.

[47] E. Borriello, L. Maccione, and A. Cuoco. Dark matter electron anisotropy: a universal upper limit. *ArXiv e-prints*, Nov. 2010.

[48] P. A. Caraveo, G. F. Bignami, R. Mignani, and L. G. Taff. Parallax Observations with the Hubble Space Telescope Yield the Distance to Geminga. *apjl*, 461:L91+, Apr. 1996.

[49] J. Chang et al. An excess of cosmic ray electrons at energies of 300-800 GeV. *Nature*, 456:362–365, 2008.

[50] C.-R. Chen, M. M. Nojiri, F. Takahashi, and T. T. Yanagida. Decaying Hidden Gauge Boson and the PAMELA and ATIC/PPB- BETS Anomalies. *Prog. Theor. Phys.*, 122:553–559, 2009.

[51] H. Cheng, J. L. Feng, and K. T. Matchev. Kaluza-Klein Dark Matter. *Physical Review Letters*, 89(21):211301–+, Oct. 2002.

[52] K. S. Cheng, C. Ho, and M. Ruderman. Energetic radiation from rapidly spinning pulsars. I - Outer magnetosphere gaps. II - VELA and Crab. *apj*, 300:500–539, Jan. 1986.

[53] I. Cholis, G. Dobler, D. P. Finkbeiner, L. Goodenough, and N. Weiner. The Case for a 700+ GeV WIMP: Cosmic Ray Spectra from ATIC and PAMELA. *Phys. Rev.*, D80:123518, 2009.

[54] P. Colin, D. Borla Tridon, D. Britzger, E. Lorenz, R. Mirzoyan, T. Schweizer, M. Teshima, et al. Observation of shadowing of the cosmic electrons and positrons by the Moon with IACT. 2009.

[55] R. Cowsik and L. Wilson. Is the Residence Time of Cosmic Rays in the Galaxy Energy-Dependent? In *International Cosmic Ray Conference*, volume 1 of *International Cosmic Ray Conference*, pages 500–+, 1973.

[56] P. D., H. J. Gebauer, E. Lorenz, and R. Mirzoyan. A method to enhance the sensitivity of photomultipliers for air cherenkov telescopes by applying a lacquer that scatters light. *Nucl. Instr. and Meth. in Phys. Res.*, A,518:619–621, 2004.

[57] T. Delahaye, R. Lineros, F. Donato, N. Fornengo, J. Lavalle, P. Salati, and R. Taillet. Galactic secondary positron flux at the Earth. *aap*, 501:821–833, July 2009.

[58] G. di Bernardo, C. Evoli, D. Gaggero, D. Grasso, L. Maccione, and M. N. Mazziotta. Implications of the cosmic ray electron spectrum and anisotropy measured with Fermi-LAT. *Astroparticle Physics*, 34:528–538, Feb. 2011.

[59] M. Doro et al. The reflective surface of the MAGIC telescope. *Nucl. Instr. and Meth. in Phys. Res.*, A,595:200–203, 2008.

[60] B. T. Draine and C. F. McKee. Theory of interstellar shocks. *araa*, 31:373–432, 1993.

[61] M. A. DuVernois et al. Cosmic-Ray Electrons and Positrons from 1 to 100 GeV: Measurements with HEAT and Their Interpretation. *apj*, 559:296–303, Sept. 2001.

[62] A. A. El Zant, S. Khalil, and H. Okada. Dark matter annihilation and the PAMELA, FERMI, and ATIC anomalies. *prd*, 81(12):123507–+, June 2010.

[63] R. Engel. Air Shower Calculations With the New Version of SIBYLL. In *International Cosmic Ray Conference*, volume 1 of *International Cosmic Ray Conference*, pages 415–+, 1999.

[64] R. Engel. Hadronic Interactions and Cosmic Ray Particle Physics. 30^th ICRC, Merida, 2007.

[65] Y. Fan, B. Zhang, and J. Chang. $e^{\pm}$ excesses in the Cosmic Ray Spectrum and Possible Interpretations. *ArXiv e-prints*, Aug. 2010.

[66] E. Fermi. On the Origin of the Cosmic Radiation. *Physical Review*, 75:1169–1174, Apr. 1949.

[67] H. Fesefeldt. The simulation of hadronic showers: Physics and Applications. PITHA-85-02.

[68] P. J. Fox and E. Poppitz. Leptophilic Dark Matter. *Phys. Rev.*, D79:083528, 2009.

[69] T. Gaisser. *Cosmic rays and particle physics*. 1990.

[70] M. Gaug. *Calibration of the MAGIC Telescope and Observation of Gamma Ray Bursts*. Phd thesis, Universitat Autonoma de Barcelona Departament de Fisica, March 2006.

[71] F. Goebel et al. The data acquisition of the MAGIC telecope. In *Proceedings of the 28th International Cosmic Ray Conference*, Japan, 2003.

[72] F. Goebel et al. Upgrade of the MAGIC telescope with a Multiplexer Fiber-Optic 2 GSamoles/s FADC Data Acquisition system. In *Proceedings of the 30th International Cosmic Ray Conference*, Merida, Mexico, 2007.

[73] H.-S. Goh, L. J. Hall, and P. Kumar. The Leptonic Higgs as a Messenger of Dark Matter. *JHEP*, 05:097, 2009.

[74] P. Goldreich and W. H. Julian. Pulsar Electrodynamics. *apj*, 157:869–+, Aug. 1969.

[75] D. Grasso, S. Profumo, A. W. Strong, et al. On possible interpretations of the high energy electron-positron spectrum measured by the Fermi Large Area Telescope. *Astroparticle Physics*, 32:140–151, Sept. 2009.

[76] K. Hamaguchi, E. Nakamura, S. Shirai, and T. T. Yanagida. Decaying Dark Matter Baryons in a Composite Messenger Model. *Phys. Lett.*, B674:299–302, 2009.

[77] K. Hamaguchi, S. Shirai, and T. T. Yanagida. Cosmic Ray Positron and Electron Excess from Hidden- Fermion Dark Matter Decays. *Phys. Lett.*, B673:247–250, 2009.

[78] Hamamatsu. *Photomultiplier tube. Principle to application.* Hamamatsu Photonics K. K., 1994.

[79] A. K. Harding, J. V. Stern, J. Dyks, and M. Frackowiak. High-Altitude Emission from Pulsar Slot Gaps: The Crab Pulsar. *apj*, 680:1378–1393, June 2008.

[80] D. Heck, J. Knapp, J. N. Capdevielle, et al. CORSIKA: A Monte Carlo Code to Simulate Extensive Air Shower. Wissenschaftliche Berichte FZKA 6019, Forschungszentrum Karlsruhe, 1998. http://www-ik3.fzk.de/ heck/corsika/.

[81] T. Heck, D. Pierog. Extensive Air Shower Simulation with CORSIKA: A User's Guide. Technical report, Forschungszentrum Karlsruhe, 2007. http://www-ik3.fzk.de/ heck/corsika/.

[82] A. M. Hillas. Cosmic rays: Recent progress and some current questions. *astro-ph/0607109*, 2006.

[83] J. A. Hinton. The status of the HESS project. *New Astron. Rev.*, 48:331–337, 2004.

[84] J. Holder et al. The first VERITAS telescope. *Astroparticle Physics*, 25:391–401, July 2006.

[85] D. Hooper, D. P. Finkbeiner, and G. Dobler. Evidence Of Dark Matter Annihilations In The WMAP Haze. *Phys. Rev.*, D76:083012, 2007.

[86] D. Hooper, A. Stebbins, and K. M. Zurek. Excesses in cosmic ray positron and electron spectra from a nearby clump of neutralino dark matter. *Phys. Rev.*, D79:103513, 2009.

[87] D. Hrupec. Extragalactic sources of rapidly variable high energy gamma radiation. 2008. PhD thesis.

[88] A. Ibarra and D. Tran. Decaying Dark Matter and the PAMELA Anomaly. *JCAP*, 0902:021, 2009.

[89] A. Ibarra, D. Tran, and C. Weniger. Decaying dark matter in light of the PAMELA and Fermi LAT data. *jcap*, 1:9–+, Jan. 2010.

[90] K. Ishiwata, S. Matsumoto, and T. Moroi. Cosmic-Ray Positron from Superparticle Dark Matter and the PAMELA Anomaly. *Phys. Lett.*, B675:446–449, 2009.

[91] K. Kadota, K. Freese, and P. Gondolo. Positrons in cosmic rays from dark matter annihilations for uplifted Higgs regions in the MSSM. *prd*, 81(11):115006–+, June 2010.

[92] T. Kamae, N. Karlsson, T. Mizuno, T. Abe, and T. Koi. Parameterization of γ, $e^{+/-}$, and Neutrino Spectra Produced by p-p Interaction in Astronomical Environments. *apj*, 647:692–708, Aug. 2006.

[93] T. M. Kneiske and K. Mannheim. BL Lacertae contribution to the extragalactic gamma-ray background. *aap*, 479:41–47, Feb. 2008.

[94] T. Kobayashi. High Energy Cosmic-Ray Electrons Beyond 100 GeV. In *International Cosmic Ray Conference*, volume 3 of *International Cosmic Ray Conference*, pages 61–+, Aug. 1999.

[95] T. Kobayashi, Y. Komori, K. Yoshida, and J. Nishimura. The Most Likely Sources of High-Energy Cosmic-Ray Electrons in Supernova Remnants. *apj*, 601:340–351, Jan. 2004.

[96] G. F. Krymskii. A regular mechanism for the acceleration of charged particles on the front of a shock wave. *Akademiia Nauk SSSR Doklady*, 234:1306–1308, June 1977.

[97] H. Kubo et al. Status of the CANGAROO-III project. *New Astronomy Review*, 48:323–329, Apr. 2004.

[98] M. Lattanzi and J. I. Silk. Can the WIMP annihilation boost factor be boosted by the Sommerfeld enhancement? *Phys. Rev.*, D79:083523, 2009.

[99] T. Li and Y. Ma. Analysis methods for results in gamma-ray astronomy. *apj*, 272:317–324, Sept. 1983.

[100] M. S. Longair. *High Energy Astrophysics*. Cambridge University Press, 1992.

[101] A. M. Hillas. Cerenkov light images of EAS produced by primary gamma rays and by nuclei. In F. C. Jones, editor, *Proceedings of the 19th International Cosmic Ray Conference*, volume 3, pages 445–448, La Jolla, August 1985.

[102] MAGIC Collaboration and J. Albert. Very-High-Energy gamma rays from a Distant Quasar: How Transparent Is the Universe? *Science*, 320:1752–, June 2008.

[103] MAGIC Collaboration, J. Albert, et al. Probing quantum gravity using photons from a flare of the active galactic nucleus Markarian 501 observed by the MAGIC telescope. *Physics Letters B*, 668:253–257, Oct. 2008.

[104] G. Maier and J. Knapp. Cosmic-Ray Events as Background in Imaging Atmospheric Cherenkov Telescopes. *Astroparticle Physics*, April 2007.

[105] R. N. Manchester, G. B. Hobbs, A. Teoh, and M. Hobbs. The Australia Telescope National Facility Pulsar Catalogue. *aj*, 129:1993–2006, Apr. 2005.

[106] J. Mardon, Y. Nomura, D. Stolarski, and J. Thaler. Dark Matter Signals from Cascade Annihilations. *JCAP*, 0905:016, 2009.

[107] N. Mayall. The Crab Nebula, a Probable Supernova. *Leaflet of the Astronomical Society of the Pacific*, 3:145–+, 1939.

[108] P. Meade, M. Papucci, A. Strumia, and T. Volansky. Dark Matter Interpretations of the Electron/Positron Excesses after FERMI. *Nucl. Phys.*, B831:178–203, 2010.

[109] P. Meade, M. Papucci, A. Strumia, and T. Volansky. Dark Matter interpretations of the $e^{\pm}$ excesses after FERMI. *Nuclear Physics B*, 831:178–203, May 2010.

[110] P. Meade, M. Papucci, and T. Volansky. Dark Matter Sees The Light. *JHEP*, 12:052, 2009.

[111] R. Mirzoyan. Conversion factor calibration for MAGIC based on the use of measured F-factors of PMTs. 2000. MAGIC-TDAS 00-15.

[112] A. Moralejo. The reflector simulation program v.0.6. 2003. MAGIC-TDAS 02-11.

[113] A. Moralejo. How to use the camera simulation programm 0.7. 2004. MAGIC-TDAS 04-07.

[114] I. V. Moskalenko and A. W. Strong. Production and Propagation of Cosmic-Ray Positrons and Electrons. *apj*, 493:694–+, Jan. 1998.

[115] E. Nardi, F. Sannino, and A. Strumia. Decaying Dark Matter can explain the electron/positron excesses. *JCAP*, 0901:043, 2009.

[116] W. R. Nelson, H. Hirayama, and D. W. O. Rogers. The EGS4 code system. SLAC-0265.

[117] Y. Nomura and J. Thaler. Dark Matter through the Axion Portal. *Phys. Rev.*, D79:075008, 2009.

[118] A. Ostankov, P. D., E. Lorenz, M. Martinez, and R. Mirzoyan. A study of the new hemispherical 6-dynodes PMT from electron tubes. *Nucl. Instr. and Meth. in Phys. Res.*, A,442:117–123, 2000.

[119] S. Ostapchenko. QGSJET-II: results of the extensive air showers. *Astroparticle Physics*, December 2004.

[120] N. Otte. *Observation of VHE γ-Rays from the Vicinity of magnerized Neutron Stars and Development of new Photon-Detectors for Future Ground based γ-Ray Detector*. Ph.d., Technische Universität München, 2007.

[121] D. Paneque. *The MAGIC Telescope: development of new technologies and first observations*. Ph.d., Technische Universitat Muenchen, 2004.

[122] R. Paoletti. The MAGIC level 2 triger, A user's manual. 2003. MAGIC-TDAS 03-04.

[123] D. J. Phalen, A. Pierce, and N. Weiner. Cosmic Ray Positrons from Annihilations into a New, Heavy Lepton. *Phys. Rev.*, D80:063513, 2009.

[124] M. Pohl. Cosmic-ray electron signatures of dark matter. *Phys. Rev.*, D79:041301, 2009.

[125] E. Ponton and L. Randall. TeV Scale Singlet Dark Matter. *JHEP*, 04:080, 2009.

[126] E. Ponton and L. Randall. TeV Scale Singlet Dark Matter. *JHEP*, 04:080, 2009.

[127] M. Pospelov and A. Ritz. Astrophysical Signatures of Secluded Dark Matter. *Phys. Lett.*, B671:391–397, 2009.

[128] M. Pospelov and M. Trott. R-parity preserving super-WIMP decays. *JHEP*, 04:044, 2009.

[129] V. Ptuskin, I. Moskalenko, F. Jones, A. Strong, and V. Zirakashvili. Dissipation of Magnetohydrodynamic Waves on Energetic Particles: Impact on Interstellar Turbulence and Cosmic-Ray Transport. *apj*, 642:902–916, May 2006.

[130] M. Rissi. Detection of pulses very high energy gamma-rays from the Crab pulsar with the MAGIC telescope using the analog sum trigger. 2009. PhD thesis.

[131] B. Rossi and K. Greisen. Cosmic-ray theory. *Rev. Mod. Phys.*, 13(4):240–309, Oct 1941.

[132] M. A. Ruderman and P. G. Sutherland. Theory of pulsars - Polar caps, sparks, and coherent microwave radiation. *apj*, 196:51–72, Feb. 1975.

[133] T. Y. Saito et al. Recent Progress of GaAsP HPD development for the MAGIC telescope project. 30^th ICRC, Merida, 2007.

[134] M. Schmelling. The method of reduced cross-entropy A general approach to unfold probability distributions. *Nuclear Instruments and Methods in Physics Research A*, 340:400–412, February 1994.

[135] F. Schmidt. CORSIKA shower images. 2007. http://www.ast.leeds.ac.uk/ fs/showerimages.html.

[136] T. Schweizer, E. Lorenz, M. Martinez, A. Ostankov, and D. Paneque. The optical calibration of the MAGIC telescope camera. *IEEE Transactions on Nuclear Science*, 49:2497–2503, 2002.

[137] J. A. Simpson. Annual Review Of Nuclear And Particle Science. 33:323, 1983.

[138] A. W. Strong, I. V. Moskalenko, and O. Reimer. Diffuse Galactic Continuum Gamma Rays: A Model Compatible with EGRET Data and Cosmic-Ray Measurements. *apj*, 613:962–976, Oct. 2004.

[139] D. Tescaro et al. The readout system of the MAGIC- II Cherenkov Telescope. 2009.

[140] A. N. Tikhonov and V. J. Arsenin. Methods of Solution of Ill-posed Problems, Nauka, Moskov. 1979.

[141] S. Torii et al. High-energy electron observations by PPB-BETS flight in Antarctica. *ArXiv e-prints*, Sept. 2008.

[142] R. M. Wagner. Temporal and spectral characteristics of the VHE gamma-ray emission of four blazars as observed with the MAGIC telescope and a comparative study of the properties of VHE gamma-ray emitting blazars. 2006. PhD thesis.

[143] T. C. Weekes et al. Observation of TeV gamma rays from the Crab nebula using the atmospheric Cerenkov imaging technique. *apj*, 342:379–395, July 1989.

[144] K. W. Weiler and N. Panagia. VELA X and the evolution of Plerions. *aap*, 90:269–282, Oct. 1980.

[145] K. W. Weiler and R. A. Sramek. Supernovae and supernova remnants. *araa*, 26:295–341, 1988.

[146] J. C. Wheeler, M. Lecar, and C. F. McKee. Supernovae in binary systems. *apj*, 200:145–157, Aug. 1975.

[147] W. Wittek. Image parameters. 2002. MAGIC-TDAS 02-03.

[148] W. Wittek. Unfolding, revised version. 2006. MAGIC-TDAS 05-05.

[149] W. M. Yao et al. Review Of Particle Physics. *Journal of Physics G*, 33:1–1232, 2006.

[150] K. o. Yoshida. Cosmic-ray electron spectrum above 100 GeV from PPB-BETS experiment in Antarctica. *Advances in Space Research*, 42:1670–1675, Nov. 2008.

[151] J. Zhang et al. Discriminating different scenarios to account for the cosmic e + /- excess by synchrotron and inverse Compton radiation. *Phys. Rev.*, D80:023007, 2009.

[152] L. Zhang, C. Weniger, L. Maccione, J. Redondo, and G. Sigl. Constraining decaying dark matter with Fermi LAT gamma-rays. *Journal of Cosmology and Astro-Particle Physics*, 6:27–+, June 2010.

[153] K. M. Zurek. Multi-Component Dark Matter. *Phys. Rev.*, D79:115002, 2009.

Fuori dai confini tuoi
mille volti attorno e poi
storie da scoprire
dentro nei pensieri tuoi
scorre ritmo e musica
e si deve vivere
trova il tempo
per guardarti dentro
e spiccare in volo
spezza il tuo silenzio
per gridare al mondo
che il presente sará, solo tuo!

Ci vuole un senso – I Nomadi

Acknowledgements

The time spent in Munich during my PhD studies made me grow up not only professionally, but also in many other aspect of my character. I met many people during this time and I shared with them many experiences. Good and bad memories are now part of me. Someone used to say: "What does not kill you make you stronger".
There are many people I want to remember and to thanks.

First, an obliged thanks goes to Prof. Dr. Sigfried Bethke for being my academic supervisor at the Technische Universität München. Certainly Prof. Dr. Masahiro Teshima for giving me the opportunity to join as a PhD student the MAGIC collaboration at the MPI. The MPI itself for the excellent working environment. Sincere thanks go to Dr. Eckart Lorenz, because he believed in me and made me believing in myself. For the many inspiring discussions and for his commitment. Many thanks to Dr. Thomas Schweizer, because as one of my supervisors always supported and guided me. Thanks to Dr. Razmick Mirzoyan, as my group leader. Thanks to Dr. Rodolf Bock for helping in finalizing the english corrections of my thesis. I want to remember Florian Göbel, his personality and his devotion to the project and to the people.
The person with who I was working every day, Pierre Colin, for always being available and finding time for discussing with me and for supporting me especially in the difficulties, thanks a lot! My two office mates, Tobias Jogler and Burkhard Steinke. I wonder how sometime they could stand me. For the great time spent with them and for the infinite discussions, thanks a lot guys. Thanks to Julian Sitarek, for his natural tendency of solving the problems. Thanks to my other colleagues, Hanna Kellermann, for her sweetness, Hiroko Miyamoto, Pratik Majumdar, Nicola Galante, Julian Krause, Dennis Häfner, Takayuki Saito, Maxim Shayduk, Emiliano Carmona, Ulisses Barres de Almeida, David Paneque, Robert Wagner, Christian Fruck, Matthias Kurz, Hajime Takami for the nice working (and not only) environment created around me. Thanks also to David Fink, Olaf Reimann, Jens Schlammer and Stefan Horn for the excellent work on the MAGIC-II camera tests. Thanks to Sybille Rodrigues for her perfect organization and to Ina Wacker for her sympathy.
Many thanks go to Villi Scalzotto, for his collaboration and help in the project of the electron studies, as well as to Michele Doro. Thanks to Christoph Weniger for the fruitful physics discussions.
My stay in Munich would not have been so pleasant without you guys: Carla Biggio,

Carlos Hernandez Monteagudo, Javi Redondo, Mattias Blennow, Fabiana Cossavella, Irene Tamborra, Davide Pagani, and each of you know why. And then, my friends of always, Moni, Mati, Fabri, Stella, Erika, Cri, Matte, Stefi, Luis, for loving me and being always with me, for colouring and enriching my life.
Finally, the greatest thanks are for my family, my brother Massimo, my mum and my dad, for their whole-hearted and unreserved love, for their support and encouragement. I love you.